# The impact of atmosphere-ocean-wave coupling on extreme surface winds over the British Isles and surrounding seas

---

Emanuele Silvio Gentile

*Thesis submitted for the degree of Doctor of Philosophy*

**PhD in Atmosphere, Ocean, and Climate**

**Department of Meteorology**

**School of Mathematical, Physical and Computational Sciences**

**September 2022**

University of Reading

# Declaration

I confirm that this is my own work and the use of all material from other sources has been properly and fully acknowledged.

Emanuele Silvio Gentile

# Abstract

The predictability of extratropical cyclone (ETC) extreme winds is limited by numerical weather prediction (NWP) model physics approximations and initial condition errors. The aim of this research is to improve our understanding of the role played by air-sea fluxes in controlling ETC extreme surface wind speeds, and how accurate modelling of air-sea fluxes can improve ETC forecasts.

First, a climatology of observed offshore extreme wind speeds, gusts, and wave heights near the British Isles is created over the period 2012-2020, and extreme events are objectively attributed to ETC conveyor belt jets by an ad-hoc algorithm. The cold conveyor belt is associated with the most hazardous jet, with the largest number of compound wind and wave hazards attributed to it. This jet is also the most underestimated by the latest ECMWF reanalysis, ERA5.

Next, the sensitivity of ETCs to air-sea fluxes is explored by running a convective-scale atmosphere-ocean-wave coupled NWP model developed by the Met Office for three ETCs crossing the British Isles. Coupling to waves reduces the ETC extreme surface wind speeds, implying young growing wind waves enhance the air-sea momentum flux by increasing the sea-surface aerodynamic roughness. Finally, the deterministic coupled system is integrated with the Met Office ensemble capabilities into the new Ensemble-RCS framework to assess the respective impacts on ETC extreme winds of coupling and ensemble perturbations. The impact of coupling to waves on ETC extreme wind speeds is at least comparable in size to that of initial condition and stochastic physics perturbations, and is consistent across the ensemble members.

Overall, this research demonstrates that coupling to waves is a fundamental aspect of model uncertainty in NWP convective-scale forecasts of ETC extreme wind speeds and that NWPs need to take into account the effect of the dynamic sea state on air-sea fluxes to reduce the model biases.

# Acknowledgements

I would like to start by thanking my main supervisor, Sue Gray. I will be forever grateful to her for the amount of knowledge she shared, the patience in working out every detailed aspect of this work, the passion for scientific research she instilled into me, and the great example she set for my future career as scientist. Then, I would like to express my gratitude to my co-supervisor Huw Lewis for being a guide to me during my internship at the Met Office and for always illuminating me with fresh scientific perspective whenever I asked for. Without Sue's and Huw's support, it would have not been possible to carry out the research in this thesis. I am also grateful to my co-supervisor Janet Barlow for the inspiring physics insights and the stimulating discussions on wind energy. I would also like to thank John Edwards, who was always there to discuss science and give his fresh insights on the Boundary Layer. Further thanks go to my monitoring committee, Steven Woolnough and Richard Allan, for the stimulating discussions, and for the grilling about my work, which widened my research perspectives, whilst pushing up my standards. Thanks also to Juan Castillo, Anne McCabe, and Joe Carr for the help with the MetUM. I would also like to thank Aurore Porson for discussing the applicability of the Fractions Skill Score to wind speeds. Lastly, I am grateful to Remi Tailleux and Miguel Teixeira for the time we spent together discussing theoretical physics in atmospheric science, while sharing a glass of wine. I hope I can collaborate with you all more in the future!

I would also like to thank everyone who is/was in Lyle 5th floor and 1U07 and all the other PhD students for the time spent together over the last four years, despite the pandemic. I would also like to thank everyone who attended the mesoscale group and put up with my pestering for giving talks. I would also like to thank the Natural Environmental Research Council for providing the funding for my project and the Met Office for supporting my research activities.

Finally, I would like to thank my parents who always supported and encouraged me to overcome the life and work difficulties posed by the pandemic. In particular, I am eternally grateful to my loving mother who inspired me the curiosity and the passion for science and mathematics.

# Table of Contents

# Chapter 1

# Introduction

## 1.1 Introduction and motivation

The weather of the UK is heavily influenced by the passage of large-scale midlatitude depressions, termed extratropical cyclones (ETCs). When ETCs make landfall on the UK (usually during winter time), they can bring extreme weather conditions (see Fig. 1.1), associated with heavy precipitation and extreme surface winds, causing widespread damage to lives and livelihoods (Craig, 2003; Hewston and Dorling, 2011; Earl *et al.*, 2017).

The most striking example of ETCs as a weather peril is the Great Storm of 1987, whose track swathed across England and Wales causing widespread damage amounting to 1.9 billion of pounds worth of insurance losses (Lamb and Frydendhal, 1991; Munich Re, 2002). A more recent example is the winter storm Xynthia, which crossed Europe in February 2010 causing 3 billion of pounds in insurance losses in Germany, France, and Spain. This made

**Figure 1.1:** Storm Ciara battering Wales coastline in February 2020. Taken from BBC (2020).

ETC Xynthia the world's third most catastrophic event in terms of economic damage, more costly than any 2010 North Atlantic hurricane (Swiss Re, 2011). Even when averaging over multiple years, ETCs consistently rank as the most significant weather hazard over Europe, causing damages even equivalent to those caused by hurricanes all over the world.

The damaging strong surface winds associated with ETCs originate from distinct airstreams (also termed low-level jets) within the cyclones (Hewson and Neu, 2015): the warm conveyor belt (WCB), the cold conveyor belt (CCB), and the sting jet (SJ) (Browning and Roberts, 1994; Clark and Gray, 2018). The WCB originates as a low-level jet and then ascends over the warm front above the cold air below, leading to intense surface wind speeds. However, some of the strongest and most damaging surface winds form on the rear, equatorward flank of ETCs, when the CCB winds wrap around the low-pressure centre and mix through the boundary layer, producing extreme gusts at the surface (returning CCB). Sometimes a finer-scale mesoscale airstream, the SJ, is also present in ETCs. The SJ exits from the tip of the hook-shaped cloud head and descends rapidly to the surface, producing an additional region of exceptionally strong gusts. Even a small increase in surface gusts associated with ETC winds can have a disproportionate effect on damage, as demonstrated by Hawker (2007), who found that a 25% increase in peak gust speed during an ETC event could result in a 650% increase in damage to buildings, and subsequent soar in insured loss.

Leckebush *et al.* (2008) proposed an objective metric, the Storm Severity Index (SSI), that assesses the potential damage of an ETC event as proportional to the cube of exceedances of the local 98th percentile of gusts. To correctly estimate the local 98th percentile threshold, it is critical to have knowledge of decadal inter- and intra-annual trends of surface winds and gusts. Towards this aim, several researchers produced wind-speed climatologies over the UK (Craig, 2003; Hewston and Dorling, 2011; Earl and Dorling, 2013). In particular, Earl *et al.* (2017) highlighted that the WCB and the CCB are most commonly associated with the top 1% of UK gusts, but smaller-scale ETC features, such as the SJ and the convective lines ahead of the ETC cold front, generate the most extreme gusts.

Numerical weather prediction systems (NWPs) generally forecast the synoptic-scale evolution of cyclones with reasonable skill (Frame *et al.*, 2015). However, due to the chaotic nature of the atmosphere (Lorenz, 1963), small errors in the initial conditions (ICs) of forecasts and in model physics approximations grow exponentially over time, limiting the predictability of the location and strength of local weather details of ETC features such as peak intense winds, gusts, and precipitation (Buizza *et al.*, 2005; Bowler *et al.*, 2008). As the ETC severity has a cubic dependence on extreme wind speeds, even small errors in wind speed forecasts have a great impact on accurate prediction and assessment of the severity of ETCs (Lamb and Frydendhal, 1991; Leckebush *et al.*, 2008). Thus, skillful and high resolution NWP forecasts of extreme surface wind speeds associated with ETCs are critical for providing actionable information to first-line responders as a basis for preparedness to act (Ricchi *et al.*, 2017; Lewis *et al.*, 2019).

The advent, in the last 10 years, of operational regional NWP systems capable of explicitly resolving convection at km-scale (also termed convective-scale NWP) has enhanced the prediction of ETCs and the warning of the associated weather hazards (Seity *et al.*, 2011; Tang *et al.*, 2013). Convective-scale NWPs have shown benefits for ETC prediction since the first numerical experiments carried out by Lean and Clark (2003), who showed that a prototype convective-scale NWP with grid-spacing of 2.2 km was capable to resolve ETC smaller-scale multiple slantwise circulations, the 3-D structure of convection lines, and the peak cyclone surface wind speed, providing realistic-looking forecasts of ETCs. Moreover, the increasing availability of computing power has allowed the further development of convective-scale NWPs capable to estimate the forecasts uncertainty due to IC and model errors by generating probabilistic realizations of events based on ensemble prediction systems (EPS) (Hagelin *et al.*, 2017). However, substantial challenges still persist in the correct estimation of model errors (Buizza *et al.*, 2005; McCabe *et al.*, 2016). Candidate sources of model errors include the sea-state independent model parametrizations of air-sea momentum, heat, and moisture fluxes that control, at convective-scale, the location and magnitude of strong winds near the ocean surface (Janssen, 2004; Lewis *et al.*, 2018, 2019). Because of the steep vertical gradients of the air-sea fluxes at the air-sea interface, small model errors in the parametrization of air-sea fluxes can result in large forecast errors and model biases. The potential importance of air-sea interaction in moderating surface wind speed has led to widespread interest in the development of NWPs capable of representing air-sea surface exchanges with high fidelity (Janssen, 2004).

The integration of atmosphere, ocean, and wave models into a convective-scale coupled multi-model NWP system is gaining popularity to accurately represent the complex air-sea interactions in numerical simulations of ETC, Mediterranean, and Tropical cyclone forecasts (Ricchi *et al.*, 2017; Lewis *et al.*, 2018; Varlas *et al.*, 2017; Lewis *et al.*, 2019; Bousquet *et al.*, 2020). Main research questions revolve around the impact of the dynamical representation of sea state on the boundary-layer characteristics of cyclone low-level jets via coupling, and how, in turn, a change in the boundary-layer characteristics affects local weather details, such as extreme winds, gusts, and precipitation. Other open research questions concern whether atmosphere-ocean-wave coupling benefits are retained when running coupled NWPs as an ensemble, and what the size is of the impact of coupling relative to those of the perturbations applied to generate the ensemble. In particular, although atmosphere-ocean-wave coupling has shown potential to reduce bias of deterministic convective-scale NWP forecasts of ETCs and Mediterranean Cyclones (Wahle *et al.*, 2017; Lewis *et al.*, 2019; Ricchi *et al.*, 2019), it is unclear whether coupling could lead to a collapse of the atmosphere or ocean or wave model variables spread in convective-scale short-range EPS forecasts (due to introduction of shocks, or imbalance, among the wave, ocean, and the atmospheric model variables at each coupled step), thus hindering the predictability of ETCs and other weather hazards.

## 1.2 Aims and structure of this PhD thesis

The aim of this PhD thesis is to investigate the sensitivity of deterministic and probabilistic forecasts of extreme surface wind speeds associated with ETCs (crossing the UK) to air-sea heat, moisture, and momentum fluxes. More in detail, the focus of the thesis is on understanding whether accounting for the effect of dynamic ocean and sea state on air-sea fluxes improves the skill of convection-permitting NWP forecasts of extreme ETC surface wind speeds, and whether the benefits of atmosphere-ocean-wave coupling are retained when running coupled NWPs as an ensemble. The state-of-art deterministic coupled multi-model NWP, developed by the Met Office, was used, as analysis tool, and then integrated, as part of this thesis, with the Met Office ensemble capabilities. Furthermore, the results of the case studies have been placed into context by assessing the systematic link between the conveyor belt jets in ETC and observed extreme wind speeds, gusts, and wave heights for the seas surrounding the British Isles.

The PhD research aims just described are summarised below by three research questions:

- How are ETC synoptic features (e.g. track) and mesoscale features (e.g. warm and cold sectors) associated with the extreme wind speed events observed in the British Isles surrounding seas?
- What is the sensitivity of extreme wind speeds associated with ETC low-level jets to air-sea surface exchanges?
- How does the sensitivity of ETC wind speed ensemble simulations to air-sea surface exchanges compare with sensitivity to initial conditions (ICs) and lateral boundary conditions (LBCs)?

This thesis is structured around three research papers, two published and one submitted for publication. While they have been reformatted for use here, along with minor typographical adjustments, they are otherwise unmodified from the published or submitted manuscripts. The outline of the thesis is now given.

Chapter 2 presents the background and literature review material useful for the reader to understand the content of the research chapters. Then, Chapter 3 describes the data, modelling tools, and forecast verification metrics used to achieve the thesis project aims.

Chapter 4 is the first research paper of the thesis, submitted to International Journal of Climatology. Although it has not gone under full peer review, it represents an important part of this thesis. The climatological analysis of the 2012-2020 timeseries of the marine extreme wind speeds, gusts, and wave heights observed over the seas surrounding the British Isles is provided and it is shown how the observed extremes have been objectively attributed by an ad-hoc algorithm to ETC conveyor belt wind jets. Then, the associated flow characteristics and compound wind and wave hazards with each ETC conveyor belt jet are illustrated.

Chapter 5 is the second research paper of the thesis. It has been published in Journal of Boundary-Layer Meteorology (Gentile *et al.*, 2021). It investigates the sensitivity of extreme surface wind speeds associated with three intense ETCs to different coupled configurations and drag parametrizations using as a tool a state-of-art convective-scale coupled modelling system developed by the Met Office. After a detailed description of the coupled and uncoupled configurations used, the impacts of atmosphere-ocean and atmosphere-ocean-wave coupling on the ETCs wind speeds, gusts, and SST fields are shown. These impacts are then compared with those that are found by changing the drag parametrization employed by the atmosphere-only configuration. The resulting changes in the boundary-layer profiles and vertical structure of the storms are also discussed. The paper concludes with the evaluation of the forecast skill of the coupled and uncoupled simulations of ETC wind speeds through the comparison of in-situ observations.

Chapter 6 is the third research paper of the thesis. It has been published in Quarterly Journal of the Royal Meteorological Society (Gentile *et al.*, 2022). The paper investigates the sensitivity of convective-scale ensemble prediction system simulations to atmosphere-ocean-wave coupling relative to IC, LBC, and stochastic model physics perturbations. To accomplish this, it was necessary to design and build, as part of this thesis, the first coupled convective-scale ensemble, termed Ensemble-RCS, focused on the British Isles domain and surrounding seas. The mean, median, standard deviation, and strike probability of the different coupled and uncoupled Ensemble-RCS forecasts are analyzed and compared for the period 7–10 February 2020 during which ETC Ciara crossed the UK, the most intense cyclone since storm Tini (from 12 February 2014: Kendon, 2020). The impact of coupling to ocean and coupling to waves on the convective-scale ensemble forecasts is placed into the context of the typical spread of an atmosphere-only EPS (computed as the spread of absolute differences of the members from the ensemble mean), arising from the perturbations to the ICs, LBCs and stochastic physics. The paper also evaluates the ensemble spread characteristics of the atmosphere-only, atmosphere-ocean, and atmosphere-ocean-wave coupled ensemble simulations by using the dispersion FSS (dFSS) and dispersion SAL (dSAL) metrics.

Chapter 7 summarises the contributions of the research findings of this thesis, and discusses their implications. Finally, areas of future further work are highlighted.

# Chapter 2

# Background theory and literature review

The background theory and the literature review, presented in this chapter, is intended to help the reader build the knowledge needed to understand the content of the research chapters, which present, in turn, their own research-specific literature review.

First, in Sect. 2.1, a discussion of the wind climate of the British Isles is given. Sect. 2.2 provides the theory describing the atmospheric boundary-layer structure, focusing on the marine boundary layer and the role of air-sea interactions in controlling the vertical profiles. In Sect. 2.3 a review of the mechanisms of formation and growth of ETCs is given. Section 2.4 discusses the impacts of ETCs, in terms of precipitation, wind, and wave height extremes. Operational NWP systems are reviewed in Sect. 2.5, where a description of current state-of-art coupled operational global NWP systems is also given. Lastly, in Sect. 2.6, a review of the existing literature on the sensitivity of ETCs to air-sea interactions is presented.

## 2.1 Wind climate of the British Isles

The British Isles and surrounding seas are characterised by a highly variable wind climate, being mainly exposed to atmospheric blocking over summer and to midlatitude cyclones over autumn and winter (though rarer, blocking can occur in winter, e.g the "Beast from the East" in winter 2018, and cyclones can cross the British Isles over summer). The wind regional variability is controlled by several factors, such as proximity to midlatitude storm tracks, altitude, and type of fetch along the British coastline. The evolution of the seasonal and inter-annual variability of the British Isles' winds can be well approximated by the North Atlantic Oscillation (NAO) index, which describes the relative changes in pressure between the high- and low-pressure regions centred, respectively, on the Azores and Iceland. A positive NAO phase represents a stronger pressure difference than usual between the two regions (Azores minus Iceland), meaning a north-eastward oriented storm track, which brings ETCs and strong warm westerly winds into the British Isles. Instead, a negative NAO phase represents a weaker pressure difference than usual between the Azores high and the Icelandic low, meaning a more zonal oriented storm track, which channels pressure lows into Mediterranean Europe, thus leading to low wind speeds over the British Isles. Below, the wind regime of the British Isles is discussed first, in the context of the broader North Atlantic and European region wind climate. A more detailed view of the wind regime over the UK land mass is then given, based on climatology studies which use the Met Office surface observation network. Finally, a brief review of several studies involving observation, reanalyses, and NWP modelled wind speeds in the British Isles surrounding seas is presented.

### 2.1.1 British Isles wind regime in the context of the North Atlantic and European region wind climate

A map of the monthly 10-m wind speed in the North Atlantic and European region was produced by Laurila *et al.* (2021) for the 40-year period 1979-2018 using the 5th generation ECMWF reanalysis (ERA5), as shown in Fig. 2.1. The mean 10-m wind speeds in the North Atlantic and European region are characterised by a strong gradient between sea and land values, as well as presenting a marked seasonal variation. The largest mean 10-m wind speeds are found, at all months, in the central North Atlantic, reaching values as high as 11 m $s^{-1}$ over January, while, in the same month, mean 10-m wind speeds vary between 3 and 7 m $s^{-1}$ over the British Isles land mass, being approximately half in value of those recorded in the surrounding seas. A comparison of Fig. 2.1 with the spatial distribution of ETC tracks given in the Fig. 2.2, obtained by Dacre and Gray (2009), reveals that the area of strongest wind speeds over the North Atlantic is associated with the main North Atlantic storm track, at whose end the British Isles are located, which indicates the important role of ETCs in driving the variability of high wind speed values in the North Atlantic region. Further results of Laurila *et al.* (2021) indicate that the British Isles landmass presents, in all months, stronger wind speeds (by $\approx 2$ m $s^{-1}$) than the rest of the European continent, with equivalent wind speeds found only in northern France and in the southern Scandinavian region.

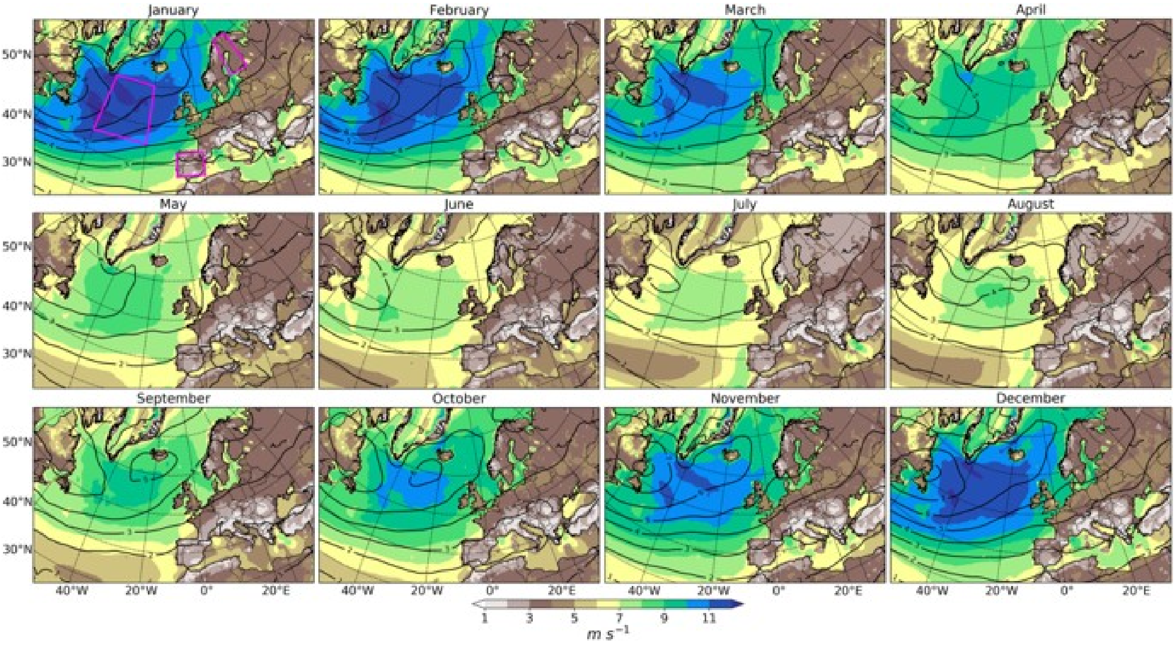

**Figure 2.1:** Monthly mean values of 10-m wind speed (colours, m s$^{-1}$) and anomalies in mean sea level pressure (contours, hPa) from 1979 to 2018. The anomalies are computed as standard deviation after processing with a 2-6 day bandpass filter. Taken from Laurila *et al.* (2021).

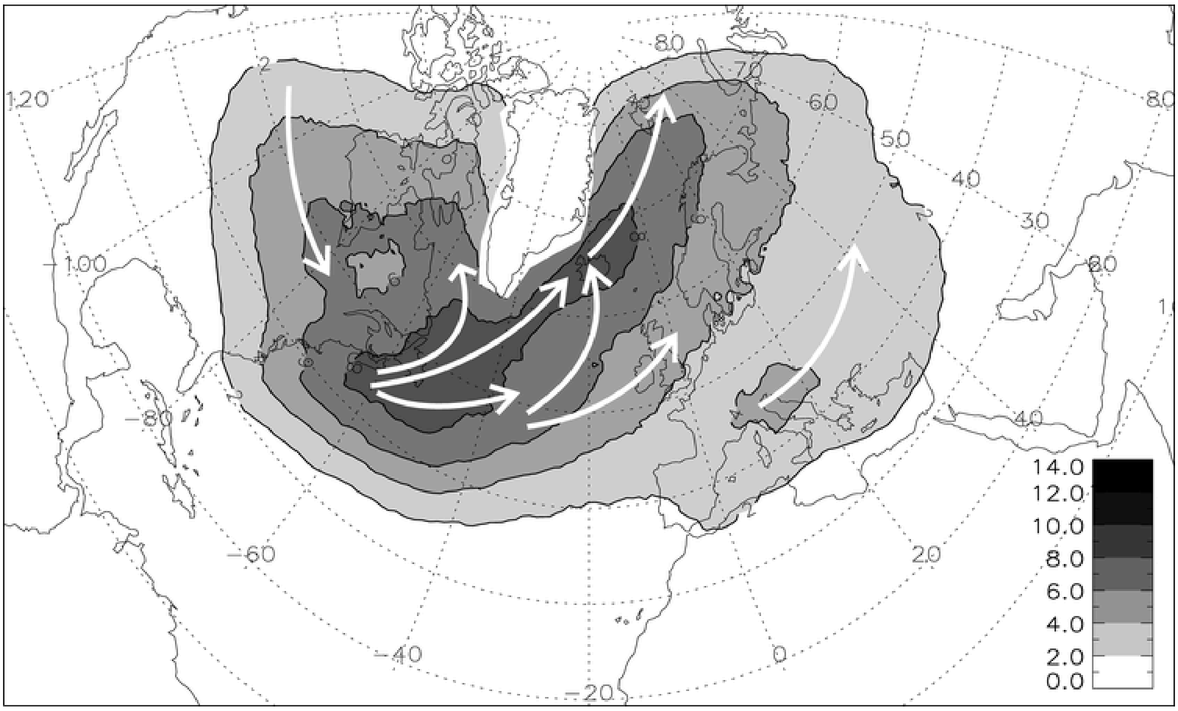

**Figure 2.2:** Schematic of cyclone track paths plotted over track density. Contours every 2 cyclones $(10^6\ \mathrm{km}^2)^{-1}$ month$^{-1}$. The tracked cyclones have been identified from the hydrostatic global Met Office Unified Model for January 2000-July 2002 and the non-hydrostatic global Met Office Unified Model for November 2002-January 2006. Taken from Dacre and Gray (2009).

Considering the UK surrouding seas, the Celtic sea presents wind speeds equivalent to the northern North Sea, possibly because both North Atlantic Ocean seas are geographically close to a storm track (see Dacre and Gray (2009)). The winds in the southern North Sea are calmer, likely due to the weakening of ETCs after they make landfall on the British Isles, and comparable in magnitude to the localised high-wind regions of the Mediterranean sea (where local wind phenomena dominate the variability of the extremes). Examples of localised high-wind regions in the Mediterranean are the Gulf of Lyon, where the Mistral blows, and the Aegean Sea, where the Etesian wind blows (especially over summer).

It is important to note that the latest generation reanalyses such as ERA5 undoubtedly proved useful for characterising the synoptic and some of the mesoscale variability of wind speeds in the North Atlantic and the European region, but, as highlighted in Molina *et al.* (2021), they may have difficulties in accurately representing the extremes of wind speed distributions at given locations. These inaccuracies occur because reanalyses are obtained for areas defined by the model grid points (e.g. 30×30km in ERA5), leading to a smoothing of the wind variability within each grid-cell. For example, using digitized mean sea level pressure maps of storm events over the 1953-1995 period, Craig (2003) found two 10-m mean wind speed hotspots, one located in the central/southern north sea (23 m $s^{-1}$ maximum) and the other located in Northern Ireland (24 m $s^{-1}$ maximum), as shown in Fig. 2.3. However, these hotspots are not represented in the ERA5-based climatology results obtained by Laurila *et al.* (2021) discussed above (though it should be noted that the temporal period considered by these studies is only partially overlapping).

### 2.1.2 Observation-based wind speed climatologies of the British Isles

The high spatial density of the land surface observation network of the UK together with the decades-long availability of hourly measurements data of mean 10-m wind speed, wind direction, and gust provide researchers with a reliable quality-controlled observational data framework to study the variability of extremes of the British Isles wind climate over land, thus complementing the climatologies extracted from the (relatively coarse) reanalysis data.

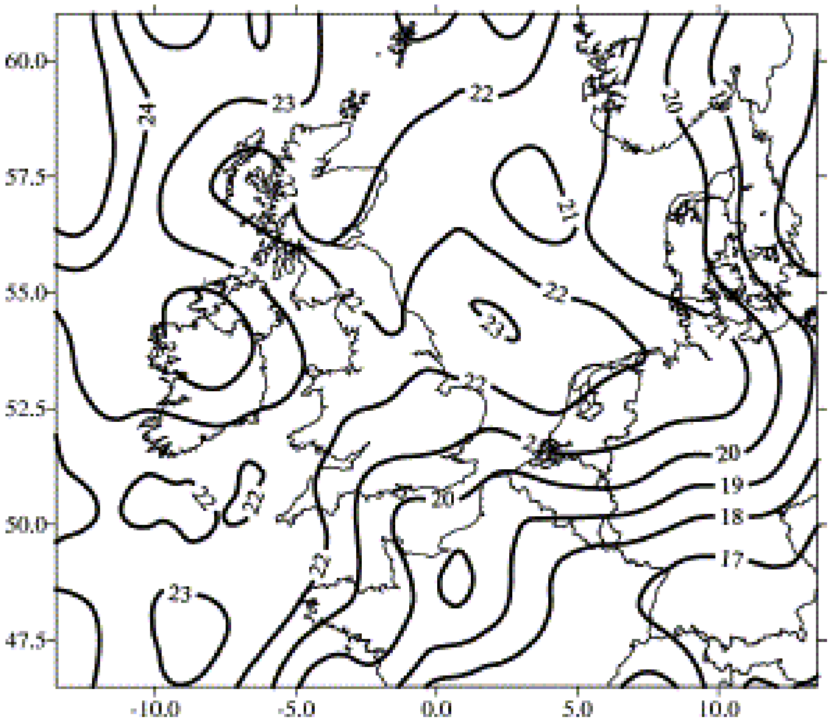

**Figure 2.3:** Calculated once in 50-year 10-min mean surface wind speeds at a height of 10 m above a surface with roughness $z_0 = 0.05$ m. Wind speeds in m s$^{-1}$, with contours at intervals of 1 m s$^{-1}$. Taken from Craig (2003).

Earl and Dorling (2013) analysed the 10th, 50th, and 90th percentiles of the hourly mean 10-m wind speeds (computed as aggregated over the network sites) using a 40-station wind monitoring network (UK based), selected over the continuous 1980-2010 period from the Met Office Land Surface Data and Met Office Integrated Data Archive System (MIDAS) Land Surface Observations station data. As can be observed from Fig. 2.4a, the 10th and 50th percentiles of the hourly mean 10-m wind speeds peak in the early 1990s, but later markedly decline until 2010. Instead, the 90th percentile of the hourly mean 10-m wind speeds is not characterised by the general decline observed for the 10th and 50th percentiles, and reaches the 1990s peak earlier than the other two percentile threshold values (Earl and Dorling, 2013). A similar trend was also found in the analysis of the daily maximum gusts (DMGSs) by Hewston and Dorling (2011) and Earl and Dorling (2013), as shown in Fig. 2.4b. The exceedances of the DMGSs thresholds were highest in the early 90s, in line with hourly mean wind results in Fig. 2.4a. This confirmed the early 1990s peak in northeast Atlantic winter storminess reported by Wang *et al.* (2009), but contrasted with the wind speed decline over whole of Europe discussed by Vautard *et al.* (2010) for the period 1979-2008 (and linked to changes

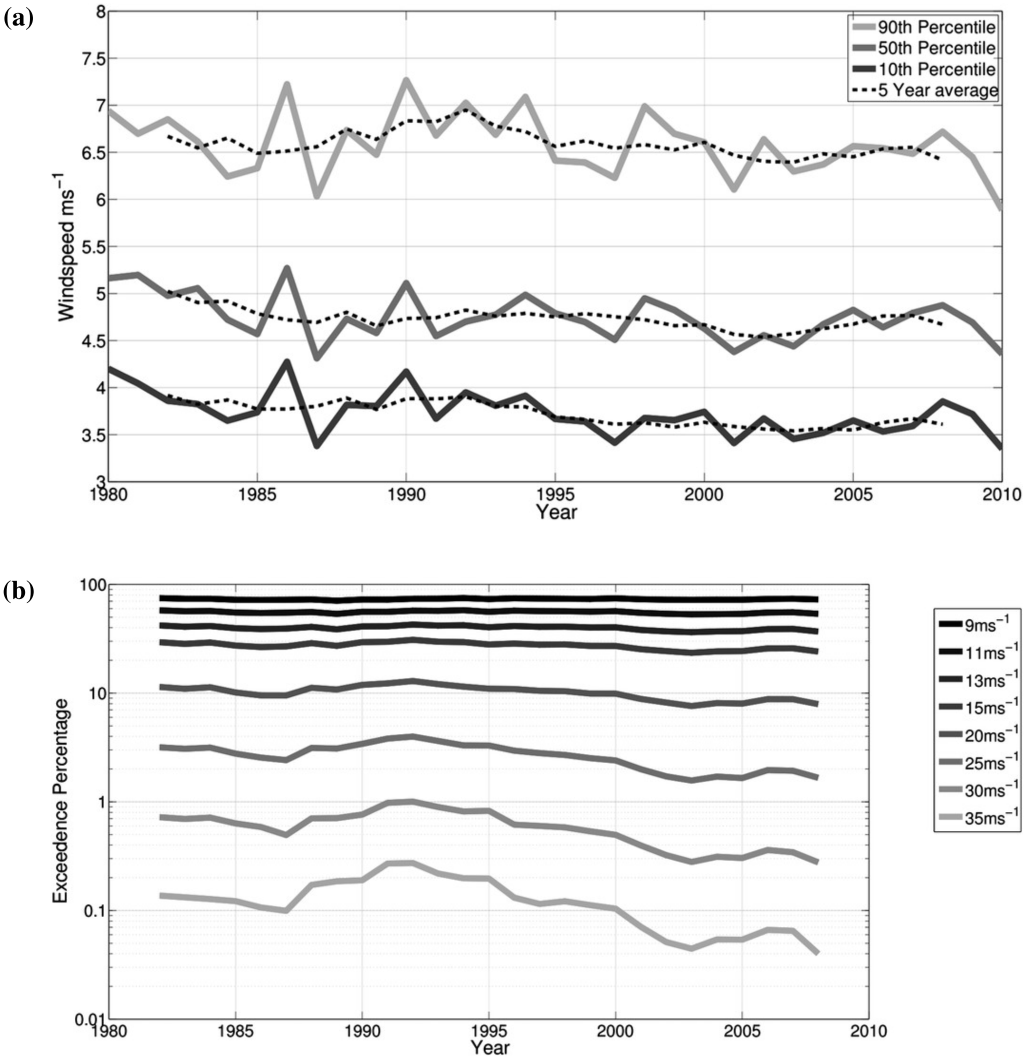

**Figure 2.4:** (a) The 10th, 50th, and 90th percentiles of annual average Hourly Mean (HM) wind speeds (m s$^{-1}$), 1980-2010, from the 40-station network, (b) Network average 5-year running mean threshold exceedance percentages for 9, 11, 13, 15, 20, 25, 30, and 35 m s$^{-1}$ DMGS. Taken from Earl and Dorling (2013).

in surface vegetation cover).

In analysing the wind direction associated with DMGSs recorded by the UK surface wind monitoring network, Hewston and Dorling (2011) established that the prevailing direction of DMGS and hourly 10-m mean wind speeds was south-westerly, as shown in Fig. 2.5a. They also noted that restricting the wind roses analysis to those DMGS exceeding the 98th percentile (the so-called extreme gusts, responsible for most of the structural damage) the prevailing direction was still south-westerly, and even more pronounced than when considering all the DMGSs. Further results of Hewston and Dorling (2011); Earl and Dorling (2013) showed that ≈ 80% of the extreme observed wind speeds occur in cyclone-dense seasons, and that

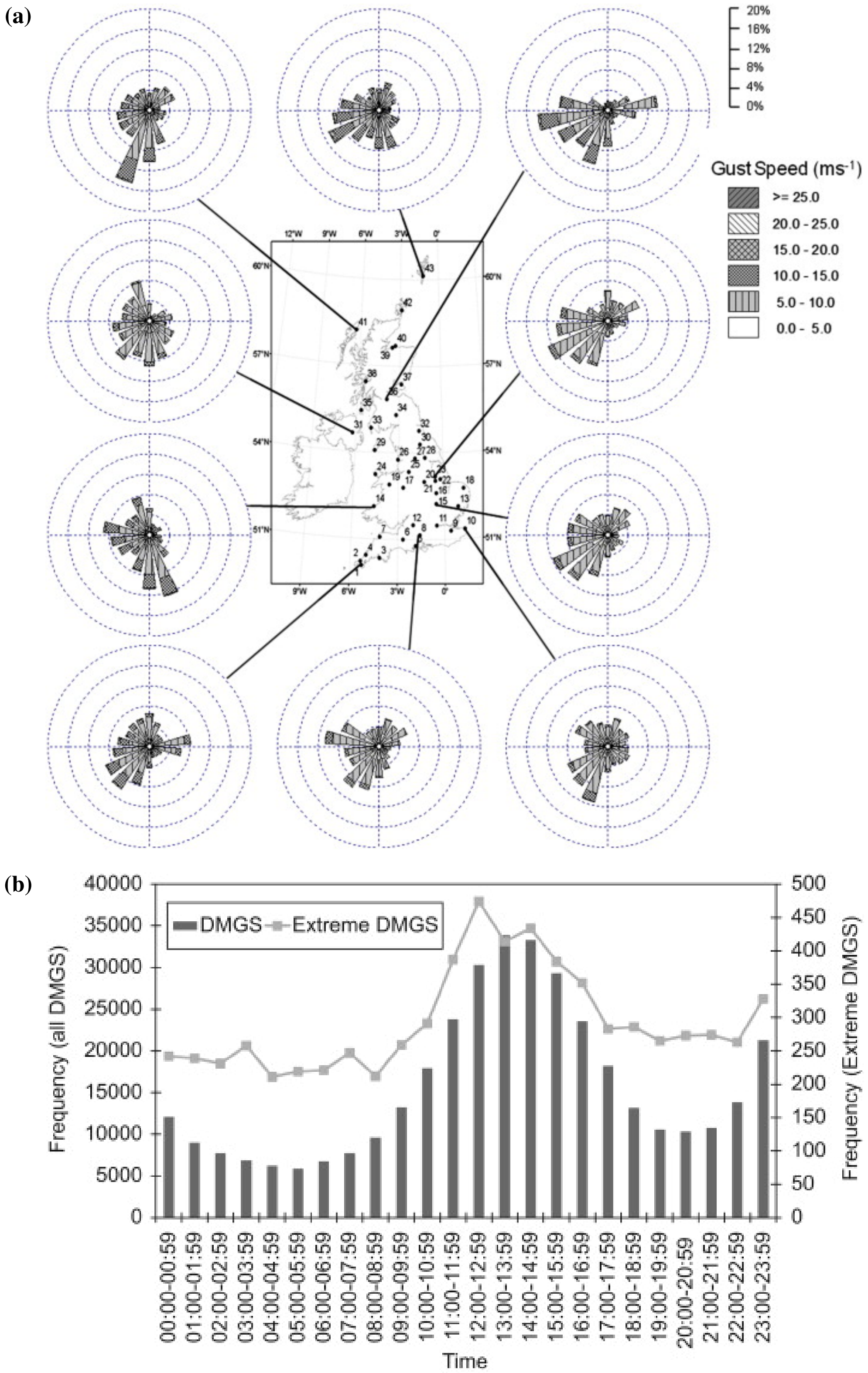

**Figure 2.5:** Left: (a) the windroses and DMGS magnitude of 9 stations selected from the UK wind monitoring network. Right: (b) daily gust variability over the climatological time span (1980-2005) from all stations. Taken from Hewston and Dorling (2011).

boundary-layer convective-scale processes and land surface characteristics can control the intensity of observed DMGs. For instance, Hewston and Dorling (2011) found that the observed land afternoon peak in DMGs resulted from a greater likelihood of atmospheric instability (potential temperature falling with height due to surface heating) which facilitates thermally driven mixing and downdraughts from the ETC conveyor belt jets at a higher level. The role played by the boundary layer in controlling gust strength was also discussed in other climatology studies focused on different geographical regions. For example, the gust climatology performed by Goyette (2008) over Switzerland highlighted how a stable boundary layer during ETC events leads to exceptionally intense wind gusts due to an enhanced production of wind shear generated turbulence.

### 2.1.3 Importance of marine wind speed observations near the British Isles

Unlike the large number of multi-decadal and relatively homogeneous surface observations of wind and gust available over the UK land, marine surface observations of wind and gust are much scarcer near the British Isles. As a result, observation-based studies of wind speeds over the seas near the British Isles relied on a much smaller number of observations than studies over the UK land (discussed in Subsection 2.1.2). For example, Coelingh *et al.* (1998) compared coastal observations to the observations of three offshore fixed platforms (three stations) in the North Sea, finding a daytime peak in surface wind speeds between 1200 UTC and 1400 UTC over the coastal stations, but hardly any diurnal variation at the offshore platforms (probably because the platforms were too far from the coast for the land surface heating to affect vertical mixing of momentum and thus surface wind speeds). Coelingh *et al.* (1998) also highlighted that wind speeds with fetch over sea tend to present similar distributions of wind speed with wind direction (aggregated by 12 different sectors) at coastal stations and offshore platforms, as expected, since in both cases the wind fetch stretches over hundreds of kilometres of sea surface.

However, much of the recent research has focused on using marine wind observations in the context of estimation of offshore wind energy resources near the British Isles, with the aid of the installation of measurements towers in the North Sea. The vertical profiles obtained from these towers which are up to 100m high, such as FINO 1 and FINO 3 off the German coasts in the North Sea, have helped researchers identify wind hazards for offshore installations (low-level jets under warm advection of air from the coast and near-surface winds associated with CCB jets from ETCs) (Beran *et al.*, 2005; Kalverla *et al.*, 2017; Pryor and Barthelmie, 2021). Moreover, FINO1 and FINO3 have been used to validate predictions of turbine flow generation in low-resolution mesoscale model coupled with a site-specific stochastic turbulence function (Vemuri, 2019). Further studies have compared the performance of reanalysis against offshore wind observations, such as Sharp *et al.* (2015) who found that the $0.5° \times 0.5°$ CFSR reanalysis for the period 1980-2010 correlated very well with the observations available from buoys and fixed platforms in the seas near the British Isles, only slightly underperforming than higher resolution mesoscale models. However, this study was limited by having employed only 12 stations none of which were located in the North Sea, where most of the offshore wind resources were (and still are) located. Other types of studies used model hindcasts in order to derive an assessment of the wind power potential. For example, Geyer *et al.* (2015) used a model hindcast to derive a 1958-2012 North Sea surface wind climatology, which was then used to analyse the North Sea wind resources variability over the same temporal period, finding a decadal variation in wind power as high as 10%.

## 2.2 Atmospheric and marine Boundary Layer

The concept of a "boundary layer" traces back to the 1904, when Ludwig Prandtl used this term to define the layer of the flow around the surface of an object, where boundary viscosity has an important impact. When applied to the Earth’s atmosphere, this concept leads to the definition of the Atmospheric Boundary Layer (ABL) as the layer of the atmosphere surrounding the Earth’s surface, whose dynamics is directly influenced by the heat, momentum, and moisture fluxes at the ground on a timescale less than a day. The ABL is typically $\approx$ 1 km deep during the day and $\approx$ 100 m deep during the night. Above the ABL the effects of the Earth’s surface become negligible and the characteristics of the atmospheric flow are similar to that of the free flow. Although substantial progress has been made in the last century, the theoretical understanding of the boundary layer is currently limited by the fact that the boundary layer is turbulent and that still a theory of turbulence is not complete (Garratt, 1992).

In this section, the key characteristics of the ABL are reviewed along with the key physical processes controlling the ABL over the sea, termed Marine Atmospheric Boundary Layer (MABL). Then, a brief review of air-sea interactions, which play a critical role in controlling wind speed, temperature, and humidity in the surface layer, as well as their vertical profile in the MABL, is given. Finally, a digression on the generation and growth mechanisms of ocean surface waves is provided.

### 2.2.1 Atmospheric boundary layer characteristics

The structure of the atmospheric boundary layer (ABL) and its diurnal evolution over land are illustrated in Fig. 2.6. The lowest layer, the closest to the Earth's surface, is the roughness sublayer, characterised by a depth of $\approx 5$ times the mean height of obstacles (such as grass, plants, trees or buildings) through which air flows. Sitting on top of this layer there is the surface layer, which accounts for 10% of the ABL depth. Within the surface layer, wind and temperature vary rapidly with height while the vertical fluxes of momentum and heat are approximately constant with height. Above this layer, lies the well-mixed layer, where the effects of the Earth's rotation start to become relevant, leading the wind direction to veer with height. Because of the vigorous turbulence occurring in this layer, the potential temperature tends to be relatively constant with altitude, though humidity is not as well mixed. As illustrated in Fig. 2.6, the well mixed layer is capped by a temperature inversion, associated with a layer of statically stable air which inhibits mixing. However, at night, the capping inversion is eroded and, as air is cooled from the surface, a new stable nocturnal boundary layer grows, while the mixed layer turns into the residual layer (Stull, 1988).

Overall, the boundary layer can be distinguished into three different types: the convective boundary layer, the stable boundary layer and the neutral boundary layer. The convective boundary layer occurs when strong surface heating (due to the sun) produces thermal instability or convection in the form of thermals and plumes, and when upside-down convection is generated by cloud-top radiative cooling. The resulting convection deepens the boundary layer and, under particularly strongly unstable conditions driven by surface heating, generates a well mixed layer, where the large amount of buoyant turbulence causes speed, temperature,

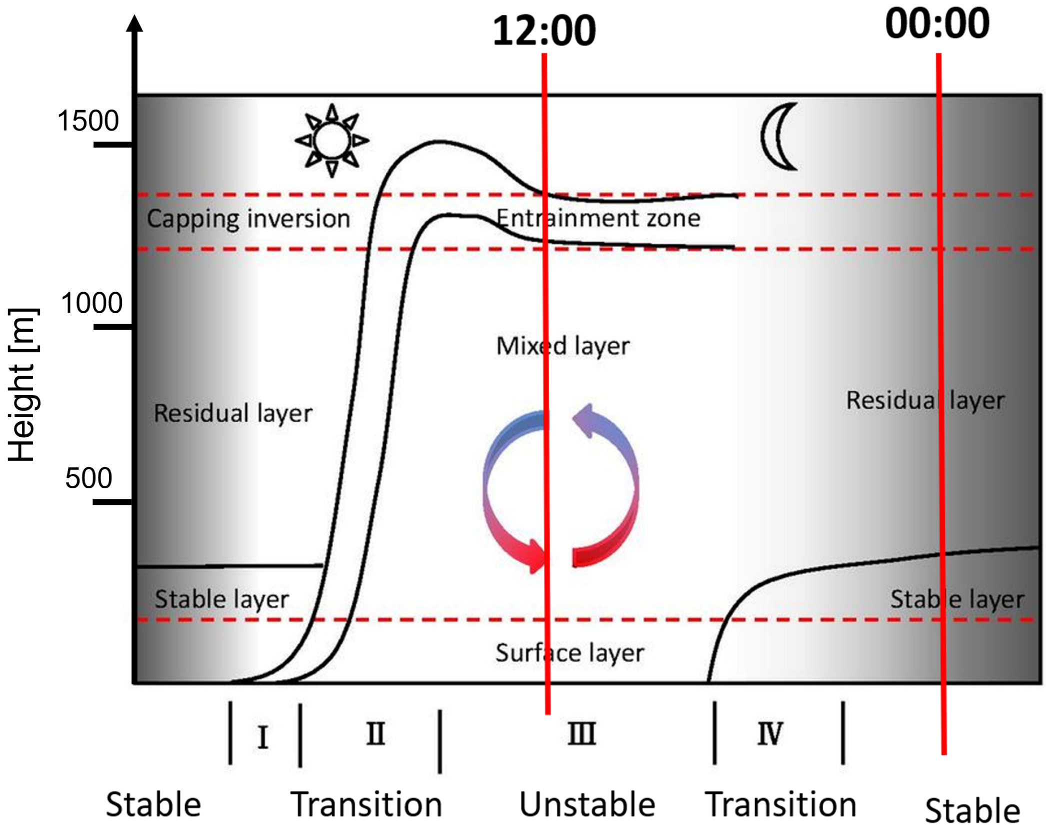

**Figure 2.6:** Diagram illustrating the structure of the ABL over land. Adapted from Stull (1988).

and humidity to be constant with height. If an upper level wind jet (e.g. ETC jet) is present at the top of the ABL, the static instability characterising the interior of the convective BL favours the downward transport of momentum, leading to strong gusts at the surface. At night, when solar heating ceases, the Earth's surface cools due to emission of longwave radiation, leading to a stably stratified boundary layer in which the generation of convective plumes is suppressed. The reduced turbulent mixing means that high momentum air from aloft cannot be brought down to low levels, resulting into reduced surface winds. Because of the reduced amount of turbulence, and thus increased static stability, surface winds tend also to be less gusty than in the convective (and more statically unstable) boundary layer. The atmospheric conditions leading to a neutral boundary layer, which requires strict neutral stability, are less frequent than those leading to the convective and the stable boundary layer. However, when the skies are overcast (complete cloud cover) the geostrophic wind is strong (large wind shear), both the sensible heat flux and the radiative cooling at the surface are minimal, and the ABL may be considered as being close to a neutral boundary layer (Garratt, 1992).

Within the boundary layer, heat and momentum are transported by turbulent motion, made up of swirls of turbulence, called eddies, which are characterised by high-frequency random fluctuations in space and time. The turbulent transport of the mean horizontal momentum by eddies towards the surface is described by the following surface stress relationship, based on semi-empirical considerations (Garratt, 1992):

$$\tau = -\rho\overline{u'w'}, \tag{2.1}$$

where $\tau$ is the surface stress, $\rho$ is the density of air, $u'$ and $w'$ are the random fluctuations of horizontal and vertical velocity, and $\rho\overline{u'w'}$ is the turbulent momentum flux. Since the wind increases with altitude, in case of downward momentum flux the covariance $\overline{u'w'}$ is negative and the surface stress $\tau$ is positive. The scaling velocity, $u_*$, in the surface layer can be derived from Eq. (2.1) and takes the form:

$$u_* = \sqrt{-\overline{u'w'}}. \tag{2.2}$$

The scaling velocity, $u_*$, is also referred to as the friction velocity. According to the Monin-Obukhov similarity theory, the friction velocity $u_*$ can be related to the wind shear via the mixing length $l_m$, which is the typical vertical depth over which parcels of air move before mixing, as:

$$u_* = l_m \frac{\partial u}{\partial z}. \tag{2.3}$$

By substituting Eq. (2.2) into Eq. (2.1), the following expression for surface stress can be obtained:

$$\tau = \rho {u_*}^2 \tag{2.4}$$

which shows that $\tau$ is always positive and proportional to the square of the scaling velocity for the surface layer.

The mean vertical transport of heat by turbulence, $H$, is defined as:

$$H = \rho c_h \overline{w'\theta'}, \tag{2.5}$$

where $c_h$ is the specific heat capacity of air, and $\theta'$ is the turbulent temperature fluctuation. When temperature decreases with height, $\overline{w'\theta'}$ is positive and vice versa. Therefore, positive values of $H$ represent an upwards heat flux from the surface.

In the simplest case of a neutral boundary layer, where turbulent heat fluxes do not play an active role and most of the turbulence is generated by the wind shear, the mixing length $l_m$ is likely to depend only on the distance from the surface, $z$, according to the relationship $l_m = kz$, where $k$ is the Von Karman constant, which is set to the value $k = 0.4$ (empirically determined). Substituting $l_m = kz$ into Eq. (2.3) and integrating, the following dependence of wind speed $u$ on height $z$, also known as the logarithmic wind profile, can be obtained:

$$u(z) = \frac{u_*}{k} \log\left(\frac{z}{z_0}\right), \tag{2.6}$$

where $z_0$ is the roughness length, defined as the height at which the wind $u$ falls to zero. The roughness length $z_0$ represents the bulk effects of roughness elements in the surface layer and has a value around 0.1 times the height of the roughness elements. The logarithmic wind profile Eq. (2.6) can be modified to account for stable and unstable conditions occurring in different boundary layer types in the following way:

$$u(z) = \frac{u_*}{k} \left[\log\left(\frac{z}{z_0}\right) - \Psi_m\right], \tag{2.7}$$

where $\Psi_m$ is the momentum similarity function.

### 2.2.2 Marine boundary layer characteristics

Over the sea, the ABL is referred to as the Marine Atmospheric Boundary Layer (MABL). The MABL differs substantially from the land ABL since the direct contact with the ocean allows for a much larger exchange of heat and moisture than over land. The difficulty of observing the atmosphere over the ocean has made studying the MABL much harder than studying the land ABL. Thus, our knowledge of the MABL remains more limited than that of the land ABL (Arya, 2001). For this reason, much research has recently been devoted to the study of the physical processes of the MABL.

A key difference between the land ABL and the MABL is that the diurnal cycle of the sea surface temperature is generally very small, compared to that over land, because of the larger heat capacity of the ocean. This occurs because the absorption of radiation in the ocean takes place over several metres along the vertical (see Fig. 2.7). Except near the coasts, the air tends to be slightly cooler (≈1 K) than the underlying sea surface, due to radiative cooling of the air, resulting in a slightly unstable surface layer, but with small surface sensible heat fluxes (Garratt, 1992). A further difference between the land ABL and the MABL is that the land surface is characterised by roughness elements of fixed geometry, while the sea surface is wavy and mobile, in relative motion with respect to the overlying flow. The waves that cover

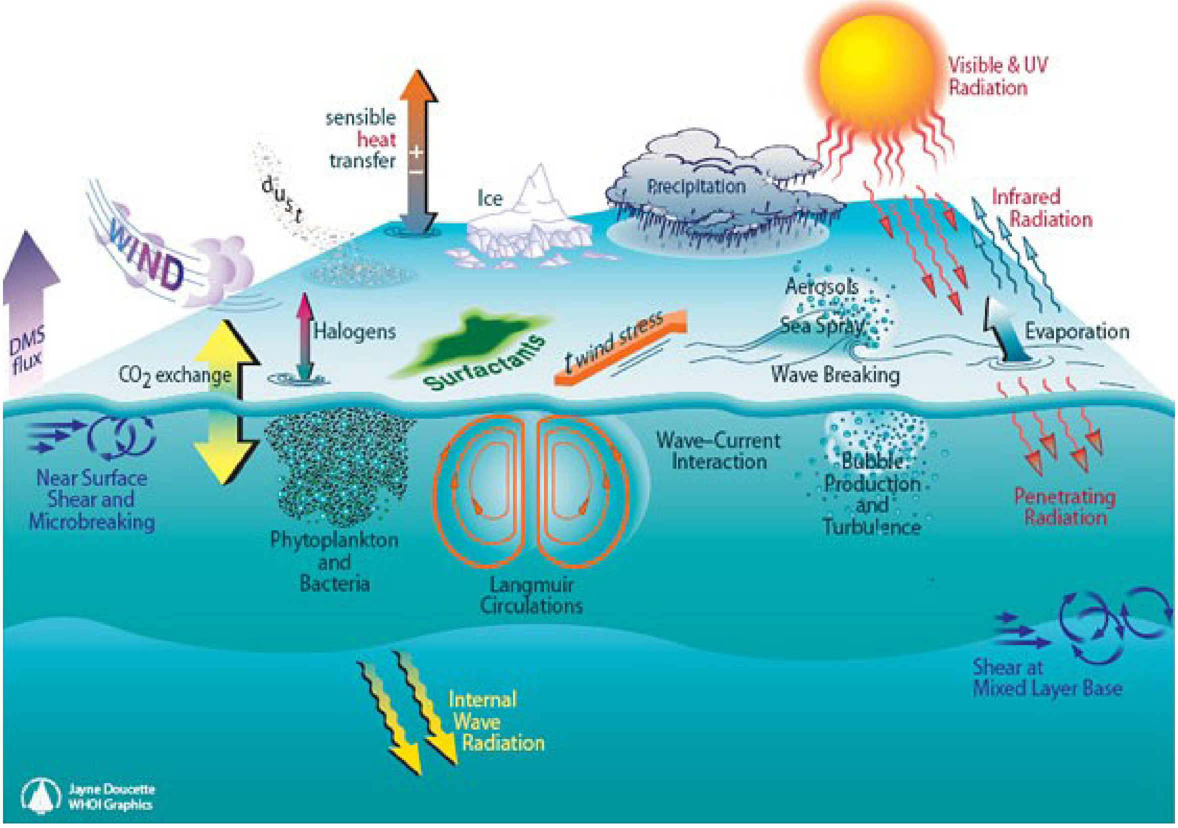

**Figure 2.7:** Schematic illustrating the complex momentum, heat, and moisture air-sea interactions, in the MABL, between atmosphere and the ocean earth system components. Taken from Woods Hole Oceanographic Institute (2022).

the sea surface mediate the air-sea momentum flux (see Fig. 2.7), which is expressed in terms of the total stress $\tau$ acting at the air-sea interface. Research carried out in the last 20 years has shown that the total stress $\tau$ is the result of the linear contribution of three different types of stress: the turbulent shear stress $\tau_t$, the wave-induced stress $\tau_w$, and the viscous stress, $\tau_{visc}$ (Janssen, 2004). Because at the air-sea interface the turbulent shear stress $\tau_t$ is close to zero, the total stress $\tau_{tot}$ is mainly supported by the wave induced stress and the viscous stress. Well above the surface $\tau_w$ becomes zero, and the total stress equals the turbulent stress (Csanady, 2001). The layer where $\tau_w$ is non-zero is called the wave boundary layer (Janssen, 2004).

The type of cloud cover which is more commonly found in the MABL is the stratocumulus cloud (see Fig. 2.8). The stratocumulus clouds are convective in nature, the overturning driven mainly by long-wave radiative cooling at cloud top and resulting in a cellular structure (Albrecht *et al.*, 1995). The formation of the stratocumulus clouds in the MABL can be explained considering the trajectory of a single air parcel. When an air parcel is at the top of the stratocumulus cloud in the MABL, it eventually acquires negative buoyancy by radiative cooling at the cloud top, causing the parcel to sink. As a result, surrounding parcels become positively buoyant, rising and then generating a well-mixed layer with large turbulent eddies in the MABL. These eddies transport humidity and heat from the air-sea surface up to the cloud layer, effectively sustaining it. However, the MABL stratocumulus clouds eventually vanish, due to the decoupling phenomenon, which occurs when the intense sunlight prevents sinking

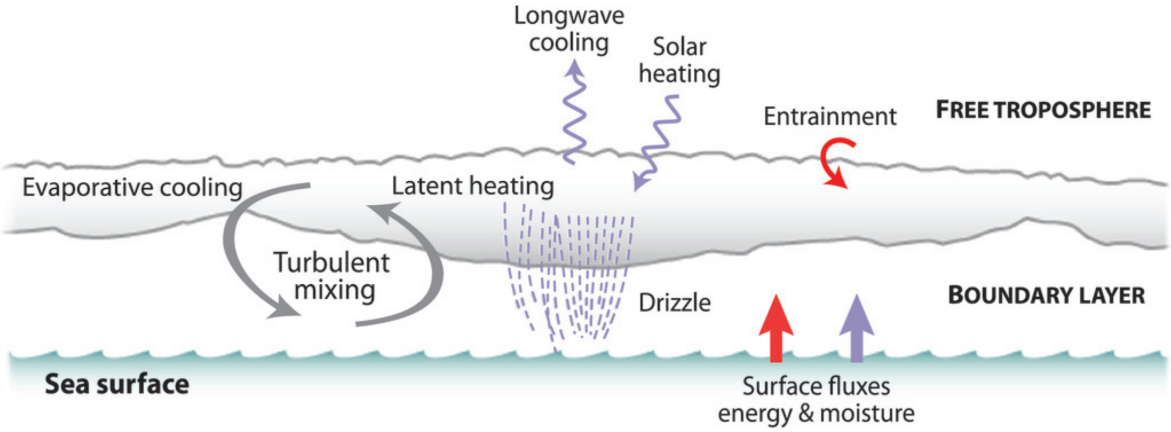

**Figure 2.8:** Schematic of the MABL. Taken from Wood (2012).

air parcels from reaching the ocean's surface (Norris, 1998). More in detail, negatively buoyant thermals are still initiated at stratocumulus cloud top, but warming of the sun allows the sinking air parcels to preserve some buoyancy, and thus they are no longer vigorous enough to reach the ocean surface. The MABL becomes decoupled, with a weakly stable transition layer which now separates an upper mixed layer (topped by the stratocumulus clouds) from a lower cooler mixed layer. Finally, because of the lack of water vapor transported by the turbulent eddies to the cloud, the cloud thins and evaporates (Wood, 2012).

### 2.2.3 Air-sea interactions

The interactions between air and sea play a critical role in controlling the near-surface wind speeds, temperature, and precipitation in the MABL. They can be distinguished into dynamical interactions and thermodynamic interactions, where the former involve exchange of momentum and mass (water vapour, sea spray, and rainfall), and the latter involve the exchange of sensible and latent heat (Black *et al.*, 2007). The air-sea interactions are characterised by a nonlinear nature, since they arise from the interaction between turbulent flows (in air and water), and wind waves (on the sea surface) (Csanady, 2001).

The wind profile over the sea can be represented by the shape described by the log-law in Eq. (2.7), and the shear interface stress, which corresponds to the air-sea momentum flux, can then be expressed as $\tau = \rho u^{*2} = \rho C_D |\Delta \mathbf{v}|^2$, where $C_D$ is the drag coefficient, and $\Delta \mathbf{v}$ is the difference vector between the surface wind and the surface ocean velocity. Because the roughness length for momentum depends on both the atmospheric surface layer flow and the underlying surface wave state, the momentum roughness length $z_{0m}(\text{sea})$ is related to the surface friction velocity, $u^*$, according to the Charnock's law:

$$z_{0m}(\text{sea}) = \frac{0.11\nu}{u_*} + \frac{\alpha}{g} u_*^2, \tag{2.8}$$

where $g$ is the gravitational constant and $\alpha$ is the Charnock parameter, which accounts for increased roughness as wave heights grow, due to increasing surface stress (Charnock, 1955; Smith, 1988). Although the Charnocks relation in Eq. (2.8) assumes that the drag coefficient

$C_D$ linearly increases with wind speed (excluding light-wind speed when viscosity effects dominate), laboratory experiments and field campaigns have shown that the drag coefficient saturates at 30 m s$^{-1}$ (see Fig. 2.9a), and, for wind speeds higher than 30 m s$^{-1}$, observations over the ocean indicated a smooth decrease of the drag coefficient with wind speed (see Fig. 2.9b) (Powell *et al.*, 2003; Hsu *et al.*, 2017). These results have been recently reconciled

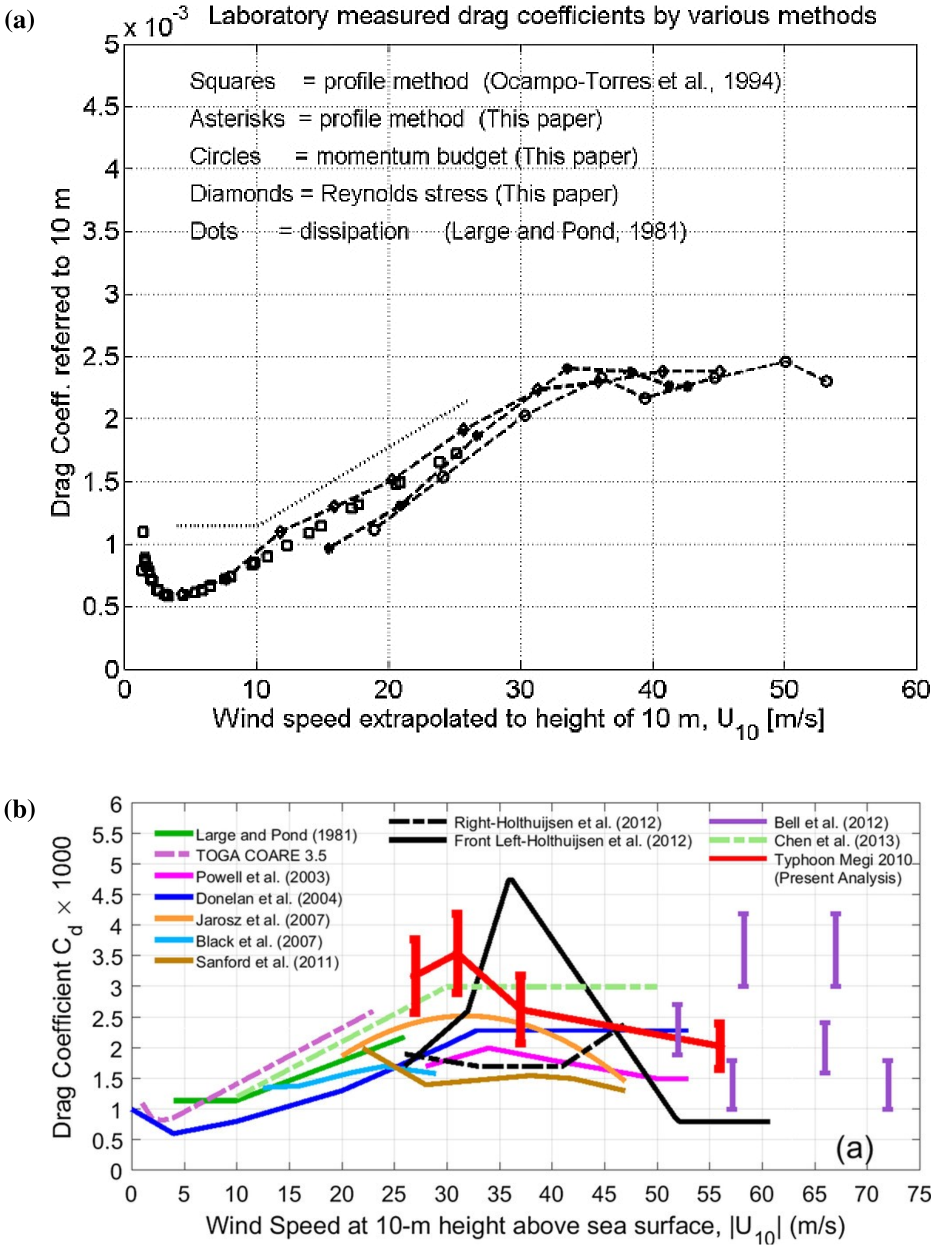

**Figure 2.9:** Top: (a) laboratory measurements of the neutral stability drag coefficient by profile, eddy correlation (Reynolds) and momentum budget methods. The drag coefficient refers to the wind speed measured at the standard anemometer height of 10 m. Taken from (Donelan *et al.*, 2004). Bottom: (b) The drag coefficient $C_d$ as a function of wind speed at 10 m above the sea surface from the analysis of Hsu *et al.* (2017) (thick red line) and as proposed by previous investigators (other colors). Taken from Hsu *et al.* (2017)

by Donelan (2018), who distinguished between two different turbulent flow regimes: a linear increase of drag coefficient for wind speeds in the range of 2.5–30 m $s^{-1}$ followed by a smooth decrease in the range of 30–50 m $s^{-1}$. The distinction between these two turbulent regimes has led to appreciable consequences on the modelling of natural hazards such as intense cyclones. As shown by Donelan (2018), the assumption of a smooth decrease of $C_D$ in the range of 30–50 m $s^{-1}$ to account for the drag saturation under extreme wind conditions leads to a better representation of the explosive deepening of Atlantic hurricanes. The saturation of the aerodynamic surface roughness, and therefore of the drag, for wind speeds exceeding $\approx$30 m $s^{-1}$ was explained by a series of laboratory experiments detailed in Donelan *et al.* (2004). Donelan *et al.* (2004) found that for winds up to $\approx$30 m $s^{-1}$, waves move slower than the wind that forces them, causing great resistance to the overlying airflow, and thus they function as a drag element (leading to the increase of drag with wind speed shown in Fig. 2.9). These waves remain in a height/wavelength proportion of roughly 1/10. However, for wind speeds exceeding $\approx$30 m $s^{-1}$, waves become much steeper than this ratio, until they undergo the process of wave breaking, which brings the waves back in line and distorts the former smooth wave shape. Indeed, the laboratory experiments of Donelan *et al.* (2004) found an abrupt change in slope associated with the breaking wave, presenting a backward (downwind) facing step to the wind. The presence of this step makes it difficult for the air flow to follow the surface, leading to separation of the flow from the water surface and thus limiting (or saturating) the aerodynamic roughness and associated drag coefficient, regardless the geometric roughness of the large waves.

Besides the momentum flux, the air and the sea also exchange sensible and latent heat fluxes, as well as mass and gases. The total heat fluxes at the air-sea interface consist in both radiative and turbulent fluxes. While the turbulent heat fluxes are affected by the MABL, the radiative fluxes are not. The Sun's radiative fluxes are emitted at a shorter wavelength (ultraviolet, visible and infra-red) than those emitted by the relatively much cooler Earth's atmosphere (clouds) and surface (ocean). Thus, the radiative fluxes can be partitioned in short wave (SW) and long wave (LW) radiative fluxes. Overall, the partitioning of the total surface heating, $Q$, at the air-sea interface (but also at the air-land interface, detailed in Best *et al.* (2011)) can be expressed as:

$$Q = \mathrm{LW}\uparrow - \mathrm{LW}\downarrow + \mathrm{SW}\uparrow - \mathrm{SW}\downarrow - H_0 - E_0, \tag{2.9}$$

where the ↑ corresponds to the upward radiative fluxes, the ↓ to the downward radiative fluxes, and $H_0$ and $E_0$ correspond to the two preferred pathways of the heat turbulent flux from the ocean to the atmosphere (the reverse rarely occurs): the sensible and latent heat turbulent transfer (Lewis *et al.*, 2018). The sensible heat transfer, $H_0$, raises or lowers the air temperature, though the bulk of the heat transfer from the ocean to the atmosphere occurs via evaporation and the associated transfer of latent heat ($E_0$).

The turbulent air-sea momentum flux, $\tau_0$, sensible heat flux, $H_0$, and moisture flux, $E_0$, are related to the vertical gradients in velocity, $\mathbf{v}$, temperature, $T$, and specific humidity (moisture), $q$, assuming that the Monin–Obukhov similarity theory holds in the surface layer, yielding (Lewis *et al.*, 2018):

$$\frac{\partial \mathbf{v}}{\partial z} = \frac{\tau_0}{\rho_0 u^*}\frac{\phi_m(z/L)}{kz}, \tag{2.10}$$

$$\frac{\partial T}{\partial z} + \frac{g}{c_p} = -\frac{H_0}{c_p \rho_0 u^*}\frac{\phi_h(z/L)}{kz}, \tag{2.11}$$

and

$$\frac{\partial q}{\partial z} = -\frac{E_0}{\rho_0 u^*}\frac{\phi_h(z/L)}{kz}, \tag{2.12}$$

where $\rho_0$ is the air surface density, $c_p$ is the specific heat capacity, and $\phi_m$, $\phi_h$ are the Monin-Obukhov stability function for momentum and scalars, which account for the effect of buoyancy (Csanady, 2001).

### 2.2.4 Generation and growth mechanisms of ocean surface waves

As noted in the previous subsection, wind waves play a central role in the air-sea transfer process. Thus, it is important to understand how they form and subsequently grow. It is well known that, on a wind-blown water surface, the initially smooth surface is deformed and small-amplitude waves are generated, which then grow with time (Ursell, 1956). Several mechanisms have been proposed in the literature to explain the formation of these tiny waves under a suddenly arising wind, and their subsequent growth. However, a general theory that can explain the formation and growth of ocean waves is still missing (Belcher and Hunt, 1993). Here, the most accepted mechanisms for wave formation and growth are described.

One of the first theories describing wave generation was proposed by Jeffreys (1925). His theory starting point was the observation that air flowing over the ocean is sheltered by its lee side, leading to the airflow separation at the wave crest (the wind has a comparatively faster velocity relative to that of the wave). This would then lead to sufficient momentum being transferred from wind to waves to account for wave growth. Using a simple energy balance equation, Jeffreys (1925) estimated that the sheltering coefficient needed to explain wave growth was equal to 0.27. Subsequent laboratory experiments from Stanton 1932 and Motzfeld (1937) confirmed that the airflow indeed separates at the wave crest, but the value of the sheltering coefficient associated with the waves profile was much smaller than that estimated by Jeffreys (1925), and thus it couldn't account for the observed wave growth rates.

Shortly after the Ursell (1956) review of wind generation of ocean waves, two pivotal wave generation and growth theories were proposed by Phillips (1957) and Miles (1957), respectively. Phillips (1957) proposed a linear theory of wave growth, where waves are generated by resonant forcing from random pressure fluctuations in the wind blowing above the water surface. The wave growth predicted by this mechanism is proportional to the variance of the spectrum of the pressure fluctuations at the resonant frequency, independent of the wave spectrum. The order of magnitude of growth in the Phillips (1957) mechanism is approximately equal to the square of the air-water density ratio. Instead, Miles (1957) suggested an exponential wave growth mechanism, which results from the resonant coupling between wave-induced pressure fluctuations and free surface waves. Later, Miles (1960) combined the Phillips (1957) and Miles (1957) theories into a quasi-linear wave growth theory, showing that wave generation and growth is initially linear (Phillips, 1957), but then, over time, the wave growth changes to exponential (Miles, 1957).

Field experiments subsequent to Miles' theory publication, showed Miles' theory underpredicted wave growth. Although the first field campaigns indicated that wave growth was underpredicted by one order of magnitude in Miles' theory (Dobson, 1971), more recent studies have suggested Miles' theory wave growth is within the same order of magnitude of that found experimentally (even if still underpredicted) (Snyder, 1974; Snyder *et al.*, 1981; Hasselmann and Bĺosenberg, 1981). The agreement between Miles' theory and experiments turned out especially good for low-frequency ocean waves, characterised by a phase speed close to the 10-m wind speed of the overlying airflow. It is worth to note that a likely cause of the variability of the outcome of these observation studies lies in the intrinsic difficulty of measuring air-sea energy transfer over open ocean sea. Indeed, Miles' theory is the source of much controversy as it assumes an inviscid flow and it does not account for non-linear interaction of waves with mean flow and it does not even account for air turbulence apart from maintaining shear flow. In particular, wave-mean flow interaction are expected to be relevant at the critical layer level height, which corresponds to the height at which the phase speed of the wave matches that of the overlying airflow. As a result, several studies have attempted to complement Miles' critical-layer wave growth mechanism. For example, Belcher and Hunt (1993), and later Cohen and Belcher (1999), proposed a non-separated sheltering mechanism that could explain the growth of slow waves and the damping of fast waves under wind forcing.

In more recent years, numerical Large Eddy Simulations (LES) carried out by Sullivan *et al.* (2000) found clear evidence of the existence of a critical layer for a wide range of dimensionless phase speeds, indicated by the rapid fall off of the wave-induced stress at the critical layer level height. Observations obtained with the sophisticated floating platform FLIP by Hristov *et al.* (2003) also found a pronounced jump in the wave-induced stress for phase speeds in the range $16 < c/u_* < 40$, as well as a good agreement between observed and modelled wind profiles. However, these studies also found that Miles' theory underpredicted values of wave growth rate. Despite the proposal of complementary mechanisms, such as the Belcher and Hunt (1993) non-separated sheltering mechanism discussed above, discrepancies between theories, models and observations of wave growth still exist.

## 2.3 Extratropical cyclones

Extratropical cyclones (ETCs) can generate strong surface wind speeds and gusts when they cross the British Isles. Here are reviewed the known mechanisms of genesis and evolution of extratropical cyclones, the structure of the main airflows (also known as conveyor belt wind jets), and the main characteristics of the ETC tracks in the North Atlantic.

### 2.3.1 Baroclinic instability

The notably larger amount of incident solar radiation, and hence energy, received by the equator over the year, compared to the pole, drives a large meridional temperature gradient between the considerably warmer equatorial regions and the colder poles, forming an unstable background state that provides the basis of the atmospheric heat engine. Along this gradient, pressure contours are sloped with respect to isotherms. This is why this background state is termed baroclinic, from the greek "baro" (pressure) and "cline" (slope). Because the slope of the isobars increases with height, the associated pressure gradient force is larger at higher elevations, while the Coriolis force is independent of height. As a result, in the midlatitudes, the geostrophic wind acquires an eastward component that grows with altitude, maximum below the tropopause, which gives rise to a midlatitude wind jet, termed jet stream. The relationship between this vertical wind shear and the meridional equator-pole temperature gradient is defined by the thermal wind balance:

$$\frac{\partial \theta}{\partial y} = -\frac{f\theta}{g}\frac{\partial u}{\partial z}, \tag{2.13}$$

where $\theta$ is the potential temperature, $y$ is the meridional axis, $f$ is the Coriolis parameter, $u$ is the zonal wind, and $z$ is the vertical direction (Hoskins and James, 2014). The jet stream is effectively a reservoir of potential energy, on which perturbations can feed off to quickly grow into intense weather systems by conversion into eddy kinetic energy, through ascending poleward moving branches of warm air and descending equatorward moving branches of cold air. This mechanism is termed baroclinic instability and it can be explained by potential vorticity (PV), which in the Ertel's form (Ertel (1942)) is defined as:

$$PV = \frac{1}{\rho}\zeta \cdot \nabla\theta, \tag{2.14}$$

where $\zeta$ corresponds to the absolute vorticity, and $\theta$ to the potential temperature. Potential vorticity has two key properties that make it suitable to describe the dynamics of weather systems. The first is that PV is conserved following a frictionless and adiabatic flow. The second is that, provided a balance approximation and lower boundary condition, PV can be inverted to obtain a three dimensional wind and pressure distribution. Thus, anomalies in temperature can be represented as anomalies in PV: a warm (cold) anomaly at the ground can be represented with a positive (negative) imaginary PV anomaly, and a warm (cold) anomaly at the tropopause can be represented with an imaginary negative (positive) PV anomaly.

Moreover, PV anomalies can interact via action-at-a-distance, leading to the growth of weather systems from initial vorticity or thermal perturbations. As illustrated in Fig. 2.10, a PV anomaly acts at a distance on far away PV anomalies by inducing a streamfunction there associated with cyclonic or anticyclonic circulation (Bishop and Thorpe, 1994). In the Northern Emisphere, when an upper-level positive (warm) PV anomaly is advected over

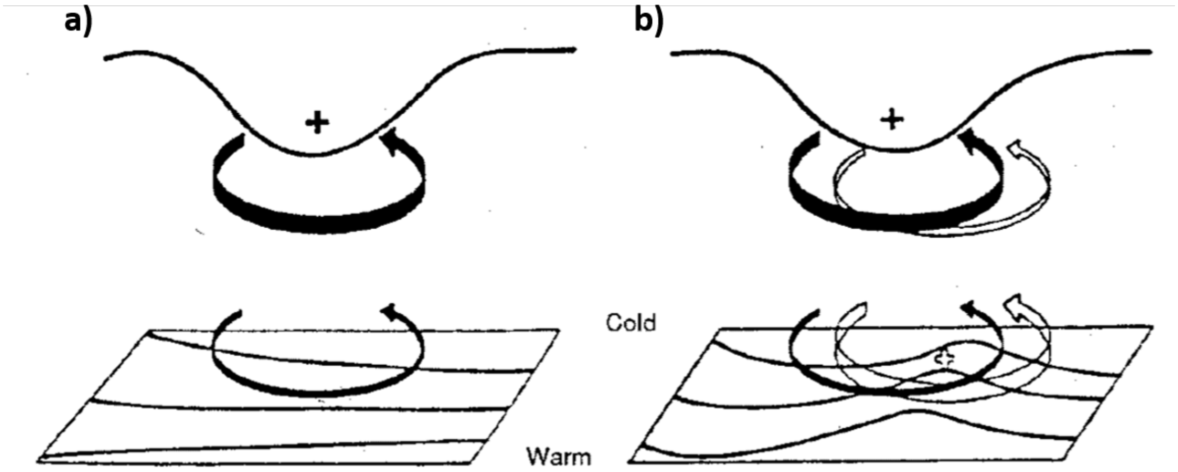

**Figure 2.10:** a) Positive PV anomaly (black arrow) advected over a baroclinic region inducing lower-level cyclonic circulation (black arrow) b) Out of phase warm anomaly (white arrow) which induces an eastward shifted circulation in the upper level (white arrow). The arrows are the circulations associated with the PV or thermal anomalies. The "+" symbols indicate the anomalies. Taken from Hoskins *et al.* (1985)

a lower level baroclinic region (characterised by a large meridional temperature gradient), the +ve PV anomaly induces a lower-level cyclonic vorticity by action-at-a-distance (see Fig. 2.10). The surface circulation acts to distort the surface meridional temperature gradient, moving warm air polewards ahead of the PV anomaly, and cold air equatorwards behind the anomaly. This advection of potential temperature leads to an out of phase warm anomaly collocated slightly east of the upper level vorticity anomaly, with the upper and lower level structures locked together. In turn, the lower level anomaly induces an eastward shifted circulation in the upper level, reinforcing the upper level anomaly and vice versa, amplifying the disturbances via a positive feedback between the two structures (Hoskins *et al.*, 1985; Holton, 1992).

### 2.3.2 Cyclogenesis - Eady model

The cyclogenesis of ETCs in the extratropics can be described by the linear model of baroclinic instability developed by Eady (1949). This model is capable to capture the main features of cyclogenesis, though it does not present the more complex mathematics of later models. The background state represented by the Eady model assumes a zonal flow with a constant vertical shear where vertical windspeed increases linearly from zero at the surface ($z = 0$) to U at the tropopause ($z = H$). The baroclinic wave is represented as a small amplitude perturbation, $q'$, to the Quasi-Geostrophic Potential Vorticity, QGPV, which is an approximation of the Ertel PV based on the Quasi-Geostrophic (QG) theory (which assumes that the flow remains close to geostrophic at all times). In the interior of the flow, no perturbations to the QGPV are allowed to exist because QGPV is initially zero and it is then conserved by definition along constant pressure surfaces, yielding at all times:

$$q' = \nabla_h^2 \Psi_g + \frac{f^2}{N^2} \frac{\partial^2 \Psi_g}{\partial z^2} = 0, \tag{2.15}$$

where $\Psi_g$ is the geostrophic streamfunction, $N$ is the Brunt-Väisälä frequency, and $\nabla_h$ is the 2D gradient. Since the thermodynamic equation, linearised with respect to the background flow, has to be satisfied at the boundaries (where $w = 0$), the Eady model is solved seeking the normal mode solutions:

$$\psi_g = \psi_0 e^{\sigma t}\left(\cos[k(x-ct)]\cosh\left(\frac{kN[z-\frac{H}{2}]}{f}\right) - \alpha\sin[k(x-ct)]\sinh\left(\frac{kN[z-\frac{H}{2}]}{f}\right)\right), \tag{2.16}$$

where $\alpha$ is a variable that gives information on the structure of the perturbation (the ratio of the edge wave amplitudes), and $\sigma$ is the growth rate. The growth rate is defined as:

$$\sigma = -\left(\frac{1}{N}\frac{g}{\theta_{ref}}\frac{\partial\theta}{\partial y}\right)\sqrt{\left(\frac{kL_R}{2} - \tanh\left(\frac{kL_R}{2}\right)\right)\left(\coth\left(\frac{kL_R}{2}\right) - \frac{kL_R}{2}\right)}, \tag{2.17}$$

where $L_R = \frac{NH}{f_0}$ is the Rossby radius of deformation, i.e. the length scale at which rotational effects become as important as buoyancy or gravity wave effects in the evolution of the flow about some disturbance, and $\frac{\partial\theta}{\partial y} < 0$ because temperature decreases northward in the baroclinic region considered. Eq. (2.17) yields three different solutions: positive growth rate $\sigma$ for a negative real root, negative growth rate for positive real root, and neutral growth rate for imaginary roots. According to Eq. (2.16), these 3 cases correspond to a decaying mode $\psi_g$ for $\sigma$ negative real number, to a neutral (not growing over time) mode $\psi_g$ for $\sigma$ imaginary number and to a growing mode $\psi_g$ for $\sigma$ real positive number. For the latter mode, the maximum growth rate of the perturbation is:

$$\sigma = -0.31\frac{1}{N}\frac{g}{\theta_{ref}}\frac{\partial\theta}{\partial y}, \tag{2.18}$$

to which the following wavenumber corresponds:

$$K = \frac{1.6}{L_R}. \tag{2.19}$$

Substituting typical midlatitude scalings in Eq. (2.18), it is obtained that the e-folding time of the cyclone is $\approx$ 1day and the wavelength is $\approx$ 4000 km. The e-folding time is in a reasonable agreement with the observed timescale for ETC growth (on the order of a few days), but the wavelength is roughly twice as large as the observed ETC length scale of $\simeq$ 2000 km, though of the same order of magnitude. This can be explained by the fact that the linear Eady model neglects the non-linear processes that characterise the atmosphere dynamics.

As can be noted from Eq. (2.17) the magnitude of the growth rate, $\sigma$, of a baroclinic system that is intensifying is directly proportional to the meridional temperature gradient $\frac{\partial \theta}{\partial y}$, which is associated with a potential energy imbalance between the pole and the equator. The baroclinc system acts to reduce this pole-equator energy imbalance by converting the associated potential energy into kinetic energy. A larger pole-equator temperature gradient leads to a stronger cyclone intensification. This relationship is in agreement with observational evidence, which shows that the strongest ETCs tend to form over regions characterised by large sea surface temperature meridional gradients driven by ocean currents, such as the Gulf Stream (off the US East Coast) and the Kuroshio Current (between China and Japan). When the atmospheric static stability is large, the cyclone intensification is suppressed since the circulation induced by the PV anomalies is unable to extend as far through the depth of the troposphere, in agreement with the inverse proportionality between the $\sigma$ and the $N$ predicted by the Eady model, see Eq. (2.17). Moreover, the Eady model is able to predict the structure of growing baroclinic instabilites. While the pressure tilts westward with height, with the surface and upper boundary pressure waves 90° out of phase with each other, the temperature field tilts eastward with height. Like the pressure field, the vertical velocity field also tilts westward with height, although not as steeply (Gill, 1982).

### 2.3.3 Conceptual models of extratropical cyclones

Well before the Eady model had been developed, Bjerknes (1919) and Bjerknes and Solberg (1922) used the sparse surface observations that were available at the time to formulate a conceptual model of North Atlantic ETCs, the so-called "Norwegian Model". In the Norwegian model an ETC is described as one consisting of a warm and a cold air mass separated by a distinct boundary surface which runs through the centre of the cyclone, as shown in Fig. 2.11. The boundary surface is inclined towards the cold air mass making a small angle with the horizon and it extends across most of the troposphere. The evolution of the Norwegian cyclone model is divided into 4 different stages, as depicted in Fig. 2.12a. Initially, a stationary boundary divides a colder airmass on its northern side from a warmer

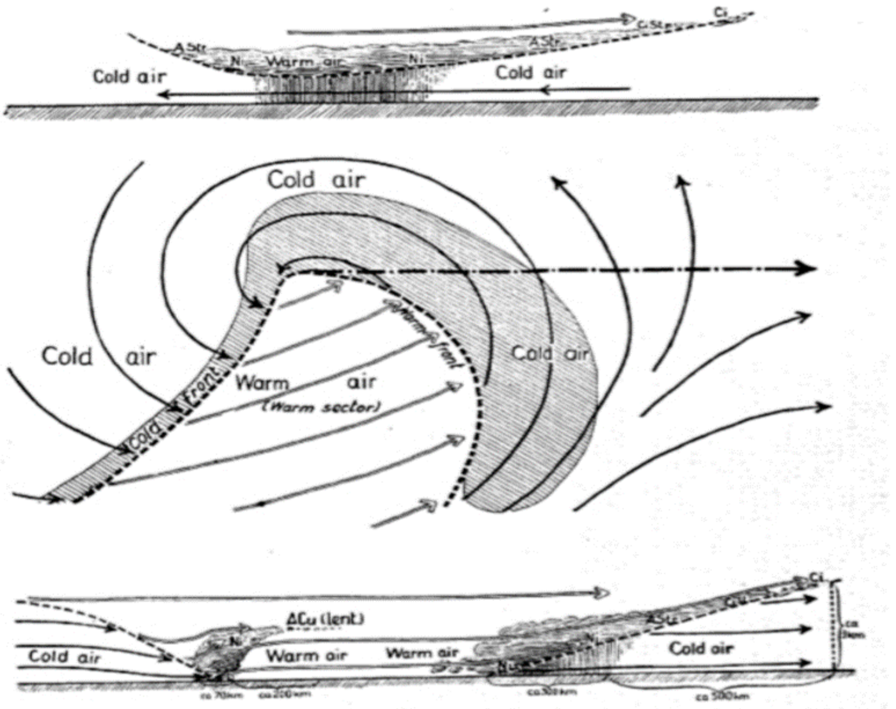

**Figure 2.11:** Main features of the idealised cyclone model, termed "Norwegian Model", adapted from Bjerknes and Solberg (1922).

air to the south (in the Northern Hemisphere) (stage I). When the denser cold air starts to flow underneath the warmer air and the less dense warm air starts to flow above the cold air mass, a wave forms on the stationary front (stage II). While the cold air at the ground is pushing under the warm air which is starting to flow above, the system forms and grows travelling eastward (stage III). When the cold air from the rear side of the cyclone reaches the warm air cutting off the warm sector, an occlusion forms, and the low pressure centre redevelops north of the cold and warm front (stage IV). After this stage, the system starts to weaken, and it eventually dies.

The Norwegian Model successfully provided a conceptual description of ETCs for 70 years until a vast amount of remote sensing and airborne observations, besides an improved theoretical understanding, revealed the Norwegian model did not always describe accurately the structure and evolution of ETCs. The availability of a large number of observations allowed Shapiro and Keyser (1990) to develop a new conceptual model which accurately describes those ETCs that do not match the characteristics predicted by the Norwegian model. As illustrated in Fig. 2.12b, in stage I, the Shapiro-Keyser model assumes the same disturbed frontal

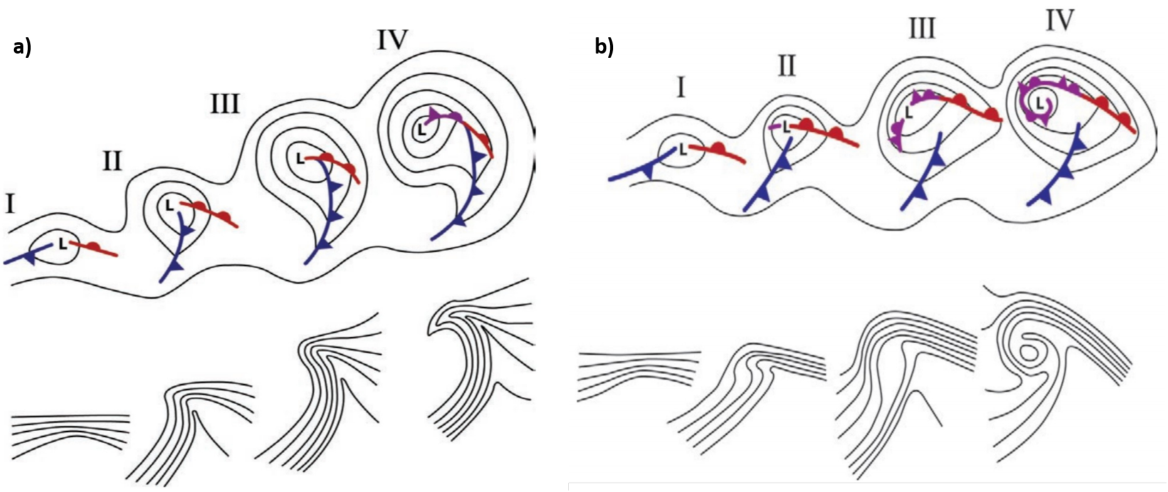

**Figure 2.12:** The four stages describing the life cycle of a) Norwegian cyclone model b) Shapyro-Keyser cyclone model. Taken from Schultz *et al.* (1998)

zone as the Norwegian model. But, in contrast to the Norwegian model where the cold front catches up the warm front, in the Shapiro-Keyser model the warm and the cold front start to separate in stage II, developing a frontal fracture, since the cold front moves perpendicularly to the warm front (T-bone structure). In stage III, this fracture is filled by the warm air mass, which penetrates the low pressure core and hooks around its rapidly deepening centre. In stage IV, the warm air, trapped near the low centre, forms a warm seclusion wrapped by the bent-back warm front, while cold air from behind the cold front encircles the warm seclusion.

Which conceptual model a cyclone most closely follows during its life-cycle can be influenced by several factors. These include the presence of surface friction (Schultz and Zhang, 2007) and of barotropic shear. The role of barotropic shear in controlling the cyclone life-cycle was examined in detail by Thorncroft and McIntyre (1993), who used two different settings. In the first setting, life-cycle 1 (LC1), no barotropic shear component was applied to the initial baroclinic wave, while in the second setting, life cycle 2 (LC2), a cyclonic barotropic shear component was applied. The cyclones developing without barotropic shear (LC1) presented the occurrence of the frontal fracture and, in later stages, of the warm seclusion, according to the Shapiro-Keyser conceptual model. Instead, the cyclone developing within barotropic shear (LC2) was stronger and followed the Norwegian cyclone conceptual model. The LC2 cyclone presented a longer life time, a weaker cold front, and a stronger warm front than the LC1 cyclone. Moreover, the LC2 cyclone showed no anticyclonic wave breaking that would cut off the cyclone PV, which instead occurred for the LC1 cyclone. A review study of Shapiro *et al.* (1999) further demonstrated that cyclones which develop within barotropic shear (LC2 life cycle) followed the Norwegian model, while cyclones which develop without barotropic shear followed the Shapiro-Keyser model. However, it is currently unknown what is the relative proportion of cyclones that follow the Shapiro Keyser life cycle and cyclones that follow the Norwegian model life cycle (Clark and Gray, 2018).

### 2.3.4 Airflows in extratropical cyclones

The three main airflows in ETCs are the warm conveyor belt (WCB), the cold conveyor belt (CCB), and the dry intrusion (DI), depicted in Fig. 2.13.

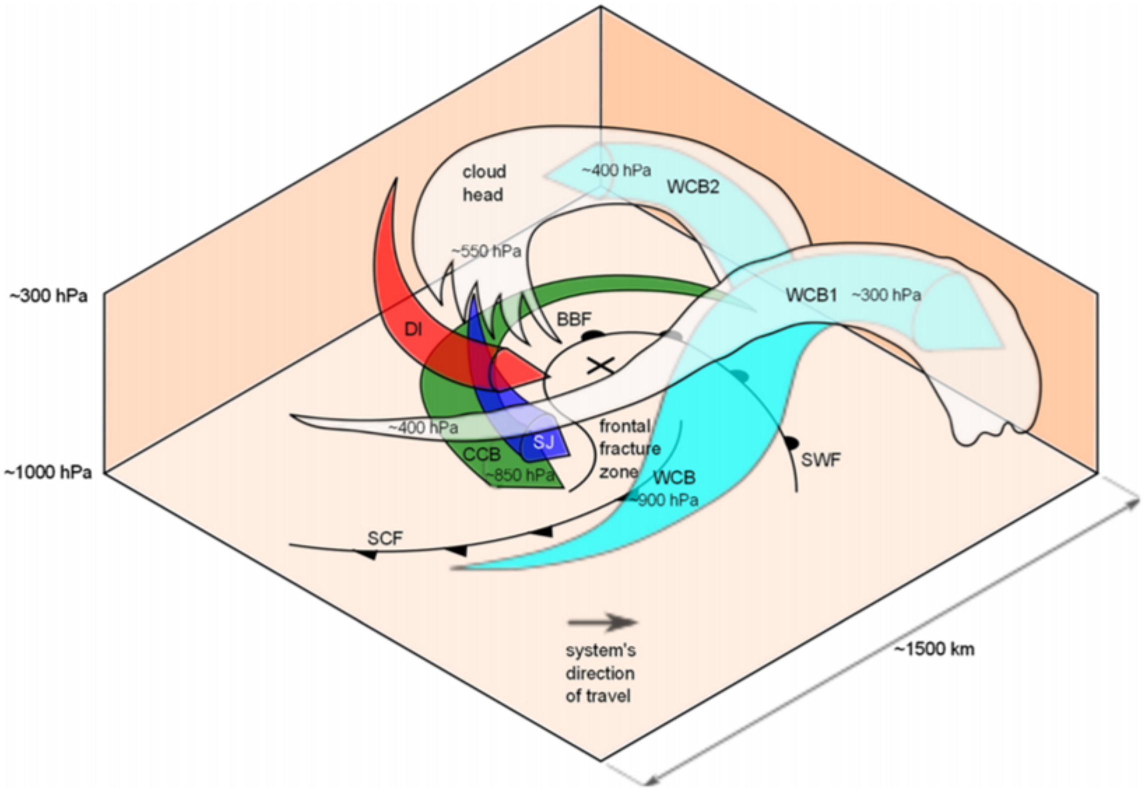

**Figure 2.13:** Three-dimensional structure of a Shapiro-Keyser ETC. The features displayed are: surface cold front (SCF), surface warm front (SWF), bent-back front (BBF), warm conveyor belt (WCB) bifurcating into an anticyclonic (WCB1) and cyclonic (WCB2) components, cold conveyor belt (CCB), dry intrusion (DI) and a sting jet (SJ) which descends into a frontal fracture region. The low pressure centre of the cyclone is marked with an X while the cloud top is illustrated with a pale shading. Taken from Martínez-Alvarado *et al.* (2014).

The WCB is a strong and well defined poleward moving airflow, ahead of the cold front. When the WCB ascends over the warm front, it moves large amounts of moisture forming clouds and producing heavy rainfall. It is the WCB that usually produces the largest amount of rainfall within ETCs. As the WCB ascends, it bifurcates, as demonstrated by Browning and Roberts (1994) and Bader *et al.* (1995), with one component (WCB1 in Fig. 2.13) turning anticyclonically away from the low, whilst the other (WCB2) component turns cyclonically around the north of the low centre.

The CCB originates from the low level air ahead of and beneath the warm front, and travels rearwards relative to the advancing system, flowing on the poleward side of the warm front and undercutting the WCB.

The DI is a stream of air from upper levels that descends rapidly behind the cyclone. It usually originates in the upper troposphere or lower stratosphere and, thus, contains little moisture, which explains why it can often be observed in satellite images as a cloud-free slot just behind the cold front. The dry air of the DI flowing above the humid air of the WCB creates potentially unstable environment that can generate convection in the region.

An additional region of distinct near-surface stronger winds can form if a coherent air flow descends from mid-levels inside the cloud head into the frontal-fracture region of the cyclone over a period of a few hours (Clark and Gray, 2018). This region of extreme wind speeds was first identified by Browning (2004) by reanalysing the Great Storm of October 1987. They called it the "sting at the end of the tail", or Sting Jet (SJ), after Grønås (1995), given that it was located near the end of the tail of the bent-back front, which resembled the tail of a poisonous scorpion. As discussed in Clark and Gray (2018), a continuum of SJ descent and speed-up mechanisms exists that allow the SJ to reach the top of the ABL, and, from there, penetrate to the surface. Probable causes of SJ descent mechanisms proposed and investigated in the literature include, but are not limited to, the release of convective slantwise instability, frontal dynamics, and evaporative cooling (Clark and Gray, 2018).

### 2.3.5 North Atlantic storm track

ETCs travel along rather narrow regions, and share common cyclogenesis areas. These narrow regions are termed storm tracks and are important drivers of the earth system's weather and climate variability. The most notable ETC storm tracks are the North Atlantic storm track, the Pacific storm track, and the Southern Hemisphere storm track. Given that the focus of this thesis is on ETCs that cross the British Isles, only the salient features of the North Atlantic storm track are reviewed here.

The ETCs in the North Atlantic storm track usually form in the lee of the major mountain ranges and along the east coasts of North America, with the main region of cyclogenesis being comprised between the Gulf Stream and the east coast of North America (Whittaker and Horn, 1984; Dacre and Gray, 2009). The fact that the most active cyclogenesis region of the North Atlantic storm track is located over the Gulf Stream is more than accidental. The geographical position of the Gulf Stream borders is near the North American cold air mass, and this, combined with the strong Gulf Stream SST gradient, makes this region very favourable for cyclone formation, providing a baroclinic environment with strong latent heat fluxes (Vries *et al.*, 2019). The baroclinic environment is due to the strong Gulf Stream SST gradient (via thermal wind shear), while the strong air-sea latent heat fluxes are due to the cold North American continental airmass flowing over the warmer Gulf Stream. After forming, ETCs generally travel north-easterly, until they start to decay, and eventually die out, in the central and eastern North Atlantic (and in the Northern North Sea), at latitudes approximately above 60° (Hoskins and Hodges, 2002).

The North Atlantic storm track is characterised by a pronounced seasonal variability. Recent studies of Hoskins and Hodges (2019a,b), which used an objective identification method for cyclones based on a combination of feature-tracking and Eulerian diagnostics, demonstrated that the North Atlantic storm track mean intensity is fairly constant in autumn, winter, and spring seasons (slightly higher in winter), while in summer it is substantially weaker and poleward shifted (≈50°N) than in winter and spring, as shown in Fig. 2.14.

Besides the seasonal variability just discussed, the North Atlantic storm track also exhibits a marked regional variability. As shown by Hoskins and Hodges (2002), cyclones whose genesis is in the Gulf stream region do not usually travel across the entire length of the storm track, but rather dissipate over the entire region spanned by the North Atlantic storm track,

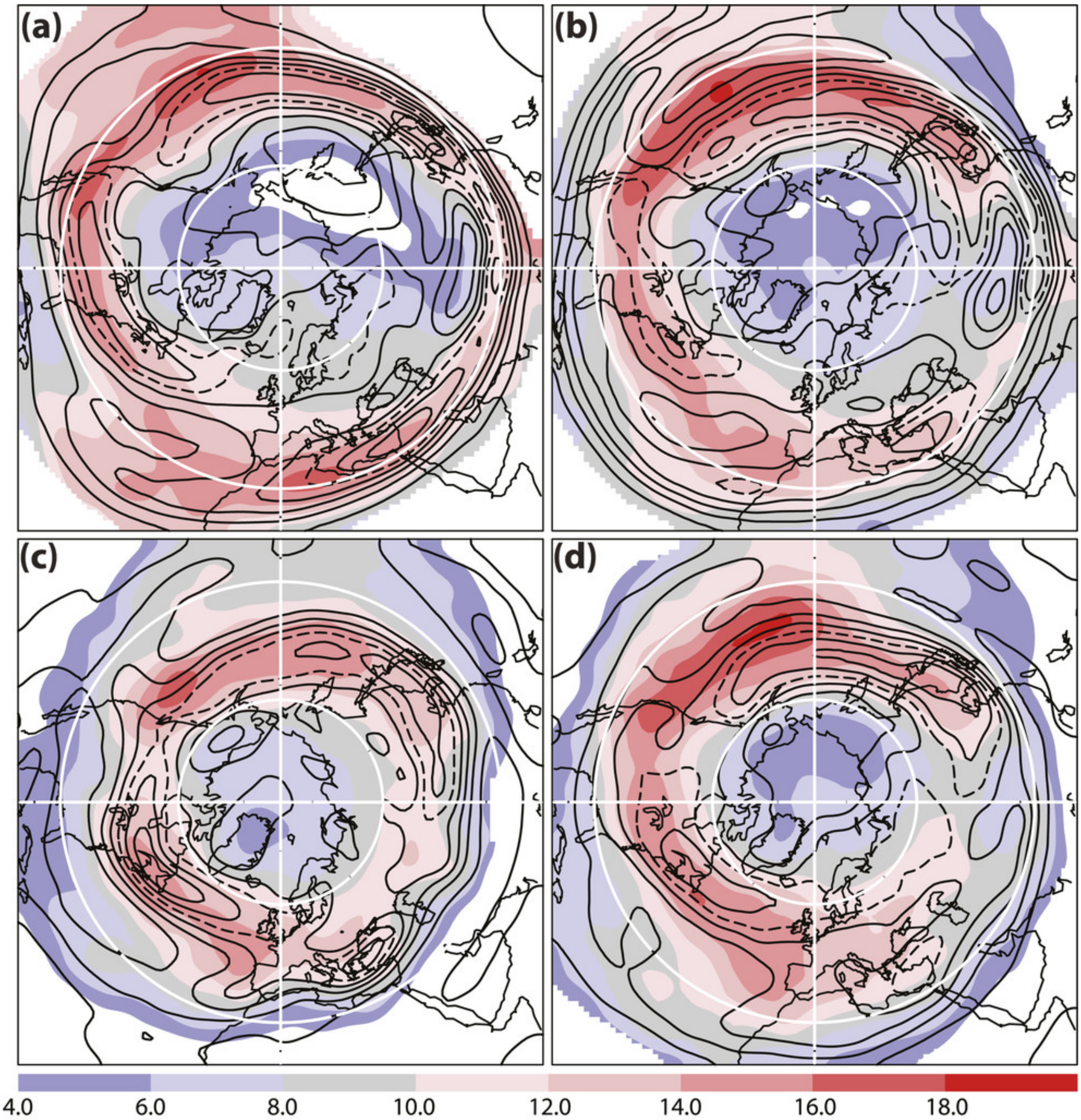

**Figure 2.14:** Track density (contours; number per month per unit area, where the unit area is equivalent to a 5ř spherical cap) and mean intensity (color; $10^{-5}$ $s^{-1}$) of 250-hPa vorticity $\zeta$250 maxima for each season: (a) DJF, (b) MAM, (c) JJA, and (d) SON. Track density contours are every 2.5 with the dashed line at 12.5. Mean intensity is suppressed for track densities below 1.0. Taken from Hoskins and Hodges (2019a).

which is in fact composed of many shorter tracks. Further analysis carried out by Dacre and Gray (2009) highlighted a secondary cyclogenesis region, located in the Eastern North Atlantic (see Fig. 2.2). Cyclones forming in this region, termed East Atlantic cyclones, were found to travel far more commonly to the British Isles and western Europe than those that formed in the Gulf Stream region. Because the baroclinicity and the SST gradients are weak in the East Atlantic cyclogenesis region, compared to the Gulf Stream region, the East Atlantic region provides a different environment than the Gulf Stream region for the formation of ETCs. Moreover, cyclones originating over the Gulf Stream region often leave trailing fronts when dissipating over the East Atlantic region. Since these trailing fronts are associated with a strip of relative vorticity, Dacre and Gray (2009) suggested that they could provide the required additional relative vorticity to explain the observed higher intensity (lower mean sea level pressure, and higher relative vorticity) of East Atlantic Cyclones compared to west Atlantic cyclones.

From the review presented in this section, it is of critical importance to develop a good understanding of the mechanisms controlling the North Atlantic storm track, due to its role in controlling the large-scale weather and climate patterns of the British Isles and Northern Europe. However, the mean perspective of the North Atlantic storm track is not very representative of the local details of the extreme weather (rain, precipitation), associated with single ETC events. A further discussion of weather extremes (wind, precipitation) associated with ETC and methods to measure their impact is given in the following section.

## 2.4 Extratropical cyclone impacts

ETCs bring exceptionally intense surface winds and heavy rainfall when they make landfall on the British Isles and North Western Europe, causing widespread flooding and vast damage (for example, falling trees, powercables interrupted). For more details on the economic damage of ETCs, see Chapter 1. Although the focus of this thesis is on ETCs extreme winds, here also the precipitation and wave height extremes associated with the ETCs are reviewed.

### 2.4.1 Precipitation impact of extratropical cyclones

The association between ETCs and extreme precipitation events has been highlighted since the earliest studies on cyclones crossing the British Isles and Northern Europe (Bjerknes and Solberg, 1922). Indeed, ETCs have been found to play a key role in the (poleward) transport of large quantities of heat and moisture through their WCB. As the WCB ascends, part of the moisture condenses, forming clouds and precipitation (which eventually reaches the surface) (Browning, 1986). Analysis of cyclone composites for the two year period 2003-2004 indicated that the stronger the cyclone the stronger the associated cyclone-mean rain rate. This behaviour can be explained by the fact that stronger cyclones are (usually) linked to an enhanced vertical motion, thus to moisture condensation, then leading to cloud formation and precipitation (Field and Wood, 2007).

Using an event-based climatology of precipitation extremes based on the ECMWF Interim reanalysis (ERA-Interim), Pfahl and Wernli (2012) demonstrated that a high percentage of precipitation extremes is directly related to ETCs, with percentage of cyclone-induced precipitation extremes exceeding up to 80% in the Mediterranean region, Newfoundland, near Japan, and over the South China Sea, as shown in Fig.2.15. As can be noted from a close examination of Fig. 2.15, also a large percentage of the precipitation over the British Isles was identified as cyclone-induced precipitation by Pfahl and Wernli (2012), varying between 60% over winter DJF months to 80% over summer JJA months. Moreover, they also showed that the North Atlantic storm track cyclones associated with extreme precipitation events were more intense than those that were not. Comparing the DJF and JJA months, Hawcroft *et al.* (2012) found that ETCs in the Northern Emisphere were associated with more precipitation events in DJF months than in the summer JJA months. Overall, they linked ≥70% of all the extreme precipitation events in northern and western Europe to ETC events.

### 2.4.2 Wind impact of extratropical cyclones

The extreme surface wind speeds associated with ETCs pose the largest natural hazard to lives and livelihoods in Europe when averaging over multiple years (Craig, 2003; Hewston and Dorling, 2011; Earl *et al.*, 2017). The Great Storm of 1987 and Windstorm Kyrill of 2007, responsible, respectively, for £1.4 and £1.0 billion of insurance losses and also for several fatalities, are just two examples of the scale of socio-economic damage caused by ETCs over the British Isles Brönnimann *et al.* (2012). Considering the period 1970-2011, 9 out of the 32 most expensive weather-related world-wide insured loss events were associated with ETCs crossing Europe and the British Isles (Hewston and Dorling, 2011).

The wind hazards result from the intense near-surface wind speeds which are associated with the ETC low level jets: the WCB, the CCB, and occasionally the SJ Hewson and Neu (2015). The WCB produces the largest footprint of strong surface wind speeds and gusts, being ≈ 500 km in width and ≈1000 km in length, but occurs early in the life of the cyclone, lasting for a maximum of 48 hours, with peak gusts in the range ≈25-35 m $s^{-1}$. The stronger winds and gusts occur later in the cyclone life, when the cyclone is at its peak intensity and the CCB has developed, hooking around the equatorward flank of the extratropical cyclone, and thus being aligned with the direction of cyclone travel. In the equatorward flank of the cyclone, south to its centre, the CCB is associated with peak gusts in the range ≈30-40 m $s^{-1}$, which usually last between 12 and 36 hours. Despite the destructive nature of the CCB, the SJ has been found to produce the strongest gusts, in the range ≈35-45 m $s^{-1}$, and characterised by

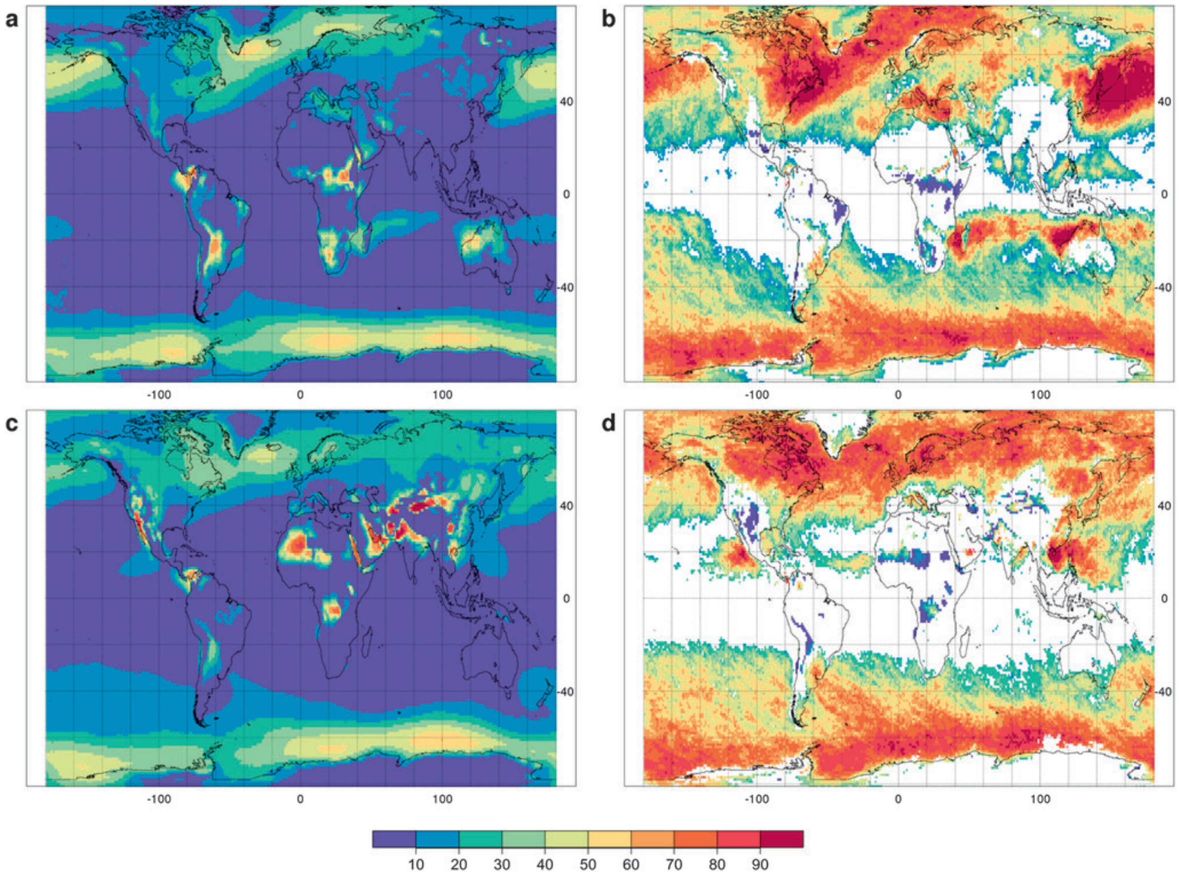

.

**Figure 2.15:** Coincidence of cyclones and precipitation extremes in different seasons: relative cyclone frequency (%) in (a) DJF and (c) JJA; percentage of precipitation extremes related to a cyclone in (b) DJF and (d) JJA. Grid points are masked in white if the relationship between cyclones and extreme precipitation events is statistically not highly significant. Taken from Pfahl and Wernli (2012).

a very short-lived life span ≈1–6 hours. However, only up to one third of the ETCs crossing the British Isles is associated with a SJ (Hart *et al.*, 2017).

A recent analysis from Earl *et al.* (2017) of the daily maximum gusts (DMGS) distribution recorded by the 39 UK surface observation network during the climatological period 2008-2014, has quantified the contribution of the cyclone conveyor belts and smaller scale features (including SJs and convective lines) to the recorded top 1% DMGSs, and 0.1% DMGSs. Findings from this study indicated that although the WCB and the CCB dominated the top 1% DMGS, smaller features such as SJs and convective lines were associated with the top 0.1% DMGS (the very extreme tail of the DMGS distribution at each observation site). Moreover, the low-level winds associated with the CCB turned out to be as destructive as the SJs when the CCB was aligned with the ETC direction of travel, as also found by Baker (2009). The generality of these results was limited by having used exclusively land surface stations. Given the growing importance of the offshore wind power industry, the extension of these studies to the North Atlantic Ocean seas surrounding the British Isles would prove beneficial for providing hazard guidance to the industries operating there.

### 2.4.3 Measuring the wind impact of extratropical cyclones

The extreme surface winds associated with ETCs impact a broad range of assets from highways to buildings and wind turbines power output. As demonstrated by Lamb and Frydendhal (1991), the wind power is the only physical quantity that can objectively measure the destruction brought by ETCs. The wind power can be thought as the work done by the wind, and can be thus computed as the dynamic pressure (fluid's kinetic energy per unit volume) multiplied by the run of the wind (distance) (Lamb and Frydendhal, 1991). Because the dynamic pressure is proportional to the square of the wind speed, the wind power, and thus the severity of a storm, can be quantified by the cube of the wind speed. Leckebush *et al.* (2008) further refined this metric, thus defining the Storm Severity Index (SSI), which takes into account that damage at a site occurs only if a certain threshold wind speed is exceeded:

$$\mathrm{SSI} = \sum_{t}^{T}\sum_{k}^{K}\left[\left(max\left(0, \frac{v_k - v_{perc,k}}{v_{perc,k}}\right)\right)^3 \times A_k\right] \tag{2.20}$$

where $t$ refers to a time index, $k$ refers to the grid boxes, $A_k$ represents the area of the associated cell divided by a reference cell at the equator, $v$ is the daily maximum wind speed, and $v_{perc}$ is defined by the local 90th, 95th, or 98th percentile value of the daily maximum wind speed. The use of such percentile thresholds is useful to characterise the extreme tail of the wind speed distribution at each model grid-cell (or observation site) (Hewston and Dorling, 2011). However, fixed thresholds are more useful than percentiles to characterise the hazard posed by extreme wind speeds to energy infrastructure. For example, for wind speeds above 25 m $s^{-1}$, wind turbines can be forced to shut, and thus several studies have focused on investigating wind speeds exceeding this important operational value (Dupont *et al.*, 2018; Molina *et al.*, 2021).

The most straightforward use of the SSI metric defined in Eq. (2.20) is the integrated measure of storminess within the investigated area (ASSI), though it may be possible that distinct events contribute to the value of the ASSI, making the assessment of the severity of a particular ETC event much harder. Rather than integrating the SSI over the whole investigated domain, at each time step coherent areas of wind threshold exceedances are identified and tracked in time with a nearest neighbour approach, as far as this ETC event affects an area of minimum size. This SSI is referred to as the Event SSI (ESSI). Its application to an ETC event, Storm Daria (1990), is illustrated in Fig. 2.16.

### 2.4.4 Sea state impact of extratropical cyclones

North Atlantic ETCs are associated with extreme precipitation and wind speeds, but are also often the driver of extreme sea state. Indeed, the North Atlantic storm track has been associated with extreme significant wave height events. More in detail, the coasts of Europe and the British Isles are exposed to the huge swells generated by ETCs in the North Atlantic as well as to more locally generated wind-driven waves (but still extreme, as high as 10 m)

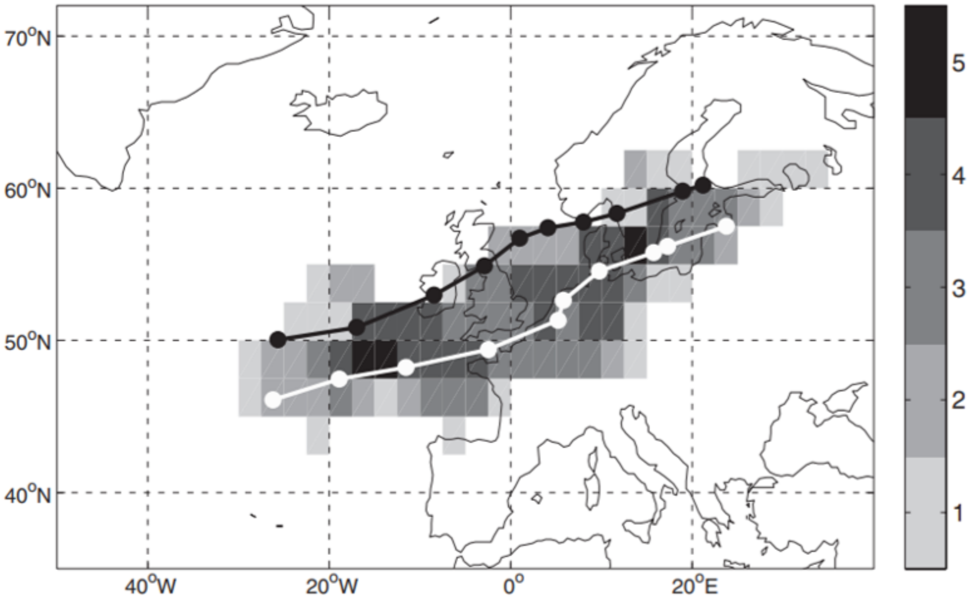

**Figure 2.16:** Wind storm Daria (24-26 January 1990). Track of wind fields exceeding the 98th percentile (white) and track of the corresponding low pressure system (black). Shading indicates the number times the wind speed exceeded the local 98th percentile (Leckebush *et al.*, 2008).

appearing when ETCs approach the coastline. It is important to note that wind-waves are waves generated under the action of the local wind by the transmission of momentum from the air to the water while swells are free waves not sustained anymore by the wind that generated them Janssen (2004).

The link between ETCs and ocean waves has been explored in a few individual case studies. For example, Ponce de León and Guedes Soares (2014) looking at two North Atlantic ETCs formed in February 2007, found that the fourth quadrant of the ETCs, measured between 90° and 180° clockwise from the ETC direction, was characterised by higher wave heights than the other quadrants. Looking at an ETC case study in the North-Western Pacific in January 2013, Kita *et al.* (2018) was able to determine the wave spectral characteristics associated with ETC warm and cold sectors, finding that both sectors were associated with a narrow spectrum of wave directions and frequency.

Bell *et al.* (2017) and Ponce de León and Bettencourt (2021) adopted a more systematic approach to study the link between ETCs and associated wave height extremes. Using a historical series of extreme ocean wave heights in the North Sea observed at the Forties oil platform, Bell *et al.* (2017) demonstrated that the largest measured wave heights were associated with north-westerly cyclone wind events, aided in the growth by the large fetch over the central North Sea, but also southerly cyclone wind events were found to create large wave heights, despite the limited fetch. Rather than using conventional surface observations of wave heights, Ponce de León and Bettencourt (2021) used satellite altimetry observations of wave height distribution of ETCs, composited for a period spanning 1958-2018. They confirmed the previous Ponce de León and Guedes Soares (2014) findings, showing that the south-eastern quadrant of the composite of the ETCs were associated with the largest wave heights. They explained this finding by the extended fetch mechanism, given that this quadrant roughly corresponds to the region of the ETC where the wind direction is aligned to the same direction of the cyclones propagation. However the robustness of all these findings was limited by the spatial sampling of the available observations, only one marine surface station was used in Bell *et al.* (2017), or by the intermittent temporal sampling intrinsic in the satellite altimeters in (Ponce de León and Bettencourt, 2021). Thus, further research is still needed to ascertain the distribution of wave heights associated with ETCs.

## 2.5 Numerical weather prediction

As discussed in the previous sections, ETCs generate intense surface wind speeds and gusts as they pass over the UK (Martínez-Alvarado *et al.*, 2014), leading to large socio-economic impacts (Hewston and Dorling, 2011). Thus, skillful forecasts of extreme surface wind speeds associated with ETCs are critical for providing actionable information to first-line responders (Ricchi *et al.*, 2017; Lewis *et al.*, 2018). Since the first attempt to weather forecasting, made in 1861 by Admiral Robert Fitzroy, which was based on observations collected from simple barometers, the accuracy of the weather forecasts has substantially improved over the last two centuries. Weather forecasts are currently carried out by Numerical Weather Prediction (NWP) models, which numerically solve an approximated version of the Navier-Stokes equations running on high performance supercomputers and ingesting the latest meteorological observations through state-of-art data assimilation systems. Here the advancements in deterministic and probabilistic NWPs forecasts are briefly reviewed and the current challenges in forecasting ETCs with NWPs are presented.

### 2.5.1 Deterministic numerical weather prediction systems

The basic idea of a deterministic NWP model, meant as an automated forecasting system capable to produce a weather forecast, was first developed in 1950 by a team led by the American meteorologist Jule Charney using the ENIAC digital computer. The limited computing power of ENIAC constrained Charney's team to use a very coarse approximation of atmospheric dynamics based on the solution of the barotropic vorticity equation over a single layer of the atmosphere (by computing the geopotential height of the atmosphere's 500 hPa pressure surface). By the 1970s, only a few nations, such as the US, West Germany, the UK, and Japan, were already capable to run operationally deterministic NWP to produce global weather forecasts. Today, the vast majority of leading weather centres across the world run global deterministic NWP forecasts on the most modern supercomputers, whose computing power allows for much more sophisticated approximations of the Navier-Stokes equations (e.g. fully compressible, nonhydrostatic Euler equations). Examples of state-of-art NWP models are the Unified Model at the Met Office (UK), the Integrated Forecasting System (IFS) at the ECMWF, and the Global Forecasting System at the National Centre for Environmental Prediction (NCEP, US). These state-of-art deterministic NWPs for operational weather forecasts are intialised with a set of initial conditions, termed "analysis", which is obtained by blending output fields from an earlier run of the forecast with the most up-to-date observations. The "analysis" represents the state of the atmosphere closest to its "true" state. Then, the dynamical core of the NWP model evolves the initial state of the atmosphere by discretising and numerically solving the Navier-Stokes equations, usually employing a semi-Lagrangian method on an Arakawa-C grid.

Current global deterministic NWPs systems can predict the synoptic-scale evolution of weather events, such as ETCs, with reasonable skill (Frame *et al.*, 2015) but, because the atmosphere is a chaotic system (Lorenz, 1963), small errors in the initial conditions (ICs) of forecasts and in model physics approximations grow rapidly over time, limiting the predictability of the location and strength of mesoscale ETC features such as intense winds

(Buizza *et al.*, 2005; Bowler *et al.*, 2008). The forecast uncertainty yielded by IC and model errors can be estimated by generating probabilistic realizations of events using ensemble prediction systems (EPS) (Buizza *et al.*, 1999). However, compared to IC errors, the correct estimation of model errors represents a much greater challenge (Buizza *et al.*, 2005). Moreover, deterministic NWP models do not calculate the confidence in the simulation of weather events, and this affects the effectiveness of early warnings to first-line responders. Hence EPS have been developed as described below.

### 2.5.2 Medium-range ensemble prediction systems

In the last 30 years, a range of different EPS has been developed to estimate the inherent forecast uncertainty. These EPS have enabled longer-range and more reliable forecasts than those achievable using conventional deterministic NWPs. The first EPS was introduced in 1992 by the ECMWF, which initially ran three times a week with a 10-day range (Buizza and Palmer, 1995; Molteni *et al.*, 1996). Soon, the NCEP, the Meteorological Service of Canada (MSC), and other meteorological centres followed (Toth and Kalnay, 1997; Houtekamer *et al.*, 1996). To estimate IC errors, the NCEP and ECMWF medium-range EPS adopt, respectively, the bred-vector and singular vector perturbation approaches, which are both based on the argument that fast-growing perturbations develop naturally in a data assimilation cycle and will continue to grow as short and medium-range forecast errors (Buizza *et al.*, 2005). The Met Office medium-range EPS uses an Ensemble Transform Kalman Filter (ETKF; Bishop *et al.* (2001)) to generate the ensemble perturbations, which could be thought of as a generalization of the bred-vector (or error-breeding) method of Toth and Kalnay (1997), in which the perturbations determined for each cycle are a linear combination of the forecast perturbations from the previous cycle, thus leading to the benefit, compared to the bred-vector method, of generating orthogonalized perturbations (Bowler *et al.*, 2008). The generation of ensemble perturbations by the ETKF is schematically illustrated in Fig. 2.17. Instead, the MSC uses the perturbed-observation (PO) approach, which generates initial conditions by assimilating randomly perturbed observations via a Monte-Carlo like procedure (Houtekamer *et al.*, 1996). All these medium-range EPS have been running operationally for more than 20

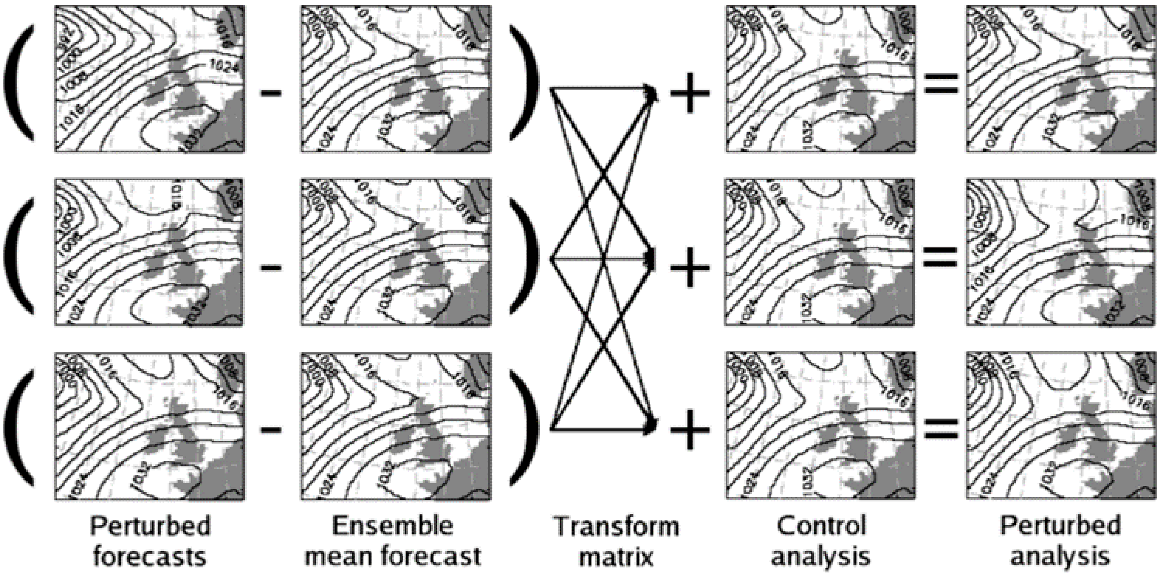

**Figure 2.17:** Graphical explanation of the ETKF method. The ETKF mixes the perturbations of different members via the transform matrix. Taken from Bowler *et al.* (2008).

years, and are capable of generating very good forecasts of ETC's large-scale development, e.g. the WCB, CCB, and DI, with several days lead time (Bowler *et al.*, 2008).

The need to capture the impact of the variability of small unresolved scales of motion (e.g. convection and boundary-layer turbulent fluxes) on the errors of the larger resolved scales (e.g. horizontal pressure gradients, wind shear and baroclinicity), has led to a development of a number of different methods to address model errors in synoptic and mesoscale EPS forecasts. These methods range from a multimodel approach (Hagedron *et al.*, 2005), which widens the sample range of possible forecast scenarios by providing each ensemble member with a different NWP forecast model, to a single-model approach, which represent the error in the physics parametrizations using multi-physics, multi-parameters, and stochastic physics schemes. The multi-physics and multi-parameters schemes represent the uncertainty in the model parametrizations directly, using different values to define the model parametrization settings in each ensemble member (Berner *et al.*, 2011). The stochastic schemes are designed to simulate the random model error component, either by randomly perturbing the increments or tendencies from parametrization schemes of the atmospheric model, as in the Stochastically Perturbed Parameterization Tendency (SPPT) scheme (Buizza *et al.*, 1999), or by providing the atmospheric model with a stochastic parametrization of missing unresolved processes, as in the Stochastic Kinetic Energy Backscatter (SKEB) scheme (Bowler *et al.*, 2009). Combinations of variations of these schemes have been adopted by the leading weather centres in medium-range EPS forecasts, yielding significant improvements in their probabilistic forecast skills (Tennant *et al.*, 2011).

Despite the increase in physics complexity and in the degree of coupling between model components, the relatively coarse resolutions of medium-range EPSs cannot provide detailed km-scale forecasts over regions of particular interest. For example, in the case of a rapidly developing cyclone, Lean and Clark (2003) established that a grid spacing of $O10$ km is good enough to represent the overall frontal structure of an ETC and the associated airflows, as shown by comparison of Fig.2.18a-c; however, a convective-scale grid spacing of $O1$ km is required to resolve smaller-scale multiple slantwise circulations, the 3-D structure of convection lines, and the peak cyclone surface wind speed. In fact, as can be seen from Fig.2.18c-d, the northernmost cyclone circulation in the $O10$ km simulation splits into two distinct features near the surface (between 100-200 km from cyclone centre and 700-900 hPa in the vertical) in the $O1$ km simulation.

### 2.5.3 Convective-scale regional ensemble prediction systems

To address the need to predict weather hazards, such as ETC extreme wind speeds, at km-scale , weather centres worldwide have developed over the last 15 years short-range regional convective-scale ensemble systems, with ICs and LBCs provided by the global EPSs. As a result, much research has recently been devoted to exploring the benefits of decreasing the ensemble grid spacing for forecast skill improvements and of increasing the ensemble size for better sampling the uncertainty. For example, Schellander-Gorgas *et al.* (2017) compared the performance of the 16-member convective-scale 2.5-km horizontal grid spacing AROME-EPS to that of the 16-member mesoscale 11-km grid spacing ALADIN-LAEF EPS. For a summer case study over the Alpine region, they found that the AROME-EPS significantly improved the precipitation forecast skill due to better resolution of the local effects of mountain topography. A further study by Raynaud and Bouttier (2017) varying resolution and ensemble size of convective-scale AROME-EPS found that increasing the resolution only led

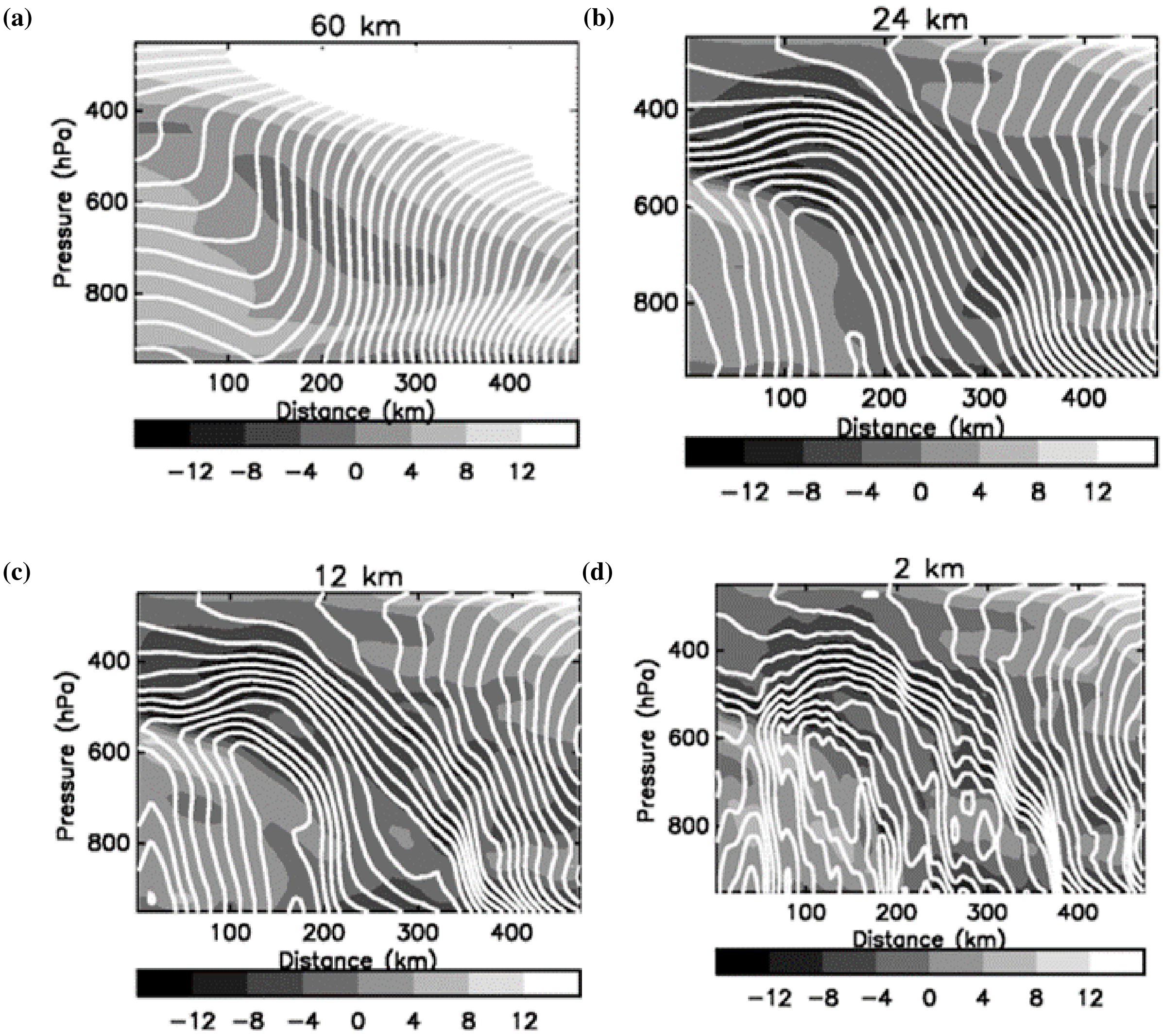

**Figure 2.18:** Cross-frontal velocity cross-sections of a rapidly developing ETC, in intensive observation period 16 of the Fronts and Atlantic Storm Tracks Experiment, simulated using the non-hydrostatic version of the Met Office Unified Model for a number of different horizontal grid spacings, varying from 60 to 2 km. The darker shadings correspond to velocities towards the cold air (i.e. to the left in the sections). The white lines are isolines of stream function derived by integrating horizontal velocity with respect to pressure downwards from the top of the cross-section. Taken from Lean and Clark (2003).

to short-range forecast improvements, whereas increasing the ensemble size exhibited a larger impact at longer forecast ranges. In this context, the Met Office developed the short-range high-resolution Met Office Global and Regional Ensemble Prediction System [MOGREPS, Bowler *et al.* (2008)], consisting of two related EPSs: the medium-range global 12-member MOGREPS-G with 33-km grid-spacing; and the short-range, limited-area (British Isles) 12-member MOGREPS-UK with 2.2-km grid-spacing (Hagelin *et al.*, 2017). Since 2016 the MOGREPS-UK has been inititalised by perturbing about an analysis of the Met Office's UK variable resolution (UKV) deterministic model using the MOGREPS-G perturbed ensemble members (Hagelin *et al.*, 2017). Investigating a three-month long summer case study, these authors found that the convective-scale ensemble MOGREPS-UK not only improved the precipitation forecast skill, compared to the deterministic UKV, but it also improved the skill of other meteorological variables of interest such as 1.5 m air temperature, 10-m wind speeds, visibility, cloud base height, and cloud cover. Further investigation by Porson *et al.* (2020) using a MOGREPS-UK configuration with 18 time-lagged members (by hourly cycling), revealed substantial improvements in skill for the same meteorological variables considered in Hagelin *et al.* (2017). The MOGREPS-UK configuration used by Porson *et al.* (2020) is detailed in Fig. 2.19. It uses uses hourly time-lagged ensemble members to exploit the hourly 4D-Var data assimilation run in the deterministic convective-scale UK model (UKV), and then creates an 18-member ensemble by running three members every hour, time-lagged over a temporal window of 6 hr.

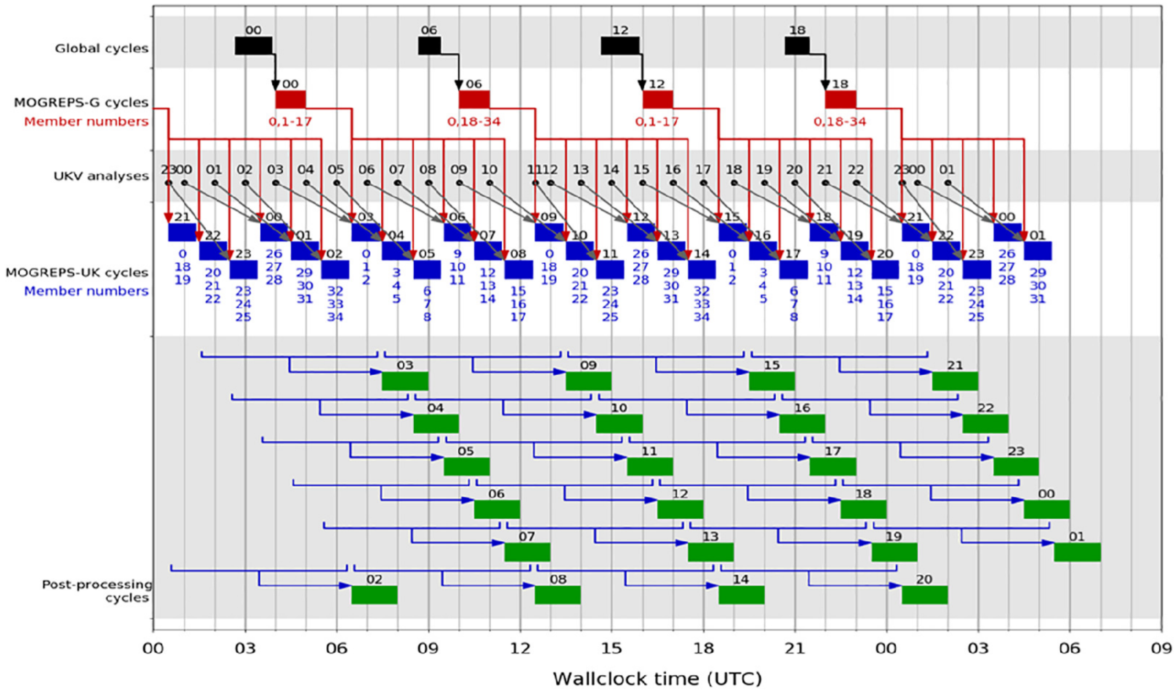

**Figure 2.19:** Diagram representing the timeliness of the time-lagged configuration of MOGREPS-UK. The blue boxes show the runtimes of a single MOGREPS-UK cycle; the blue numbers show the ensemble members of MOGREPS-UK (where member zero is the control).The black dots/grey arrows show the UKV analyses around which a given MOGREPS-UK cycle is centred. The red boxes, arrows and numbers show the MOGREPS-G members that provide the initial-condition perturbations and lateral boundary conditions. The blue arrows and green boxes show the members that are time-lagged into 18-member ensembles through post-processing. Taken from Porson *et al.* (2020).

Despite the many benefits of convective-scale EPS compared to their medium-range counterparts described above, representation of model error at convective scale remains challenging because the smaller scales of motion simulated by convective-scale EPS lead to a faster error growth (Clark *et al.*, 2010; Baker *et al.*, 2014; Hagelin *et al.*, 2017). Clark *et al.* (2021), investigating a series of precipitation events simulated by a convective-scale EPS, demonstrated that model error impact is greatest when it arises from parametrization of boundary-layer structure. Moreover, Flack *et al.* (2021) further demonstrated that uncertainty from stochastic perturbations applied to the model boundary-layer parametrization is statistically comparable to IC and LBC uncertainty. These findings clearly indicate that convective-scale EPS need a more accurate representation of boundary-layer processes to reduce forecast error and better estimate model uncertainty of the meteorological variables that are sensitive to boundary-layer parametrizations. Candidate sources of errors in boundary-layer processes include the sea-state independent model parametrizations of air-sea momentum, heat and moisture fluxes that control, at convective-scale, the location and magnitude of strong winds near the ocean surface (Janssen, 2004; Lewis *et al.*, 2018, 2019). Because of the steep vertical gradients of the air-sea fluxes at the air-sea interface, small model errors in the parametrization of air-sea fluxes can result in large forecast errors and model biases. A number of studies (Wahle *et al.*, 2017; Lewis *et al.*, 2019) have shown that the direct simulation of the effect of the dynamical ocean and wave state on air-sea surface exchange coefficients, in a deterministic coupled system, has a great potential to improve the prediction of cyclone wind speed forecasts at or close to convective-scale.

### 2.5.4 Coupled operational global prediction systems

It has been hypothesised that a more accurate representation of the air-sea interactions is a possible way for increasing skill in short-range and medium-range NWP forecasts (Lewis *et al.*, 2018, 2019). As a result, to account for the dynamic ocean and sea state effects on the atmospheric flow, several centres worldwide have started to integrate the atmosphere, ocean, and wave model components feedbacks into a single coupled NWP system. Since deterministic convective-scale coupled NWPs are already reviewed in the introduction sections of Chapter 5 and Chapter 6, here is presented a brief review of global coupled medium-range EPS, which have reached operational maturity. The ECMWF runs operationally an ensemble coupled atmosphere-ocean-wave-ice model, while both the Canadian Centre for Meteorological and Environmental Prediction (CCMEP) and the Met Office run a deterministic coupled atmosphere-ocean-ice model. These fully coupled NWPs cover the whole globe with a horizontal grid-spacing of $\approx$ 18km for both the ECMWF and the Met Office NWP, and a horizontal grid-spacing of $\approx$ 25km for the CCMEP NWP. While the Met Office coupled NWP only became operational this year, the CCMEP and ECMWF coupled NWPs have been operational for a few years.

A series of forecasts for summer and winter periods run by Smith *et al.* (2018) using the atmosphere-ocean-sea-ice coupled CCMEP NWP, have shown encouraging results. The coupled simulations were found to decrease tropical cyclone intensification, leading to a smaller false alarm ratio. Moreover, the simulation of geopotential height, wind, temperature, and humidity fields benefited from coupling, with a decrease of up to 15% decrease in standard deviation errors observed for 120-h forecasts in regions of tropical cyclogenesis. On the other hand, the results of coupled simulations performed with the ECMWF atmosphere-ocean-wave fully coupled NWP were not so promising. For instance Mogensen *et al.* (2017) found that coupling had a substantial impact only on some of the tropical cyclone cases considered, while having only a negligible impact on the others. Moreover, Mogensen *et al.* (2017) identified the upper ocean stratification as the process which controlled the strength of the coupled feedback on the tropical cyclone induced atmospheric flow: the coupling impact was noticeable when the ocean heat content of the ocean upper layer was low, while the coupling impact was weak whenever the ocean was characterised by a thick warm mixed layer. A more systematic assessment of the skill of operational coupled NWP has been performed by Vellinga *et al.* (2020) using the Met Office atmosphere-ocean-sea-ice coupled system. The Met Office coupled NWP turned out more skillful than its atmosphere-only counterpart in the middle and upper troposphere up to 7 days lead time. The observed improvements were found to be much stronger in the tropics than in the midlatitudes, where the effect of coupling was largely neutral.

Despite the skill improvements in operational forecasts on coupling reported by meteorological centres worldwide, further research is required to assess the benefit of atmosphere-ocean-wave coupling in operational global NWPs. More specifically, further research is needed to better explore the role of coupling on ETCs, and the effect of dynamic modelling of sea ice on polar lows and arctic cyclones.

## 2.6 Sensitivity of simulations of extratropical cyclones to air-sea interactions

Diabatic processes, such as the release of latent heat by cloud condensation, can play an important role in controlling the intensifcation of ETCs by providing a large energy supply to the cyclone evolution. Large amounts of latent heat are released when the WCB warm and moist air masses ascend, leading to the formation of upper-tropospheric negative PV anomalies in addition to the positive PV anomalies at lower level. The diabatically induced low-level anomalies can interact with the upper-level PV anomalies, resulting into an enhanced cyclogenesis process. Also moisture anomalies in the boundary layer of ETCs, during cyclogensis, can control the cyclones' intensification, as well as the strength of surface wind speeds. The ocean also impacts the cyclogenesis and development via surface waves. The strong winds associated with ETCs blow over the ocean seas. Waves form, enhancing the sea surface roughness and surface friction, thus creating a more turbulent boundary layer. The larger eddies associated with the deeper boundary layer enhance the downward momentum transfer, reducing surface wind speeds, and leading to a faster decay of the ETC systems via Ekman pumping Janssen (2004). Combined with the fact that ETCs generally form and grow over the open ocean, air-sea interactions are important factors in controlling ETCs lifecycle and associated impacts.

First, a brief review of studies examining the sensitivity of idealised cyclone simulations to surface sensible and latent heat fluxes is presented, followed by a summary of the results of numerical experiments determining the sensitivity of cyclones to SST and boundary layer moisture perturbations. Finally, studies investigating the impact of atmosphere-ocean-wave coupling on ETCs are discussed.

### 2.6.1 Sensitivities of idealised cyclone simulations to sensible and latent heat fluxes

Idealised cyclone simulations have shown that air-sea latent and sensible heat fluxes have a varied effect on ETC lifecyle, from reducing the growth rate of ETC by 25% to enhancing it by 15% (Nuss and Anthes, 1987). However, the examination of the cyclone associated fluxes per cyclone conveyor belt has revealed systematic patterns. The WCB turns out to be often associated with downward sensible heat fluxes, while the CCB is associated with upward sensible heat fluxes. This is explained by the fact that the WCB is often warmer than the underlying SST, while the CCB is often colder. Since the heat fluxes warm the cold air associated with the CCB more than the warm air associated with the WCB, the temperature contrast between the two conveyor belts is reduced. Consequently, also the available baroclinicity in the ETC lower-levels is reduced (Sinclair *et al.*, 2010).

This dipole structure characterising the sensible heat fluxes is not mirrored by latent heat fluxes, which are usually upward for both cyclone conveyor belts (Zhang *et al.*, 1999), sometimes leading to a dampening of cyclone growth (and thus also having a direct effect on the ETC development). When the suitable precursor environmental conditions are present, such as cold air outbreaks over notably warm oceans, surface sensible heat fluxes associated with the WCB can turn from negative to positive (Haualand and Spengler, 2020). These strong upward oceanic sensible heat surface fluxes can not only strengthen the cyclone growth, but can also destabilize the boundary layer of the CCB, reducing its static stability while enhancing baroclinicity. Unlike sensible heat fluxes, which affect the cyclone growth and development only directly, air-sea latent heat fluxes also have an indirect effect on the cyclogenesysis and development of ETCs, by changing the moisture supply to the cyclone boundary layer. It has been found that this enhanced moisture supply, transferred from the ocean to the atmosphere, increases the release of latent heat in the WCB, leading to a stronger cyclone deepening. This source of moisture is usually located in the peripheral areas of the cyclone rather than underneath the cyclone lower levels, because it often originates from the surface latent heat fluxes induced by the cold sector of the preceding cyclones, which have already decayed (Boutle *et al.*, 2010).

### 2.6.2 Sensitivities of cyclone simulations to changes in sea surface temperature and moisture fields

Several studies explored the sensitivity of ETC simulations to sea surface temperature (SST) and moisture, with the aim to quantify the role of sensible, latent heat, and momentum air-sea surface fluxes in controlling the development of ETC growth and intensification. Numerical simulations of the explosive ETC Xynthia, performed by Ludwig *et al.* (2014) using the regional climate model COSMO-CLM forced by ERA-Interim data, showed that applying, in the cyclogenesis region, perturbations of both the SST and the heat laminar boundary roughness could influence the cyclone development, as illustrated in Fig.2.20. In particular, they found that a step-wise reduced SST (from 1 to 3K) and an increased heat boundary layer roughness (by up to 10 times than its empirically-determined value) both reduced the ocean surface latent heat fluxes, leading to a weaker and retarded cyclone growth of the cyclone (and associated PV tower). Figure 2.20a-b illustrates the temporal evolution of the

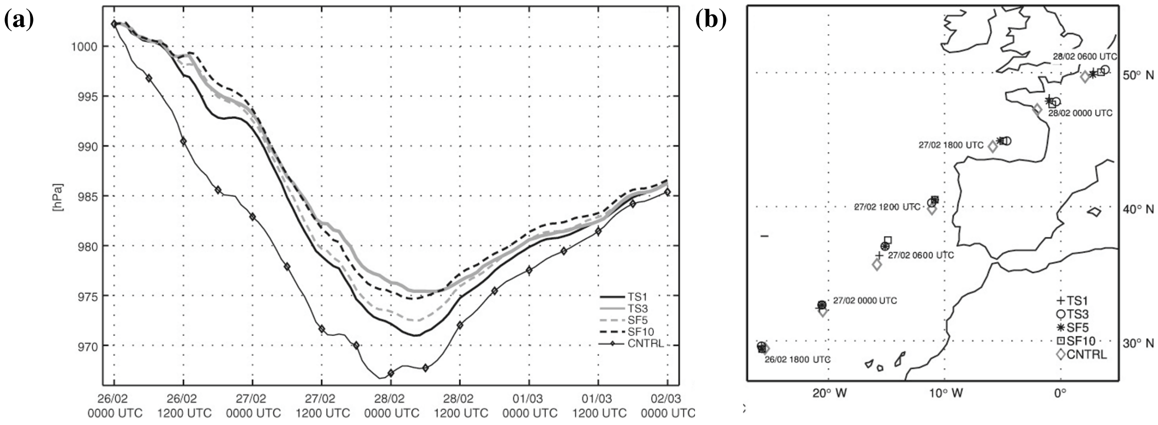

**Figure 2.20:** (a) Core-pressure evolution and (b) cyclone locations for various sensitivity experiments. For better presentation of the results, only results for TS1 (black/plus symbol), TS3 (grey/circle), SF5 (dashed grey/asterisk) and SF10 (dashed black/square) are included. For reference the core-pressure evolution and location for the control (CNTRL, diamond symbols) are included. TS1, TS2, and TS3 experiments correspond to SST reductions of 1, 2, and 3 K, respectively. Instead, SF1 and SF5 correspond to experiments with heat boundary layer roughness increased by 5 and 10 times, respectively. Taken from Ludwig *et al.* (2014).

core pressure and track of Xynthia on changing SST and heat boundary layer roughness obtained in Ludwig *et al.* (2014) numerical experiments. Figure 2.20a shows that as the SST gradually decreases, the mean sea level pressure of Xynthia progressively increases, with the maximum core-pressure difference with respect to the control run being 8.7 hPa (obtained for a reduction of 3 K in SST). However, the weakening of Xynthia intensification on SST reductions (and heat boundary layer roughness increases) does not lead to appreciable changes in Xynthia storm track, as can be observed from Fig. 2.20b. Further numerical simulations of Xynthia performed by Doyle *et al.* (2014), using the adjoint high resolution model Coupled Ocean-Atmosphere Mesoscale Prediction System (COAMPS), indicated how the cyclone development and associated intense surface wind fields were strongly sensitive to both changes in the boundary layer temperature and moisture. According to their findings, the largest impacts on the magnitude and footprint of Xynthia extreme surface winds were associated with the front just prior to making landfall. Analysis of moisture sensitivities also revealed that a relatively small filament of moisture within the atmospheric river, present at the initial time of the simulation, was critical for controlling the formation and evolution of Xynthia, thus confirming the importance of left-over moisture preceding cyclogenesis for explosive cyclone development (Doyle *et al.*, 2014).

A number of studies focusing on Mediterranean cyclones, in which baroclinicity was an important factor for development, highlighted how changes in SST and associated surface and latent heat fluxes were important for the control of near-surface wind and precipitation fields, but these changes did not affect the evolution of the simulated cyclones. For example, Katsafados *et al.* (2011) compared numerical simulations of an explosive cyclone in the eastern Mediterranean obtained by providing the Weather Research and Forecasting (WRF) limited area model with different sources of SST. They found considerable changes in rain bands and surface fluxes (reduced overestimation in hourly precipitation by 6 mm), but only small changes in the storm track and structure (changes in MSLP minimum ranging between 0.1 and 0.8 hPa).

### 2.6.3 Atmosphere-ocean-wave coupled numerical simulations of cyclones

Ocean feedbacks play an important role in marine cyclogenesis modulating sensible and latent heat fluxes (as discussed above). Moreover, growing young wind-generated ocean waves can have an important influence on cyclone life cycle by modifying the wave-induced surface stress, which accounts for a non-negligible proportion of the total surface stress in the surface layer (Janssen, 1989, 1991). For example, taking into account the increased roughness of surface waves in modelling of the Southern Hemisphere storm track, Ulbrich *et al.* (1993) found a reduction of tropospheric winds by up to 10% near the storm track. The results obtained by Weber (1994) with a coupled global circulation and wave model further highlighted the sensitivity of storm tracks and large-scale circulation to coupling to waves, thus suggesting the importance of including a dynamical simulation of the sea state in any atmospheric model for accurate prediction of ETCs.

These results motivated Doyle (1995) to use a mesoscale atmosphere-wave coupled model, running at a resolution of $\approx$ 30 km, to perform one of the first idealised coupled simulation of a cyclone that took into account the effect of young ocean waves on the atmospheric flow. They found that coupling to waves led to a marked increase in surface roughness (attributed to the sea being covered by young growing ocean waves). This, in turn, enhanced the air-sea momentum transfer, leading to reductions as high as 20% in cyclone near-surface wind speeds compared to the atmosphere-only simulation values. Further results of Doyle (1995) showed that coupling to waves reduced the kinetic energy of the cyclone by up to 8%, due to the enhanced roughness at the air-sea interface associated with young growing ocean waves. A later study by Ren *et al.* (2004) explored the impact of atmosphere-ocean coupling (but not of wave coupling) to the ETC Earl (1998) and to an intense winter cyclone (2000), which were both explosive cyclones formed off the east coast of the US. They found that coupling to ocean did not shift cyclone Earl storm track, but it reduced its intensity by $\approx 3hPa$, and the cyclone near-surface wind speeds by up to 3m $\text{s}^{-1}$. A slightly larger reduction in intensity (by $\approx$ 4 hPa) and near-surface wind speeds (by $\approx$ 4 m $\text{s}^{-1}$) was found for the intense winter cyclone case analysed by Ren *et al.* (2004), but again, no appreciable change to the storm track was found. The impacts on cyclone wind speeds and intensity were attributed to the increased boundary-layer stability and reduced available boundary-layer moisture, due to the cooling of SST simulated by coupling to the ocean. Although these early studies indicated that coupling an atmosphere model to an ocean and to a wave model led to noticeable impacts on the intensity and magnitude of wind speeds associated with ETCs (but not track), most of the subsequent studies focused on exploring the impact of atmosphere-ocean-wave coupling on tropical cyclones or Mediterranean cyclones rather than ETCs.

The advent of high-resolution regional modelling tools has sparked renewed interest in exploring the impact of atmosphere-ocean-wave coupling on ETCs. For example, Wahle *et al.* (2017) simulated a historical series of ETCs that cross the southern North Sea, demonstrating that coupling the Wave Model WAM (Komen *et al.*, 1994), run at 5-km grid spacing, with the COnsortium for Small-scale MOdelling COSMO (Rockel *et al.*, 2008), run at 10-km grid spacing, reduced wave heights and wind speeds by up to 8% and 3%, respectively, with associated improvements in the forecast skill of the wind speed and wave height. Comparable reductions in wind speeds and wave heights, associated with mean skill improvements of 20% and 5%, respectively, were achieved by Lewis *et al.* (2019) in coupled simulations of part of the October month of the 2014 UK cyclone season, as can be observed from Fig. 2.21a-b. These simulations were carried out using the deterministic Met Office Regional Coupled System (RCS), termed UKC3 in Lewis *et al.* (2019), which couples models of the atmosphere, land-surface, shelf-sea ocean, and ocean surface waves. However, despite these recent advancements, open questions remain regarding the role of atmosphere-ocean-wave coupling on numerical simulations of ETCs. These include aspects such as the hierarchy of ocean and wave feedbacks which control the development and impacts on ETCs, and how strong are the impacts of coupling compared to those of perturbations in the initial atmospheric and ocean state of the ETC simulations.

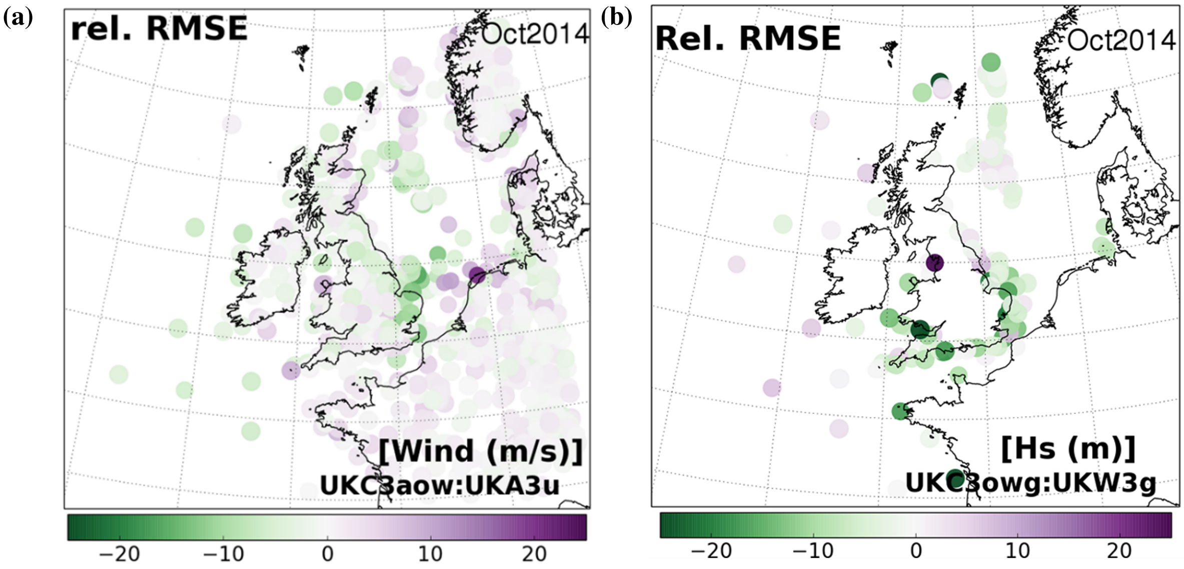

**Figure 2.21:** Percentage difference relative Root Mean Square Error for a) 10-m wind speed b) significant wave height of the fully atmosphere-ocean-wave coupled relative to the atmosphere-only configuration of the Met Office coupled model. Taken from Lewis *et al.* (2019).

# Chapter 3

# Methods

This thesis is structured around three papers, thus in each paper chapter is already contained an extensive description of the specific methods used. The aim of this chapter is solely that of providing the reader with the preparatory material to understand the data, modelling tools, and forecast verification metrics discussed in detail in the paper chapters. First, details are given of the observation data and ERA5 reanalysis dataset used to build the British Isles seas extreme wind speed climatology. Then, a description is provided of the Met Office Unified Model (MetUM) atmosphere dynamical core of the convective-scale coupled regional NWP model (used to simulate the cyclone case studies reported in this thesis). A description of the wave model component of the Met Office convective-scale coupled regional NWP model is also provided. Finally, the metrics used for the evaluation of the convective-scale coupled ensemble experiments are presented.

## 3.1 Data

### 3.1.1 Observations used for climatology study

The observed winds, gusts, and wave heights over the British Isles land and surrounding seas, used in this thesis, are taken from the hourly mean observations of 10-m wind speeds, direction, wind-wave height, and hourly or six-hourly maximum 10-m wind gusts collected by the Met Office MetDB System and stored at CEDA (Met Office, 2008). Over land, observations are acquired by land surface stations and reported to the MetDB system in LAND SYNOP code. Over the sea, observations are acquired by ships, buoys, and fixed platforms and reported to the MetDB system in the SHIP SYNOP code. The mean 10-m wind speeds are reported hourly to the nearest m $s^{-1}$ and 10 degrees, while maximum gusts are reported hourly and six-hourly, depending on the station. The hourly mean 10-m wind speed is measured by the sites stations by averaging the wind fluctuations (sampled every 0.25 s due to their turbulent nature) over the 10-min period leading up to the hourly reporting time. Instead, the maximum 10-m gust is the maximum 3-s average wind speed recorded over the full time period leading up to the reporting time (i.e., one or six hours).

In this thesis, only the observations of the MetDB system that passed the rigorous quality control of the Met Office performed by means of checks on the equipment and raw data were used (Met Office, 2008; Hewston and Dorling, 2011). After collecting the MetDB data locally, a series of further tests was performed (as part of the work presented in this thesis) to ensure the reliability of the observations, deleting duplicate data rows, detecting missing values, and ensuring data consistency and homogeneity for neighbouring stations. A careful analysis of the selected maximum gust time series suggested that each station that reported maximum gusts had a threshold above which gusts were classified as “worthy" recording. Although no formal documentation of this threshold can be found, both private communication with CEDA and direct analysis of the timeseries placed the lower limit of the threshold at $\approx 15\ \mathrm{m\,s^{-1}}$ for a gust measurement to be classified as "worthy" recording. To ensure temporal homogeneity, different thresholds for different observations field were employed to filter out those sites that did not report sufficient observations for the type of study to be performed in this thesis (model verification, or climatology study). More details can be found in the methods section of the paper Chapter 4 and the paper Chapter 5.

### 3.1.2 ERA5 dataset used for climatology study

ERA5 is the fifth generation hourly reanalysis of the European Centre for Medium-Range Weather Forecasts (ECMWF) (Hersbach *et al.*, 2020). It provides estimates for atmospheric, ocean, wave, and land surface variables, with a horizontal grid resolution of 0.25°, corresponding to $\approx 31$ km. It is produced using 4D-Var data assimilation and model forecasts of the ECMWF Integrated Forecast System (IFS). The atmospheric component is interpolated to 37 pressure levels in the vertical from the surface up to 1 Pa. The ECMWF model version of the IFS, on which ERA5 is based, is the Cy41r2, which was used in the ECMWF operational medium-range forecasting system from 8 March to 21 November 2016, thus incorporating most of the latest advancements for all its model components (atmosphere, land, ocean waves, and observations), and the improvements in the Data Assimilation methodology. In the IFS, the atmosphere, land, ocean, and wave model components are coupled (Hersbach *et al.*, 2020).

Observations are assimilated in ERA5 from over 200 satellite instruments, together with conventional observations (Dee *et al.*, 2011; Hersbach *et al.*, 2020). Satellites provide ERA5 with observations of radiances which are sensitive to upper-air temperature, humidity, ozone, ocean vector wind, ocean-wave height, land soil moisture, and snow cover. The conventional observations assimilated by ERA5 consist of in-situ observations of 10-m wind over sea, 2-m humidity over land, pressure over land and sea, radiosondes and aircraft measurements of upper-air observations of wind, temperature and humidity. The conventional observations also consist of information on rain rate from ground-based radar-gauge composite observations. They are distinguished into the following five types:

- SYNOP, which consists of measurements made near the surface by land stations (surface pressure, relative humidity, 2-m temperature, and snow depth) including airport weather reports (surface pressure), and of measurements made by ships and fixed offshore platforms (surface pressure, wind components at 10 m)
- DRIBU, which consists of drifting and moored buoys (surface pressure, 10-m wind components);
- TEMP, which consists of radiosondes and dropsondes (temperature, wind components, and specific humidity);
- PILOT, which consists of balloon observations (wind components), and wind profilers (wind components)
- AIRCRAFT-based atmospheric observations (temperature, wind components and specific humidity),

The radiation forcings terms and boundary conditions are provided to ERA5 by state-of-art datasets that describe well the low-frequency variability of the climate system (Hersbach *et al.*, 2020). Compared to the previous-generation ERA-INTERIM reanalysis, in ERA5, long-term forcing fields from the WCRP's initiative CMIP5 are implemented as options providing the total solar irradiance (TSI) and fields of aerosols, greenhouse gases, and ozone. Lower boundary conditions of Sea Surface Temperature (SST) and Sea Ice Cover (SIC) are provided by a blend of different products. For SST, ERA5 employs a combination of the Met Office Hadley Centre HadISST2, the Climate Change Initiative (ESA CCI) SST v1.1 (Merchant *et al.*, 2014), and the Met Office OSTIA product (Donlon *et al.*, 2012). For SIC, the EUMETSAT OSI SAF reanalysis (Lavergne *et al.*, 2019) and various flavours of the HadISST2 sea ice data (Titchner and Rayner, 2014) are used in combination with the operational OSI SAF that is also part of OSTIA (Donlon *et al.*, 2012). As discussed in Donlon *et al.* (2012), the global-mean SST can represent the impact of global warming from the 1970s on, as well as the influence of El Niño events and of major volcanic eruptions. Moreover, the SIC field shows a general decline over time for the Arctic Sea Ice, especially during summer.

## 3.2 Met Office Unified Model dynamical core

The MetUM atmosphere component is always used in all the coupled deterministic and ensemble numerical experiments carried out in this thesis. Therefore, a general review of the MetUM atmosphere dynamical core is provided below.

The MetUM dynamical core is a computational scheme which solves, without using shallow atmosphere approximations, the full, deep-atmosphere, compressible Navier-Stokes equations (Staniforth *et al.*, 2006):

$$\frac{D\mathbf{u}}{Dt} = -2\Omega \times \mathbf{u} - \frac{\nabla p}{\rho} + \mathbf{g} + \mathbf{S}^{\mathbf{u}} \tag{3.1}$$

$$\frac{\partial \rho}{\partial t} + \nabla \times (\rho \mathbf{u}) = 0 \tag{3.2}$$

where $\mathbf{u} = (u, v, w)$ is the velocity vector, $\Omega$ is the rotation rate of the Earth, $p$ is the atmospheric pressure, and $\mathbf{S}^u$ is the frictional force per unit mass. In addition to numerically solve (3.1) and (3.2), the MetUM also solves the first law of thermodynamics and the equation of state, which are given, respectively, by:

$$\frac{D\theta}{Dt} = S^{\theta} \tag{3.3}$$

$$p = \rho RT \tag{3.4}$$

where $\theta$ is the potential temperature, $T$ is temperature, $R$ is the gas constant for dry air, and $S^{\theta}$ is a heat source term. Moisture is represented by the MetUM in terms of the moist mixing ratios, $m_X$, where $X$ denotes a given water phase, such as vapour, liquid, and frozen. The prognostic equation for the moist mixing ratios, $m_X$, is given by:

$$\frac{Dm_x}{Dt} = S^{m_x}, \tag{3.5}$$

where $S^{m_x}$ is a source (or sink) term of moisture.

The MetUM discretises the Navier-Stokes equations using a regular latitude ($\lambda$) and longitude ($\phi$) “Arakawa C" staggered grid, and a terrain-following hybrid-height Charney-Phillips grid in the vertical (Charney and Phillips, 1953) that becomes horizontal at higher levels. The horizontal grid stores the variables $\rho$, $\Pi$, $\theta$, and $w$ on a centre point, setting $u$ and $v$ at half a level. The vertical grid also staggers prognostic variables, keeping $u$, $v$, $\Pi$, and $\rho$ at rho- (or full-) levels, with $\theta$ and $w$ at $\theta$- (or half-) levels. The advantage of using the “Arakawa C" grid is twofold: it prevents decoupling between modelled vector and scalar fields, and it reduces the computational cost, since, by using this grid, it is not necessary to compute all variables at all nodes. The advantage of the Charney-Phillips grid lies in being more consistent (for example, compared to the Lorenz grid) with the hydrostatic equation, since it does not allow the additional computational mode. The spacing of the vertical levels is defined by a quadratic function, with higher resolution at lower levels, in order to better represent the boundary layer, low-level fluxes, and vertical gradients.

The MetUM uses a semi-implicit, semi-Lagrangian time-integration method, which integrates the MetUM dynamical equations along parcel trajectories. The semi-implicit time stepping uses a predictor-corrector scheme, designed so that explicit diffusion is not required for stability (Davies *et al.*, 2005).

## 3.3 Met Office Unified Model parametrization schemes

Given that this thesis focuses on the impact of atmosphere-ocean-wave coupling on near-surface wind speeds associated with ETCs, only a general overview of the MetUM parametrizations is now given, followed by a detailed overview of the representation of turbulent surface exchanges and interior boundary-layer processes.

### 3.3.1 General overview of parametrization schemes

As discussed above, the MetUM dynamical core solves the compressible non-hydrostatic equations of motion with semi-lagrangian advection and semi-implicit time stepping, but the sub-grid scale processes, such as convection, boundary-layer turbulence, radiation, cloud, microphysics, and orographic drag, need to be parametrised.

The large-scale clouds are parametrised by the Smith (1990) scheme, which generates cloud amount and water content assuming a simple triangular distribution around their grid-box-mean values (peaking at the grid-box mean), incorporating a parameterization of the rate of depletion of cloud water by precipitation. For each model grid box, the scheme derives its fraction of cloud and water content cover from the fraction of the distribution where the specific humidity is greater than the saturation specific humidity. The critical relative humidity parameter, which varies from 91% near the surface to 80% above the boundary layer, controls the width of the simple triangular distribution of cloud amount and water content. Thus, the model predicts cloud formation when the relative humidity in a grid box exceeds this critical value.

Microphysical processes are parametrised by the physically-based transfer scheme of Wilson and Ballard (1999), which uses the four water contents of vapour, cloud liquid water, ice, and rain to describe the moisture in the atmosphere. This scheme considers the highest model level, and then uses the physical process equations to compute any transfer between water phases, releasing any precipitating water or ice from the level considered to the level just below, iterating the calculation until the surface is reached. Then, at the surface, the scheme computes the precipitation rate as the amount of precipitating water or ice removed from the atmosphere.

Convection is parametrised by the scheme of Gregory and Rowntree (1990), which represents an ensemble of convective clouds employing a“bulk" cloud model and simulates the effects of shallow, midlevel, and deep convection. This scheme uses a simple buoyancy closure, which consists of the initial convective mass flux being proportional to the parcel initial buoyancy on ascent. In contrast to other schemes that require large-scale convergence to be present to initiate convection, in this scheme only positive buoyancy is required to initiate convection (defined by a minimum temperature excess of 0.2 K). The scheme diagnoses convection as shallow if the buoyancy becomes zero or negative within a height of 2.5 km, or the level of neutral buoyancy is below the freezing level. Although the scheme parametrises mid-level and deep convection in the same way, mid-level convection is initiated by instability above the boundary layer while deep convection is initiated by instability of the lifting of surface parcels. The shallow convection scheme differs from the mid-level and deep convection scheme because it uses the boundary-layer turbulence kinetic energy closure of Grant (2001), which determines the cloud-base mass flux from the sub-cloud turbulent kinetic energy budget and includes more mixing with the environment.

Radiation is parameterised by the scheme developed by Edwards and Slingo (1996). The purpose of the radiation scheme is to calculate upward and downward longwave and shortwave radiative fluxes with a two-stream method, from which the heating rates and the related quantities are determined. The scheme incorporates: 1) the interaction of radiation with ice crystals and liquid water, 2) gaseous and continuum absorption; 3) a treatment of the optical properties of clouds.

### 3.3.2 Surface Fluxes parametrization scheme

The length-scales of turbulent processes mediating momentum, moisture, and heat turbulent fluxes are much smaller than the grid-spacing. Given that the smallest scale of these processes is $\approx 1\times 10^{-3}$ m (corresponding to viscous processes), their explicit representation would require a computing power currently unavailable. Therefore, momentum, heat, and moisture surface fluxes need to be parametrised in the surface layer. The surface scheme adopted by the MetUM is that proposed by Lock (2001, 2007), and is summarised below.

Between the lowest model level and the surface, wind speed must reduce to zero and both temperature and humidity must approach their surface values, usually leading to large exchanges of momentum and heat fluxes within this layer. The MetUM assumes that the Monin-Obukhov theory holds in surface layer, and that the gradients of model variables in the surface layer are related to the momentum $\tau_0$, heat $H_0$, and moisture $E_0$ surface fluxes by:

$$\frac{\partial \mathbf{v}}{\partial z} = \frac{\tau_0}{\rho_0 u^*} \frac{\phi_m(z/L)}{kz}, \tag{3.6}$$

$$\frac{\partial T}{\partial z} + \frac{g}{c_p} = -\frac{H_0}{c_p \rho_0 u^*} \frac{\phi_h(z/L)}{kz}, \tag{3.7}$$

$$\frac{\partial q}{\partial z} = -\frac{E_0}{\rho_0 u^*} \frac{\phi_h(z/L)}{kz}, \tag{3.8}$$

where $\rho_0$ is the surface air density; $c_p$ the specific heat capacity; and $\phi_m$, $\phi_h$ the Monin-Obukhov stability function for momentum and scalars which account for the effect of buoyancy (Csanady, 2001). The Monin-Obukhov length scale $L$ is defined as:

$$L = \frac{-u*^3}{kF_{B0}/\rho_0}, \tag{3.9}$$

where $F_{B0}$ is the surface buoyancy flux, defined as:

$$F_{B0} = \frac{g}{c_p}\beta_{T1} H_0 + g\beta_{q1} E_0, \tag{3.10}$$

with $\beta_{T1}$ and $\beta_{q1}$ representing the buoyancy parameters.

Integrating from the surface, which corresponds to the roughness height where the surface variables are defined, to a reference height in the surface layer, chosen as the bottom model layer height, $z_1$, the surface turbulent fluxes of momentum, heat, and moisture can be parametrised as:

$$\frac{\tau_0}{\rho_0} = C_D|\Delta \mathbf{v}|^2, \tag{3.11}$$

$$\frac{H_0}{c_p\rho_0} = -C_h U\left(\Delta T + \frac{g}{c_p}(z_1 + z_{0m} - z_{0h})\right), \tag{3.12}$$

and

$$\frac{E_0}{\rho_0} = -C_h U \Delta q, \tag{3.13}$$

and the turbulent buoyancy flux can be parametrised as:

$$\Delta B = g\beta_{T1}\left(\Delta T + \frac{g}{c_p}(z_1 + z_{0m} - z_{0h})\right) + g\beta_{q1}\Delta q. \tag{3.14}$$

The drag and scalar surface transfer coefficients $C_D$ and $C_h$ are given by:

$$C_D = \left(\frac{k}{\ln\left(\frac{z}{z_{0m}}\right) - \Psi_m}\right)^2, \tag{3.15}$$

$$C_h = \frac{k^2}{\left(\ln\left(\frac{z}{z_{0m}}\right) - \Psi_m\right)\left(\ln\left(\frac{z}{z_{0h}}\right) - \Psi_h\right)}, \tag{3.16}$$

where $k = 0.4$ is the von Kármán constant, $\Psi_m$ and $\Psi_h$ are the Monin–Obukhov stability functions for momentum and scalar fluxes (integrated from $\phi_m$ and $\phi_h$), and $z$ is the vertical height coordinate.

The form of the stability functions $\Psi_m$ and $\Psi_h$ is determined empirically, and thus varies whether the boundary layer is stable or unstable (Beljaars and Holtslag, 1991). In a stable boundary layer, where $L > 0$, their form is given by:

$$\Psi_m = \ln(z/z_{0m}) + \frac{z - z_{0m}}{L} + \frac{2}{3}\left(\frac{z}{L} - \frac{5}{0.35}\right)\exp\left(-0.35z/L\right) \tag{3.17}$$

$$-\frac{2}{3}\left(\frac{z_{0m}}{L} - \frac{5}{0.35}\right)\exp(-0.35z_{0m}/L), \tag{3.18}$$

$$\Psi_h = \ln(z/z_{0m}) + \left(1+\frac{2}{3}\frac{z}{L}\right)^{3/2} + \frac{2}{3}\left(\frac{z}{L}-\frac{5}{0.35}\right) \tag{3.19}$$

$$-\left(1+\frac{2}{3}\frac{z_{0h}}{L}\right)^{3/2} - \frac{2}{3}\left(\frac{z_{0h}}{L}-\frac{5}{0.35}\right)\exp(-0.35 z_{0h}/L), \tag{3.20}$$

while for unstable boundary layers ($L < 0$) their form becomes:

$$\Psi_m = \ln(z/z_{0m}) - 2\ln\left(\frac{1+X_1}{1+X_0}\right) - \ln\left(\frac{1+{X_1}^2}{1+{X_0}^2}\right) + 2\left(\arctan(X_1)-\arctan(X_0)\right), \tag{3.21}$$

$$\Psi_h = \ln(z/z_{0h}) - 2\ln\left(\frac{1+Y_1}{1+Y_0}\right), \tag{3.22}$$

where:

$$X_0 = (1-16 z_{0m}/L)^{1/4} \quad \text{and} \quad X_1 = (1-16z/L)^{1/4},$$

$$Y_0 = (1-16 z_{0h}/L)^{1/4} \quad \text{and} \quad Y_1 = (1-16z/L)^{1/4}.$$

When the boundary layer becomes neutral, $H_0 \longrightarrow 0$ and $L \longrightarrow \pm\inf$, thus $\Psi_{m,h}$ approach their neutral values.

To allow for the effect of turbulent and cloud-scale gusts on the surface turbulent fluxes, the MetUM surface scheme replaces the friction velocity $u_*$ with the scaling velocity $\upsilon_*$, which can be written as:

$${\upsilon_*}^2 = {u_*}^2 + {\gamma_t}^2{w_*}^2 + {\gamma_c}^2{w_c}^2. \tag{3.23}$$

The second term of the RHS in Eq. (3.23) represents the effects of turbulent eddy-scale convective gusts, with $\gamma_t$ being an empirically-determined dimensionless constant, and $w_*$ being the turbulent convective scaling velocity. When the buoyancy flux $F_{B0} > 0$, $w_*$ is defined as a function of the height of the top of the surface-based turbulent mixing layer $z_i$:

$$w_* = (z_i \frac{F_{B0}}{\rho_0})^{1/3} \tag{3.24}$$

but otherwise takes the value of zero. The third term of the RHS in Eq. (3.23) represents the effects of deep convective cloud-scale gusts in which the velocity scale, $w_c$, is a function of the convective downdraught mass-flux at cloud base, and $\gamma_c$ is, similarly to $\gamma_t$, an empirically-determined dimensionless parameter. As a result, the Monin-Obukhov length scale, $L$, can be redefined as:

$$L = \frac{-{\upsilon_*}^3}{kF_{B0}/\rho_0}. \tag{3.25}$$

Once $L$ is computed, the MetUM surface scheme allows to calculate the surface momentum, heat, and moisture fluxes $\tau_0$, $H_0$, and $E_0$. However, $L$, through $F_{B0}$, depends on the $\tau_0$, $H_0$, and $E_0$ surface fluxes. In order to calculate the surface fluxes, the MetUM first makes a guess for the Monin-Obukhov length scale, $L$, and then applies an iterative procedure, where at each step the surface fluxes and $L$ are updated, until $L$ converges. The Met Office documents that five iteration steps are sufficient to obtain the convergence and then the final values of the Monin-Obukhov Length $L$ and of surface fluxes $\tau_0$, $H_0$, and $E_0$.

### 3.3.3 Diagnosis of boundary-layer type and top

The MetUM categorises the boundary layer into seven different types. Six of these boundary-layer types are schematically illustrated in Fig. 3.1:

- Type I: Stable boundary layer (with or without cloud) - turbulent diffusivities are calculated by the local scheme
- Type II: Boundary layer with stratocumulus over a stable near-surface layer  as Type I but with a turbulently mixed cloud layer driven from its top
- Type III: Well-mixed boundary layer  the classic single mixed layer which may be cloud-topped or clear but is predominantly buoyancy-driven
- Type IV: Unstable boundary layer with a decoupled stratocumulus layer not over cumulus the surface based and cloud-top-driven non-local boundary-layer profiles may or may not overlap and cloud-top entrainment can still include the surface forcing
- Type V: Boundary layer with a decoupled stratocumulus layer over cumulus  the cumulus (treated by the models mass-flux convection scheme) provides coupling with the surface

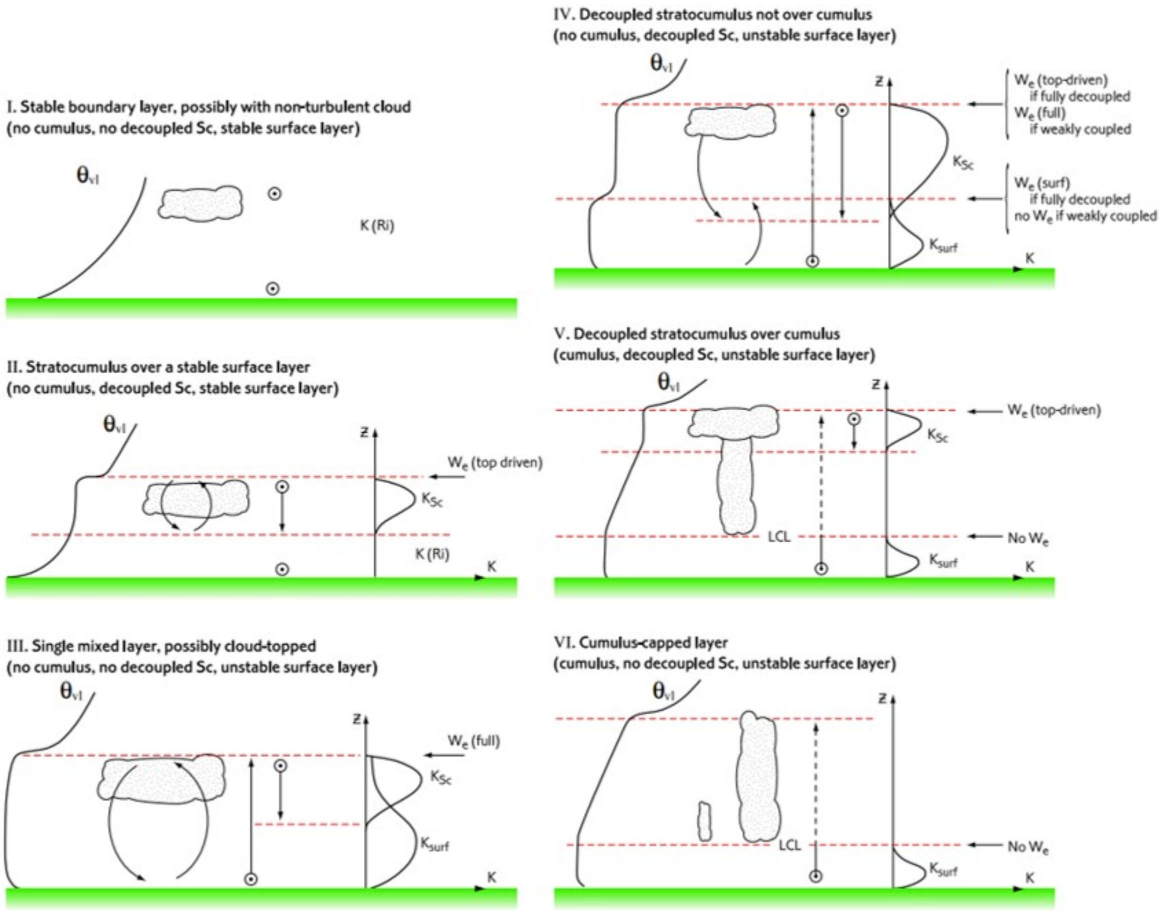
I. Stable boundary layer, possibly with non-turbulent cloud (no cumulus, no decoupled Sc, stable surface layer)

II. Stratocumulus over a stable surface layer (no cumulus, decoupled Sc, stable surface layer)

III. Single mixed layer, possibly cloud-topped (no cumulus, no decoupled Sc, unstable surface layer)

IV. Decoupled stratocumulus not over cumulus (no cumulus, decoupled Sc, unstable surface layer)

V. Decoupled stratocumulus over cumulus (cumulus, decoupled Sc, unstable surface layer)

VI. Cumulus-capped layer (cumulus, no decoupled Sc, unstable surface layer)

**Figure 3.1:** Schematic representation of boundary-layer types I to VI. The top of the upward arrows indicate the height $z_par$ while the top of their solid line portions indicate $z_h$. Taken from Lock (2007).

mixed layer

- Type VI: Cumulus-capped boundary layer  no turbulent diffusivities are allowed at or above the lifting condensation level (LCL) as the mass-flux convection scheme operates here
- Type VII: Shear-dominated unstable layer  potentially wind-shear might allow deeper turbulent mixing in unstable boundary layers than it is apparent purely from the thermodynamic profiles (sufficient even to inhibit the formation of cumulus).

To compute the boundary-layer height, $z_h$, the MetUM boundary-layer scheme, as an initial step, distinguishes the stable from the unstable boundary layers, using the surface buoyancy flux, $F_{B0}$. When $F_{B0} > 0$, the boundary layer is unstable, and the level of neutral buoyancy, $z_{par}$, associated with thermals is obtained by employing the moist parcel ascent method. The height of the boundary layer, $z_h$, corresponds to the level of neutral buoyancy determined by parcel ascent, $z_{par}$, if the layer is well-mixed (clear or stratocumulus capped). In contrast, when cumulus convection is present, the height of the boundary layer is taken as the lifting condensation level (LCL). For a stable boundary layer (diagnosed when $F_{B0} < 0$), $z_h$ corresponds to the height for which the Richardson number ($Ri$) is greater than one.

Because for each grid cell $z_h$ depends on the boundary-layer type diagnosed in that given grid cell, sharp discontinuities can occur in the value of $z_h$ between neighbouring grid boxes which are categorised by different boundary layer types. To obtain a more spatially smooth boundary layer-top height field, the boundary-layer height is calculated throughout this thesis using the output of the MetUM diagnostic based on the bulk Richardson number. This new diagnosis of the boundary-layer top height is similar in methodology to the diagnosis of $z_{par}$, which, as already discussed, uses a parcel ascent to calculate the level of neutral buoyancy for surface-based thermals. First, the bulk Richardson number is computed at each level of the MetUM model as:

$$Ri_b = \frac{\frac{g}{\theta_{v0}}(\theta_v - \theta_{v0})z}{u^2 + v^2} \tag{3.26}$$

where $\theta_{v0}$ is an approximation of the air virtual potential temperature above the surface. (For more details on how to compute $\theta_{v0}$ see Troen and Mahrt (1986).) Then, the boundary-layer height is diagnosed as the model-level height where the Richardson number exceeds the critical Richardson number, $R_{i_{crit}} = 0.25$. Since this method provides a height of the boundary-layer top which is spatially smooth, it allows the warm and cold sectors of ETCs to be qualitatively inferred as well as some of the boundary-layer characteristics associated with the ETC sectors.

## 3.4 The wave model WAVEWATCH III

Given that the role of atmosphere-wave interactions in controlling ETC wind speeds is analysed in depth in the coupled model experiments of the research chapters, in this section only a brief review of the model wave component WAVEWATCH III of the Met Office coupled model is provided, covering the wave modelling approach, the wave action balance equation used to simulate the wave propagation, and the wave balance equation source terms.

### 3.4.1 Wave modelling

WAVEWATCH III is a third-generation spectral wave model, whose details are given in Tolman (2016). It describes the spectral wave components using wavevector **k**, wavenumber $k$, and wave direction $\theta$. The wave direction, $\theta$, is by definition perpendicular to the crest of the wave (or spectral component), and equals the direction of the wave vector **k**. The model assumes that the scales of variation of depths and currents are much larger than those of a single wave, and therefore the quasi-uniform (linear) wave theory can be applied locally. The quasi-uniform theory neglects the phenomena of diffraction, scattering and interference effects, but these can be represented, a posteriori, as source terms in the wave action equation as it will be described later. According to the quasi-uniform theory, the intrinsic wave phase parameter $\sigma$ (which is observed in a frame of reference moving with the mean current) and the absolute (radian) frequency $\omega$ (which is observed in a fixed frame of reference) are interrelated by the following dispersion relation and Doppler-type equation:

$$\sigma^2 = gk\tanh(k \cdot d), \tag{3.27}$$

$$\omega = \sigma + \mathbf{k} \cdot \mathbf{U}, \tag{3.28}$$

where $d$ is the mean water depth and **U** the wave current velocity. Solving Eq. (3.27) and Eq. (3.28), together with the crests' wave number number conservation equation given by:

$$\frac{\partial \mathbf{k}}{\partial t} + \nabla\omega = 0, \tag{3.29}$$

the rates of change of the spectral wave parameters can be calculated.

The wave spectrum of choice within WAVEWATCH III is the action density spectrum $N(k,\theta) \equiv F(k,\theta)/\sigma$, where $F(k,\theta)/\sigma$ is the energy (or variance) density spectra of the waves' surface elevation which depends on the two independent wave phase parameter $\mathbf{k},\theta$. The reason why the action density spectrum is chosen instead of the energy density spectrum is that the former is conserved for waves propagating when currents are present, while the latter is not, because of the work done by current on the mean momentum transfer of waves.

Then, the wave propagation is described in WAVEWATCH III by the wave action balance equation:

$$\frac{DN}{Dt} = \frac{S}{\sigma} \tag{3.30}$$

where $\frac{DN}{Dt}$ is the material derivative with respect to time $t$, and $S$ represents the net effect of sources and sinks for the wave spectrum.

### 3.4.2 Wave propagation

Equation (3.30), to be solved numerically, it must be expressed in an Eulerian form. In particular, WAVEWATCH III is based on the conservation form of Eq. (3.30), which holds for arbitrary spectral formulations, as long as the corresponding Jacobian transformation from the energy spectrum $F(k,\theta)$ to the traditional frequency-direction spectrum $F(f_r,\theta)$ (on which the model is output) is well behaved. Moreover, the total wave energy and action are conserved in the Eulerian conservation equation formulation. The balance equation for the spectrum $N(k,\theta;x,t)$ employed by WAVEWATCH III can be formulated in its conservation form based on the spherical coordinates (which are more suitable than the Cartesian ones for large-scale applications, i.e. ocean waves prediction):

$$\frac{\partial N}{\partial t} + \frac{1}{\cos\phi}\frac{\partial}{\partial \phi}\dot{\phi}N\cos\theta + \frac{\partial}{\partial \lambda}\dot{\lambda}N + \frac{\partial}{\partial k}\dot{k}N + \frac{\partial}{\partial \theta}\dot{\theta}_g N = \frac{S}{\sigma}, \tag{3.31}$$

$$\dot{\phi} = \frac{c_g\cos\theta + U_\phi}{R}, \tag{3.32}$$

$$\dot{\lambda} = \frac{c_g\sin\theta + U_\lambda}{R\cos\phi}, \tag{3.33}$$

$$\dot{\theta}_g = \dot{\theta} - \frac{c_g\tan\phi\cos\theta}{R}. \tag{3.34}$$

where $R$ is the radius of the Earth, $c_g$ the group velocity, $\lambda$ the wavelength, and $U_\phi$ and $U_\lambda$ are current components. The spherical coordinates are discretized in WAVEWATCH III by using quadrangles, in particular by using the unstructured Spherical Multiple Cells.

### 3.4.3 Source terms

The net source term $S$ in Eq. (3.30) differs for deep water and shallow water processes.

In deep water, the net source term $S$ consists of three parts, an atmosphere-wave interaction term $S_{in}$, a nonlinear wave-wave interactions term $S_{nl}$, and a wave-ocean interaction term that contains the dissipation $S_{ds}$. Therefore, $S$ can be represented as:

$$S = S_{in} + S_{nl} + S_{ds}. \tag{3.35}$$

The source term $S_{in}$ is the most relevant for atmosphere-wave coupling, since it mainly represents the wind-wave feedback. In the case of young growing wind-waves it is generally positive, but it can act as a sink (negative) in the case of swells. Since a detailed parametrization of the $S_{in}$ source term (based on the Miles' growth theory) used in the WAVEWATCH III model component of the Met Office regional coupled system can be found in Lewis *et al.* (2018), here it is only described how the Charnock parameter, $\alpha$, is computed starting from the input source term $S_{in}$, modelling wave growth. First, WAVEWATCH III computes the wave-supported stress $\tau_w$ as:

$$\tau_w = \left| \int_0^{k_{max}} \int_0^{2\pi} \frac{S_{in}(k', \theta)}{C} (\cos\theta, \sin\theta) dk' d\theta + \tau_{hf}(u_*, \alpha)(\cos\theta_u, \sin\theta_u) \right| \tag{3.36}$$

where $\tau_{hf}$ is the short waves' supported stress, tabulated beforehand using the assumption that for high frequencies the stress is in the wind direction, $\theta_u$, and the spectral shape is known. Given the 10-m wind, $U_{10m}$, (received by the atmosphere model component in coupled mode), and the wave-supported stress, $\tau_w$, WAVEWATCH III computes (through a lookup table) the total surface stress (the air-sea momentum flux) $\tau_0$. Then, the momentum roughness length, $z_{0m}$, is computed by WAVEWATCH III iteratively as:

$$z_{0m} = \frac{z_{00}}{\sqrt{1 - \frac{\tau_w}{\tau_0}}} \tag{3.37}$$

where $z_{00}$ is the WAVEWATCH III initial guess for $z_{0m}$, given by $z_{00} = \alpha_{00}\tau_0/g$, where $\alpha_{00}$

specifies a minimum possible Charnock coefficient (value of 0.0095 set in the Met Office coupled model WAVEWATCH III component). At each step, $\tau_0$ is updated, and $u_*$ computed from $\tau_0$ as $u_* = \sqrt{\tau_0/\rho_0}$. The Met Office documents that ten iteration steps are sufficient to obtain the convergence and then the final value of $z_{0m}$, $\tau_0$, and $u_*$ (Lewis *et al.*, 2018). Then, the Charnock parameter, $\alpha$, is computed as $\alpha = gz_{0m}/{u_*}^2$. Finally, the value of the Charnock parameter $\alpha$ is sent to the MetUM atmosphere model component of the Met Office regional coupled system, which updates the momentum roughness length $z_{0m}$ over the sea according to Eq. (2.8).

In shallow water, additional processes become relevant, and thus the source term $S$ in Eq. (3.30) takes the form:

$$S = S_{ln} + S_{in} + S_{nl} + S_{ds} + S_{bot} + S_{db} + S_{tr} + S_{sc} + S_{ice} + S_{ref}, \tag{3.38}$$

where $S_{bot}$ models wave-bottom interactions, $S_{db}$ the depth-induced breaking, $S_{ln}$ the initial linear wave growth, $S_{tr}$ the triad wave-wave interactions, $S_{sc}$ the scattering of waves by bottom features, $S_{ice}$ the wave-ice interactions, and $S_{ref}$ reflection off shorelines or floating objects such as icebergs.

The spectrum integration is carried out by WAVEWATCH III only up to a cut-off frequency $f_{hf}$ (or corresponding wavenumber). Although ideally $f_{hf}$ should be set to the highest discretization frequency, the parameterization of the source terms and the choice of the temporal discretization step (timestep) could not allow the model to maintain balance. Thus, WAVEWATCH III model takes $f_{hf}$ within the model frequency range, and for frequencies higher than $f_{hf}$ it applies a parametric tail.

## 3.5 Evaluation of convective-scale Met Office Unified Model forecasts

Although convective-scale deterministic and EPS forecasts have shown many benefits in skill and realistic modelling of weather hazards, the convective-scale simulations of precipitation and wind fields tend to be noisy. Therefore, the use of well-established grid-point forecast verification metrics often leads to the double penalty problem where a small spatial displacement of localised precipitation in a forecast is penalised twice: one for being absent where the precipitation was observed, and one for being present where no precipitation was observed. To overcome this problem, the neighbourhood-based fractions skill score (FSS; Roberts (2008)) and the object-based structure, amplitude, location (SAL; Wernli *et al.* (2008)) metrics can be used. Even though FSS and SAL were developed for verifying deterministic convective-scale forecast precipitation against radar observations, they have now become quite popular for use with ensembles where they are used in a dispersions form, introduced by Dey *et al.* (2014) and Zschenderlein *et al.* (2019) for FSS and SAL respectively (dFSS and dSAL). These two dispersion metrics also allow to verify and characterise the spread of convective-scale EPS forecasts of precipitation and wind gusts. Because these two metrics are described in detail in paper Chapter 6, where they are used to characterise and compare the spread of the coupled ensemble simulations, here only the basic frameworks of FSS and SAL are provided.

### 3.5.1 Fractions Skill Score metric

The neighbourhood-based FSS metric is a convective-scale spatial verification metric that has been designed to measure, without the need for identification of features, how the forecast skill varies with neighbourhood size, and also to determine the smallest scale at which the forecasts are deemed useful. To accomplish this, the fraction of occurrences of specified wind or rainfall percentile exceedances within different-sized sampling areas (neighbourhoods) are computed for the forecast and the corresponding verification data. Then the forecast and verification field fractions are compared with the FSS, based on a variation of the Brier score (Brier, 1950) that allows spatial comparison, rather than point comparison, between model and verification data.

First, the model forecast, $M$, and the verification data, $O$, are projected onto the same grid and converted into binary fields $I_M$ and $I_O$ as:

$$I_M = \begin{cases} 1, & \mathrm{M} \geq q, \\ 0, & \mathrm{M} < q, \end{cases} \qquad I_O = \begin{cases} 1, & \mathrm{O} \geq q \\ 0, & \mathrm{O} < q \end{cases}$$

where $q$ is the value corresponding to either the percentile threshold or the accumulation value threshold chosen for verification. The advantage of choosing a percentile threshold rather than a fixed threshold is the removal of any impact of the bias in precipitation amounts or wind speed magnitude when focusing on evaluating the spatial accuracy of the model forecasts. After the model and verification binary fields are computed, they are used by the FSS to generate the fractions, similarly to the nearest-neighbour method in Theis *et al.* (2005). For a neighbourhood size $n$ and a grid cell defined by $i, j$ (where $i$ ranges from 1 to $N_x$, $N_x$ being the number of columns in the domain, and $j$ ranges from 1 to $N_y$, $N_y$ being the number of rows) the model and verification fraction fields $M(n)(i,j)$ and $O(n)(i,j)$ are computed by assigning every grid cell in the binary fields $I_M$ and $I_O$ to the fraction of surrounding points within a neighbourhood of size $n$ that have a value of 1. Thus $M(n)(i,j)$ and $O(n)(i,j)$ can be written as:

$$M(n)(i,j) = \frac{1}{n^2} \sum_{k=1}^{n} \sum_{l=1}^{n} I_M \left[ i + k - 1 - \frac{n-1}{2}, j + l - 1 - \frac{n-1}{2} \right], \tag{3.39}$$

and,

$$O(n)(i,j) = \frac{1}{n^2} \sum_{k=1}^{n} \sum_{l=1}^{n} I_O \left[ i + k - 1 - \frac{n-1}{2}, j + l - 1 - \frac{n-1}{2} \right]. \tag{3.40}$$

By varying $n$, the $M(n)(i,j)$ and $O(n)(i,j)$ fractions, corresponding to different spatial scales, are obtained. The maximum value of $n$ is $2N-1$, where $N$ is the number of points along the longest side of the domain on which the model and verification fields are projected.

Then the $M(n)(i,j)$ and $O(n)(i,j)$ fractions can be used to compute the mean square error (MSE), as:

$$MSE(n) = \frac{1}{N_x N_y} \sum_{i=1}^{N_x} \sum_{j=1}^{N_y} \left[ O(n)(i,j) - M(n)(i,j) \right]^2, \tag{3.41}$$

from which, the FSS can be calculated as:

$$FSS = 1 - \frac{MSE_{(n)}}{MSE_{(ref)}}, \tag{3.42}$$

where the $MSE_{(ref)}$ is defined as:

$$MSE_{(ref)} = \frac{1}{N_x N_y}\left[\sum_{i=1}^{N_x}\sum_{j=1}^{N_y} O^2_{(n)(i,j)} + \sum_{i=1}^{N_x}\sum_{j=1}^{N_y} M^2_{(n)(i,j)}\right]. \tag{3.43}$$

FSS can take any value between 0 and 1 and an illustration of how the FSS varies as the neighbourhood size increases can be found in Fig. 3.2. The FSS increases with the size of the neighbourhood and when the FSS reaches the level of desired forecast skill (referred to as target skill in Fig. 3.2) the corresponding neighbourhood size tells the finest grid spacing for which to present the forecast output field is both skillful and useful. From an inspection of Fig. 3.2, it can be seen that for FSS values larger than the target skill, the skill improves further, though this is balanced by a more limited (smoothed) information content of the forecasts. For $n \rightarrow$ inf, the asymptote of the FSS curve in Fig. 3.2 represents the forecast

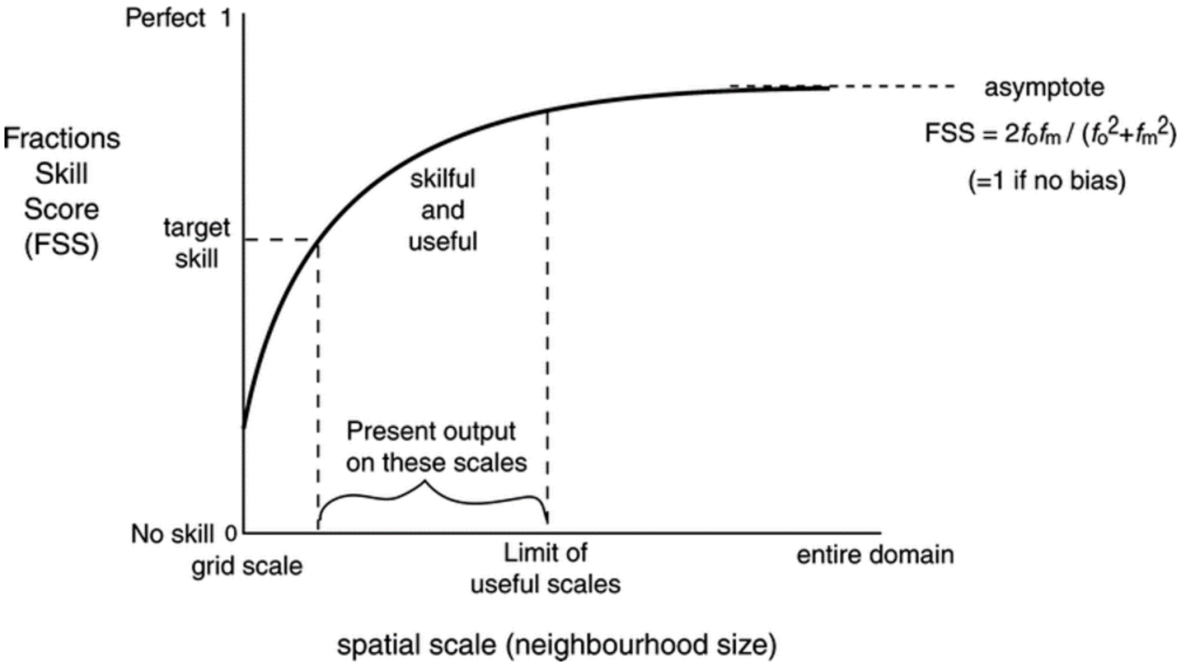

**Figure 3.2:** Schematic graph of skill against spatial scale. Taken from Roberts and Lean (2008).

model bias.

### 3.5.2 Structure, Amplitude, Location metric

The object-based SAL convective-scale metric is based on three distinct components that take into account the structure (S), amplitude (A), and location (L) of the precipitation or wind speed field. The algorithm requires the identification of individual wind or precipitation objects within the considered model and verification (radar or analysis) field domain. A percentile wind speed or precipitation threshold value is applied both to the model and verification field to identify contiguous wind speed objects. Then the S, A, L components of the SAL scores can be computed as follows.

The amplitude component $A$ of the SAL score is computed as:

$$A = \frac{D(R_M) - D(R_O)}{0.5[D(R_M + R_O)]}, \tag{3.44}$$

where $R_M$ is the forecast model and $R_O$ is the verification field, while the $D$ operator performs the average of a forecast field over the model domain as:

$$D(X) = \frac{1}{N} \sum_{(i,j) \in D} X_{ij} \tag{3.45}$$

where $X$ represents either $R_M$ or $R_O$. Positive values of A indicate an overestimation of total precipitation or wind; negative values indicate an underestimation.

The location component $L$ is the sum of two parts $L = L_1 + L_2$. The first term, $L_1$, measures the normalized distance between the two centres of mass of the model $\mathbf{x}(R_M)$ and verification $\mathbf{x}(R_O)$ fields:

$$L_1 = \frac{|\mathbf{x}(R_M)| - |\mathbf{x}(R_O)|}{d}, \tag{3.46}$$

where $d$ is the largest distance between two boundary points of the domain. The second term, $L_2$, is defined as:

$$L_2 = 2\left[\frac{r(R_M) - r(R_O)}{d}\right] \tag{3.47}$$

where $r$ is the weighted averaged distance between the centres of mass of the individual objects, $\mathbf{x}_n$, and the centre of mass of the total precipitation or wind field, $\mathbf{x}$. The weighted average distance $r$ is computed as:

$$r = \frac{\sum_{n=1}^{M} R_n |\mathbf{x} - \mathbf{x}_n|}{\sum_{n=1}^{M} R_n} \tag{3.48}$$

where $R_n$ is the integrated amount of wind or precipitation calculated for every object model and verification field object.

The structure component, $S$, describes the shape and size of the forecast objects. It is computed as the difference between the weighted means of the scaled forecast field volume, $V$, of all objects in the forecast model, $R_M$, and the verification field, $R_O$:

$$S = \frac{V(R_M) - V(R_O)}{0.5[V(R_M + R_O)]}. \tag{3.49}$$

The weighted mean of all objects scaled precipitation or wind volume, V, is determined for both model and verification fields as:

$$V(R) = \frac{\sum_{n=1}^{M} R_n V_n}{\sum_{n=1}^{M} R_n} \tag{3.50}$$

where $V_n$ is the scaled volume of each object. In turn, the scaled volume, $V_n$, of each model or verification field object is determined as $V_n = R_n / R_n^{max}$, with $R_n^{max}$ taken as the largest precipitation or wind value within the object. As a result, the structure component S is constructed in such a way that positive values occur if forecast model objects are too large and/or too flat, and negative values occur if the objects are too small and/or too peaked.

Moreover, the amplitude, $A$, and structure, $S$, components are scaled so that their values range from -2 to +2, and the possible values of location component, $L$, range from 0 to 1. The closer $A$, $S$, and $L$ are too zero, the more skillful is the forecast model.

# Chapter 4

# Attribution of observed extreme marine wind speeds and associated hazards to midlatitude cyclone conveyor belt jets near the British Isles

This chapter has been submitted for publication in *International Journal of Climatology* with the following reference:

**Gentile, E.S.**, Gray, S. L.: Attribution of observed extreme marine wind speeds and associated hazards to midlatitude cyclone conveyor belt jets near the British Isles (2022). *Submitted to International Journal of Climatology*.

Estimated contribution: 80%. ESG designed the study, developed the methodology, performed all the analysis and wrote the manuscript with input and suggestions from SLG. Both authors commented on the manuscript and discussed and interpreted the results at all stages. In particular, ESG performed the 95% of the research, with guidance from supervisor SLG via meetings. SLG also guided the development of the attribution algorithm, presented as part of the work of this chapter.

## Abstract

Extreme wind speeds, gusts and wind wave heights associated with midlatitude cyclones pose a hazard to shipping lanes and offshore infrastructure operating in the North Atlantic ocean seas surrounding the British Isles. Several studies have assessed the variability of wind and waves in this region using reanalyses, but few have used surface observations of extreme wind speeds and wave heights. Here, we use a network of marine surface stations to derive the 2012-2020 climatology of daily maximum wind speed events. An algorithm is used to attribute the extreme wind events, characterised as exceeding the 20 and 25 m $s^{-1}$ thresholds, to the cyclone warm conveyor belt (WCB), and early (CCBa) and returning (CCBb) cold conveyor belt jets; cyclones are matched with up to 90% of extreme wind events. The CCBb is most frequently associated with the strong wind speeds, accounting for 46% and 59% of the events exceeding the two thresholds, respectively. The CCBb also leads to the largest number of compound wind and wave hazard events (37 out of 87). Although the WCB is associated with the second largest number of extreme wind events, the CCBa accounts for the second largest number of compound extreme wind and wave events (24).

The ERA5 reanalysis underestimates the observed extreme wind speeds, and associated gusts and wind-wave heights, during extreme wind events for all the conveyor belt jets. The wind speeds and associated gusts are most underestimated, by median values of 4.5 and 5.5 m $s^{-1}$ respectively, when associated with the CCBb; however, the wind-wave heights are most underestimated, by a median of 3.4 m, when associated with the CCBa. Hence, while the marine CCBb jet, found in mature cyclones, is both most hazardous and underestimated in the ERA5 near the British Isles, the CCBa jet can be nearly as hazardous when considering compound wind-wave events.

## 4.1 Introduction

Midlatitude cyclones pose a major threat to shipping lanes and offshore installations located in the seas surrounding the British Isles (Bell *et al.*, 2017). Associated strong winds and waves batter wind farms and oil production platforms, leading to structural damage and hindering manning and de-manning operations (Cardone *et al.*, 2014). Offshore energy industries and weather centres could benefit from an improved understanding of cyclone features associated with observed extreme surface wind speeds and wind-wave heights: offshore industries could better assess the compound wind-wave risk posed by midlatitude cyclones, while weather centres could better diagnose and attribute biases in model analyses and reanalyses to specific cyclone features. In this paper we present a climatology of observed offshore extreme wind speeds and objectively partition events according to the associated cyclone features.

Many studies have linked the extreme wind speeds observed by land weather stations and by soundings in the mid-troposphere to three different airflows within midlatitude cyclones (Parton *et al.*, 2010; Martínez-Alvarado *et al.*, 2012; Neu *et al.*, 2013; Hewson and Neu, 2015): the warm and cold conveyor belt wind jets (WCB and CCB, respectively) and the sting jet (SJ). These air flows can be represented by the conveyor belt conceptual model (Browning and Roberts, 1994), illustrated in Fig. 4.1a. The WCB originates as a near-surface jet and then ascends over the warm front above the cold air below, leading to intense surface wind speeds (Martínez-Alvarado *et al.*, 2014). However, some of the strongest and most

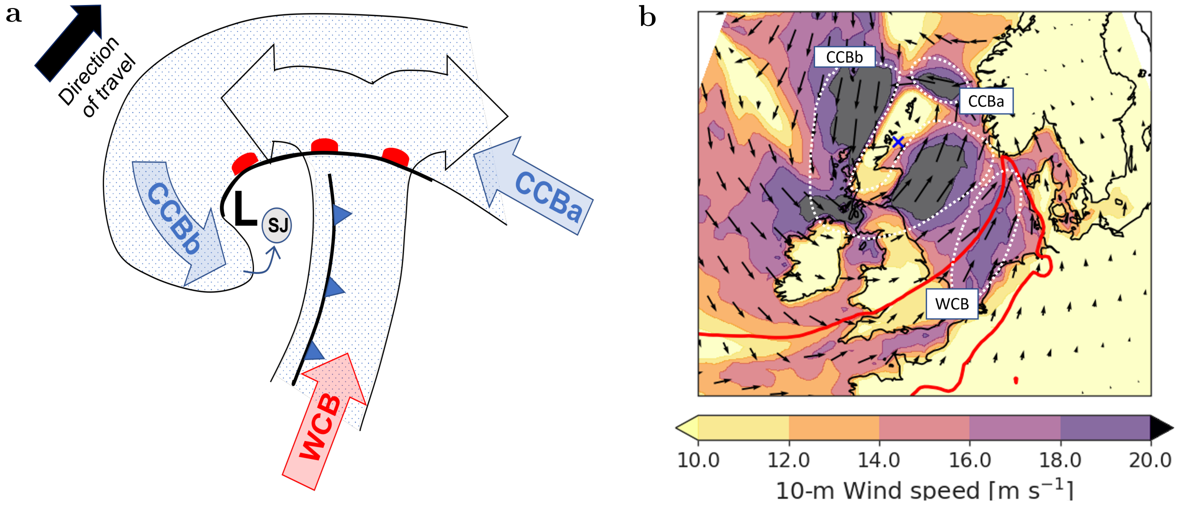

**Figure 4.1:** a) Conceptual model of a sting jet cyclone with the WCB, CCBa and CCBb indicated. Fronts are marked conventionally, "L" indicates the cyclone centre and stippling indicates cloud. b) Illustration of the conveyor belt jets of cyclone Friedhelm (8 December 2011, 1700 UTC) using ERA5 data. The jet regions are enclosed by white dashed lines and 10-m winds are shown by arrows with speeds shaded. The blue cross indicates the mean sea level pressure minimum of the cyclone, while the thick red line indicates the boundary between the warm and cold sectors (as defined in Section 4.2.4).

damaging surface winds form on the rear, equatorward flank of midlatitude cyclones, when the CCB jet wraps around the low-pressure centre and the winds are mixed through the boundary layer, producing extreme gusts at the surface (Sinclair *et al.*, 2010; Hart *et al.*, 2017). In earth-relative winds, the CCB often appears split into two components due to the jet, which has a easterly system-relative component, opposing the typically north-eastwards direction of travel of the cyclone (as shown in Fig. 4.1a). The part of the CCB leading to strong winds on the rear equatorward flank of the cyclone, termed CCBb, is distinct from the early part of the CCB, termed CCBa. Sometimes a finer mesoscale airstream, the SJ, is present in midlatitude cyclones. The SJ exits from the tip of the hook-shaped cloud head and descends to the surface over several hours, producing an additional region of strong winds and exceptionally strong gusts (Clark and Gray, 2018). Besides sting jets, there are also other fine-scale features associated with midlatitude cyclones responsible for damaging surface winds, such as the lines of organized convection that occur along cold frontal boundaries, and (less so) near occluded fronts (Clark, 2013; Earl *et al.*, 2017). The strong wind regions associated with the cyclone conveyor belts are illustrated in Fig. 4.1b for a real-world example cyclone, windstorm Friedhelm (2011), using 10-m wind speeds derived from European Centre for Medium-range Weather Forecasts (ECMWF) fifth generation hourly reanalysis (ERA5). The strongest winds, exceeding 20 $\mathrm{m\,s^{-1}}$, are associated with the CCB, while the slightly weaker winds, not exceeding 18 $\mathrm{m\,s^{-1}}$ and located in the warm sector of the cyclone, are associated with the WCB. The CCB flow is initially south-easterly (CCBa), but as the CCB wraps around the cyclone centre (located off the east coast of northern Scotland) it changes from northerly to south-westerly (CCBb). The unusual fairly pronounced southerly component of the latter part of the CCBb flow is probably due to distortion by northern Scotland orography. Since the WCB is also characterised by a south-westerly flow, knowledge of the boundary between the cold and the warm sector air masses is required to distinguish between the two features. Previous studies have shown that the CCB and WCB can be easily detected from reanalysis data alone by combining information on location of fronts (e.g., diagnosed from the location of the sharpest equivalent potential temperature gradient) with wind direction (Hart *et al.*, 2017; Catto and Raveh-Rubin, 2019; Eisenstein *et al.*, 2022; Volonté *et al.*, 2022). The CCB and WCB can also be identified objectively using criteria applied to air parcel trajectories. For example Madonna *et al.* (2014) used this method to produce a climatology of WCBs using reanalysis data.

Reanalyses are among the most popular datasets for the assessment of both land and marine wind variability. Besides to being easy to use, reanalyses also provide a physically coherent wind field. However, reanalyses' coarse resolution (the highest being ≈ 30 km in the midlatitudes) and boundary-layer parametrization issues (Smart and Browning, 2014) make reanalyses less suitable for detecting wind speed extremes and associated weather hazards, such as high waves (Hewson and Neu, 2015; Molina *et al.*, 2021). This shortcoming can be overcome by the use of surface observation data, which, despite their inhomogeneity, have proved useful to investigate extreme wind and wave events (Earl and Dorling, 2013; Bell *et al.*, 2017). Besides surface observations, also satellite-derived datasets have been used to detect weather extremes, such as North Atlantic extreme wave heights (Rulent *et al.*, 2020; Ponce de León and Bettencourt, 2021) though, compared to surface observations, they present the disadvantages of rain contamination, a lack of data near land (usually within ≈15 km from the coast), and intermittent temporal sampling (Bourassa *et al.*, 2019).

There are many studies that have investigated the variability of the extreme wind speeds and gusts associated with mesoscale cyclone features by utilising surface observations over the UK land (Hewston and Dorling, 2011; Earl and Dorling, 2013; Earl *et al.*, 2017). In summary, these studies find that the prevailing direction of strongest winds and daily maximum gusts (DMGs) is westerly (ranging from north-westerly to south-westerly), that ≈ 80% of the extreme observed wind speeds occur in cyclone-dense seasons, and that boundary-layer convective-scale processes and land surface characteristics can control the intensity of observed DMGs. Combining the DMGSs observed by a land surface station network for the period 2008–2014 with radar imagery and UK surface pressure charts, Earl *et al.* (2017) manually attributed the recorded DMGSs to sub-synoptic cyclone features, deriving a statistics of the frequency with which each cyclone feature (WCB, CCB, SJ, convective lines) produced extreme DMGSs.

In contrast to the large number of observation-based wind and gust climatologies focusing on the UK land, only a few studies have focused on the North Sea and other North Atlantic Ocean seas that surround the British Isles. Because of the dearth of historical time series of wind, gust and wave height observations, these studies have had to rely on model hindcasts, reanalysis data, and just a few surface observations. A common trait of these studies is the focus on wind energy applications rather than on the physical understanding of circulation patterns and wind on gust and wave heights extremes. For example, Geyer *et al.* (2015) investigated the 1958–2012 North Sea surface wind climatology from a model hindcast in order to derive an assessment of the wind power potential, finding a decadal variation in wind power as high as 10%. The earlier study of Coelingh *et al.* (1998) compared coastal observations to those from surface stations located on three different offshore platforms in the North Sea, finding a daytime peak in surface wind speeds between 1200 and 1400 UTC at the coastal stations, but hardly any diurnal variation at the offshore platforms. Further results from Coelingh *et al.* (1998) highlighted that winds with fetch over the sea presented similar distributions of wind speed with wind direction (aggregated by 12 different sectors) at coastal stations and offshore platforms, as expected given that in both cases the wind fetch stretches over hundreds of km of sea surface (excluding the southerly winds which were shielded at the coastal stations). The link between synoptic-scale flow in intense midlatitude cyclones and associated extreme ocean wave heights has been explored either by looking at individual case study hindcasts (Pinto *et al.*, 2014; Cardone *et al.*, 2014) or by analysing historical series of extreme wind speeds and ocean wave heights for a selected surface observation station, the Forties oil platform in the North Sea (Bell *et al.*, 2017). The latter study demonstrated that the largest measured wave heights were associated with north-westerly cyclone wind events aided in growth by the large fetch over the central North Sea, but southerly cyclone wind events were found to create large wave heights despite the limited fetch.

In this study, we explore the systematic link between the conveyor belt jets in midlatitude cyclones and observed extreme wind speeds, gusts and wave heights for the seas surrounding the British Isles. Towards this aim, a climatological analysis has been performed using the 2012–2020 timeseries of extreme wind speeds, gusts, and wave heights observed at 26 stations spread across the seas surrounding the British Isles and then the observed extremes objectively attributed using an algorithm to midlatitude cyclone conveyor belt wind jets. The attribution algorithm detects the frontal boundary between the cyclone cold and warm sectors and then uses the observed surface wind direction to distinguish between the WCB, CCBa, and CCBb jets. Using this partitioning we have quantified the absolute and relative 2012–2020 compound wind-wave risk and ranked the jets accordingly. Finally, we have analysed the ERA5 biases associated with each jet. We expect that the results of this study could contribute to more accurate estimation of wind power resources and compound wind-wave hazards, and so benefit offshore economic actors.

The remainder of the paper is structured as follows. Section 5.2 describes the marine observations, reanalysis data and jet attribution algorithm used. Results are given in Sect. 4.3, where we show the prevailing wind direction of the extreme wind speeds across the selected marine observation stations along with an analysis of their inter- and intra-annual variability. We also determine at each station whether the WCB, CCBa or CCBb jet is more likely to lead to an extreme wind speed event, and then discuss the associated flow characteristics and compound wind-wave hazards. Finally, we present the partitioning of ERA5 bias according to the jets. Further discussion and conclusions are given in Sect. 4.4.

## 4.2 Data and Methods

### 4.2.1 Observations of wind, maximum gust, and wind-wave heights

We analysed hourly reported 10-m wind speeds, direction, wind-wave height (waves still under the action of the winds that created them, rather than free waves such as swells), and hourly or six-hourly maximum 10-m wind gusts (depending on availability), observed by ship, buoy and fixed platform surface stations. The observations from these stations are reported in the SHIP synop code and archived by the Met Office MetDB System at CEDA (Met Office, 2008). The analysed time period was the nine-year period 2012–2020 (inclusive), selected because it was the longest period for which surface observation data were available in all the North Atlantic Ocean seas surrounding the British Isles considered in this study: the Celtic

Sea, the English Channel, and the southern, central, and northern North Sea. The 10-m wind speeds are reported hourly to the nearest 0.1 $\mathrm{m\,s^{-1}}$ and 10 degrees by all observation stations, while maximum gusts are reported hourly or six-hourly, depending on the single station. The hourly 10-m wind speed is measured by averaging the wind fluctuations (sampled every 0.25 s due to their turbulent nature) over the 10-min period leading up to the hourly reporting time. The maximum 10-m gust is the maximum 3-s average wind speed recorded over the full time period leading up to the reporting time (i.e., one or six hours).

All the observations considered in this study have passed the rigorous quality control by the Met Office via checks on the equipment and raw data (Met Office, 2008; Hewston and Dorling, 2011). The dataset was further filtered to guarantee a good temporal coverage of the 2012–2020 period. First, we discarded the stations for which more than 10% of the 10-m wind speed measurements were missing (discarding 25, though mostly located in the central and northern North Sea where a dense network of stations was available), obtaining a network of 26 stations which were labelled from A to Z (see map in Fig. 4.2a). Then, for each station we discarded the maximum gusts and wind-wave height timeseries with reports for fewer than 50% and 10%, respectively, of the times available. A less strict threshold was used for the gusts because of the dearth of gust measurements over the seas. At the end of the filtering process, of the 26 stations reporting 10-m wind, 22 also report wind-wave heights and 10 also report maximum gusts (7 hourly and 3 six-hourly), as shown in Fig. 4.2a.

### 4.2.2 Characterisation of the extreme tail of the observed wind speeds

In the literature, extreme wind speeds are typically defined as exceeding an upper percentile of wind speed and so characterise the upper (or extreme) tail of the wind speed distribution at a given observation station or over a given geographical region (e.g. Hewston and Dorling (2011); Earl and Dorling (2013); Earl *et al.* (2017)). Here, we define extreme wind speeds as those exceeding the 20 $\mathrm{m\,s^{-1}}$ or 25 $\mathrm{m\,s^{-1}}$ threshold. The 20 $\mathrm{m\,s^{-1}}$ threshold corresponds to a Beaufort scale of 8 (strong gale), which, over the sea, is associated with moderately high waves with their crests beginning to topple, tumble and roll over, and probable maximum wave heights of up to 7 m (WMO, 1970). The 25 $\mathrm{m\,s^{-1}}$ threshold corresponds to an important operational value because wind turbines can be forced to shut for wind speeds exceeding this threshold (IMAREST, 2018; Dupont *et al.*, 2018). Moreover, extreme wind and waves exceeding these thresholds can damage the offshore infrastructure or prevent any offshore manning/de-manning operations (PAFA Consulting Engineers, 2001; IMAREST, 2018). Consequently, we define a compound wind-wave hazard as the simultaneous occurrence of a 10-m wind speed exceeding 25 $\mathrm{m\,s^{-1}}$ and significant wind-wave height exceeding 7 m.

To select only independent extreme wind speed events at each network station, we consider daily maximum wind speed (DMWS), i.e., the strongest wind speed reported between 0000–2359 UTC each day, and define a DMWS event if this exceeds the 20 $\mathrm{m\,s^{-1}}$ or 25 $\mathrm{m\,s^{-1}}$ threshold. Moreover, wind directions, gusts, and wind-wave heights associated with the DMWS events (i.e. at the same time as the DMWS) are used to better characterise the atmospheric flow and sea state. For the three stations for which the maximum gust is reported six-hourly, the gust associated with the event is that at the nearest reporting time ahead of the DMWS time.

### 4.2.3 ERA5 data

ERA5 is the fifth generation hourly reanalysis of the ECMWF (Hersbach *et al.*, 2020). It provides values for atmosphere, ocean, wave, and land surface variables with a horizontal grid resolution of 0.25ř, corresponding to $\approx$ 31 km. The atmospheric component is interpolated to 37 pressure levels from the surface up to 1 Pa. Observations are assimilated in ERA5 from many satellite and conventional surface stations instruments. While 10-m wind speed over the sea and wind-wave heights are assimilated, maximum gusts are not (more details in Hersbach *et al.* (2020)).

We extracted from ERA5 the following fields: the horizontal components of 10-m wind, 10-m wind direction, and 10-m maximum gust since previous post-processing, along with wind-wave height, boundary-layer depth, and 850-hPa relative vorticity, $\xi_{850}$, temperature, and relative humidity. To select the ERA5 data corresponding to each observation station we extracted the temporal time series of the nearest-neighbour ERA5 grid point. Although it could occur that this method attributes the same ERA5 grid points to different stations, this did not happen in our study.

It is important to note that we compared the observed maximum gust and wind-wave height observations with the corresponding ERA5 fields defined in the same way as for the network stations. Thus, the observed maximum gust was compared with ERA5 10-m maximum gust, $F_{gust}$, which ERA5 computes based on the argument that the difference between $F_{gust}$ and the mean 10-m wind speed, $F_{10}$, is proportional to the standard deviation of the horizontal wind, $\sigma_u$. The standard deviation of the horizontal wind, $\sigma_u$, is computed in ERA5 following the similarity relation of Panofsky *et al.* (1977):

$$\sigma_u = \begin{cases} 2.29u_* \left(1 - \frac{0.5z_{blh}}{12L}\right)^{\frac{1}{3}} & L < 0 \\ 2.29u_* & L > 0, \end{cases}$$

where $L$ is the Monin-Obukhov length, and $L < 0$ indicate an unstable boundary layer, while $L < 0$ indicate a stable boundary layer. Then, the wind gust, $F_gust$, is computed in ERA5 as:

$$F_{gust} = F_{10} + c_{ugn}u_*f(z_i/L) \tag{4.1}$$

where $c_{ugn} = 7.71$ is a dimensionless number determined from the universal turbulence spectra for a 50% exceeding probability of the three-second wind gust (Beljaars, 1987). ERA5 model, IFS, computes the maximum gust, $F_{gust}$, every time step, writing out for archiving its maximum since previous post-processing. To account for the effect of deep convection on ERA5 maximum gust, $F_{gust}$ in strong convective events, a convective contribution as a function of the vertical wind shear is added to Eq. 4.1, which becomes:

$$F_{gust} = F_{10} + c_{ugn}u_*f(z_i/L) + C_{conv}\max(0, U_{850} - U_{950}) \tag{4.2}$$

where $C_{conv}$ is the convective mixing parameter, set to $C_{conv} = 0.6$, and $U_{850}$ and $U_{950}$ are the wind speeds at 850 hPa and 950 hPa, respectively.

### 4.2.4 Attribution of daily maximum wind speed (DMWS) events to conveyor belt jets

To determine which conveyor belt jet (WCB, CCBa, and CCBb) each DMWS event (with winds exceeding 20 or 25 m $s^{-1}$) is attributed to, the algorithm outlined below was followed.

1. Calculate the cyclone tracks in the Northern Hemisphere using the TRACK algorithm (Hodges, 1995; Hodges *et al.*, 2011) applied to hourly $\xi_{850}$, smoothed to spectral T63 resolution.

2. For every DMWS event, determine, within a 1000 km radius, the nearest midlatitude cyclone track point defined by the mean sea level pressure minimum and matching the same time (to the hour) of the observed DMWS event. If a cyclone track point like this exists, the event is classified as "cyclone-associated" (found to be true for $\approx$ 85% and 90% of events for 20 and 25 m $s^{-1}$ thresholds, respectively).

3. For each "cyclone-associated" DMWS event, compute the cyclone 850-hPa equivalent potential temperature, $\theta_e$ (derived from Bolton (1980) formula) representative of the frontal boundary, $\tilde{\theta}_e$, following the methodology of Hart *et al.* (2017). In more detail, the frontal $\tilde{\theta}_e$ is computed as the mean $\theta_e$ value at the ERA5 grid points where the gradient, $\nabla\theta_e$, exceeds the 99th percentile of values for all points within 750 km of the cyclone centre. As in Manning *et al.* (2021), grid points at elevations above 500 m are masked before calculating the 99th percentile of $\nabla\theta_e$ to remove noise introduced by orography.

4. Attribute the "cyclone-associated" DMWS events to the cyclone cold or warm sector by comparing the nearest grid point ERA5 850-hPa $\theta_e$ with the $\tilde{\theta}_e$ value which represents the cyclone frontal boundary.

5. Further partition the cold and warm sector DMWS events according to the observed DMWS Earth-relative wind direction $\alpha$ (based on Dacre *et al.* (2012)), in the following way:

- A cold sector DMWS event is attributed to the CCBa jet if it has a southeasterly wind direction, i.e.
  $90° \leq \alpha \leq 210°$.
- A cold sector DMWS event is attributed to the CCBb jet if it has a northwesterly wind direction, i.e.
  $240° \leq \alpha \leq 360°$.
- A warm sector DMWS event is attributed to the WCB jet if it has a wind direction ranging from south-easterly to southwesterly, i.e.
  $130° \leq \alpha \leq 250°$.
- All the cold and warm sector DMWS events that have not been attributed to any of the conveyor belt jets are labelled as "other".

This classification method attributes DMWS events to midlatitude cyclone early CCBs (CCBa), returning CCBs (CCBb), or WCBs. It is likely that some of the DMWS events classified as "other" correspond to other causes of strong 10-m winds in cyclones such as convective lines, quasi-convective lines, and embedded frontal convection. Also, some of the events attributed to the CCBb jet could actually be associated with a SJ as this feature occurs in the same part of the cyclone as the CCBb (when it occurs). However, all these features are too fine scale to be represented by the (relatively) coarse $\simeq$ 31 km resolution of the model used to generate ERA5.

## 4.3 Results

### 4.3.1 Wind speed variability over the British Isles surrounding seas

The geographic variability of the observed 10-m wind speeds and directions for the period 2012–2020, is shown in Fig. 4.2a-b, along with the map of the location of the 26 network stations. In Fig. 4.2a, a sample of 12 wind roses illustrates the prevailing wind direction across the network stations, which is overall dominated by the westerly sector of the compass. However, some variations in the wind speed direction occur with latitude, longitude, and

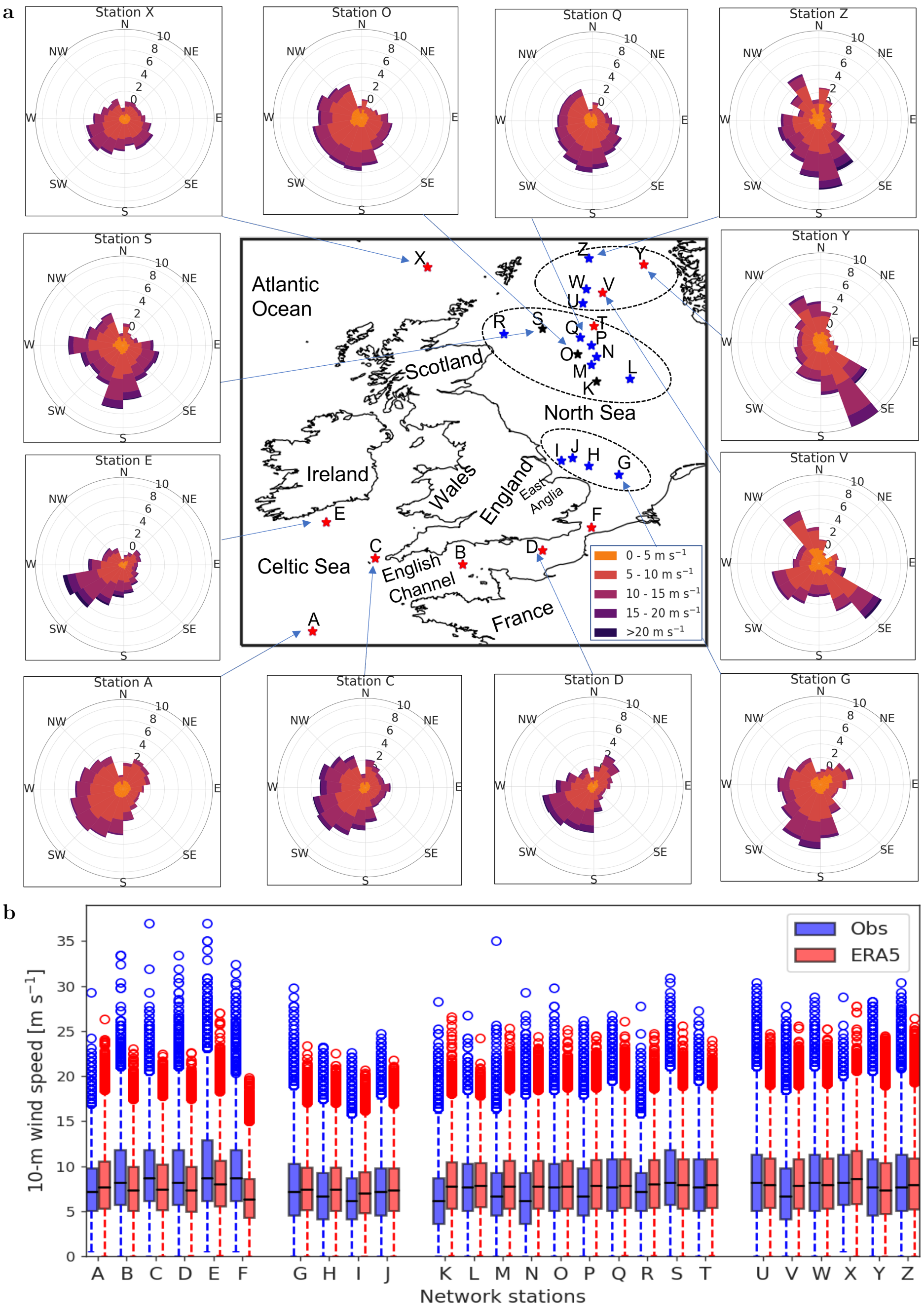

**Figure 4.2:** (a) Map of 10-m wind speed, wind-wave height, and maximum gust observation stations for the 2012–2020 time period, surrounded by wind roses for a set of 12 representative stations showing wind speed distribution per wind direction sector (of 20° width each). The 26 stations are labelled with letters from A to Z, following an order of increasing latitude. Stations are marked with a black star, blue star, or red star according to whether they report 10-m wind speed, 10-m wind speed and wind-wave height, and 10-m wind speed, wind-wave heights, and gust speeds, respectively. The three dashed circles illustrate the cluster of stations in the Northern, Central, and Southern North Sea. (b) Box and whisker plot of observed (blue) and corresponding ERA5 (red) 10-m wind speed at each station. The minimum and maximum values (within $3\sigma$ from the mean) are indicated by the ends of the whiskers, with the median, 25th and 75th percentile values marked by the middle, lower and upper parts of the box, respectively.

distance from the British Isles coasts. The winds for the more southerly stations (A–G) are mainly dominated by the south-western quadrant, and less so by the north-western quadrant. In comparison, the central (K–T) and northern North Sea stations (U–Z) generally show less dominance of the south-western quadrant. For the three northern North Sea stations (V, Y, and Z), the contributions of the north-western and south-eastern quadrants of the compass strongly exceed that of the south-western quadrant. When considering only 10-m wind speeds exceeding 25 $\mathrm{m\,s^{-1}}$, a similar pattern is revealed. The predominant south-easterly and north-westerly wind directions in the northern (and less so central) North Sea stations suggest a more important role of the CCBa and CCBb in producing strong surface winds here than for the rest of the network stations. Indeed, due to their geographic location, the central and northern North Sea stations are exposed to more mature midlatitude cyclones in which the CCB has had time to develop (eroding the warm sector). However, the large number of westerly/south-westerly wind events exceeding 20 $\mathrm{m\,s^{-1}}$ at the more southerly stations could also indicate that the CCBb plays an important role in generating gale-force surface winds in this region. In Sect. 4.3.3 the method presented in Sect. 5.2 is used to distinguish the different conveyor belt jets.

To better characterise the 10-m wind speed variability at each network station, we plotted the median, quartiles and extremes of the 10-m wind speed distribution observed at each station along with the corresponding ERA5 values (see Fig. 4.2b). The strongest wind speeds are 37.5 $\mathrm{m\,s^{-1}}$ at stations C (off Cornwall, at the tip of England's southwest peninsula) and E (Celtic Sea, south of Ireland), followed by station M (central North Sea, 35.1 $\mathrm{m\,s^{-1}}$). Station B (English Channel) and stations S, U, and Z (central and northern North Sea) also occasionally report 10-m wind speeds exceeding 30 $\mathrm{m\,s^{-1}}$, but below 35 $\mathrm{m\,s^{-1}}$. The median of the observed 10-m wind speed distribution at each station varies between $\approx 6$ and $\approx 9$ $\mathrm{m\,s^{-1}}$. Stations B, D,and F located in, and west of, the English Channel are characterised by median and upper/lower quartiles $\approx 1.5$ $\mathrm{m\ s^{-1}}$ higher than those of the southern North Sea stations (G–I), but in line with the median of the distribution reported by the central North Sea stations.

Figure 4.3 shows the number of exceedences in the observations and ERA5 data for both thresholds and for each station. The northern North Sea and western English Channel stations experience more wind speed events exceeding the 20 and 25 m s$^{-1}$ thresholds than those in the southern/central North Sea, besides presenting higher median and quartile values. For example, station E, in the Celtic Sea immediately south of Ireland, experiences ≈ 1900 wind speed events exceeding 20 m s$^{-1}$ and ≈ 300 events exceeding 25 m s$^{-1}$, the largest number of exceedances of the two wind speed thresholds across all the network stations. The other stations in the Atlantic Ocean, English channel and northern North Sea exceed the thresholds ≈ 50% less often than station E, and even fewer exceedances are observed at the stations in the central North Sea and off the coast of East Anglia (in the southern North Sea). In particular, the stations H–J off East Anglia report between 20 and 50 exceedances of the 20 m s$^{-1}$ threshold and between 0 and 5 exceedances of the 25 m s$^{-1}$ threshold, the fewest among the stations.

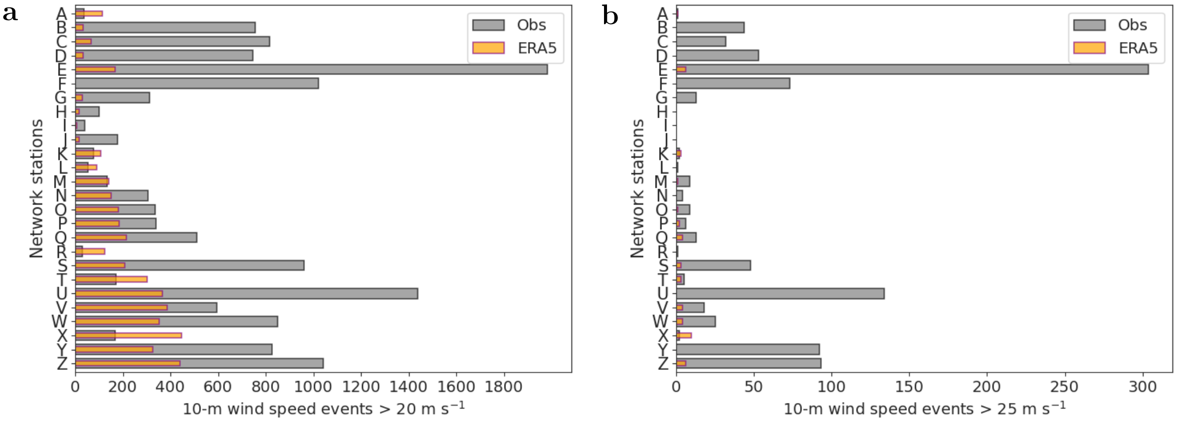

**Figure 4.3:** Bar chart showing, at each network station, the number of observed (grey) and ERA5 (orange) (a) 20 m s$^{-1}$ and (b) 25 m s$^{-1}$ threshold exceedances of 10-m wind speed events

The variability of the ERA5 10-m wind speed distribution across the stations mirrors that of the observed distributions, as shown in Fig. 4.2b. However, non-negligible differences can be noted in the median, quartiles and also extremes of the ERA5 and observed distributions for several stations. The largest negative differences between the median and the upper/lower quartiles of the ERA5 and observed 10-m wind speed distributions can be seen in the Celtic Sea and English Channel stations B–F, for which ERA5 underestimates the observed median and quartiles by up to $\approx 2$ m s$^{-1}$. Instead, ERA5 overestimates median and quartiles by up to $\approx 2$ m s$^{-1}$ for the stations off East Anglia in the southern North sea (for instance, see stations H and I), and for some of the stations in the central and northern North Sea (for instance, see stations M, N, R, and V), with negligible differences $\leq 0.5$ m s$^{-1}$ found for the other stations. The differences between ERA5 and observed winds have a symmetrical distribution for the low to moderate wind speed values (2–20 m s$^{-1}$ range), but consistently smaller ERA5 values for wind speeds exceeding the 20 m s$^{-1}$ threshold, and even more so for those exceeding the 25 m s$^{-1}$ threshold.

Further comparison of observed and ERA5 10-m wind speeds considering the number of exceedances of the 20 m s$^{-1}$ threshold shows that the ERA5 exceedances drop to between half and one third of those observed for most of the stations (Fig. 4.3a). The reduced magnitude of the ERA5 wind speeds compared to observed values is even more accentuated for station E, just south of Ireland, which is the only station to report a ten-fold reduction in 20 m s$^{-1}$ threshold exceedances. Considering the higher threshold of 25 m s$^{-1}$, only 10 out of the 26 network stations report ERA5 wind speed exceedances (Fig. 4.3b). Station E reports the largest number of ERA5 exceedances (six), followed by X and Z with five each. In general, the number of observed 25 m s$^{-1}$ exceedances is disproportionately higher than for the ERA5 (up to 20 times as higher). However, for station T and X the ERA5 and observed wind speeds exceedances of the 25 m s$^{-1}$ threshold are similar. Apart from these two stations, the ERA5 underestimates the exceedences over the Celtic Sea, the English Channel, and the North Sea. In summary, the higher the observed 10-m wind speed, the more likely it is that the corresponding speed from the ERA5 will have a negative bias. These results confirm and extend previous findings of Molina *et al.* (2021), that indicated that European land stations reporting more frequent exceedances of the 25 m s$^{-1}$ threshold (the only threshold used) were generally associated with larger negative bias in the ERA5.

### 4.3.2 Inter-annual and monthly variability of wind speeds over the British Isles seas

To characterise the inter-annual and monthly variability of extreme wind speed events over the British Isles surrounding seas the number of 10-m wind speed exceedances of the two thresholds, 20 and 25 m s$^{-1}$, are aggregated over each station by year in Fig. 4.4a and by month in Fig. 4.4b. Overlain on the intra-annual variability plot is the correspondingly averaged monthly North Atlantic Oscillation (NAO) index. The NAO is a major mode of wind variability in the northern hemisphere and exhibits strong decadal and seasonal variability, the latter evident from Fig. 4.4b.

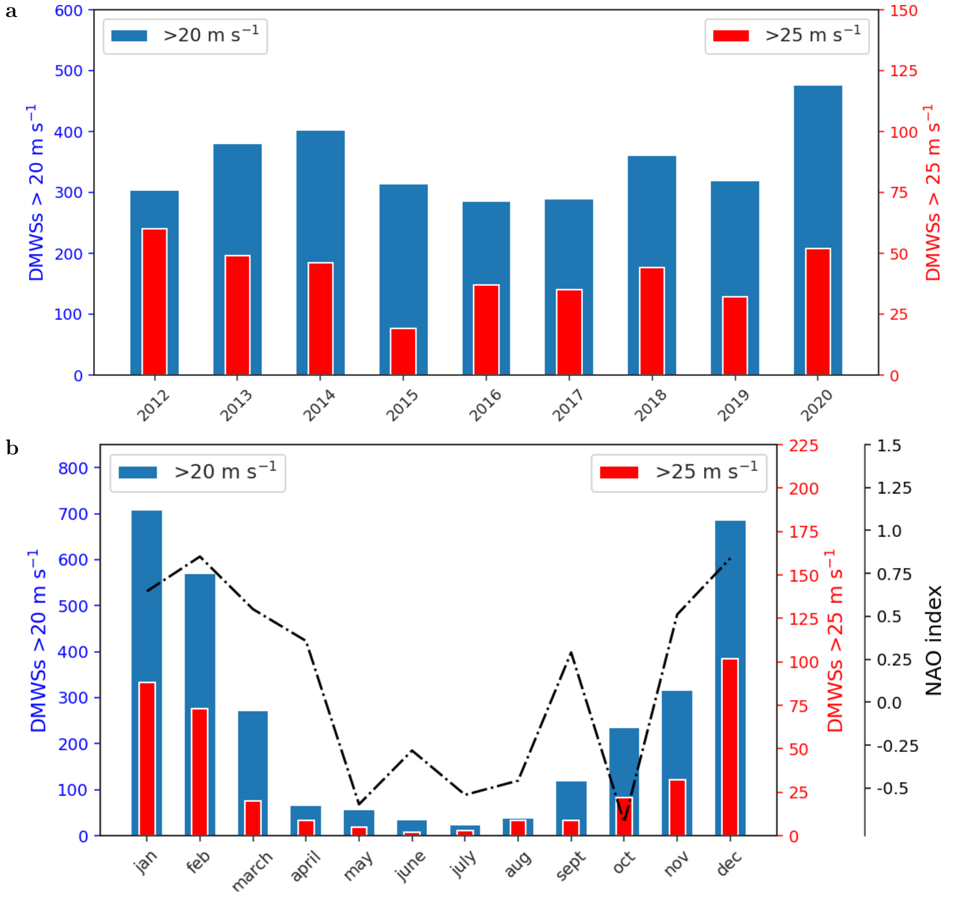

**Figure 4.4:** (a) Inter-annual 2012–2020 variability of number of 10-m wind speed events exceeding the 20 and 25 m s$^{-1}$ threshold, aggregated over all network stations (b) Monthly, intra-annual variability of 10-m wind speeds exceeding the 20 and 25 m s$^{-1}$ thresholds, aggregated over all network stations, and overlaid by the averages for each month of the 2012-2020 NAO index calculated from the monthly averages produced by the Climate Prediction Center at the National Oceanic Atmospheric Administration (NOAA, 2020)

Figure 4.4a reveals that the number of exceedances of the 20 $\mathrm{m\,s^{-1}}$ threshold is typically about 300 events per year for the network stations, about ten times larger than that associated with the 25 $\mathrm{m\,s^{-1}}$ threshold. Some inter-annual variability can be observed for the 20 $\mathrm{m\,s^{-1}}$ threshold exceedances, with the years 2013, 2014 and 2020 presenting the three highest number of exceedances (381, 402, and 477 events, respectively). Figure 4.4b shows that the winter months, December to February, account for $\approx$ 80% of the 20 $\mathrm{m\,s^{-1}}$ threshold exceedances and $\approx$ 90% of the 25 $\mathrm{m\,s^{-1}}$ threshold exceedances, with December being the dominant contributor for both thresholds. Apart from the NAO index value for September, the monthly NAO index averaged over the 2012–2020 period correlates well with the monthly threshold exceedances, being both highest in the late-autumn and winter months and lowest over spring and summer months. This correlation was expected as a positive NAO index is associated with a stronger North Atlantic jet stream and a northward shift of the storm track leading to northern Europe (including the British Isles) experiencing more cyclones (Hoskins and Hodges, 2019a).

### 4.3.3 Climatology of conveyor belt jets contributing to extreme observed 10-m wind speeds

To investigate the attribution of independent extreme wind speed events exceeding the 20 and 25 $\mathrm{m\,s^{-1}}$ thresholds to cyclone WCB, CCBa, and CCBb jets, DMWS events (computed as the strongest wind speeds observed in the period 0000–2359 UTC each day; for more details see Section 5.2) are considered. Pie charts in Fig. 4.5a-b summarise the resulting partitioning. Over the 2012–2020 period, the cold sector (which includes CCBa and CCBb jets) accounts for most of the DMWS events with $\approx$ 60% of the events exceeding the 20 $\mathrm{m\,s^{-1}}$ threshold (across all network stations, Figure 4.5a). This percentage rises to $\approx$ 75% of the total events for those exceeding the 25 $\mathrm{m\,s^{-1}}$ threshold. Considering separately the two CCB jets, the returning CCBb is approximately three times more likely to generate an event exceeding the 20 $\mathrm{m\,s^{-1}}$ threshold than the early CCBa (16% CCBa versus 46% CCBb events), and nearly four times more likely to generate an event exceeding the 25 $\mathrm{m\,s^{-1}}$ threshold (15% of CCBa versus 59% CCBb events). The CCBb also accounts for the increase in cold sector events

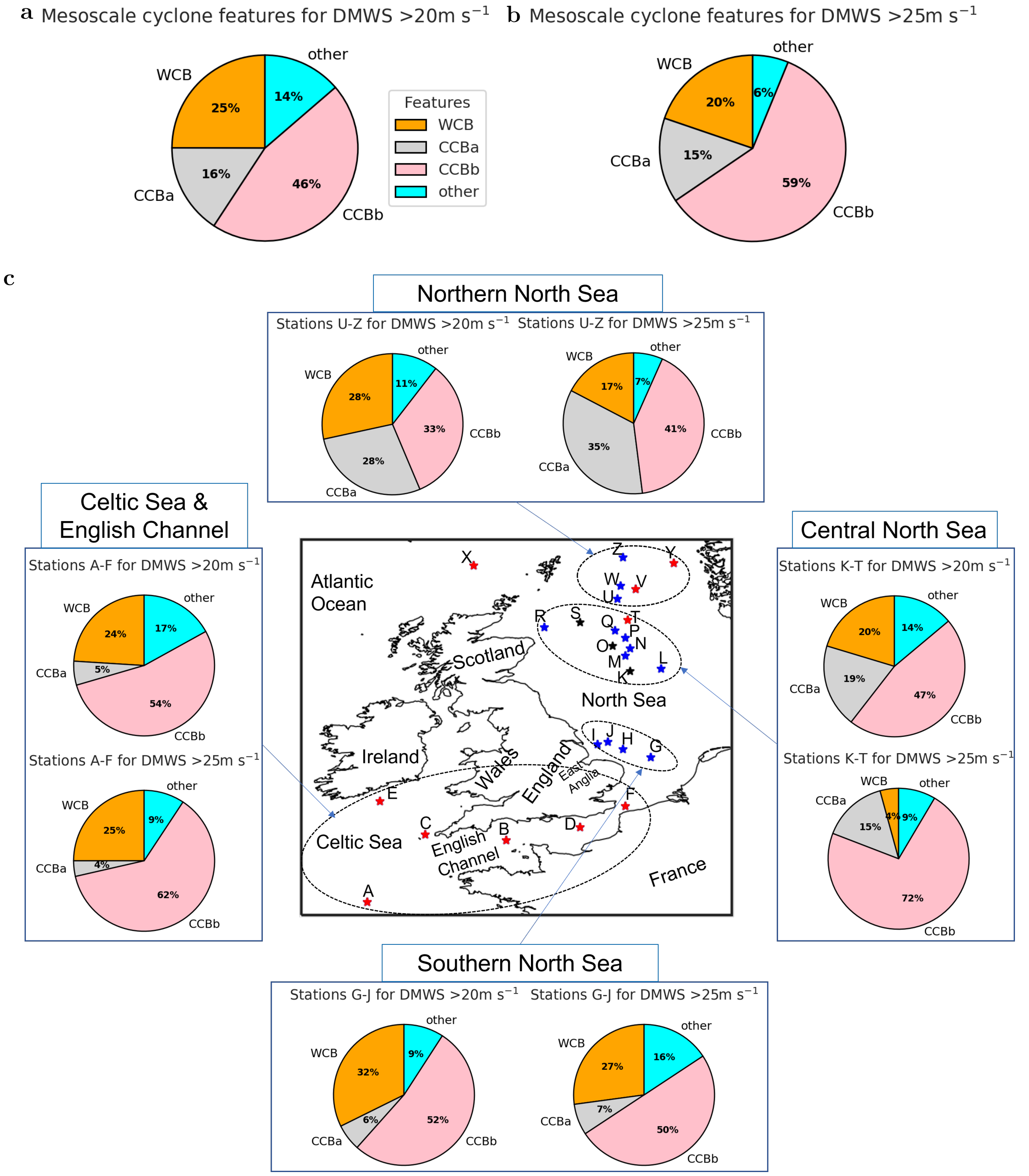

**Figure 4.5:** Pie charts showing the percentage of conveyor belt jets associated with (a) >20 m s$^{-1}$ and (b) >25 m s$^{-1}$ DMWSs, aggregated over all observation stations. (c) Distribution of conveyor belt jets associated with DMWSs aggregated over distinct geographical regions of the British Isles surrounding seas: Celtic Sea & English Channel, Southern North Sea, Central North Sea, Northern North Sea, illustrating how the relative percentage of features vary with latitude and longitude across the network. Orange sector corresponds to WCB events, grey sector to CCBa events, pink to CCBb events, and light blue to DMWSs which could not be associated with any of the cyclone features WCB, CCBa, and CCBb. In total there are 2267 DMWS events exceeding the 20 m s$^{-1}$ threshold, and 267 DMWS events exceeding the 25 m s$^{-1}$ threshold associated with a midlatitude cyclone track point.

between the two thresholds, being associated with 3/5 of the strongest events recorded across the network. In comparison, the WCB accounts only for 25% of the events exceeding the 20 $\mathrm{m\,s^{-1}}$ threshold and 20% of the events exceeding the 25 $\mathrm{m\,s^{-1}}$ threshold. Consequently, the CCBb is the most likely conveyor belt to cause strong surface winds across the network stations, followed by the WCB and then CCBa. Note that warm or cold sector DMWS events that did not exhibit the wind directions typically associated with conveyor belts in those sectors (S/SW for WCB, W/NW for CCBb, and S/SE for CCBa) were classified as "other" (grey segment in Fig. 4.5a) and represent $\approx$ 14% and $\approx$ 6% of the total number of events exceeding the 20 and 25 $\mathrm{m\,s^{-1}}$ thresholds, respectively. An examination of Met Office surface analysis charts for some randomly-picked events labelled as "other", suggested they could plausibly be associated with convective lines, quasi-convective lines, or convective systems in the sectors, but the lack of radar data over the sea and the relatively coarse resolution of ERA5 prohibited their objective classification. Note that, compared to the 20 $\mathrm{m\,s^{-1}}$ threshold, the contribution of these unidentified events halved when considering the 25 $\mathrm{m\,s^{-1}}$ threshold.

The CCBb jet is the dominant conveyor belt jet for DMWS events exceeding both wind thresholds for each cluster of neighbouring stations considered (see Fig. 4.5c) as well as when aggregating over all stations. In contrast, the contribution of the WCB and CCBa jets to events is not homogeneous across the network stations. The Celtic Sea, English Channel, and southern North Sea stations are more affected by WCB jets than CCBa jets (with the exception of station C) for both wind speed thresholds. As the latitude and the longitude of the stations increase, the contribution of the CCBa jets becomes larger than WCB jets, with central North Sea and northern North Sea stations exhibiting CCBa events up to twice as often as WCB events (for instance, see northern North Sea 25 $\mathrm{m\,s^{-1}}$ exceedances in Fig. 4.5c).

### 4.3.4 Flow characteristics of conveyor belt wind jets

The characteristics of the flow associated with each of the conveyor belt jets are depicted in Fig. 4.6a-c for the DMWS events exceeding the 20 and 25 $\mathrm{m\,s^{-1}}$. The cold sector winds (associated with CCBa and CCBb) are more intense than the warm sector winds (associated with the WCB) (Fig. 4.6a): the median and the upper quartile of the CCBa and CCBb events exceeding the 20 and 25 m s$^{-1}$ thresholds are up to 0.5 m s$^{-1}$ and 1 m s$^{-1}$ higher, respectively, than the corresponding WCB values. A closer look at the wind speeds exceeding the higher threshold shows that, excluding the outliers of each distribution, the upper tail (whisker) of the CCBb events is the most intense, ranging between 28.2–30.8 m s$^{-1}$, but no appreciable difference can be seen between the upper tails for the CCBa and WCB events (both ranging between 27.1 and 29.6 m s$^{-1}$). The gustiness of the conveyor belt wind jets events, shown in

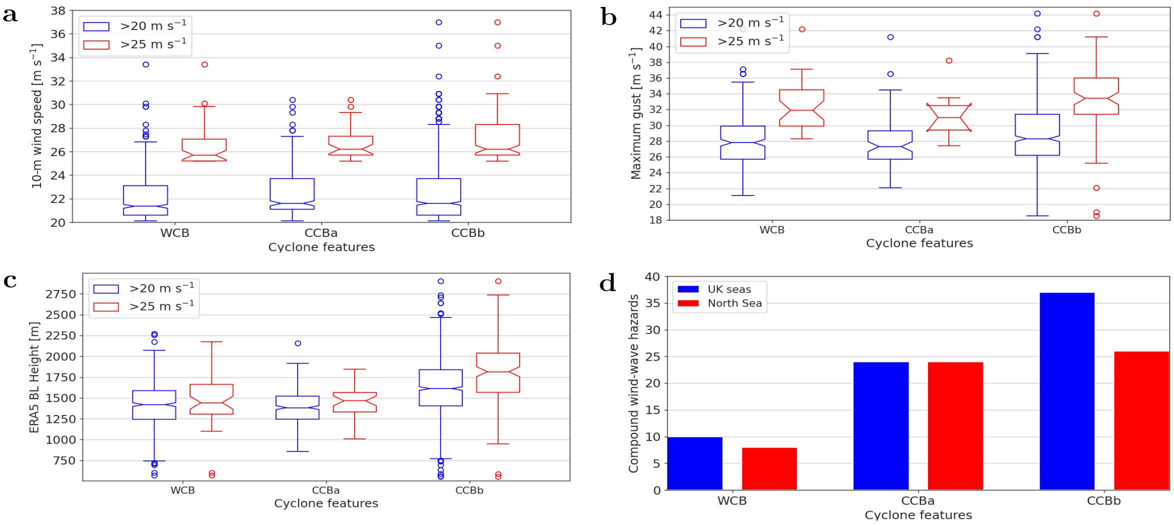

**Figure 4.6:** Box plot of (a) observed 10-m wind speed, (b) observed gust, and (c) ERA5 boundary-layer height distributions for the WCB, CCBa, and CCBb jets associated with the DMWS events exceeding 20 m s$^{-1}$ (blue) and 25 m s$^{-1}$ (red). Box plots are defined as for Fig. 4.2. (d) Histogram of number of DMWS events exceeding 25 m s$^{-1}$ co-occurring with observed significant wind-wave height events exceeding 7 m height, associated with WCB, CCBa, and CCBb jets. The blue histogram bars show the number of the wind-wave compound events aggregated over all the network stations in the British Isles surrounding seas, while the red histogram bars are for the North and Central North Sea station clusters only.

Fig. 4.6b, has been derived from the observed gusts associated with the DMWS events (i.e., taking the gust value closest to the time of each DMWS event, as described in Sect. 4.2.2). The median and upper quartile values of the gusts for the CCBb events (exceeding 20 m s$^{-1}$) are 28.1 and 31.8 m s$^{-1}$, respectively, with extreme values reaching 39.1 m s$^{-1}$ (excluding outliers). The WCB and CCBa median and upper quartile values are smaller than the CCBb ones: 27.8 and 30.2 for the WCB median and upper quartile and 27.3 and 29.3 for the corresponding CCBa values. Both the median and upper quartile of the gusts observed for CCBb, CCBa, and WCB events exceeding the 25 m s$^{-1}$ threshold are ≈ 5, ≈ 4, and ≈ 3 m s$^{-1}$ larger, respectively, than the corresponding 20 m s$^{-1}$ values.

Figure 4.6c shows that the CCBb events are associated with deeper boundary layers (diagnosed from ERA5) than WCB and CCBa events. The median and upper quartile of the boundary-layer height of the CCBb events exceeding 20 $\mathrm{m\,s^{-1}}$ are $\approx$ 200m higher than those of the WCB events and $\approx$ 250 m higher than those of the CCBa events. For the higher 25 $\mathrm{m\,s^{-1}}$ threshold, the CCBb boundary-layer height distribution median and upper quartile are $\approx$ 400 m higher than those for the WCB and CCBa, almost twice as large as those observed for the lower 20 $\mathrm{m\,s^{-1}}$ threshold. When considering only the CCBb boundary-layer height values lying above the distribution upper quartile, these can reach $\approx$ 2750m, compared to maximum WCB and CCBa values of $\approx$ 2200m and $\approx$ 1800m, respectively (excluding outliers).

Overall, these results indicate that the CCBb is associated with the strongest observed winds, the highest gustiness, and the deepest boundary layers. The WCB and CCBa can also produce very strong winds, but not as strong as those attributed to the CCBb. This is likely influenced somewhat by the instability in the surface layer generated when the cool air of the CCBb hooks around the cyclone pressure low and descends over warmer ocean waters facilitating the downward mixing of fast flowing air from the top of the boundary layer and thus producing stronger and gustier winds, compared to the other cyclone features. Despite slightly stronger winds in the CCBa events, the median of the CCBa gusts is $\approx$ 1 $\mathrm{m\,s^{-1}}$ less intense than for WCB events. A possible explanation is that the typically deeper boundary layer associated with the WCB is more turbulent, leading to enhanced momentum transport towards the surface and consequently stronger gusts.

Figure 4.6d shows the compound wind-wave hazard reported by the network stations (wind speed exceeding 25 $\mathrm{m\,s^{-1}}$ co-occurring with wind-wave height exceeding 7 m at the same time as a DMWS event). The CCBb jet is the most hazardous followed by the CCBa jet and then the WCB jet. The network stations reported 37 compound wind-wave hazards associated with the CCBb jet, 24 associated with the CCBa jet, and 10 associated with the WCB jet. Considering the North Sea stations only, the gap between the number of compound wind-wave hazards produced by the CCBb and CCBa jets is even smaller, with the CCBb jet producing only 2 more compound wind-wave hazards, 26, than the CCBa jet, 24. Moreover, Fig. 4.6d shows that the CCBa is more than twice as likely as the WCB jet to produce a compound wind-wave hazard for the full set of network stations and more than three times more likely when considering only the North Sea stations, despite the WCB jet being responsible for 5% more cyclone-associated DMWS events exceeding 25 $\mathrm{m\,s^{-1}}$ than the CCBa (Fig. 4.5b). Overall, these findings indicate that the most likely wind speed directions for compound wind-wave hazards are westerly/north-westerly flow (associated with the CCBb) followed by the south/south-easterly flow (associated with the CCBa). A plausible explanation for the highest number of compound wind-wave hazards attributed to the CCBb being is that the long fetch of its intense north-westerly/westerly winds favors the formation of extreme wind-wave heights, as noted by Ponce de León and Guedes Soares (2014), Bell *et al.* (2017) and Ponce de León and Bettencourt (2021). The fact that the south-easterly CCBa jets also lead to a large number of compound wind-wave events could be attributed to freak waves, whose formation is likely favored by the steep sea state (Gibson *et al.*, 2014) induced by the short fetch and extreme values of the winds (larger than the WCB).

### 4.3.5 ERA5 bias of the conveyor belt jet winds and waves

The distribution of the bias of the ERA5 10-m winds, gusts and wind-wave heights associated with the observed WCB, CCBa, CCBb jet events is shown in the box plots in Fig. 4.7. On average the ERA5 underestimates all three fields for the events. The CCBb events have the highest negative bias with a median at $-4.6$ $\mathrm{m\,s^{-1}}$, roughly 0.5 $\mathrm{m\,s^{-1}}$ larger in magnitude than for WCB events and 1.2 $\mathrm{m\,s^{-1}}$ larger than for CCBa events (Fig. 4.7a). The same pattern occurs for the lower tails (larger negative biases) of the distributions, as defined by the lower whiskers of the box plots, with values reaching $-12$ $\mathrm{m\,s^{-1}}$ for CCBb events (though the lower outliers extend to similar values for the WCB and CCBb). The differences between the ERA5 gust bias distributions for each jet event follow a similar pattern to those for the 10-m wind speed biases (Fig. 4.7b): the lower tail of the CCBb events gust bias extends to $-20.2$ $\mathrm{m\,s^{-1}}$ (with outliers extending to $-23.3$ $\mathrm{m\,s^{-1}}$). As discussed in Sect. 4.2.2, three stations only report gusts six hourly. However, virtually identical median and quartiles were obtained if observations from these stations were excluded (although there were slight changes to the extreme values of gust bias distribution). This similarity implies that the results are robust to the different reporting frequencies.

The distribution of the biases for the WCB events, and more so for the CCBa events, are narrower than the CCBb events for all fields considered, even when considering the outliers. However, while the gust and 10-m wind speed bias distributions of the CCBa and WCB events are characterised by a smaller magnitude medians than for the CCBb events, the CCBa

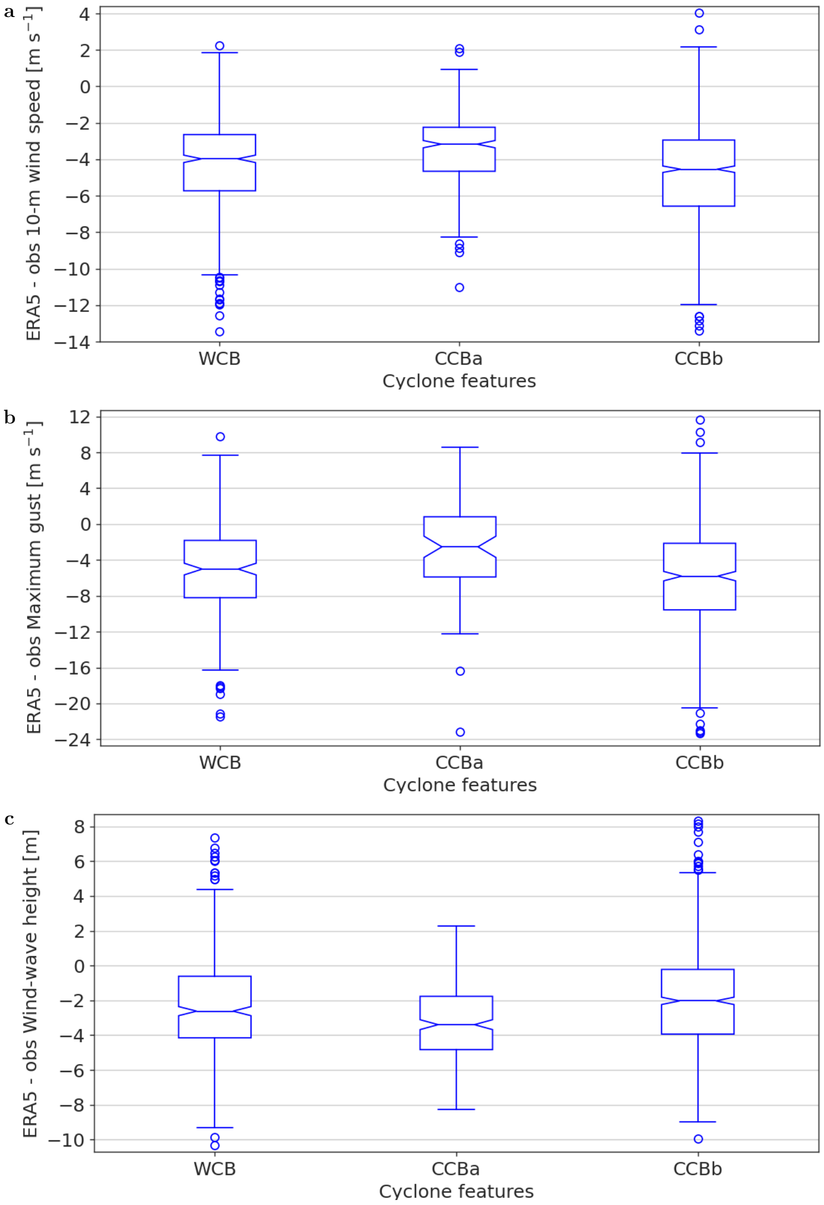

**Figure 4.7:** Box plot showing the bias of ERA5 for (a) 10-m wind speed, (b) gust, and (c) wind-wave heights values of the DMWSs, computed as the difference between ERA5 and observed values and partitioned by the conveyor belt jets (WCB, CCBa, and CCBb). Box plots are defined as for Fig. 4.2.

and WCB events wind-wave height bias distributions are characterised by a larger magnitude median than for the CCBb events (−3.4 m, −2.7 m, −2.0 m for CCBa, WCB and CCBb events, respectively).

## 4.4 Discussion and conclusion

In this study, a climatology of observed marine extreme wind speeds over the seas surrounding the British Isles has been produced for a nine-year time period (2012–2020) based on a network of 26 stations, and extreme events have been attributed to midlatitude cyclone conveyor belt jets. Extreme DMWS events were defined as occurring for 10-m wind speeds exceeding the 20 and 25 $\mathrm{m\,s^{-1}}$ thresholds; these two thresholds characterise the extreme tail of the wind speed distribution, with the upper threshold being the reference value over which the wind turbines shut down to prevent damage. The extreme DMWS events were objectively attributed to a cyclone conveyor belt jet (WCB, CCBa, or CCBb) by a two-step algorithm. First, these events are attributed to a cyclone if they occurred within a 1000 km radius from a midlatitude cyclone track point defined by the mean sea level pressure minimum at a coincident time. Then each event is objectively attributed to a jet based on whether the event is in the cold or warm sector of the cyclone (diagnosed from ERA5 data) and the observed wind direction. We also analysed the distributions of observed gusts and wind-wave heights, and ERA5 boundary-layer heights, associated with each jet event. The climatological compound hazard of each jet was determined by computing the number of DMWS events with wind speeds exceeding 25 $\mathrm{m\,s^{-1}}$ and co-occurring wind-wave heights exceeding 7 m. Lastly, we calculated the ERA5 bias in the DMWS events associated with the jets to demonstrate the limitations of ERA5 for evaluation of marine wind speeds and the associated gusts and wind-wave heights.

The climatology showed that the winds recorded by the network stations located in the Celtic sea and English Channel were predominantly westerly and south-westerly, consistent with previous extreme wind and gust climatologies over the UK land (Hewston and Dorling, 2011), but stations located in the central North Sea and northern North Sea also recorded pronounced north-westerly and south-easterly wind direction components. The stations in the English Channel and northern North Sea recorded up to 1 $\mathrm{m\,s^{-1}}$ higher median wind speeds than those in the central and southern North Sea, the latter reporting virtually no exceedances of the higher 25 $\mathrm{m\,s^{-1}}$ threshold due to sheltering from the nearby land. Comparable differences in magnitude between mean wind speeds in the northern North Sea and central and southern North Sea were also found by Laurila *et al.* (2021) for a longer time period climatology (1979–2018) of wind speeds from the ERA5 over the North Atlantic and European domain.

The DMWS events did not show a clear inter-annual trend. However, the two years that exhibited the most events exceeding the 20 $\mathrm{m\,s^{-1}}$ threshold (2014 and 2020 with approximately 400 and 500 exceedances, respectively) were also characterised by the most dense midlatitude cyclone seasons, as reported by (Kendon, 2020). When considering the seasonal trend, the winter months (December–February) were the dominant contributors, accounting for 70% and 80% of the extreme wind speeds exceeding the 20 and 25 $\mathrm{m\,s^{-1}}$ thresholds, respectively; this is consistent with Earl *et al.* (2017) results based on extreme maximum gusts (top 2% and 0.1%) observed by the UK land stations.

Objective attribution, by means of an algorithm, of the extreme DMWS events exceeding the 20 $\mathrm{m\,s^{-1}}$ threshold (over the period 2012–2020) to the conveyor belt jets demonstrated that the CCBb jet, occurring when the direction of the CCB jet is aligned with the cyclone direction of travel, accounts for most DMWS events (46%), followed by the WCB (25%), and then the early part of the CCB, the CCBa (15%). The CCBb is found to play an even larger role in influencing the DMWS events exceeding the higher 25 $\mathrm{m\,s^{-1}}$ threshold (59%). In contrast, the role of the WCB is reduced, accounting just for 20% of these events, consistent with results found for cyclone feature association over land (Earl *et al.*, 2017). When considering separately the different regions of the North Atlantic ocean seas surrounding the British Isles, the CCBb is confirmed as the most dominant feature in all regions, but for the central and northern North Sea regions the CCBa replaces the WCB as the second most dominant jet. Cold sector (CCBa and CCBb) events are three to four times more likely than warm sector (WCB) events for both thresholds considered, and this can be explained by the British Isles being at the end of the North Atlantic storm track (Dacre and Gray, 2009). Because the WCB develops earlier than the CCB in the midlatitude cyclone lifecycle (see Fig. 1 in Hewson and Neu (2015)), by the time the cyclones reach the British Isles the warm sector has already been eroded. In fact, the central North Sea stations reported the smallest number of DMWS events associated with the WCB, with these stations being the farthest from the storm tracks reaching the British Isles.

The CCBb jet led to stronger winds at the surface and, during DMWS events, is associated with higher gusts than CCBa and WCB, probably because the CCBb boundary layer is buoyancy driven, as suggested by the deeper CCBb ERA5 boundary-layer heights than the CCBa and WCB jets. The cool air of the CCB, while hooking around the cyclone low pressure centre and flowing over warmer ocean water, forces large and positive heat fluxes, in addition to the large momentum fluxes associated with wind shear (Sinclair *et al.*, 2010). The resulting unstable and turbulent surface layer facilitates the downward mixing of high momentum air from the boundary layer top and produces stronger and gustier winds compared to the other jets (Coronel *et al.*, 2016). Instead, the warm air of the WCB, while flowing over the cooler ocean water, forces negative heat fluxes which enhance the static stability of the boundary layer, leading to a more shallow, shear-driven boundary layer, as suggested by the shallower boundary-layer heights than the CCBb events. Lastly, that the CCBa events are characterised by smaller gusts than WCB events despite being associated with larger surface wind speeds can be plausibly explained by the smaller magnitude of the (positive) surface heat fluxes than on the equatorward flank of the cyclone (where the CCBb occurs), given that in the CCBa (the early part of the CCB) the CCB cool air has not already mixed down to the surface layer.

Besides being associated with the largest number of extreme DMWSs events, the CCBb jet was also found to be responsible for the largest number of compound wind-wave hazards, followed by the CCBa and then WCB jets. Although the CCBa accounted for fewer events exceeding the 25 $\mathrm{m\,s^{-1}}$ threshold than the WCB, it led to more than twice the number of compound wind-wave hazards than the WCB, only $\approx 30\%$ less than for the CCBb. When restricting the analysis to the North Sea stations only, the southerly/south-easterly CCBa events were found to cause 24 compound wind-wave hazards, just 2 fewer than those caused by westerly/north-westerly CCBb events. This result extends previous findings of Bell *et al.* (2017) who also found that cyclone-associated southerly winds can create nearly as many large wave heights as north-westerly winds despite their limited fetch over the North Sea; However, unlike in this paper they did not perform an objective attribution to the conveyor belt jets.

The partitioning of the ERA5 biases showed that the ERA5 typically underestimated the observed extreme wind speeds, gusts and wave heights for all jets events. The extreme winds and gusts were most underestimated for the CCBb events, with median biases of $-4.5$ and $-5.5\ \mathrm{m\,s^{-1}}$, respectively. However, the largest underestimate of the wind-wave heights was associated with the CCBa events, with a median bias of $-2.88$ m. A plausible explanation could be that the generation of large wind-waves occurring when the wind has a short fetch (as for the CCBa jet events in the North Sea) is less well represented in ERA5 than when the fetch is longer (as for the CCBb jet events, associated with the smallest bias).

Overall, our results reveal that hazardous marine wind (both 10-m wind and gust) and compound wind-wave events near the British Isles are most commonly associated with the CCBb jet that occurs when the CCB hooks around the low-pressure cyclone centre into the southwest quadrant of a mature cyclone. However, the CCBa jet can be nearly as hazardous when considering compound wind-wave events, especially in the North Sea with 24 CCBa events over the nine-years analysed compared to 26 CCBb events. Hence, accurate simulation of these cyclone conveyor belt jets is critical for assessment of marine hazards in both weather forecasts and climate integrations.

It is worthwile to note, that, because the resolution of ERA5 ($\approx$ 30 km) is not capable to represent finer-scale ETC features associated with strong winds and gusts at the surface, in this work it was not possible to attribute extreme DMWSs to SJ, which require a horizontal resolution of at least $\approx 20\ km$, as discussed in Clark and Gray (2018). While waiting that the new generation reanalysis products are capable to obtain the required finer resolution, the SJ precursor tool developed by Martínez-Alvarado *et al.* (2012) could be used to determine the likelihood that some of the events attributed to the CCBb by the ad-hoc algorithm developed here are instead associated with the SJ. By combining the attribution algorithm with the SJ precursor tool, it would be possible to obtain both an estimate of the ERA5 bias associated with the SJ as well as a more accurate estimate of the ERA5 bias associated with the CCBb.

# Chapter 5

# The impact of atmosphere-ocean-wave coupling on the near-surface wind speed in forecasts of extratropical cyclones

This chapter has been published in *Journal of Boundary-Layer Meteorology* with the following reference:

**Gentile, E.S.**, Gray, S.L., Barlow, J.F., Lewis, H. W., and Edwards, J. M. The Impact of Atmosphere-Ocean-Wave Coupling on the Near-Surface Wind Speed in Forecasts of Extratropical Cyclones. *Boundary-Layer Meteorology* **180**, 105-129 (2021).
https://doi.org/10.1007/s10546-021-00614-4

Estimated contribution: 80%. ESG designed the study, developed the methodology, performed the analysis and wrote the manuscript with input and suggestions from SLG, JFB, HWL, and JME. All authors commented on the manuscript and discussed and interpreted the results at all stages. Three anonymous reviewers provided comments on an earlier version of the manuscript. ESG performed the 90% of the research, with guidance from supervisor SLG, HWL, JFB, and also JME, via meetings. In particular, the deterministic coupled system used in this research chapter was developed by the Met Office and without the Met Office support it would have not been possible to set up and run the coupled experiments.

## Abstract

Accurate modelling of air–sea surface exchanges is crucial for reliable extreme surface wind speed forecasts. While atmosphere-only weather forecast models represent ocean and wave effects through sea-state independent parametrizations, coupled multi-model systems capture sea-state dynamics by integrating feedbacks between the atmosphere, ocean and wave model components. Here, we investigate the sensitivity of extreme surface wind speeds to air–sea exchanges at the kilometre scale using coupled and uncoupled configurations of the Met Office's U.K. Regional Coupled Environmental Prediction system. The case period includes the passage of extra-tropical cyclones Helen, Ali, and Bronagh, which brought maximum gusts of 36 $\mathrm{m\,s^{-1}}$ over the U.K. Compared with the atmosphere-only results, coupling to the ocean decreases the domain-average sea surface temperature by up to 0.5 K. Inclusion of coupling to waves decreases the 98th percentile 10-m wind speed by up to 2 $\mathrm{m\,s^{-1}}$ as young, growing wind waves decrease the wind speed by increasing the sea-surface aerodynamic roughness. Impacts on gusts are more modest, with local reductions of up to 1 $\mathrm{m\,s^{-1}}$, due to enhanced boundary-layer turbulence which partially offsets air–sea momentum transfer. Using a new drag parametrization based on the Coupled Ocean–Atmosphere Response Experiment 4.0 parametrization, with a cap on the neutral drag coefficient and decrease for wind speeds exceeding 27 $\mathrm{m\,s^{-1}}$, the atmosphere-only model achieves equivalent impacts on 10-m wind speeds and gusts as from coupling to waves. Overall, the new drag parametrization achieves the same 20% improvement in forecast 10-m wind speed skill as coupling to waves, with the advantage of saving the computational cost of the ocean and wave models.

## 5.1 Introduction

Every year several extra-tropical cyclones (ETCs) hit the British Isles, bringing extreme surface wind speeds that cause widespread damage of varying harshness to lives and livelihoods (Browning and Roberts, 1994; Craig, 2003; Hewston and Dorling, 2011; Earl *et al.*, 2017). The severity of the resulting damage can be estimated using the storm index first introduced by Klawa and Ulbrich (2003), which is proportional to the cube of exceedances of the local

98th percentile of wind speeds. Evaluation of the applicability of this index demonstrates that even relatively small forecast errors of extreme surface wind speeds can have a large impact on the accurate prediction and assessment of the severity of ETCs (Hewston and Dorling, 2011; Earl and Dorling, 2013). Thus, skillful forecasts of extreme surface wind speeds associated with ETCs are critical to providing actionable information to first-line responders as a basis for preparedness to act (Ricchi *et al.*, 2017; Lewis *et al.*, 2018). The potential importance of air–sea interactions in moderating surface wind speed has led to widespread interest in the development of numerical weather prediction (NWP) systems capable of representing air–sea surface exchanges with high fidelity (Janssen, 2004; Lewis *et al.*, 2019). Here we use the Met Office's U.K. Regional Atmosphere–Ocean–Wave Coupled Environmental Prediction (UKC4) system to explore the sensitivity of extreme surface wind speeds and gusts to the physical mechanisms underpinning air–sea interactions.

Although the magnitude of the near-surface wind speeds and gusts are controlled at the synoptic scale by the baroclinicity, and associated large wind shear, which favours the formation of ETCs with strong horizontal pressure gradients, the strengths are moderated by local mesoscale and convective-scale processes. These processes include the convective-scale vertical momentum exchange between the cloud layer and boundary layer, and the turbulent vertical mixing of heat, moisture, and momentum flux that controls the effect of the boundary-layer structure on the magnitude of near-surface wind speeds (Schultz *et al.*, 2019). As turbulent eddies cannot be resolved by current NWP models, turbulent fluxes need to be parametrized (Lock *et al.*, 2013). The parametrized turbulent fluxes that control the magnitude of the near-surface wind speed can be very sensitive to the surface-layer parametrization used due to the steep gradients of momentum, heat, and moisture at the base of the marine atmospheric boundary layer (MABL) (Janssen, 2004; Ricchi *et al.*, 2017; Lewis *et al.*, 2019). Other boundary-layer processes such as moist convection and dry entrainment can dry the boundary layer, consequently increasing the evaporation rate of the ocean. While all these processes are important for the near-surface wind speed and gust magnitude, here we focus on air–sea momentum exchange and the way the sea surface temperature (SST) is communicated to the atmosphere model; the roles of moist convection and processes at the top of the boundary layer are not considered.

The exchange of turbulent momentum flux at the air–sea interface is the focal point of theoretical studies that reveal the importance of dynamically evolving ocean waves in controlling the magnitude of the near-surface wind speed (Charnock, 1955; Smith, 1988; Smith *et al.*, 1992; Janssen, 2004). Turbulent fluctuations of atmospheric pressure induce, over the sea surface, small regular waves (Phillips, 1957), which can continue to grow in height if forced by sufficiently high wind speeds (Miles, 1957). As the young waves grow, they extract momentum and energy from the overlying airflow, acting in the MABL as roughness elements, which reduce the near-surface wind speed (Janssen, 1989, 1991; Donelan, 1982; Jenkins *et al.*, 2012). However, the impact of ocean waves is not exclusively confined to the near-surface wind speed. Since ocean waves support turbulence generation, they are responsible for changing the amount of mixing within the MABL, which in turn modifies the air–sea turbulent fluxes (Donelan, 1982; Donelan *et al.*, 1993) and the vertical wind speed profiles across the MABL (Sullivan *et al.*, 2008). At wind–wave equilibrium, when the waves are no longer growing, the MABL profiles can be well approximated by Monin–Obukhov similarity theory (MOST) (Sullivan *et al.*, 2014). The theory accounts for the impact of waves and the deformation of the sea surface through surface exchange coefficients, including the neutral drag coefficient, whose parametrization requires no other knowledge of the sea state except that of the 10-m wind speed (Belcher and Hunt, 1993; Cook and Renfrew, 2014). By employing boundary-layer parametrizations based on MOST, atmosphere-only operational NWP models, including the Met Office's variable resolution model UKV (Tang *et al.*, 2013), can be run without evolving the ocean and wave state, reducing the complexity of the simulated physics and therefore reducing the computational cost.

Over the past 50 years, measurements of the drag coefficient over the sea have yielded reliable information for wind speeds less than 20 m s$^{-1}$. These measurements show that the neutral drag coefficient increases quasi-linearly with the wind speed, as predicted by MOST. However, large-eddy simulations have shown that MABL wind speed profiles at extreme wind speeds deviate from those predicted by MOST theory, demonstrating that drag cannot be assumed to always grow linearly with wind speed (Sullivan *et al.*, 2014). Laboratory experiments have shown that the drag coefficient saturates at 30 m $s^{-1}$, while for wind speeds higher than 30 m $s^{-1}$, observations over the ocean indicate a smooth decrease of the drag coefficient with wind speed (Powell *et al.*, 2003). Donelan (2018) reconciled these results distinguishing between two different turbulent flow regimes: a linear increase of drag coefficient for wind speeds in the range of 2.5–30 m $s^{-1}$ followed by a smooth decrease in the range of 30–50 m $s^{-1}$, with the latter regime explaining the explosive deepening of Atlantic hurricanes. As near-surface wind speeds associated with the ETCs can approach those of hurricanes, it follows that both the steepness in the linear-drag regime and the decrease in the saturated-drag regime can affect the skill of wind speed forecasts. Over the last decade, a number of coupled multi-model simulation systems have been developed to directly integrate the feedbacks between the ocean and wave single-component models and the atmosphere-only models. These systems have shown potential for more accurate predictions of severe weather events, such as extreme surface wind speeds (Katsafados *et al.*, 2016; Lewis *et al.*, 2018). For example Wahle *et al.* (2017) simulated a historical series of winter storms that hit the southern North Sea, demonstrating that coupling the Wave Model WAM (Komen *et al.*, 1994), run at 5-km grid spacing, with the COnsortium for Small-scale MOdelling COSMO (Rockel *et al.*, 2008), run at 10-km grid spacing, reduced wave heights and wind speeds by up to 8% and 3%, respectively, with associated improvements in the forecast skill of the wind speed and wave height. Comparable reductions in wind speeds and wave heights were documented by Varlas *et al.* (2017) for a cyclonic event over the Mediterranean simulated using a two-way coupled system of the Weather Research and Forecasting atmosphere (Skamarock and Klemp, 2008) and WAM wave models, both run at 10-km grid spacing; the associated improvements in the forecast skill for wave height and wind speed were 20% and 5%, respectively.

Ricchi *et al.* (2017) performed a case study of a tropical-like cyclone in the Mediterranean sea, confirming that coupling improved the skill of extreme surface wind speed forecasts compared with atmosphere-only simulations, but also finding that the atmosphere-only simulations with a suitable boundary-layer parametrization achieve improvements equivalent to those of coupling. In particular, they found that the sensitivity of the heat and momentum flux to parametrizations of surface roughness is greater than the sensitivity to air–sea coupling. The latter result highlights the need to consider the physical assumptions of coupling in NWP systems as well as the parametrizations embedded within the atmosphere-only model.

In this context, the Met Office has developed a kilometre-scale-resolution coupled-modelling system, UKC4, (Lewis *et al.*, 2018) for a domain focused on the U.K. and north-west shelf region. The UKC4 system enables assessment of the kilometre-scale sensitivity of rapidly varying meteorological fields, such as near-surface wind speeds, to the air–sea surface exchanges represented by atmosphere–ocean–wave coupling (Lewis *et al.*, 2018, 2019).

The aim here is to quantify, in a case study, the sensitivity of extreme surface wind speeds to different coupled configurations and drag parametrizations using the UKC4 modelling system as a tool. The period 17–20 September 2018 provides a paradigmatic case study because it includes three intense ETCs that brought severe weather over the U.K., with maximum recorded gusts of 36 m $s^{-1}$. Four different configurations of the UKC4 system were used: two atmosphere-only configurations, one provided with the operational UKV drag parametrization and the other one with the Coupled Ocean–Atmosphere Response Experiment COARE 4.0 drag parametrization with the drag coefficient capped for wind speeds exceeding 27 $\mathrm{m\,s^{-1}}$ (Donelan, 2018) and then decreases for wind speeds exceeding 33 $\mathrm{m\,s^{-1}}$ (Hsu *et al.*, 2017); a partially-coupled atmosphere–ocean configuration; and a fully-coupled atmosphere–ocean–wave configuration.

Below, in Sect. 5.2, the UKC4 regional coupled modelling system and the coupled and uncoupled configurations are described. In Sect. 5.3, the impacts of atmosphere–ocean and atmosphere–ocean–wave coupling are compared to the two different drag parametrizations employed by the atmosphere-only configurations and the resulting changes in the boundary-layer profiles and vertical structure of the storms are discussed. The forecast skill of the simulations are then evaluated by comparison to in situ observations, with conclusions given in Sect. 5.4.

## 5.2 Methodology

The UKC4 system is a regional coupled multi-model NWP system (Lewis *et al.*, 2018), which incorporates models of the atmosphere [Met Office Unified Model MetUM (Walters *et al.*, 2017)], land-surface [the Joint U.K. Land Environment Simulator JULES (Best *et al.*, 2011)], shelf-sea ocean [the Nucleus for European Modelling of the Ocean NEMO (Madec, 2016)] and ocean surface waves [the WAVEWATCH III$^{\text{\textcopyright}}$ (Tolman, 2016)]. A feature of the system is the ability to set up different levels of coupling by connecting or excluding model components. The UKC4 domain is represented in Fig. 5.1.

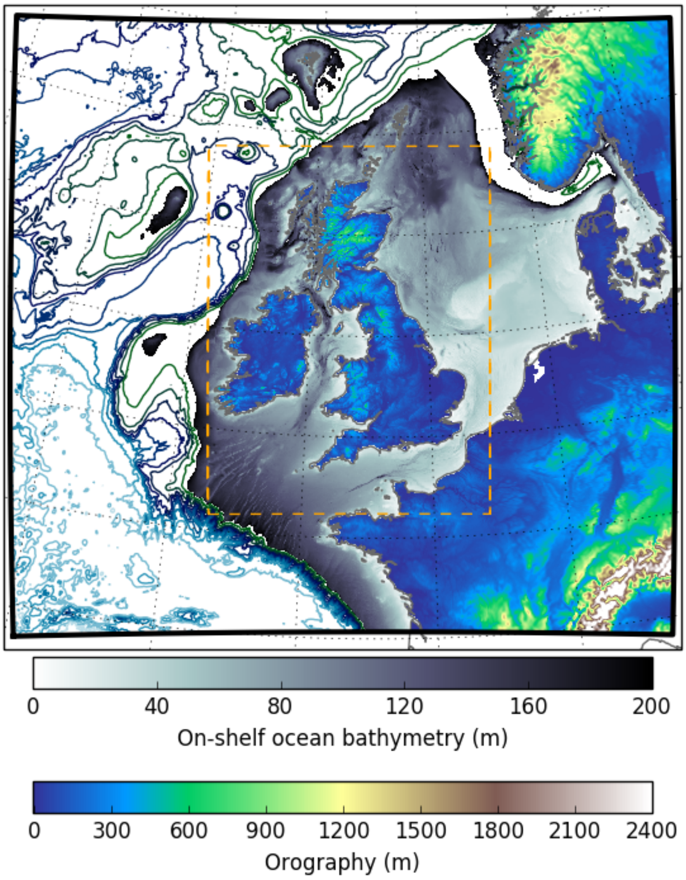

**Figure 5.1:** The UKC4 domain (black boundary) used to define the atmosphere, ocean, and wave model components. The model orography and bathymetry are also shown. The upper colourbar relates to on-shelf bathymetry (depths < 200 m), while contour lines are plotted in the open ocean every 500 m depth. The lower colourbar relates to the orography over land (heights < 2400 m). The orange dashed box shows the approximate extent of the regular 1.5 km × 1.5 km inner region of the atmospheric component grid.

### 5.2.1 Model components

A brief description of the UKC4 model components is now given.

**Atmosphere component:** based on the UKV configuration of the MetUM (Tang *et al.*, 2013), this employs a variable resolution with 1.5 km × 1.5 km horizontal grid cells in the inner region increasing to 1.5 km × 4 km in the outer region and 4 km × 4 km in the corners of the domain (950 × 1025 grid cells). The atmospheric model domain is nested within the global model. The model uses a hybrid height vertical coordinate system with 70 vertical levels and a lid at 40 km. The SST lower boundary condition is provided by the Operational Sea Surface Temperature and Sea Ice Analysis [OSTIA (Donlon *et al.*, 2012)], and persisted for the entire duration of a simulation. Surface ocean currents are initialized to zero so that the lower boundary is at rest. The effect of roughness from surface waves is specified setting the Charnock parameter to the constant operational UKV value of $\alpha = 0.011$ across the whole domain.

**Land component:** based on the JULES land-surface model, this component provides the exchanges of momentum, heat, and water between the land-surface and the atmospheric boundary layer, and it shares the grid with the atmosphere component grid.

**Ocean Component:** based on the mesoscale eddy-resolving coastal ocean model [regional version of NEMO (Tonani *et al.*, 2019)] this employs 1.5 km × 1.5 km horizontal grid cells throughout the domain (1458 × 1345 grid cells). The vertical domain is discretized into 51 vertical levels. The ocean model is initialized from the operational ocean model [the Atlantic Margin Model AMM15 (Graham *et al.*, 2018)].

**Wave component:** based on the WAVEWATCH III third-generation spectral-wave model, this shares its model grid with the ocean model. The spectral boundary conditions are provided by the archived operational global wave model output.

### 5.2.2 Basis of the coupling parametrizations

A brief description of the coupling parametrizations used by the UKC4 system follows. These are consistent with those employed in the previous model version, UKC3, and a full discussion of those can be found in Lewis *et al.* (2018, 2019).

The UKC4 system parametrizes momentum, heat, and moisture air–sea turbulent fluxes by assuming that MOST holds in the surface layer. Therefore, in the surface layer, the dependence of wind speed, $U$, on height, $z$, is parametrized by the log-law:

$$U = \frac{u_*}{k}\left[\log\left(\frac{z}{z_0}\right) - \Psi_m\right], \tag{5.1}$$

where $u_*$ is the friction velocity, $z_0$ the momentum roughness length, $\Psi_m$ is the Monin–Obukhov stability function for momentum, and $k = 0.4$ is the von Kármán constant. In the UKC4 approach, Eq. 5.1 is used to compute the 10-m wind speed, $U_{10}$, which, together with the standard deviation of their distribution, $\sigma_u$, is used to parametrize the gust strength $U_{gust}$ following Panofsky *et al.* (1977) as:

$$U_{gust} = U_{10} + \sigma_u \frac{1}{k}\log\left(\frac{5e^{kc_{ugn}} + z_{0(eff)}}{5 + z_{0(eff)}}\right), \tag{5.2}$$

where $z_{0(eff)}$ is the effective roughness length, and $c_{ugn} = 4$ is a dimensionless number determined from the universal turbulence spectra (Beljaars, 1987). The standard deviation is computed following:

$$\sigma_u = \begin{cases} 2.29u_*\left(1 - \frac{z_{blh}}{24L}\right)^{\frac{1}{3}} & L < 0 \\ 2.29u_* & L > 0, \end{cases}$$

which depends on three different boundary-layer characteristics: the friction velocity $u_*$, the boundary-layer height $z_{blh}$, and the Obukhov length $L$.

Over the sea, the momentum roughness length, $z_0$, depends on both the atmospheric surface layer flow and the underlying surface wave state, as described by the generalized Charnock formula:

$$z_0(\text{sea}) = \frac{0.11\nu}{u_*} + \frac{\alpha}{g}u_*^2, \tag{5.3}$$

where $\nu = 14 \times 10^{-6}\ \text{m}^2\ \text{s}^{-1}$ is the kinematic viscosity of air, and $\alpha$ is the Charnock parameter (Charnock, 1955; Smith, 1988).

In the UKC4 uncoupled atmosphere-only mode, $z_0$ is computed using the empirical constant $\alpha = 0.011$ for the Charnock coefficient. When the atmosphere model is coupled to the wave model, the latter calculates a spatially varying Charnock parameter field and exchanges it hourly with the atmosphere component. The transfer coefficient for the momentum flux, $C_D$, also termed drag coefficient, is parametrized at the ocean surface as a function of atmospheric stability and momentum roughness length $z_0$ by:

$$C_D = \left[\frac{k}{\log\left(\frac{z}{z_0}\right) - \Psi_m}\right]^2, \tag{5.4}$$

and it is used to calculate the friction velocity, $u_*$, as $u_* = \sqrt{C_D}U_{10}$, which, together with the value of the momentum roughness length $z_0$, determines the wind speed in Eq. 5.1. Since latent heat fluxes are dominant over the sea, the UKC4 approach takes the roughness length for scalar fluxes $z_{0h}(\text{sea})$ as the roughness length for moisture flux, $z_{0q}$, and computes it by parametrizing the momentum roughness length, $z_0$, according to the surface-divergence theory from Csanady (2001), as explained by Edwards (2007):

$$z_{0h}(\text{sea}) = \max\left(7 \times 10^{-8}, \frac{2.56 \times 10^{-9}}{z_0}\right). \tag{5.5}$$

To represent aerodynamically smooth conditions that occur for low wind speeds, $z_{0h}(\text{sea})$ is computed as $z_{0h}(\text{sea}) = \max\left(\tilde{z}_{0h}(\text{sea}), 2.52 \times 10^{-10}/u_*\right)$ where $\tilde{z}_{0h}(\text{sea})$ is calculated according to Eq. 5.5. Then, over the ocean, the scalar transfer coefficient, $C_h$, can be expressed as a function of atmospheric stability, momentum roughness length $z_0$, and scalar roughness length $z_{0h}$ as:

$$C_h = \frac{k^2}{\left[\log\left(\frac{z}{z_0}\right) - \Psi_m\right]\left[\log\left(\frac{z}{z_{0h}}\right) - \Psi_h\right]}. \tag{5.6}$$

Therefore, the air–sea turbulent momentum flux, $\tau_0$, sensible heat flux, $H_0$, and latent heat flux, $E_0$, are parametrized according to:

$$\frac{\tau_0}{\rho_0} = C_{\mathrm{D}} |\Delta \mathbf{v}|^2,$$

$$\frac{H_0}{c_p \rho_0} = -C_h U \left( \Delta T + \frac{g}{c_p} (z_1 + z_0 - z_{0h}) \right),$$

and:

$$\frac{E_0}{\rho_0} = -C_h U \Delta q,$$

where $\rho_0$ is the air surface density, $c_p$ is the specific heat capacity at constant pressure, $z_1$ is the height of the bottom model layer above the surface, and $\Delta \mathbf{v}$, $\Delta T$, and $\Delta q$ are the gradients between the surface and bottom model level of the velocity vector $\mathbf{v}$, temperature $T$, and specific humidity $q$ fields, respectively. In particular, the surface specific humidity is 98% of its saturation value at SST due to salinity.

### 5.2.3 Experimental configurations

Four different configurations of the UKC4 system were set up (whose characteristics are summarized in Table 5.1): two atmosphere-only configurations which use different parametrizations of the neutral drag coefficient (hereafter Adrag1 and Adrag2); a partially-coupled atmosphere–ocean configuration (hereafter A–O); and a fully-coupled atmosphere–ocean–wave configuration (hereafter A–O–W). The JULES land-surface model is coupled to the MetUM atmosphere model in all configurations.

The two atmosphere-only configurations (Adrag1 and Adrag2) use the MetUM only. The Adrag1 configuration, referred to as UKA4g in Lewis *et al.* (2018, 2019), uses the regional UKV drag parametrization: $z_0$ in Eq. 5.4 is computed at each grid cell using a constant Charnock parameter $\alpha = 0.011$, which is independent of the wind speed. As illustrated in Fig. 5.2a, the Adrag1 parametrization uses an approximately linear growth of the neutral drag coefficient, $C_D$, for 10-m wind speeds greater than $\approx 5$ m s$^{-1}$. The Adrag2 configuration uses a new drag parametrization which combines the COARE 4.0 parametrization at lower

| Name | Components | Mode | Description | Node hours |
|---|---|---|---|---|
| Adrag1 | Atmosphere only | Uncoupled | Global OSTIA, SST boundary condition persisted and UKV regional drag parametrization | 32 |
| Adrag2 | Atmosphere only | Uncoupled | Global OSTIA, SST boundary condition persisted and new drag formulation based on the COARE 4.0 drag parametrization with the Donelan (2018) cap and reduction at high wind speeds | 32 |
| A–O | Atmosphere–Ocean | Partially coupled | Atmosphere-ocean coupling, no wave interactions | 35 |
| A–O–W | Atmosphere–Ocean–Wave | Fully coupled | Atmosphere-ocean-wave, fully coupled | 43 |

**Table 5.1:** Summary of the four configurations of the UKC4 multi-model system. For each configuration name, the model components involved, the coupling mode, the description of some of the key features, and the computational cost in node hours per forecast simulation day are given. All configurations were run on the Met Office and NERC joint supercomputer system (MONSooN)

wind speeds with the Donelan (2018) cap and reduction of the value of the drag coefficient at higher wind speeds. In contrast to the UKV drag parametrization, the COARE 4.0 scheme, based on many in situ observations, models a linear growth of the Charnock parameter $\alpha$ with wind speeds, capped at 22 m s$^{-1}$, which effectively models an empirical weak dependence of the parameter $\alpha$ on the wave age. In particular, Fig. 5.2a shows that the neutral drag coefficient, $C_D$, modelled by the Adrag2 configuration increases steeply for wind speeds from 2.57–27 m s$^{-1}$, before plateauing at $\approx 3 \times 10^{-3}$ for wind speeds from 27–33 m s$^{-1}$, before declining and flattening out at $\approx 2 \times 10^{-3}$ for wind speeds more than 55 m s$^{-1}$. The plateau value was tuned from the recommended Donelan (2018) value of $C_D \approx 1.3 \times 10^{-3}$ to $C_D \approx 2 \times 10^{-3}$, consistent with findings from Hsu *et al.* (2017) and still within the error bars of the Donelan (2018) drag coefficient. Note that the variation of the drag coefficient

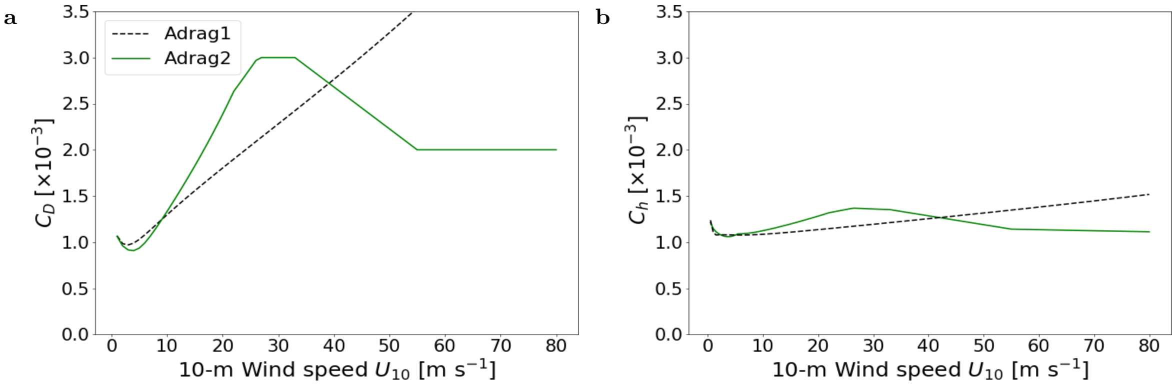

**Figure 5.2:** The Adrag1 (black) and Adrag2 (green) parametrizations of the (a) neutral drag coefficient and (b) transfer coefficient for scalar flux (moisture) in neutral conditions as a function of the 10-m wind speed, $U_{10}$. (a) The dashed black line represents the operational UKV drag parametrization employed in the Adrag1 configuration, while the solid green line represents the COARE 4.0 parametrization with the Donelan (2018) cap at $C_D = 3.0 \times 10^{-3}$ and decrease on drag values at high wind speeds to $C_h = 2.0 \times 10^{-3}$ employed in the Adrag2 configuration. (b) The dashed black line represents the operational UKV moisture-flux parametrization employed in the Adrag1 configuration, while the solid green line represents the COARE 4.0 moisture parametrization with a cap at $C_h = 1.4 \times 10^{-3}$ and then a decrease to $C_h = 1.1$ employed in Adrag2. The approximately linear trend in Adrag1 drag and scalar-flux parametrization continues indefinitely above $C_D = 3.5 \times 10^{-3}$ and $C_h = 1.6 \times 10^{-3}$ though not shown.

$C_D$ with wind speeds exceeding 31 m s$^{-1}$ is not relevant for this case study. For consistency, the Adrag2 configuration uses, over the ocean, a scalar (moisture) transfer coefficient based on the COARE4.0 parametrization and then a cap and decrease for wind speeds greater than 27 m s$^{-1}$. As can be noted from Fig. 5.2b, the Adrag2 $C_h$ parametrization is relatively close to that of Adrag1 until 45 m s$^{-1}$, and thus likely to lead to negligible impacts on ocean heat and moisture fluxes for the range of wind speeds simulated in this case study.

The partially coupled A–O configuration has two-way coupling of the MetUM and NEMO models at hourly frequency. The SST and the surface ocean currents are sent by NEMO to the MetUM, which uses the SST and ocean currents data as boundary conditions and in turn sends the scalar and momentum surface fluxes, pressure and velocity fields to the NEMO model. The A–O configuration uses the same regional UKV drag parametrization used by the Adrag1 configuration. Finally, the fully coupled A–O–W configuration includes coupling to waves in addition to coupling to ocean by implementing two-way coupling between the MetUM, NEMO, and WAVEWATCH III models. The MetUM sends the velocity field to both

NEMO and WAVEWATCH III, with the latter providing the MetUM a spatially and temporally varying, wave-dependent Charnock parameter $\alpha$ used by the atmosphere component in Eq. 5.3 to update the aerodynamic surface-roughness estimate. All the simulations were initialized at 0000 UTC 16 September 2018 and run until the 0000 UTC 21 September 2018. However, the analysis of meteorological fields of interest started from 0000 UTC on 17 September 2018.

### 5.2.4 Evaluation of model forecast skill

To assess the forecast skill of the UKC4 experiments, outputs of different model configurations were compared to a variety of in situ observations sourced from the Met Office's meteorological database, accessed from the U.K. Centre for Environmental Data Analysis. The Met Office meteorological database includes land observations, collected by automatic weather stations managed by the national weather services operating across Europe, and ocean observations, provided by offshore oil installations, drifting buoys, moored buoys, and ships. Three different meteorological fields were considered: mean 10-m wind speed, 10-m gust, and SST. Mean 10-m wind speed is measured at 10-m height and obtained by averaging the wind fluctuations (sampled every 0.25 s due to their turbulent nature) over the ten-minute period leading up to the hourly reporting time. The 10-m gust is the maximum three-second average wind speed recorded over the ten-minute period at 10-m height.

Some issues were addressed to effectively use the large amount of data available. First, SST data taken by ships and fed into the MetDB database were incomplete due to being transmitted from changing locations along ship tracks. Thus, only sites that recorded the SST data for at least 75% of the case-study duration, such as oil platforms and stationary ships, were considered for comparison to simulated results, following Lewis *et al.* (2018). Second, similarly to the SST observations, the gust observations collected over the sea were intermittent and therefore the same rejection threshold of the SST datasets was applied. In contrast, due to the much greater availability of temporally complete 10-m wind series from observation sites, only those data were selected as this provided a sufficient number of different observation locations.

The relative forecast skill between two model configurations is quantified by calculating the relative root-mean-square error ($RMSE_{rel}$) over the four-day duration of the case study, defined as:

$$\begin{aligned} RMSE_{rel} &= \frac{RMSE_{\mathrm{X}} - RMSE_{\mathrm{Y}}}{RMSE_{\mathrm{Y}}} \\ &= \left( \sqrt{\frac{\Sigma(O-X)^2}{n}} \Big/ \sqrt{\frac{\Sigma(O-\mathrm{Y})^2}{n}} \right) - 1, \end{aligned}$$

where $O$ are the in situ observations used for comparison, $n$ is the number of in situ observations, and $X$ and $Y$ are the model outputs at the observation locations from two different configurations of the UKC4 system.

## 5.3 Results and discussion

Below, Sect. 5.3.1 provides a description of the extreme weather conditions affecting the U.K. from 17–20 September 2018 along with the numerical bias of the atmosphere-only Adrag1 configuration. The following subsections analyze and compare the impacts of the Adrag1, Adrag2, and coupled configurations on the SST, 10-m wind speeds, and gusts for the surface fields, boundary-layer structure, and forecast biases.

### 5.3.1 Synoptic overview of case study and Adrag1 atmosphere-only simulation biases

The sensitivity of extreme surface wind speeds to air–sea surface exchanges is investigated in the extreme weather conditions brought by Helene, Ali, and Bronagh as they crossed the U.K. from 17–20 September 2018. Helene transitioned from a hurricane to an ETC on 17 September 2018 (Fig. 5.3a), accompanied by increasing pressure gradients with fronts forming, and then approached and made landfall on Ireland, and subsequently on the U.K., on 18 September 2018 (Fig. 5.3b).

On 19 September 2018 (Fig. 5.3c), while Helene decayed after crossing the North Sea, the track of Ali crossed Ireland and the U.K. prior to Ali's intensification over the North Sea. On the last day of the case study (Fig. 5.3d), while Ali crossed Norway, Bronagh approached

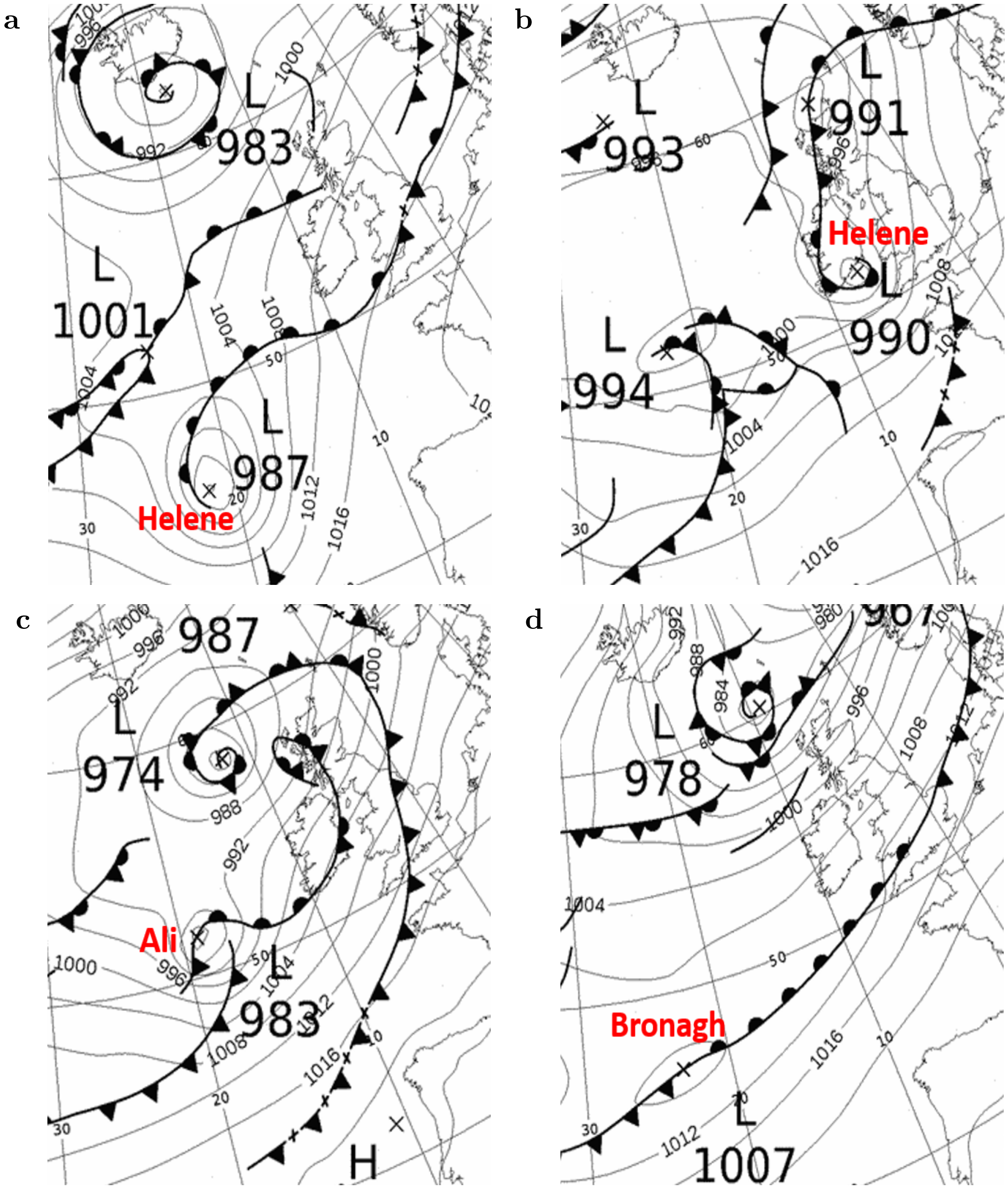

**Figure 5.3:** Surface mean sea level pressure 0000 UTC analysis maps (hPa) for (a) 17, (b) 18, (c) 19, and (d) 20 September 2018. The maps are derived from Met Office's surface analyses archive, ©Crown Copyright.

the U.K. Of the three ETCs, Ali had the lowest central mean sea level pressure of 969 hPa over the North Sea at 1800 UTC 19 September (not shown), with maximum gusts peaking at 36 m $s^{-1}$ over the North of the U.K. (MetOffice, 2018).

As the most severe weather conditions occurred between 0000 UTC 19 September 2018 and 0000 UTC 20 September 2018, this time period was chosen to explore the bias of the uncoupled atmosphere-only Adrag1 simulation under extreme wind speeds. Observed 10-m wind speeds, 10-m gusts and SSTs are overlaid on the corresponding Adrag1 simulations in Fig. 5.4a, c, e and this reveals that the Adrag1 configuration overestimates all three fields at most of the observation sites. For example, over the North Sea, 10-m wind speeds are overestimated by up to 5 m s$^{-1}$ while SST values are overestimated by up to 1.5 K. The biases for 10-m wind speed, gust, and SST fields depicted in Fig. 5.4b, d, f are consistent with Lewis *et al.* (2019), who reported results over a longer time period relative to a month-long autumn

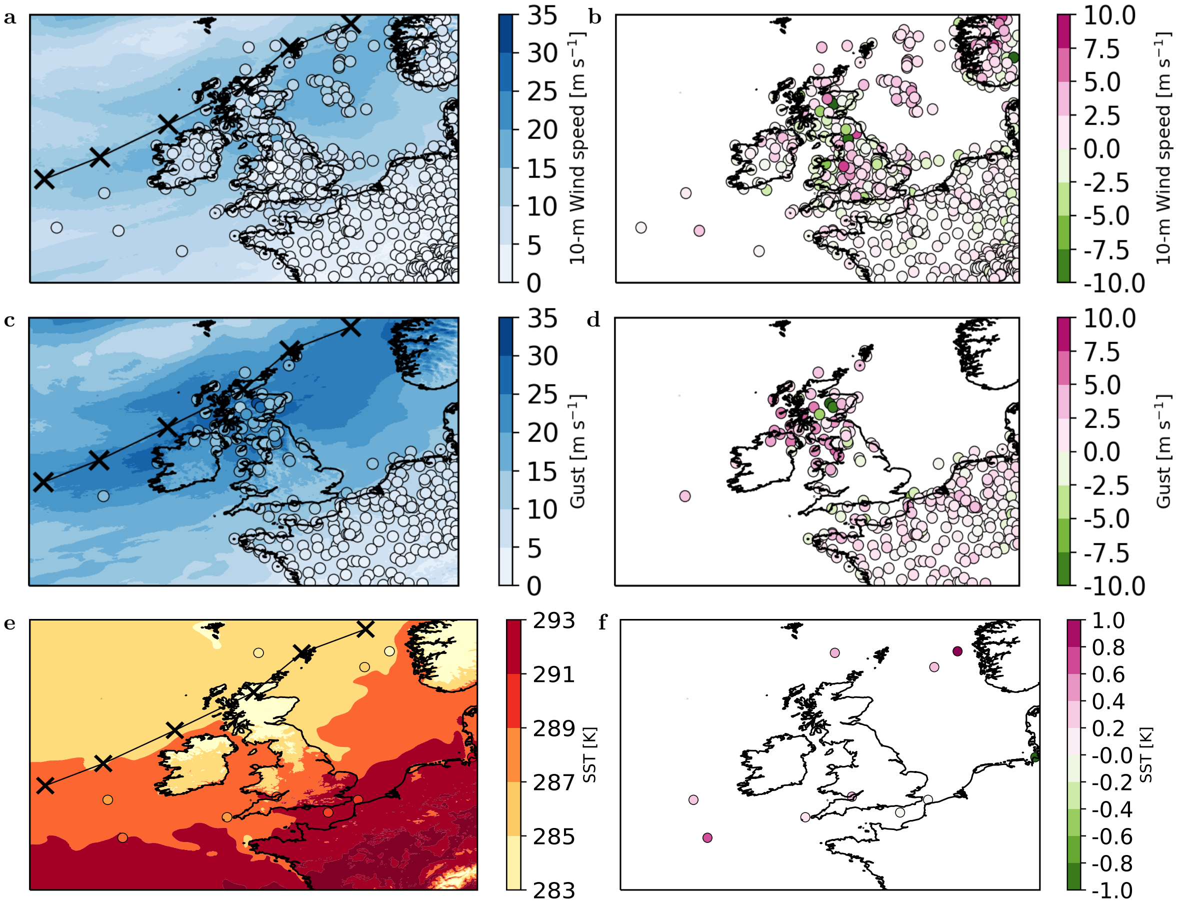

**Figure 5.4:** (a, b) Maps of (a) coloured circles showing observed mean 10-m surface wind speed (581 stations) overlaying the corresponding field from the atmosphere-only Adrag1 simulation, and (b) coloured circles showing the simulated minus observed difference in mean 10-m wind speed. (c, d) and (e, f) are the same as (a, b) but for gusts (255 stations) and SST (10 stations), respectively. The panels show averages of hourly data from 0000–2300 UTC 19 September 2018. The black line joining the crosses in each of the left-column panels represents the track of Ali, diagnosed from the Adrag1 run, with the crosses indicating the position of the mean sea-level-pressure minimum every 4 h, starting at 0000 UTC 19 September 2018. Ali is tracked until it exits the model domain.

case study. The size of the bias across the domain suggests that the atmosphere-only Adrag1 forecast may not provide a satisfactory representation of the air–sea interactions at high wind speeds.

### 5.3.2 Impact of coupling and using a new drag parametrization on 10-m wind speed and sea surface temperature

For comparisons of the simulation results to be meaningful (given the limited domain and time period), the tracks and structures of the ETCs that occurred during the case study must not diverge strongly. The tracks and structures must also compare reasonably well with analyses for a sensible discussion of forecast bias and skill. Comparison of all the four UKC4 simulations at 1800 UTC 19 September, when Ali crossed the North Sea and the wind speeds were highest, revealed reassuringly small differences (not shown). The low-pressure centres of Ali in the fully coupled atmosphere–ocean–wave A–O–W and uncoupled atmosphere-only Adrag2 simulations were both shifted by approximately 20 km eastward compared with the position of the low-pressure centre in the partially coupled atmosphere–ocean A–O and uncoupled atmosphere-only Adrag1 simulation. The intensity of Ali was slightly reduced in these simulations with an increase of the mean sea-level-pressure minimum from $\approx$ 966.2 hPa (Adrag1 and A–O) to $\approx$ 967.7 hPa (A–O–W and Adrag2). A less pronounced pressure minimum is also systematically observed across the case study simulation days, with the maximum difference being up to 2 hPa. This behaviour in the A–O–W and Adrag2 configurations is attributed to the enhanced momentum-transfer coefficients (as discussed in Sect. 5.3.3) leading to more frictional drag at the air–sea interface and so enhanced Ekman pumping. Lionello *et al.* (1998), Doyle (2002), and Varlas *et al.* (2017) reported similar pressure reductions in cyclones when using wave coupling in simulations.

To focus on the low-level-jet regions in the ETCs, where air–sea interactions are strongest, we consider the 98th percentile 10-m wind speed and gust. Figure 5.5 shows time series of sea-only 98th percentile 10-m wind speeds, 98th percentile gusts, and mean SSTs for the different simulations averaged across the UKC4 domain. The 10-m wind speeds and gusts follow a similar pattern in all the UKC4 model configurations used here, peaking at the same time on 19 September 2018 when storm Ali brought extreme weather conditions over the U.K. (Fig. 5.5a, b).

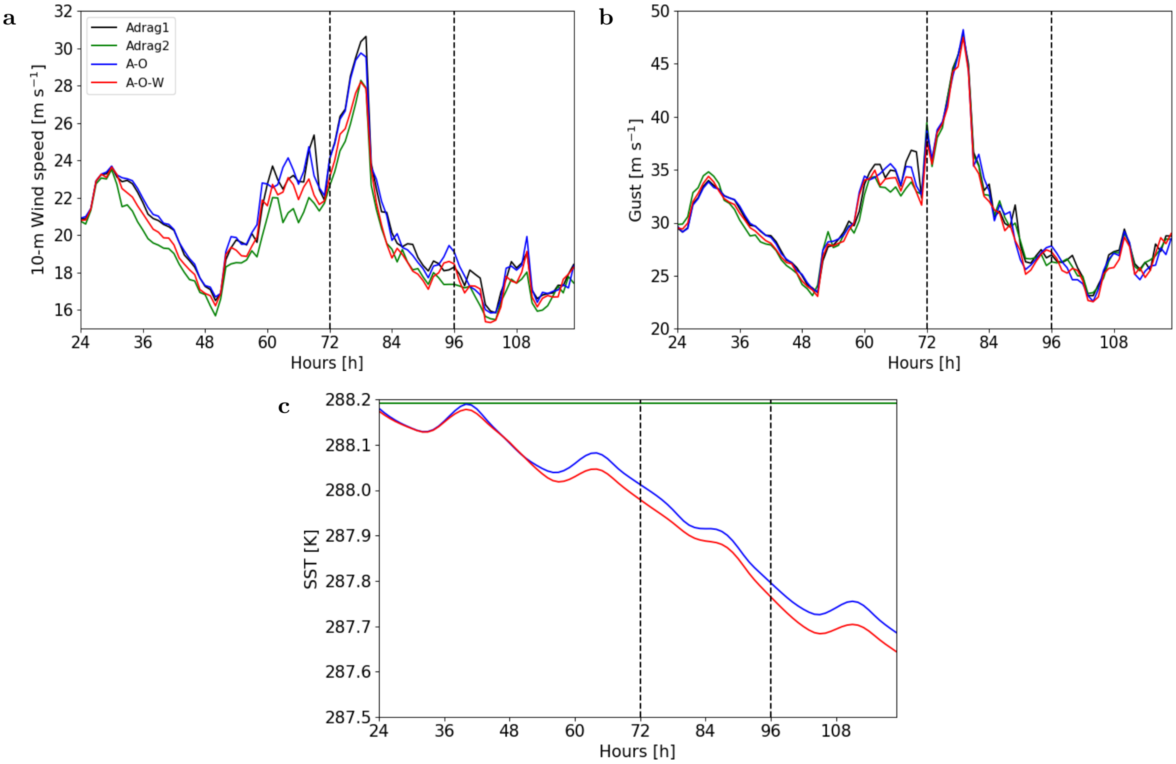

**Figure 5.5:** Time series for 17–20 September 2018 of (a) 98th percentile 10-m wind speeds, (b) 98th percentile gusts, and (c) mean SST for the Adrag1 (black), Adrag2 (green), A–O (blue), and A–O–W (red) configurations and sea-only grid points. Adrag2 and Adrag1 SST values are identical and thus overlap in (c). Vertical dashed lines at +72 h and +96 h indicate the start and end of 19 September.

As the magnitudes of the 98th percentile 10-m wind speeds increase over time, the partially coupled A–O simulation closely follows the atmosphere-only Adrag1 simulation, with the wind speeds peaking at 30.3 and 30.6 m s$^{-1}$, respectively, at 0600 UTC on 19 September 2018 (see Fig. 5.5a). The 98th percentile of the A–O–W and Adrag2 10-m wind speeds are consistently lower than those simulated by Adrag1 and A–O with maximum differences of up to 2 m s$^{-1}$ at peak time. Prior works of Wahle *et al.* (2017) and Lewis *et al.* (2019) documented a similar reduction of the 10-m wind speed, attributing it to the impact of atmosphere–ocean–wave coupling. However, the close correspondence between Adrag2 and A–O–W results in Fig. 5.5a suggests that Helene, Ali, and Bronagh extreme surface wind speeds are equally sensitive to the Adrag2 new drag parametrization and to coupling to waves. In comparison, Fig. 5.5b shows that there is much less sensitivity of simulated gust values to the change in drag parametrization, and coupling to ocean and waves: Adrag1 and A–O peak gusts reach 47.7 m $s^{-1}$ and A–O–W and Adrag2 reach 47.2 m $s^{-1}$ at 0600 UTC on 19 September 2018. Compared to the A–O results, the slight reduction of 0.5 m $s^{-1}$ in 98th percentile of the A–O–W and Adrag2 simulated gusts could be accounted for by the reduction of 10-m wind speed upon coupling to waves and change in the drag parametrization.

The SSTs in the A–O and A–O–W simulations generally decrease with time by more than 0.5 K over the five days (Fig. 5.5c). This reduction contrasts with the constant SSTs in the two atmosphere-only configurations. The near overlap of the SSTs produced by the A–O and A–O–W simulations reveals that, in this case, SST changes are primarily a consequence of the ocean coupling rather than the additional wave coupling, as also found by Lewis *et al.* (2018). Since the ocean is slightly stably stratified after surface heating through the summer, the oceanic mixing modelled by the ocean component implies surface cooling, consistent with earlier remarks.

To distinguish the impacts of coupling to the ocean from that of coupling to waves, we first compared the mean 10-m wind speed, gust, and SST differences between the A–O and Adrag1 approaches to isolate the impact of ocean feedbacks, and then between the A–O–W and A–O to isolate the impact of waves feedbacks. The left column in Fig. 5.6 shows maps of the differences between the A–O and Adrag1 simulations, while the right column shows differences between A–O–W and A–O simulations, all averaged over the day when the strongest ETC, Ali, crossed the U.K. The largest magnitude for the 10-m wind-speed differences between the A–O and Adrag1 simulations are found to the north of Ali's track, possibly associated with slightly different positioning of the bent-back front (i.e. different frontal structure) in the two simulations (Fig. 5.6a). However, the overall lack of coherency of the wind-speed differences is consistent with the negligible impact of ocean coupling seen in the domain-average time series (Fig. 5.5a). In contrast, compared with the 10-m wind speed in the partially coupled A–O simulation, the fully coupled A–O–W 10-m wind speeds are consistently decreased, by up to 2 m s$^{-1}$, in the high-wind-speed region extending south of the track of Ali (Fig. 5.6b). Also, gusts are generally decreased by coupling to both the ocean and additionally to waves south of Ali's track (Fig. 5.6c, d), particularly in the North Sea, although only by up to 1 m s$^{-1}$. Figure 5.6e, f, consistent with the results shown in Fig. 5.5c, indicates that the dominant impact of coupling on SSTs is the result of coupling to the ocean component with reductions across most of the ocean regions peaking at ≈2.2 K. The additional impact of coupling to the wave component is smaller and localized with a 0.5-K increase in the Dogger Bank region, characterized by shallow bathymetry, and a 0.5-K decrease near the southern boundary of the model domain (see Fig. 5.6f).

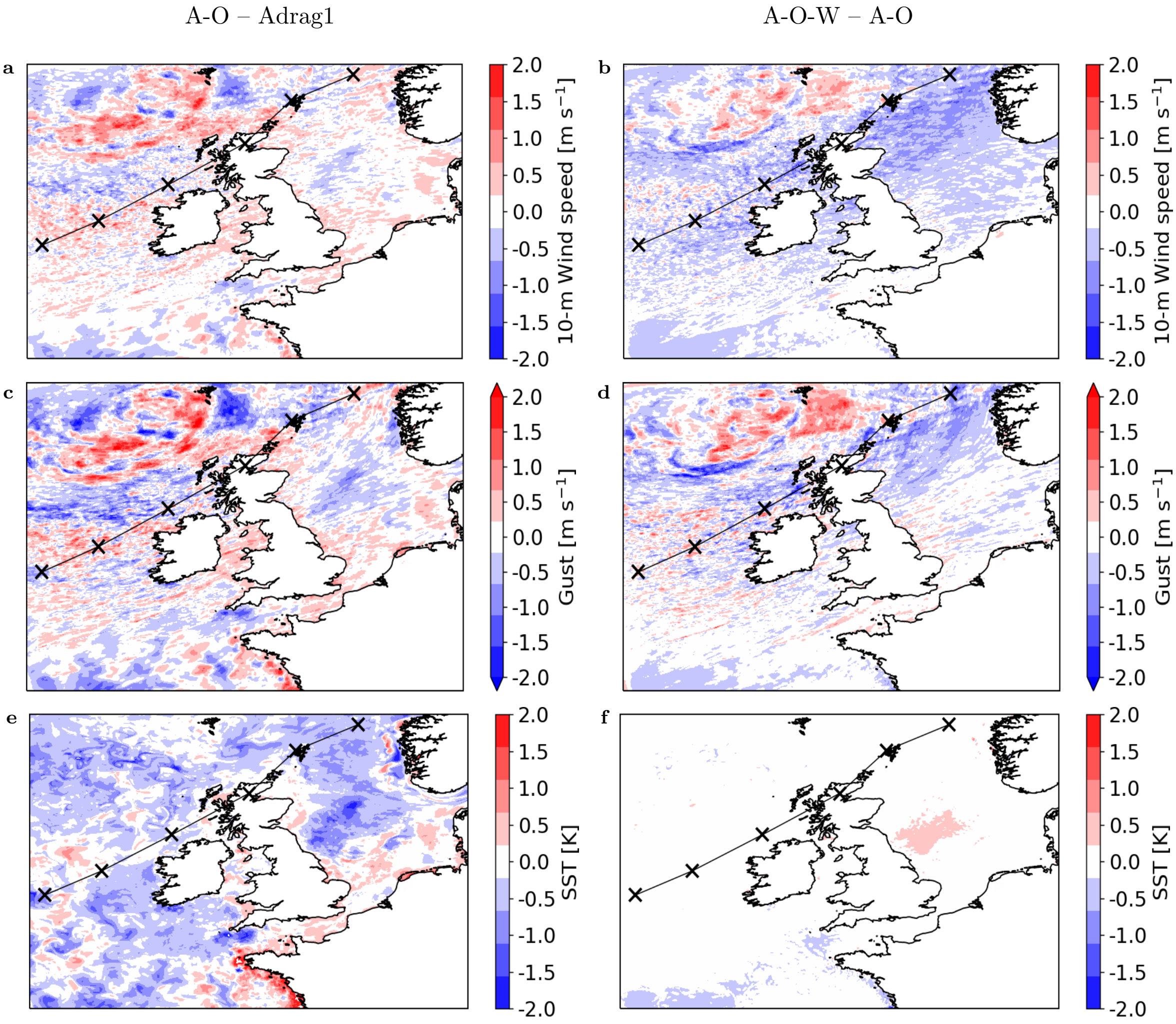

**Figure 5.6:** Maps of differences between A–O and Adrag1 simulated (a) 10-m wind speeds, (c) gusts, and (e) SSTs, and differences between A–O–W and A–O simulated (b) 10-m wind speeds, (d) gusts, and (f) SSTs over the whole model domain (masking land) averaged over 19 September 2018. The track of Ali is marked in each panel as in Fig. 5.3.

### 5.3.3 Impact of coupling and using a new drag scheme on boundary-layer characteristics

The impact of coupling and using the new drag scheme Adrag2 on boundary-layer characteristics is assessed by comparing simulated boundary-layer profiles at a point in the North Sea south of the track of Ali, where the wind speed reduction in the A–O–W simulation compared wth the Adrag1 simulation (Fig. 5.6b) is largest at 1800 UTC on 19 September 2018. Figure 5.7a shows that the selected point (cyan star) lies within Ali's cold sector, behind the cold front that stretches from Norway to southern England and characterized by a MABL height of ≈1.2 km, in contrast to a depth of ≈0.4 km in the warm sector. This marked change in boundary-layer height, and associated stability characteristics, on crossing the cold front is characteristic of ETCs (Sinclair *et al.*, 2010). The model-output MABL height is diagnosed using a “dynamic criterion" (Lock *et al.*, 2013), according to which the boundary layer corresponds to the model level height where the Richardson number $Ri$ exceeds the critical threshold of 0.25. The boundary-layer profiles (Fig. 5.7b, c) reveal that the MABL simulated by Adrag1 is unstable at this point and time, being characterized by a negative near-surface gradient of potential temperature and a strong wind shear.

The A–O configuration yields a weaker near-surface gradient of potential temperature than that simulated by the Adrag1 configuration. This is associated with reduced wind speed values at 200 m but approximately the same surface wind speeds, and therefore a reduced wind-speed gradient (Fig. 5.7b, c), and leads to a MABL height of 780 m, reduced from the 1100 m diagnosed in the Adrag1 simulation. The resulting decreased MABL instability simulated by the A–O configuration is most likely caused by the reduction of SST in the region of the North Sea located underneath the cold sector. Coupling to the wave model and changing the atmospheric drag parametrization both reduce the potential temperature gradients near the surface, leading to a small reduction in instability (comparing A–O to A–O–W) and a larger change from an unstable (Adrag1) to a neutral (Adrag2) surface layer, as inferred from the vertical potential temperature gradients (Fig. 5.7b). These changes are associated with similar magnitude increases in the wind-shear turbulence and hence with

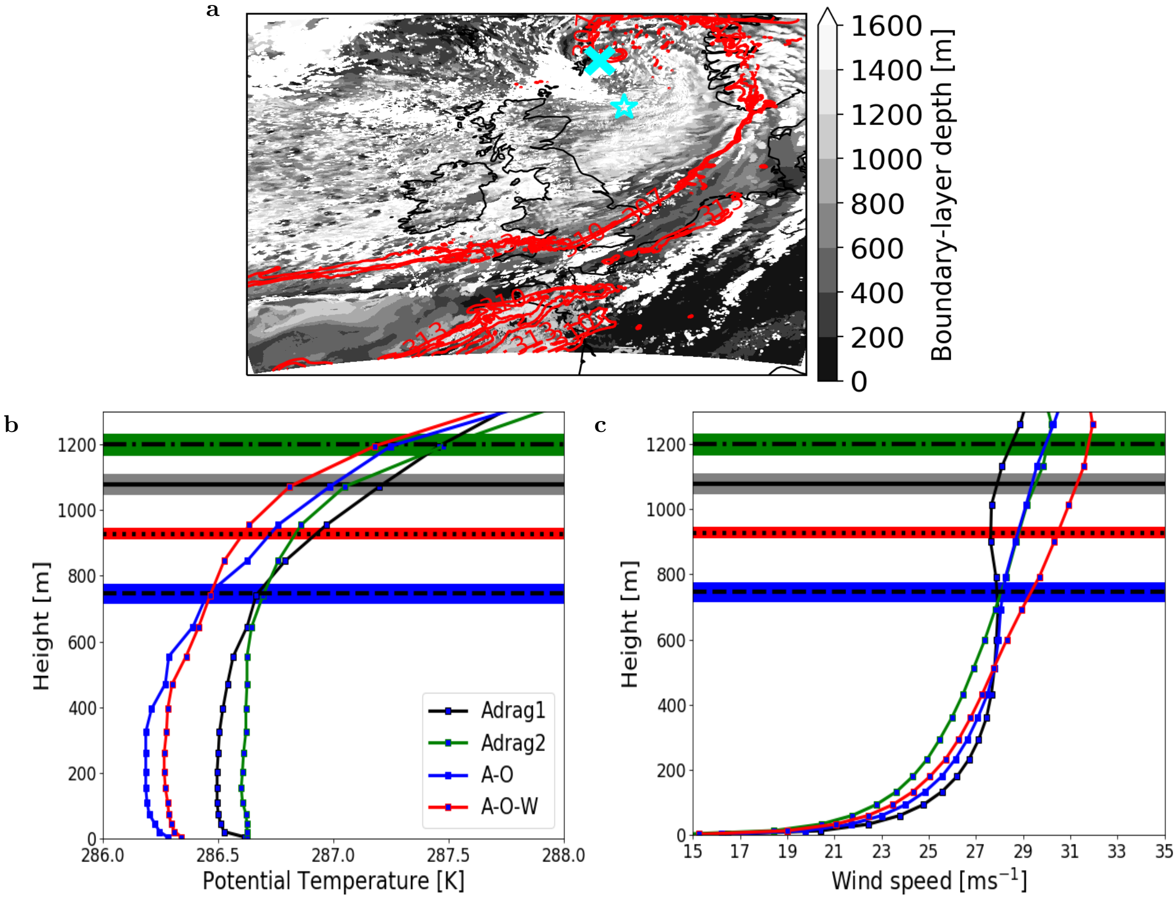

**Figure 5.7:** (a) Selected 850-hPa equivalent potential temperature contours (307, 310, and 313 K) at 1800 UTC 19 September 2018 overlaying the boundary-layer depth obtained from the Adrag1 simulation. The cold front lies along the strong thermal gradient between Norway and southern England with the short occluded front extending northwards, wrapping round the cyclone centre beyond the domain shown. The mean sea-level-pressure minimum of Ali is denoted by a cyan cross. The cyan star corresponds to the site of the profiles of (b) potential temperature and (c) wind speed (all profiles averaged over 5×5 grid cells). The lowest height value of each of the profiles correspond to the bottom UKC4 model level height. Horizontal lines in (b), (c) represent the boundary-layer height diagnosed as the model level height where the Richardson number exceeds the critical Richardson number $Ri_{crit} = 0.25$. Horizontal grey, green, blue, and red filled strips represent the standard error associated with the boundary-layer height diagnosed by each UKC4 configuration.

diagnosed MABL height (compare the A–O–W to the A–O results and the Adrag1 to the Adrag2 results). The increased turbulent eddies likely enhance momentum transfer from the air to the sea, leading to the reduction in near-surface wind speeds already noted in Fig. 5.6b.

To better understand how the momentum-flux enhancements depend on the numerical modelling of air–sea surface exchanges, the maps of the surface MABL characteristics of the A–O–W and the Adrag2 simulations are compared to those of the A–O simulation. Coupling to waves enhances momentum fluxes in the whole region extending south of the track of Ali (Fig. 5.8b), where reductions in the range of moderate to extreme 10-m wind speeds occur (see Fig. 5.6b). The young wave ages, corresponding in Fig. 5.8a to $c_p/u_*$ values less than 20, indicate that the sea is covered by young growing waves that enhance the Charnock coefficients by up to 0.02 (see Fig. 5.8c), which means that the Charnock coefficients increase nearly three times from the constant value $\alpha = 0.011$ used by the Adrag1 and A–O simulations to $\alpha = 0.031$, with corresponding enhancements in the momentum roughness length $z_0$ by up to $1.5 \times 10^{-3}$ m (see Fig. 5.8d). The increase in the magnitude of $z_0$ is associated with a larger momentum loss at the air–sea interface compared with the A–O simulation, resulting in lower wind speeds. This suggests that the waves give rise to a force proportional to the wave-induced stress, which effectively acts as frictional drag at the air–sea interface. Similar results were documented by Janssen (1989), Doyle (1995, 2002), Wahle *et al.* (2017), and Varlas *et al.* (2017).

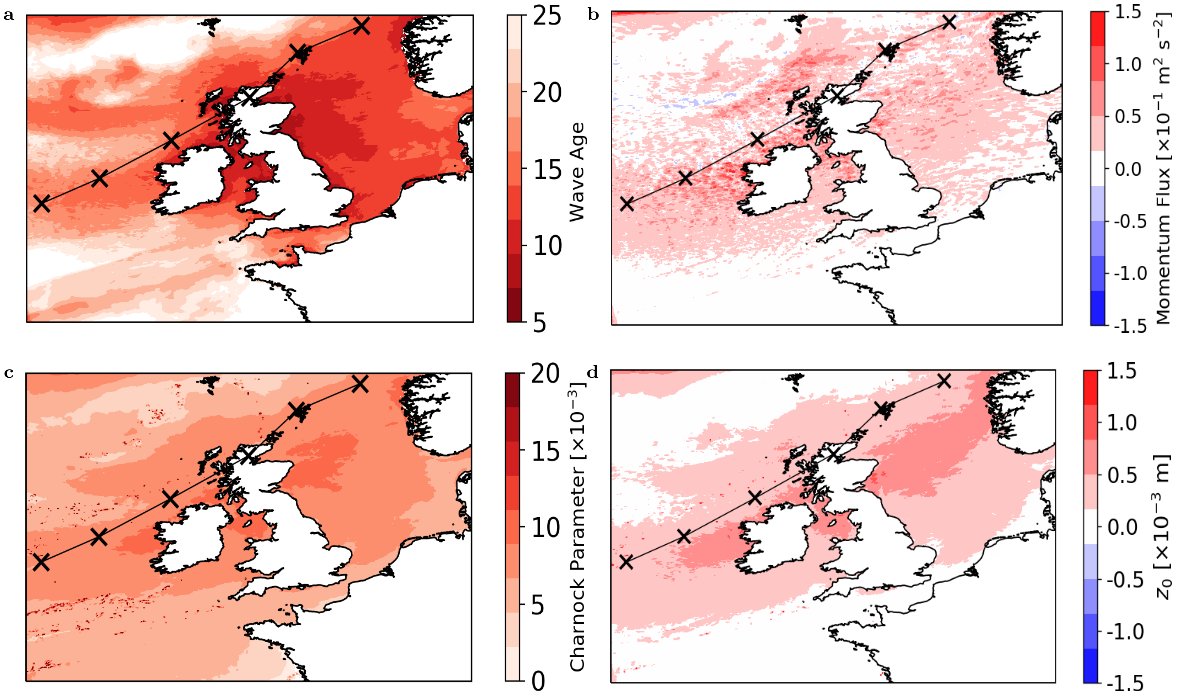

**Figure 5.8:** (a) Map of wave age in the A–O–W simulation, and maps of differences between the A–O–W and A–O simulations of (b) momentum flux, (c) Charnock parameter, and (d) surface roughness, $z_0$, all averaged over 19 September 2018. The non-dimensional wave age is computed as $c_p/u_*$ where $c_p$ is the phase speed of the peak of wave spectrum as defined by Cohen and Belcher (1999) and Sullivan *et al.* (2008). Ali's track is marked in each panel as in Fig. 5.4

The new drag parametrization used in the Adrag2 simulation enhances the momentum fluxes in the whole region south of the track of Ali compared with those in the A–O simulation (Fig. 5.9b), leading to a reduction in the moderate to extreme surface wind speeds, which is similar to that found by comparing the A–O–W and the A–O simulations (compare Fig. 5.9a and Fig. 5.6b). Hence, the new drag parametrization must produce a frictional surface stress at the air–sea interface, which is comparable in size to that induced by the growing young waves in the A–O–W simulation. To verify this, the dependence of the drag coefficient $C_D$ on the 10-m wind speed is presented for the four different UKC4 configurations in the two different sea regions, both south of the track of Ali, marked by the two black dots in Fig. 5.9a: one located in the Atlantic Ocean, off the west coast of Ireland, and the other one located in the northern North Sea. A close inspection of Fig. 5.10a, b shows that in the range 5–27 m s$^{-1}$ the drag coefficients $C_D$ of the A–O–W and Adrag2 parametrizations increase with the 10-m wind speed more steeply than those produced by the Adrag1 and A–O parametrizations, therefore leading to a larger surface stress at the air–sea interface. The fact that the gradient of $C_D$ for Adrag2 is even a little steeper than for A–O–W explains

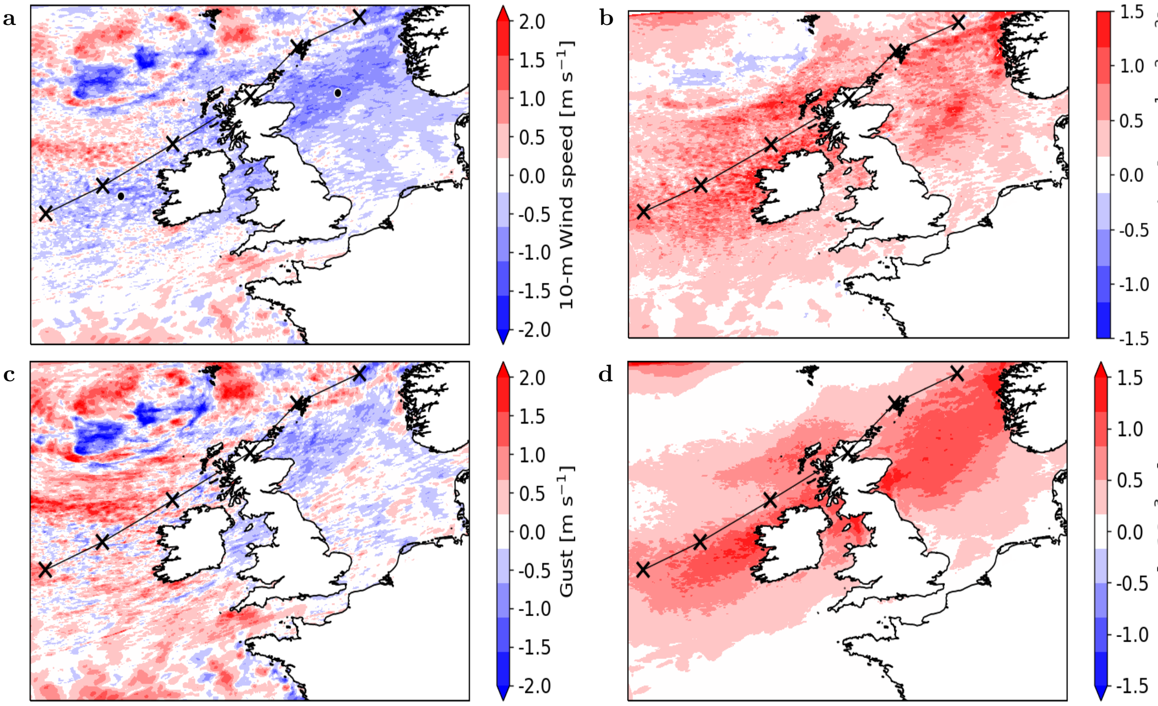

**Figure 5.9:** Maps of differences between Adrag2 and A–O simulations of (a) 10-m wind speed, (b) momentum flux, (c) gusts, (d) surface roughness, $z_0$, and averaged over 19 September 2018. The track of Ali is marked in each panel as in Fig. 5.3.

the corresponding slightly larger reductions in surface wind speed observed for the Adrag2 parametrization. In the Atlantic Ocean region considered in Fig. 5.10b, modelled 10-m wind speeds reach values above 27 m $s^{-1}$ where the implementation of the Adrag2 cap on the magnitude of $C_D$ is relevant. Here, there is a suggestion that the A–O–W $C_D$ also seems to flatten above 27 m $s^{-1}$, although at a slightly lower value ($C_D = 2.8 \times 10^{-3}$) indicating that the atmosphere-only Adrag2 is likely capable of mimicking the physics of the air–sea momentum surface exchange incorporated in the atmosphere–ocean–wave configuration for the whole range of the simulated wind speeds.

The comparison, in the region of strongest surface roughness, of vertical cross-sections of the differences in wind speed and turbulence kinetic energy between A–O–W and A–O, and between Adrag2 and A–O (not shown), revealed that the wind speed differences spread up to 8 km (near the tropopause), but are contained within the cyclone extent. Part of the cyclone's energy is dissipated through enhanced momentum loss at the air–sea interface, offering an explanation for the reduction of the pressure minimum of Ali (see Sect. 5.3.2) as well as likely leading to its quicker decay, in line with findings from Katsafados *et al.* (2016).

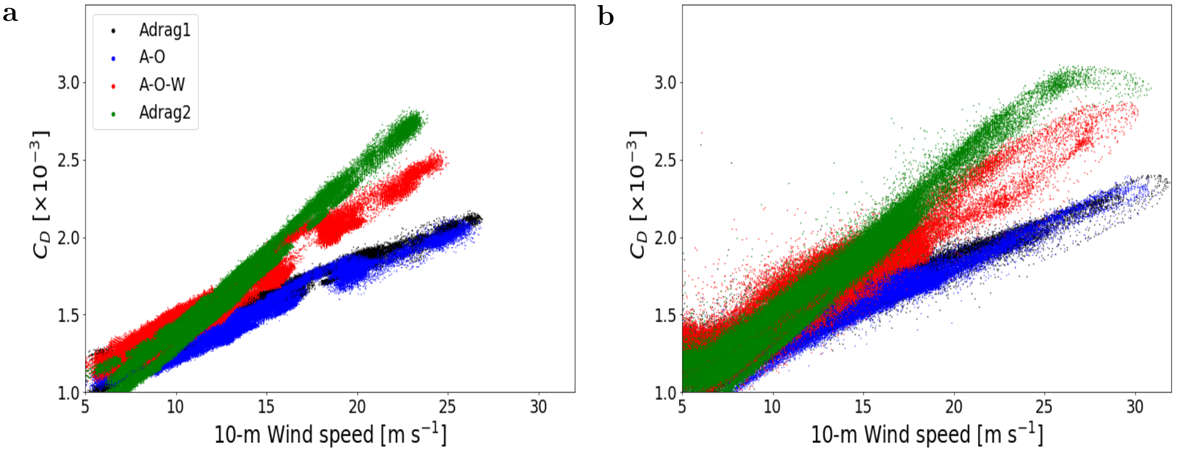

**Figure 5.10:** Drag coefficient dependence on 10-m wind speeds computed as the value of $C_D = \tau/\rho U_{10}^2$ over a 15 × 15 grid-cell area centred on points in the (a) North Sea (58.2°N, 0.9°E) for the Adrag1 (black), A–O (blue), A–O–W (red), and Adrag2 (green) parametrizations, and (b) North Atlantic Ocean (52.98°N, 12.46°W) configurations. Scatter points at hourly intervals from 0000 UTC 17 September to 0000 UTC 20 September 2018.

Compared with the impacts on the 10-m wind speed, both coupling to waves and using the Adrag2 new drag parametrization reduces the gusts less in the regions contiguous with the track of Ali (compare Fig. 5.6d and Fig. 5.9c). In these regions, the comparatively weak reduction in gusts arises from the formulation of the MetUM gust parametrization (Eq. 5.2), which is a sum of two terms, one representing the 10-m wind speeds and the other taking into account the friction velocity and surface roughness. Thus, a reduction of 2 $\mathrm{m\,s^{-1}}$ in 10-m wind speed due to coupling to waves or the new drag parametrization is balanced by the increase in friction velocity and aerodynamic surface roughness in regions contiguous to the track of Ali (see Fig. 5.8d and Fig. 5.9d), leading to weaker simulated gusts. However, in the north-west quadrant of the model domain, far from the track of Ali, the Adrag2 and A–O–W simulations yield localized increases and decreases in gusts of comparable magnitude to the corresponding changes in 10-m wind speeds. Again, this can be explained as arising from the MetUM gust parametrization, according to which the negligible change in aerodynamic surface roughness implies gusts only depend on changes in 10-m wind speeds.

### 5.3.4 Impact of coupling and using a new drag scheme on forecast bias

The biases in the SST and 10-m wind speeds are (1) assessed for the four UKC4 configurations over the case-study period as time series of a domain-averaged bias (Fig. 5.11) and (2) compared using spatial distributions of time-averaged root mean square error for one simulation relative to another simulation as illustrated in Fig. 5.12. Only five stations from the analyzed database reported gust values over the U.K. consistently enough in time to be statistically significant across the case-study period. Thus a bias plot for gusts is not included here.

Figure 5.11a shows that the magnitude of the spatially averaged 10-m wind-speed bias is larger over sea-observation sites than over land observation sites with values up to 3 $\mathrm{m\ s^{-1}}$. Over land-observation sites the biases for the four UKC4 simulations are indistinguishable and generally positive with values up to $\approx 1\ \mathrm{m\ s^{-1}}$; over sea-observation sites, the biases in the A–O–W and Adrag2 simulations are typically less than those in the Adrag1 and A–O simulations where the biases are positive and vice versa, consistent with the reduced wind speeds found in these simulations.

The spatially averaged SST biases (Fig. 5.11b) vary with time between about −0.5 K to 1 K.

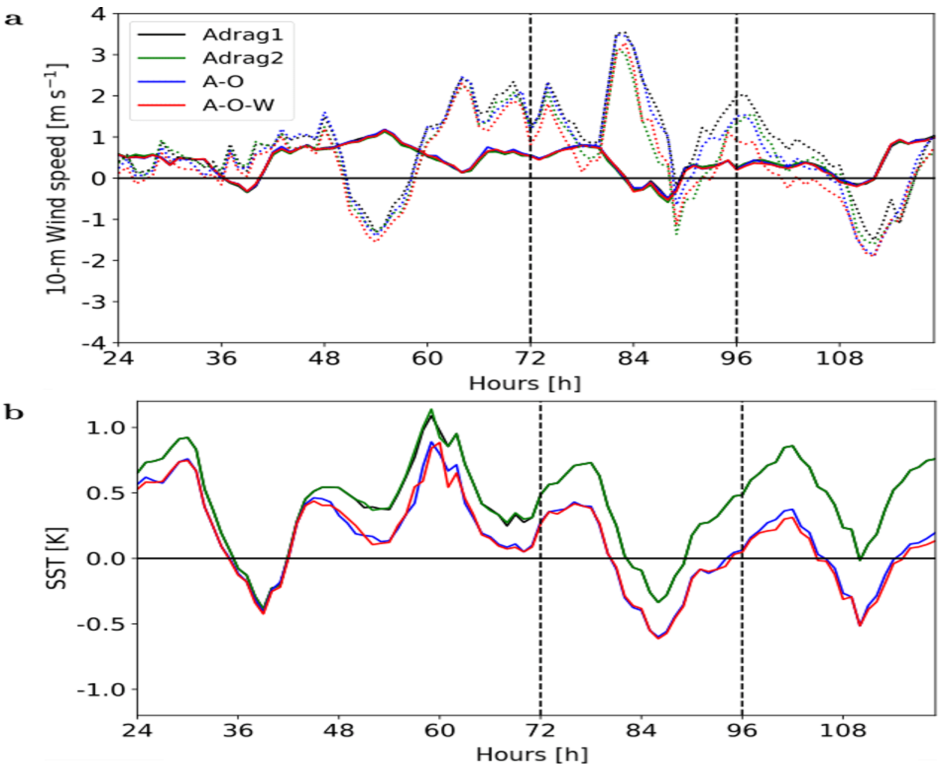

**Figure 5.11:** Time series of spatially averaged biases for the different model simulations of (a) 10-m wind speed across land-only (solid lines) and sea-only (dashed lines) observation sites (600 and 60 respectively) and (b) SST (10 observation sites) for 17–20 September 2018. The lines correspond to the Adrag1 (black), Adrag2 (green), A–O (blue), and A–O–W (red) simulations. The Adrag1 and Adrag2 lines are identical in panel (b).

As shown in Fig. 5.5c, the SSTs for the A–O and A–O–W simulations are similar and generally cool with time, diverging from the fixed SSTs in the atmosphere-only simulations. As the SSTs in the A–O and A–O–W simulations cool, the associated biases improve, changing from generally positive to varying about zero (Fig. 5.11b). This contrasts with the biases for the atmosphere-only simulations which, despite the variability with time, stay generally positive. These results corroborate the findings of Lewis *et al.* (2018) in which coupling to the ocean reduced the SST bias by up to 1 K.

The impact of coupling to ocean, of coupling to waves, and of the new Adrag2 parametrization on 10-m wind speed $RMSE_{rel}$ forecast skill is quantified by computing the value of the $RMSE_{rel}$ of A–O relative to Adrag1, A–O–W relative to A–O, and A–O–W relative to Adrag2. As can be seen from the prevalence of light over dark coloured dots in Fig. 5.12a, partially coupling to ocean neither appreciably improves nor degrades the 10-m wind-speed forecast compared with the atmosphere-only Adrag1 configuration. In contrast, the prevalence

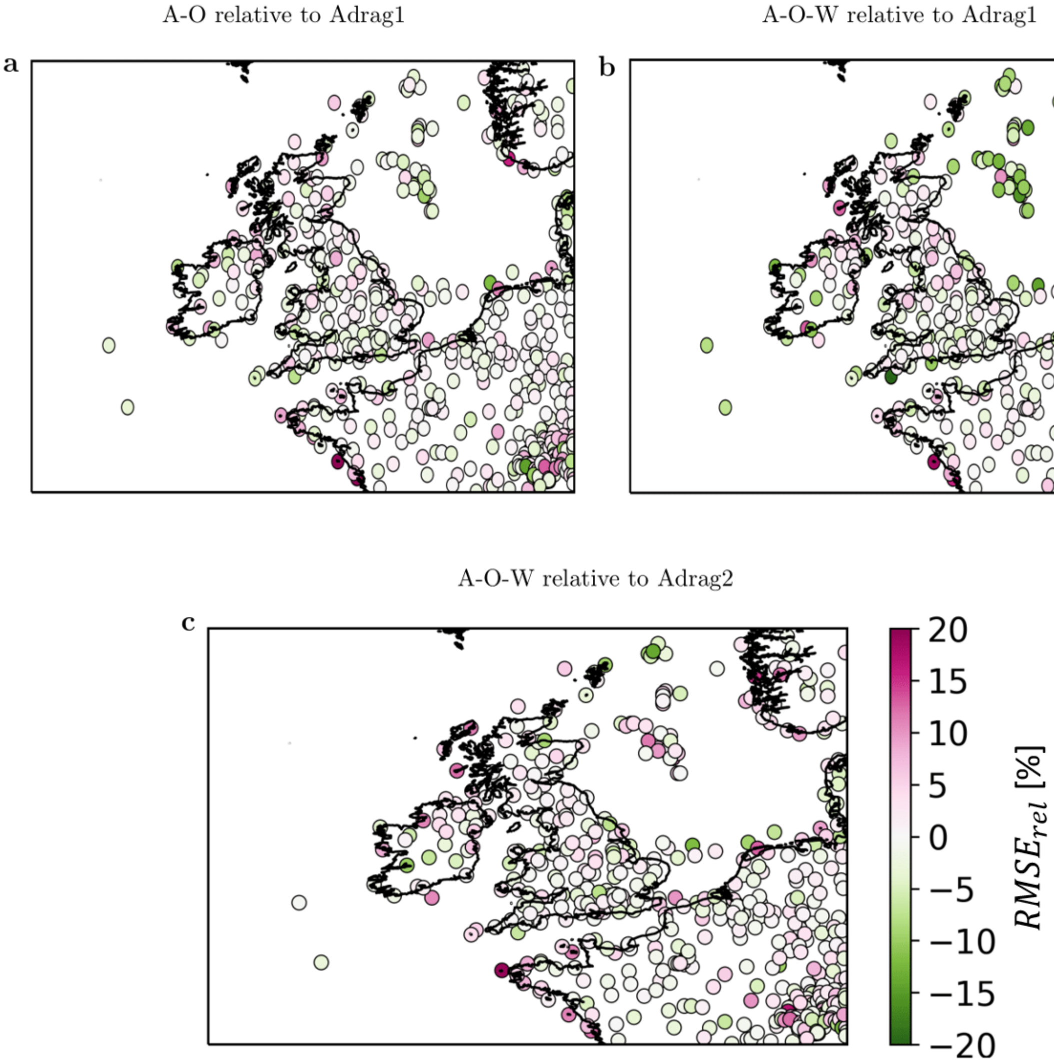

**Figure 5.12:** Percentage difference in wind speed $RMSE_{rel}$ for (a) A–O relative to Adrag1, (b) A–O–W relative to Adrag1, and (c) A–O–W relative to Adrag2 averaged over 17–20 September 2018.

of dark green dots over the North Sea in Fig. 5.12b highlights that coupling to waves improves the 10-m wind-speed-forecast skill by up to 20% over the ocean-grid cells (comparing the A–O–W and A–O simulations). However, changes over land are much smaller and show, at most, a small reduction in skill in the few areas of the U.K. indicated by the pink dots. Compared with the atmosphere-only Adrag2 simulation, the fully coupled A–O–W configuration slightly improves the 10-m wind-speed forecast in the northern part of the North Sea, but degrades it in the central part of the North Sea (Fig. 5.12c). Hence, for most of the observation sites, the atmosphere-only Adrag2 simulation with the new drag parametrization is able to achieve the same improvement in 10-m wind-speed -forecast skill as that obtained from fully coupling the atmosphere to ocean and waves (A–O–W) with the benefit of saving 25% of the computational cost (estimated in node hours per simulation day, see Table 5.1).

## 5.4 Conclusions

Prior work has documented the importance of a high-fidelity representation of air–sea surface exchanges in NWP models to obtain an accurate forecast of extreme surface wind speeds (Janssen, 2004). Usually, this has been achieved either by providing uncoupled atmosphere-only NWP models with a suitable boundary-layer parametrization [e.g., the UKV system (Tang *et al.*, 2013)] or by setting up a coupled multi-model NWP system which integrates the feedbacks of ocean and wave models with an atmosphere-only model [e.g., CHAOS-2-way system developed by (Katsafados *et al.*, 2016)]. In this context, the Met Office developed the UKC4 multi-model system, which couples the atmospheric (MetUM) model (and JULES land-surface model), with the ocean (NEMO), and wave (WAVEWATCH III) models. The UKC4 system is a robust and flexible research tool characterized by different coupling options at kilometre-scale resolution (Lewis *et al.*, 2018, 2019).

The purpose of the current study was to quantify the sensitivity of extreme surface wind speeds to air–sea surface exchanges by using the UKC4 multi-model system in coupled and uncoupled modes. The extreme weather period of 17–20 September 2018 (which included ETCs Helene, Ali, and Bronagh), was used as the case study. Four UKC4 configurations were used: the uncoupled atmosphere-only configuration Adrag1, provided with the operational UKV drag parametrization; the uncoupled atmosphere-only configuration Adrag2, provided with a new drag parametrization based on the COARE 4.0 drag parametrization corrected with the Donelan (2018) cap and decrease the drag coefficient at high wind speeds; the partially coupled A–O atmosphere–ocean configuration; and the fully coupled A–O–W atmosphere–ocean–wave configuration.

For this case study, coupling to the ocean (A–O configuration) does not strongly impact the 10-m wind speeds, but it does have an important impact on SSTs, decreasing them by up to 0.5 K compared with the persisted SST field used in the two atmosphere-only Adrag1 and Adrag2 configurations. Unlike coupling to ocean, coupling to waves reduces the 10-m wind speeds by up to 2 m $s^{-1}$ compared with the atmosphere-only Adrag1 and partially coupled A–O configurations. The atmosphere-only Adrag2 configuration provides equivalent reductions in wind speeds. Comparison of the boundary-layer profiles at a point in the North Sea, where the impacts of wave coupling and Adrag2 parametrization scheme are most prominent, demonstrate that the Adrag2 configuration is capable of simulating the same enhancement of the air–sea turbulent momentum flux as the fully coupled A–O–W configuration.

The investigation of A–O–W air–sea momentum-flux enhancements revealed that young growing waves extract momentum and energy from the overlying atmospheric flow, increasing the frictional drag at the sea surface and thus reducing near-surface wind speeds. As an effect of the increase in the sea-surface aerodynamic roughness of this evolving sea state, Charnock parameter values simulated by the WAVEWATCH III model, and then passed to the MetUM, exceed the semi-empirical constant value of $\alpha = 0.011$ set in the uncoupled and partially coupled configurations. Although an increase of comparable size in aerodynamic roughness and frictional drag over the sea due to young growing waves simulated by coupling a NWP model to a wave component has already been documented by Varlas *et al.* (2017), Wahle *et al.* (2017), and Lewis *et al.* (2018, 2019), here an equivalent increase in aerodynamic roughness and frictional drag has also been achieved by the atmosphere-only Adrag2 simulation. It was verified that the Adrag2 drag coefficient linear growth with 10-m wind speeds is significantly steeper than that of the UKV drag coefficient in the range 5–27 m $s^{-1}$ and above 27 m $s^{-1}$ it limits the value of $C_D$ at $C_D = 3 \times 10^{-3}$, effectively mimicking the physics of the momentum air–surface exchange incorporated in the fully coupled A–O–W configuration.

The increase in surface roughness and surface friction exhibited by the A–O–W and Adrag2 simulations generates a more turbulent and thus deeper MABL resulting, in both configurations, in areas of enhanced gustiness across the boundary layer. However, this effect is balanced by an increase in friction velocity resulting in a modest impact on gust values at the surface, regardless of the changes in the simulated physics across the configurations. Moreover, the increased aerodynamic sea surface roughness in the A–O–W and Adrag2 configurations affects the cyclone's vertical structure and increases the mean sea level pressure by up to 2 hPa through dissipation of its energy at the air–sea interface.

Coupling to the ocean (in both the A–O and A–O–W simulations) improves the SST bias compared with the atmosphere-only Adrag1 and Adrag2 simulations, in agreement with results from Lewis *et al.* (2018), but has a negligible impact on the 10-m wind-speed bias. However, coupling to waves (A–O–W) and using the new drag parametrization (Adrag2) improves the wind-speed bias over sea-observation sites. Fully coupling (the A–O–W simulation) improved the $RMSE_{rel}$ forecast skill of 10-m wind speeds (over open waters) by up to 20% compared with the atmosphere-only Adrag1 and partially coupled A–O simulations, in agreement with the literature (Wahle *et al.*, 2017; Varlas *et al.*, 2017). The same forecast-skill improvements relative to the A–O and Adrag1 simulations are achieved by the uncoupled Adrag2 configuration, with the advantage of saving 25% of the computational cost, estimated in node hours per simulation day, of running a fully coupled A–O–W configuration.

A limitation of this research is the short length of the time period investigated. It would be useful to repeat the study over longer time periods to determine the statistical significance of the results. Moreover, although coupling or changing the drag parametrization reduces the model error in 10-m wind speeds, the relatively small improvements (respect to the biases) imply that errors in initial and/or lateral boundary conditions, or model physics parametrizations, dominate over errors in air–sea coupling. However, taken together, the findings of this study demonstrate that, for this case study, an atmosphere-only model provided with the new drag parametrization based on the COARE 4.0 parametrization with the Donelan (2018) cap and drag reduction (as that used in Adrag2) has the same physical and numerical impacts on the wind speeds in ETCs as a fully coupled model system, with the notable advantage of reducing the computational cost associated with the ocean and wave model components.

# Chapter 6

# The sensitivity of probabilistic convective-scale forecasts of an extratropical cyclone to atmosphere-ocean-wave coupling

This chapter has been published in *Quarterly Journal of the Royal Meteorological Society* with the following reference:

**Gentile, E.S.**, Gray, S.L Lewis, H.W.: The sensitivity of probabilistic convective-scale forecasts of an extratropical cyclone to atmosphere-ocean-wave coupling. *Quarterly Journal of the Royal Meteorological Society*, **148**, 685-710, (2022), https://doi.org/10.1002/qj.4225

Estimated contribution: 80%. ESG designed the study, developed the methodology, performed all analysis and wrote the manuscript with input and suggestions from SLG, HWL. All authors commented on the manuscript and discussed and interpreted the results at all stages. Two anonymous reviewers provided comments on an earlier version of the manuscript. ESG performed the 95% of the research with guidance from supervisors SLG and HWL via meetings. SLG and HWL also gave advice on the visualisation of the ensemble output, besides interpretation of results, as already noted. In particular, the development of the novel ensemble coupled system Ensemble-RCS, presented in this research chapter, was carried out by ESG in collaboration with HWL. The onset of the COVID-19 pandemic in March 2020 meant that this collaboration was carried out remotely for 90% of its duration.

# Abstract

The benefits of dynamical atmosphere-ocean-wave coupling in probabilistic weather forecasts generated using convective-scale ensemble prediction systems are to date unknown. We investigate the respective impacts of atmosphere-ocean-wave coupling, and initial condition (IC), lateral boundary condition (LBC) and stochastic physics perturbations within a convective-scale ensemble coupled system for an extratropical cyclone case study. Towards this aim, we developed the first 18-member, 2.2-km grid spacing ensemble regional coupled system (Ensemble-RCS) with domain covering the British Isles and surrounding seas. Ensemble-RCS coupled and uncoupled simulations of cyclone Ciara (February, 2020) were performed.

Adding stochastic perturbations to the model physics parametrizations enhances the ensemble spread of the uncoupled atmosphere-only ensemble driven by IC and LBC perturbations, while slightly reducing (by up to 0.5 m $s^{-1}$) the median of the ensemble $95^{\text{th}}$ percentile 10-m wind speeds from its value of about 24 m $s^{-1}$ at peak time. A substantial proportion of this impact is attributable to Charnock parameter perturbations alone. By coupling the atmosphere-only ensemble, with stochastic physics, to the ocean, the ensemble median and spread is mainly unaffected. However, additionally coupling to wave reduces the median wind speed by 1 m $s^{-1}$, which leads to reductions of up to 70% in strong wind strike probability, and halving of the spatial coverage of high values (>50%) of this probability. Finally, we demonstrate the usefulness of two metrics originally developed for precipitation verification, the neighbourhood-based Fraction Skill Score (FSS) and the object-based Structure, Amplitude, Location (SAL), for examining the spread in convective-scale ensemble forecasts. It is concluded that coupling has a consistent impact across the ensemble members. Remarkably, the impact of coupling to waves is found to be comparable in size to that of adding IC, LBC and stochastic physics perturbations to the uncoupled atmosphere-only ensemble simulation, implying that the dynamical coupling to ocean and sea-state are important aspects of model uncertainty.

## 6.1 Introduction

Extratropical cyclones can generate intense surface wind speeds and gusts as they pass over the UK (e.g, Martínez-Alvarado *et al.*, 2014), leading to large socio-economic impacts (e.g, Hewston and Dorling, 2011). Numerical weather prediction systems can predict the synoptic-scale evolution of cyclones with reasonable skill (Frame *et al.*, 2015) but, because the atmosphere is a chaotic system (Lorenz, 1963), small errors in the initial conditions (ICs) of forecasts and in model physics approximations grow exponentially over time, limiting the predictability of the location and strength of mesoscale cyclone features such as intense winds (Buizza *et al.*, 2005; Bowler *et al.*, 2008). The forecast uncertainty yielded by IC and model errors can be estimated by generating probabilistic realizations of events using ensemble prediction systems (EPS) (Buizza *et al.*, 1999). Compared to IC errors, the correct estimation of model errors represents a much greater challenge (Buizza *et al.*, 2005). Candidate sources of model errors include the sea-state independent model parametrizations of air-sea momentum, heat and moisture fluxes that control, at convective-scale, the location and magnitude of strong winds near the ocean surface (Janssen, 2004; Lewis *et al.*, 2018, 2019). Because of the steep vertical gradients of the air-sea fluxes at the air-sea interface, small model errors in the parametrization of air-sea fluxes can result in large forecast errors and model biases. A number of studies (Wahle *et al.*, 2017; Lewis *et al.*, 2019) have shown that the direct simulation of the effect of the dynamical ocean and wave state on air-sea surface exchange coefficients in a deterministic coupled system has a great potential to improve the prediction of cyclone wind speed forecasts at or close to convective-scale. However, to date, a study based on the development of a dynamically coupled convective-scale EPS has not yet been published. Here we develop such a system and, by applying it to a cyclone case study, determine the sensitivity of convective-scale ensemble forecasts of wind speeds to ocean and wave coupling and the relative sensitivity to coupling compared to sensitivity to IC, lateral boundary condition (LBC) and stochastic model physics perturbations.

Medium-range EPS ave been used operationally for 30 years and are now capable of generating accurate and reliable forecasts of the synoptic-scale development of cyclones with several days lead time (Toth and Kalnay, 1997; Buizza and Palmer, 1995; Molteni *et al.*, 1996; Houtekamer *et al.*, 1996; Buizza *et al.*, 2005; Bowler *et al.*, 2008). Medium-range EPS focus mainly on the uncertainties associated with synoptic-scale baroclinic instability (Bowler *et al.*, 2008), but also attempt to represent the uncertainty at the convective scales of motion (Tennant *et al.*, 2011) either by using multiple physics parametrization schemes, by using multi-parameter schemes within a single-model approach (Bowler *et al.*, 2009; Berner *et al.*, 2011) or by widening the sample range of possible forecast scenarios by using a multi-model approach (Hagedron *et al.*, 2005). To represent the interaction between the uncertainty in the atmospheric and oceanic boundary layers, the European Centre for Medium-Range Weather Forecasts (ECMWF) (Bauer *et al.*, 2020) and the Naval Research Laboratory (NRL) (Holt *et al.*, 2011) have dynamically coupled the atmospheric dynamical core of their operational medium range EPS with their operational ocean and wave models. Also the Met Office plans to run an operational medium-range atmosphere-ocean coupled ensemble due to the promising results obtained by the corresponding global deterministic forecast system (Vellinga *et al.*, 2020). Despite the increase in physics complexity and in the degree of coupling between model components, medium-range EPS cannot exploit the full benefits of dynamical integration of the atmosphere, ocean, and wave feedbacks (Holt *et al.*, 2011) as the relatively coarse resolutions cannot provide detailed km-scale forecasts over regions of particular interest. For example, in the case of a rapidly developing cyclone, Lean and Clark (2003) established that a grid spacing of $O10$ km is sufficient to represent the overall frontal structure of an extratropical cyclone and the associated airflow; however, a convective-scale grid spacing of $O1$ km is required to resolve smaller-scale multiple slantwise circulations, the 3-D structure of convection lines, and the peak cyclone surface wind speed.

At convective-scale, coupling atmosphere, ocean, and wave model components in deterministic prediction systems has shown potential to reduce the biases of cyclone wind speed deterministic simulations. For example, Wahle *et al.* (2017), simulating a historical series of cyclones that hit the southern North Sea, demonstrated that coupling the deterministic WAM wave model (Komen *et al.*, 1994) with the deterministic COSMO regional atmosphere model (Rockel *et al.*, 2008) (run at 5 and 10-km grid spacing, respectively) reduced wave heights and wind speeds by up to 8% and 3%, respectively, with associated equivalent improvements in the forecast skill of wind and waves. Comparable reductions in wind speeds and wave heights, associated with skill improvements of 20% and 5%, respectively, were achieved by Lewis *et al.* (2019) in coupled simulations of part of the 2014 UK cyclone season. These simulations were carried out using the deterministic Met Office Regional Coupled System (RCS), termed UKC3 in Lewis *et al.* (2019), which couples models of the atmosphere, land-surface, shelf-sea ocean, and ocean surface waves. A further study (Gentile *et al.*, 2021) demonstrated that the improvements in cyclone wind speed forecasts generated by the RCS are mainly due to the impact of coupling to the wave model component. Bias reductions in wind speeds associated with severe weather conditions on coupling to a wave model have also been demonstrated for cyclonic events over the Mediterranean Sea (Katsafados *et al.*, 2016; Ricchi *et al.*, 2017; Varlas *et al.*, 2017; Ricchi *et al.*, 2019).

Although experimental convective-scale coupled deterministic systems have undoubtedly shown benefits for the prediction of severe weather events, it has not yet been established whether the benefits from coupling are still retained when running as an ensemble, or what the size is of the impact of coupling relative to those of the perturbations applied to generate the ensemble. When convective-scale EPS were designed about 15 years ago, researchers mainly focused on exploring the benefits of increasing the ensemble grid spacing for forecast skill improvements and of increasing the ensemble size for better sampling the uncertainty; at the time, there were not enough computational resources to additionally implement coupling of the atmospheric dynamical model core with the ocean and the wave models (Holt *et al.*, 2011). For example, Schellander-Gorgas *et al.* (2017) compared the performance of the 16-member convective-scale 2.5 km horizontal grid spacing AROME-EPS to that of the 16-member mesoscale 11 km grid spacing ALADIN-LAEF EPS. For a summer case study over the alpine region, they found that the AROME-EPS significantly improved the precipitation forecast skill due to better resolution of the local effects of mountain topography. A further study by Raynaud and Bouttier (2017) varying resolution and ensemble size of convective-scale AROME-EPS found that increasing the resolution only led to short-range forecast improvements, whereas increasing the ensemble size exhibited a larger impact at longer forecast ranges. In this context, the Met Office developed the short-range high-resolution Met Office Global and Regional Ensemble Prediction System [MOGREPS, Bowler *et al.* (2008)], consisting of two related EPSs: the medium-range global 12-member MOGREPS-G with 33 km grid-spacing and the short-range, limited-area (British Isles) 12-member MOGREPS-UK with 2.2-km grid-spacing (Hagelin *et al.*, 2017). Since 2016 the MOGREPS-UK has been inititalised by perturbing about an analysis of the Met Office's UK variable resolution (UKV) deterministic model using the MOGREPS-G perturbed ensemble members (Hagelin *et al.*, 2017). Investigating a three-month long summer case study, these authors found that the convective-scale ensemble MOGREPS-UK not only improved the precipitation forecast skill compared to the deterministic UKV but also the skill of other meteorological variables of interest such as 1.5 m air temperature, wind speeds, visibility, cloud base height, and cloud cover. Further investigation by Porson *et al.* (2020) using a MOGREPS-UK configuration with 18 time-lagged members, revealed substantial improvements in skill for the same meteorological variables considered in Hagelin *et al.* (2017). However, convective-scale EPS forecasts are more challenging to verify than coarser-scale ones because of the well known "double penalty" problem : i.e., that a forecast with a slightly misplaced weather feature is penalised both for not having forecast the feature in the correct place and for forecasting the feature in a place where it did not occur. To avoid this problem new metrics have been developed such as the neighbourhood-based fraction skill score (FSS: Roberts, 2008) and the object-based structure, amplitude location (SAL: Wernli *et al.*, 2008) score. Dey *et al.* (2014) and Zschenderlein *et al.* (2019) introduced and successfully used a dispersion form of FSS and SAL metrics to verify convective-scale EPS forecasts of precipitation events against radar observations.

Despite the many benefits of convective-scale EPS compared to their medium-range counterparts described above, representation of model error at convective scale remains challenging because the smaller scales of motion simulated by convective-scale EPS lead to a faster error growth (Clark *et al.*, 2010; Baker *et al.*, 2014; McCabe *et al.*, 2016; Hagelin *et al.*, 2017). Clark *et al.* (2021), investigating a series of precipitation events simulated by a convective-scale EPS, demonstrated that model error impact is greatest when it arises from parametrization of boundary-layer structure. Moreover, Flack *et al.* (2021) further demonstrated that uncertainty from stochastic perturbations applied to the model boundary-layer parametrization is statistically comparable to IC and LBC uncertainty. These findings clearly indicate that convective-scale EPS need a more accurate representation of boundary-layer processes to reduce forecast error and better estimate model uncertainty of the meteorological variables that are sensitive to boundary-layer parametrizations. Although dynamical coupling of atmosphere, ocean, and wave models has been shown to improve the accuracy of boundary-layer parametrizations in deterministic simulations, its potential benefits for convective-scale EPS have not yet been explored, with the exception of a single study from Bousquet *et al.* (2020) which investigated the performance of the ensemble configuration of the convective-scale atmosphere model AROME-IO (Indian Ocean) coupled with a 1D ocean mixed layer model, for eleven major storms. As shown by Bousquet *et al.* (2020), coupling AROME-EPS to a 1D ocean mixed layer model rather than to a dynamical 3D ocean model led to important limitations in capturing the simulated physics, such as not reproducing the outward horizontal transport of warm waters located near the tropical cyclone core as well as underestimating the storm-core sea surface cooling. A further limitation of the ensemble 1D-ocean-coupled AROME-IO of Bousquet *et al.* (2020), was that the model did not incorporate coupling to a wave model, despite atmosphere-wave feedbacks having proven equivalently important to atmosphere-ocean feedbacks for simulations of idealised cyclones (Doyle, 1995, 2002), tropical cyclones (Holt *et al.*, 2011), Mediterranean cyclones (Varlas *et al.*, 2017; Ricchi *et al.*, 2019), and extratropical cyclones affecting the UK and the North Sea (Wahle *et al.*, 2017; Lewis *et al.*, 2018, 2019; Gentile *et al.*, 2021).

To address this question, we present the first study, to date, on the sensitivity of convective-scale ensemble prediction system simulations to dynamical atmosphere-ocean-wave coupling relative to IC, LBC and stochastic model physics perturbations. Towards this aim, we have developed the first coupled convective-scale ensemble, termed Ensemble-RCS, focused on the British Isles domain and surrounding seas. This EPS is an ensemble implementation of the RCS for an atmosphere model domain with 2.2-km horizontal grid-spacing, matching that used in the MOGREPS-UK ensemble, with the atmosphere component uncertainty driven by MOGREPS-UK ICs, LBCs, and stochastic perturbations. Coupled (ocean and wave model), partially coupled (only ocean model) and uncoupled Ensemble-RCS simulations were run from 7–10 February 2020 during which time cyclone Ciara crossed the UK, the most intense cyclone since storm Tini (from 12 February 2014: Kendon, 2020). The mean, median, standard deviation and strike probability of the different coupled and uncoupled Ensemble-RCS forecasts are analyzed and compared. The ensemble spread characteristics are also evaluated using the dispersion FSS (dFSS) and dispersion SAL (dSAL) methods. Moreover, we evaluate the robustness of the Ensemble-RCS forecasts of Ciara's intense wind speeds on atmosphere-ocean-wave coupling and on perturbations of ICs, LBCs, and model parametrizations. The atmosphere, ocean, and wave feedbacks on which we focus are the air-sea turbulent momentum and heat exchange, mediated by the way the Charnock parameter and the sea surface temperature (SST), respectively, are simulated and communicated to the atmosphere model.

The remainder of this article is organised as follows. Section 6.2 describes the weather conditions associated with the case study cyclone, Ciara. The Ensemble-RCS coupled and uncoupled configurations are described in Section 6.3, where the neighbourhood and object-based metrics used to characterize the ensemble spread are also explained in detail. Results on the relative sensitivity of stochastic perturbations to ICs and LBCs perturbations are presented and discussed in Section 6.4 followed by results of the sensitivity to coupling to ocean and coupling to waves and comparison of coupled and uncoupled Ensemble-RCS configuration spread characteristics. Conclusions are given in Section 6.5.

## 6.2 Case study: storm Ciara

Cyclone Ciara, officially named on 5 February 2020 by the Met Office, was selected as a case study because it was the most intense and damaging cyclone to have hit the British Isles since 2014 (Kendon, 2020). After originating from a weak area of low pressure in the south-eastern US on 5 February 2020, cyclone Ciara entered the Met Office's high resolution analysis (UKV) domain at 0000 UTC 9 February 2020. It then separated from the left exit region of the jet stream (not shown), continuing to intensify until 0900 UTC on that day when the central mean sea level pressure (MSLP) reached a minimum of 950 hPa. At this time, as represented by the UKV analysis field in Fig. 6.1b, the vertical pressure structure exhibited only a slight westward tilt from comparison of the MSLP field with with that of 500 hPa geopotential height (Fig. 6.1b), as expected given that the cyclone had already undergone most of its rapid intensification stage by this time. As can be seen from the Met Office analysis

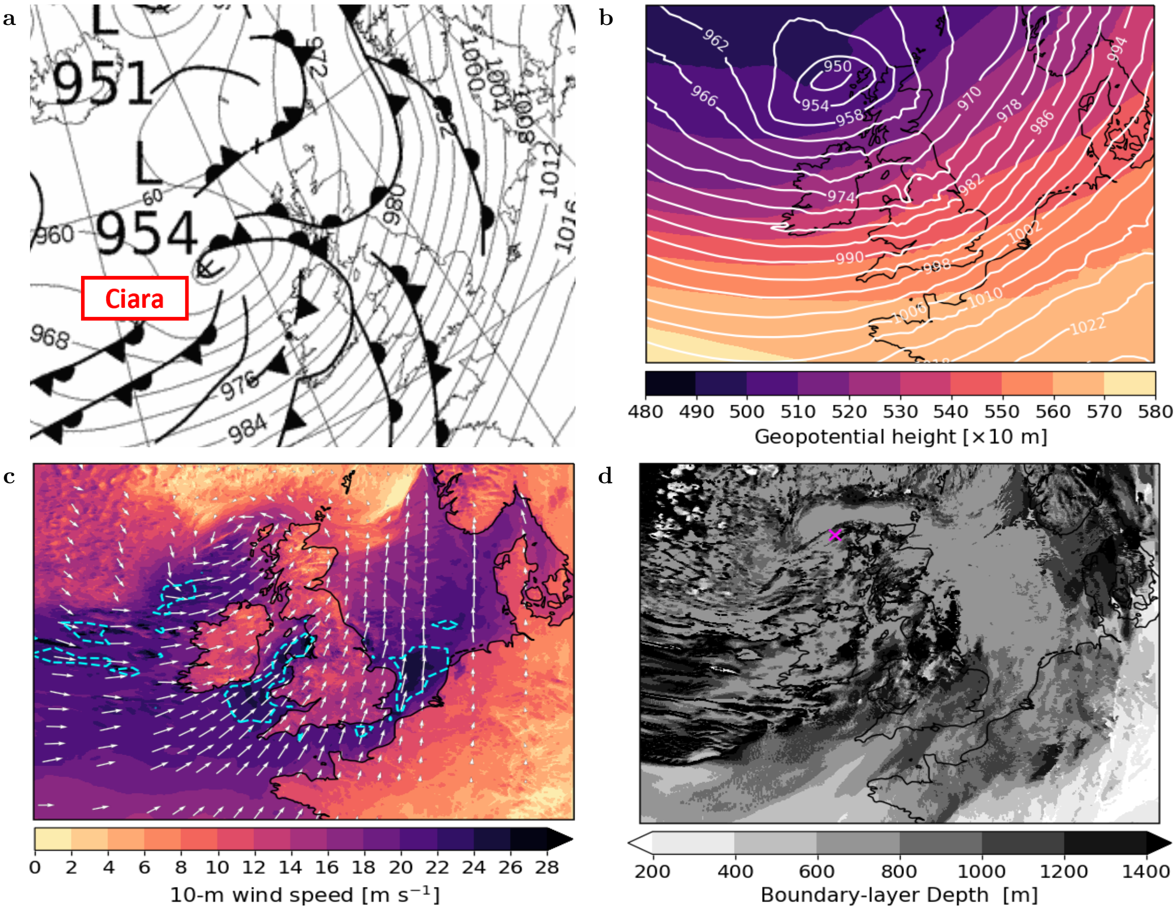

**Figure 6.1:** (a) Met Office's surface analysis at 0600 UTC 9 February 2020. UKV analysis maps at 0900 UTC 9 February 2020 for (b) mean sea level pressure (white solid contours, interval 4 hPa), and 500 hPa geopotential height (colours), (c) 10-m wind and direction (white arrows), and speed (colours), with $95^{\text{th}}$ percentile of 10-m wind speed field plotted as a countour (dashed red lines), (d) boundary-layer depth (grayscale colours). The mean sea level pressure minimum is marked by a purple cross in (d).

at 0600 UTC 9 February 2020 in Fig. 6.1a, Ciara has a complex frontal structure (with a possible frontal wave) and we therefore use information from the boundary layer depth rather than a temperature field to characterise the warm and cold sectors of the cyclone. The map of boundary layer depth, Fig. 6.1d, shows cold sector air, characterised by localised regions of deeper depth (≈ 1400 m) interspersed with shallower regions, primarily to the south and west of the pressure low centre, while the warm sector, characterised by a broad region of consistent shallower depth (≈ 600 m), lies east of the centre as well as wrapping round the centre to the north.

Ciara was associated with gale-force ($> 17$ m s$^{-1}$) near-surface wind speeds over large regions of the North Atlantic (off the coast of Ireland), the Irish Sea, English Channel, and parts of the southern North Sea (Fig. 6.1c). Consequently, waves as high as 10 m battered the exposed coastlines of Ireland, Wales, and Cornwall, over-topping sea defences in many places (Kendon, 2020). Although over the land surface winds were reduced due to increased surface friction, the vast majority of the UK's land surface stations reported widespread gusts exceeding 30 m s$^{-1}$, most likely due to the unstable conditions of the daytime boundary layer, which favoured turbulent transport of fast-flowing air from Ciara's low-level jets to the surface. These extreme weather conditions, together with the exceptionally intense precipitation brought by Ciara (totalling 50–75% of the 1981–2020 February average of rain for some UK regions), resulted in widespread flooding across the British Isles, 675 thousand homes without power for several hours, £1.6 billion damage, and tragically three fatalities (Kendon, 2020).

## 6.3 Methodology

### 6.3.1 The ensemble regional coupled system

We developed the new 18-member Ensemble-RCS, a convective-scale regional ensemble coupled modelling framework, to integrate the features of the operational regional atmosphere ensemble forecast system MOGREPS-UK (Hagelin *et al.*, 2017) with the atmosphere-ocean-wave coupled modelling framework RCS (Lewis *et al.*, 2018). RCS incorporates convective-scale atmosphere, land, ocean and wave model components that can be run in coupled and uncoupled modes. The atmosphere and land component feedbacks are integrated in each coupled and uncoupled RCS mode, consistently with the latest MOGREPS-UK version (Porson *et al.*, 2020). In this implementation, the RCS atmosphere [Met Office Unified Model

MetUM (Walters *et al.*, 2017)] and land surface [the Joint U.K. Land Environment Simulator JULES (Best *et al.*, 2011)] components are run on a domain with 2.2-km horizontal grid spacing, matching the grid of the operational MOGREPS_UK system, and use the RAL1-M convective-scale science configuration (Bush *et al.*, 2020). As described in Lewis *et al.* (2019), the shelf-sea ocean component uses the Atlantic Margin Model (AMM15) regional configuration of the Nucleus for European Modelling of the Ocean [NEMO; (Madec, 2016)] coded on a grid with 1.5-km grid spacing and ocean surface waves are simulated using the corresponding regional configuration of WAVEWATCH III$^{©}$ (Tolman, 2016), defined on the AMM15 domain using spherical multi-cell grid (Li, 2011; Valiente *et al.*, 2021) with 1.5-km grid spacing (termed AMM15-SMC). The LBCs for the regional wave model configuration are taken from a global wave model simulation, as described in Lewis *et al.* (2019), which accounts for sizeable waves in the domain which are generated by storms located outside the domain. The surface flux parametrizations and ensemble perturbations used by the Ensemble-RCS are described in the following two subsections, and more details can be found in Lewis *et al.* (2018); Gentile *et al.* (2021).

#### 6.3.1.1 Surface flux parametrizations

The turbulent air-sea momentum flux, $\tau_0$, sensible heat flux, $H_0$, and moisture flux, $E_0$, are parametrized assuming that the Monin–Obukhov similarity theory holds in the surface layer scheme, yielding:

$$\frac{\tau_0}{\rho_0} = C_D|\Delta\mathbf{v}|^2, \tag{6.1}$$

$$\frac{H_0}{c_p\rho_0} = -C_h U\left(\Delta T + \frac{g}{c_p}(z_1 + z_{0m} - z_{0h})\right), \tag{6.2}$$

and

$$\frac{E_0}{\rho_0} = -C_h U \Delta q, \tag{6.3}$$

where $\rho_0$ is the air surface density; $C_D$ the momentum transfer coefficient; $c_p$ the specific heat capacity; $C_h$ the scalar transfer coefficient; the log-law wind speed $U$; the momentum and scalar roughness length $z_{0m}$ and $z_{0h}$; $z_1$ is the height of the bottom model layer above the surface; and $\Delta\mathbf{v}$, $\Delta T$, and $\Delta q$ are the gradients between surface and bottom model level of the velocity vector **v**, temperature $T$, and specific humidity $q$ fields, respectively.

In Eq. 6.1–6.3, the transfer coefficients for momentum, $C_D$, and scalar flux, $C_h$, depend on atmospheric stability, $\Psi$, and momentum, $z_{0m}$, and scalar roughness length, $z_{0h}$ (Bush *et al.*, 2020) as:

$$C_D = \left[ \frac{k}{\ln\left(\frac{z}{z_{0m}}\right) - \Psi_m} \right]^2, \tag{6.4}$$

$$C_h = \frac{k^2}{\left[\ln\left(\frac{z}{z_{0m}}\right) - \Psi_m\right]\left[\ln\left(\frac{z}{z_{0h}}\right) - \Psi_h\right]}, \tag{6.5}$$

where $k = 0.4$ is the von Kármán constant, $\Psi_m$ and $\Psi_h$ are the Monin–Obukhov stability function for momentum and scalar fluxes, and $z$ is the vertical height coordinate. In neutral conditions, parametrizations described in Eq. 6.4 and Eq. 6.5 model an approximately linear growth of transfer coefficients $C_D$ and $C_h$ with 10-m wind speeds. Over the sea, the momentum roughness length, $z_{0m}$, is described by the generalized Charnock formula:

$$z_{0m}(\text{sea}) = \frac{0.11\nu}{u_*} + \frac{\alpha}{g}u_*^2, \tag{6.6}$$

where $\nu = 14 \times 10^{-6}$ m$^2$ s$^{-1}$ is the kinematic viscosity of air, $u_*$ is the friction velocity, and $\alpha$ is the Charnock parameter, which accounts for increased roughness as wave heights grow due to increasing surface stress (Charnock, 1955; Smith, 1988). The RCS computes roughness length for scalar fluxes over the sea, $z_{0h}(\text{sea})$, based on $z_{0m}$ according to the surface divergence theory from Csanady (2001), full details in Edwards (2007) and Gentile *et al.* (2021). The friction velocity, computed as $u_* = \sqrt{C_D}|\Delta\mathbf{v}|$, together with the value of the momentum roughness length $z_{0m}$, determines the wind speed, $U$, according to the log-law:

$$U = \frac{u_*}{k}\left[\ln\left(\frac{z}{z_{0m}}\right) - \Psi_m\right]. \tag{6.7}$$

The Ensemble-RCS can be run in the uncoupled atmosphere-only mode, the partially coupled atmosphere-ocean mode and the fully coupled atmosphere-ocean-wave mode. When the RCS runs in uncoupled atmosphere-only mode (Atm-only), the momentum, heat and moisture fluxes are parametrized by the MetUM by making the following assumptions:

- the lower boundary of the atmosphere is at rest;
- the SST lower boundary condition provided by the Operational Sea Surface Temperature and Sea Ice Analysis OSTIA (Donlon *et al.*, 2012), is persisted throughout the simulation;
- the Charnock parameter, $\alpha$, in Eq. 6.6 is set to the empirically-based value, $\alpha = 1.1 \times 10^{-2}$, and it is persisted throughout the simulation.

In the partially coupled atmosphere-ocean (AO) mode, the MetUM atmosphere component receives hourly SST and ocean currents fields from the AMM15 ocean model to update the lower temperature and velocity boundary conditions, respectively, and in turn the scalar and momentum surface fluxes, surface pressure and velocity fields are used to drive the ocean component. As in the Atm-only mode, the Charnock parameter is a constant set to the empirically-based value $\alpha = 0.011$. Consequently, both the Atm-only and AO modes compute the momentum roughness length, $z_{0m}$, and the momentum and scalar transfer coefficients as a function of only the atmospheric surface layer.

In the fully coupled atmosphere-ocean-wave (AOW) mode, the MetUM atmosphere component sends the velocity field to both the AMM15 ocean model and the AMM15-SMC wave model. In turn, AMM15-SMC sends to the MetUM a spatially and temporally varying Charnock parameter which the MetUM uses to update the aerodynamic surface-roughness estimate through Eq. 6.6. As a result, the momentum roughness length $z_{0m}$ and, therefore, the scalar and momentum transfer coefficients, $C_D$ and $C_h$, depend on both the atmospheric surface layer flow and the underlying dynamic wave state via Eq. 6.4-6.5. A more detailed description of the RCS coupling can be found in Lewis *et al.* (2018, 2019) and Gentile *et al.* (2021).

#### 6.3.1.2 Ensemble perturbations

The 18-member Ensemble-RCS comprises a reference simulation (without perturbations) and 17 perturbed simulations that implement perturbations of the atmospheric state, but not of the ocean or wave state. The atmosphere components of the 17 perturbed members are initialised by perturbing about the upscaled UKV analysis with the downscaled perturbations from MOGREPS-G, while the reference member is initialised from the unperturbed upscaled UKV analysis. The design and workflow of the perturbations of the ICs and LBCs of the atmospheric component of the Ensemble-RCS forecast is represented in Fig. 6.2, along with the scheme of coupling between the ensemble atmosphere members and the deterministic ocean and wave models. A detailed explanation of the workflow is now given.

The Ensemble-RCS builds the perturbed ICs for the perturbed ensemble members by adding to the UKV analysis fields (upscaled from 1.5 to 2.2 km grid spacing) the 17 difference fields between the MOGREPS-G ensemble members and the ensemble mean at analysis time (downscaled from 20 to 2.2-km grid spacing) through the Incremental Analysis Update scheme (Bloom *et al.*, 1991). The reference member uses unperturbed ICs from the UKV analysis upscaled to 2.2-km grid spacing and uses LBCs from the unperturbed MOGREPS-G forecast downscaled to 2.2-km grid spacing. The perturbed ensemble members use the corresponding downscaled LBCs from the perturbed MOGREPS-G forecasts.

MOGREPS-G uses an Ensemble Transform Kalman Filter ETKF (Bishop *et al.*, 2001) to generate the ensemble perturbations of all the IC and LBC fields except the LBC SST field. The perturbations of the SST field are generated using the following perturbation approach of Tennant and Beare (2014):

1. compute the power spectrum of the climatological average of day-to-day differences in SST;
2. set the amplitude of each mode of the power spectrum to that of each mode of a triangular spherical harmonic expansion in the horizontal;
3. map back to the physical space; and finally
4. multiply the mapped spectrum by a monthly-mean day-to-day change, calibrating perturbations in the range $\approx +/-2$ K.

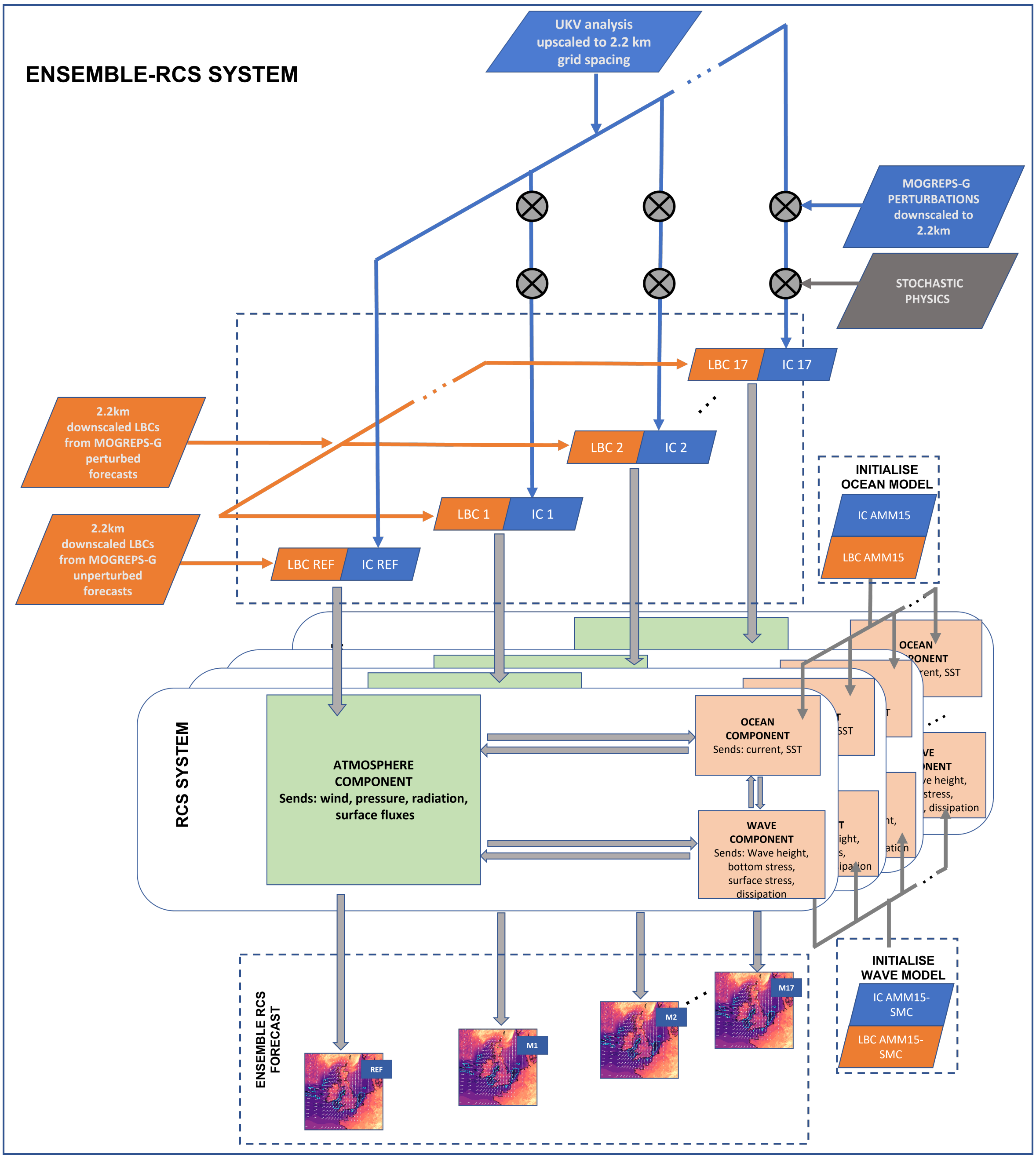

**Figure 6.2:** Ensemble-RCS design and workflow: integration of the atmosphere-only regional ensemble MOGREPS-UK capabilities with the regional coupled system RCS. Ensemble-RCS creates an ensemble of 17 RCS perturbed members and the reference unperturbed member, the latter initialised from the upscaled UKV deterministic analysis. RCS ocean component IC and LBC are taken from the deterministic AMM15 ocean model, while RCS wave model IC and LBC are taken from the AMM15-SMC wave model.

This perturbation methodology generates greater SST uncertainty in regions where day-to-day fluctuations are greater, e.g. the Gulf Stream, Kuroshio Current and the Polar front, which are also the regions above which cyclones form. Optionally, stochastic uncertainty is added to the physics parametrizations via the Random Parameter 2 scheme (RP2: McCabe *et al.*, 2016). A total of ten parameters from the boundary layer and microphysics parametrization schemes are perturbed in the RP2 scheme affecting boundary layer mixing, cloud formation, precipitation and droplet settling near the surface. Unlike the operational MOGREPS-UK system, in which the parameters are updated every five minutes via a firstorder autoregression model, the RECS-UK stochastic perturbations can only be applied once at the start. More precisely, each parameter $P$ is computed as:

$$P = \mu + \epsilon, \tag{6.8}$$

where $\mu$ is the arithmetic average $(P_{min} + P_{max})/2$, $P_{min}$ and $P_{max}$ are the minimum and maximum values bounds, and $\epsilon$ is the stochastic shock term sampled from a uniform distribution in the range $\pm(P_{max} - P_{min})/3$. The $P_{min}$ and $P_{max}$ bounds are estimated by experts of the field as the values that guarantee the perturbations are physically meaningful and realistic. It is important to note that the arithmetic average $\mu$ is different from the model default value of $P$ used in the unperturbed forecasts.

When the Ensemble-RCS is run in the partially coupled atmosphere-ocean mode, the atmosphere component of each of the 18 ensemble members is coupled to the AMM15 ocean model component, which runs on the 1.5 km grid and uses the OASIS3-MCT libraries (Valcke *et al.*, 2015) to map the ocean fields on the atmosphere component 2.2-km model grid. When the Ensemble-RCS is run in the fully coupled atmosphere-ocean-wave mode, the atmosphere component of each of the 18 ensemble members is coupled to both the AMM15 ocean and the AMM15-SMC wave components. Identical ocean ICs and LBCs are applied to the ocean component of all ensemble members, and thus, in the absence of additional perturbations, differences between ocean members are due solely to the differences in atmospheric forcing. Hence, to maintain the spread in SST for the atmosphere when run in coupled mode, the IC perturbations derived from MOGREPS-G (Tennant and Beare, 2014) are added back to the coupled SST after the SST field is passed from AMM15 to MetUM at each coupling time step (hourly frequency).

### 6.3.2 Ensemble regional coupled system experiments

Three Ensemble-RCS experiments (defined below) were carried out to investigate the sensitivity of Ensemble-RCS forecasts to atmosphere-ocean-wave coupling, and to three types of perturbations (to IC, LBC, and model physics parametrizations) for intense wind speeds during cyclone Ciara. Table 6.1 summarizes the five Ensemble-RCS configurations used in the three experiments, indicating for each ensemble configuration the perturbation strategy and degree of coupling.

| Ensemble Configuration | Perturbations | | | | Coupling | |
|---|---|---|---|---|---|---|
| | IC | LBC | Stochastic Charnock | Full Stochastic Physics | Ocean | Wave |
| Control_ENS | ✓ | ✓ | | ✓ | | |
| Atm-only_ENS | ✓ | ✓ | | | | |
| Atm-crk_ENS | ✓ | ✓ | ✓ | | | |
| AO_ENS | ✓ | ✓ | | ✓ | ✓ | |
| AOW_ENS | ✓ | ✓ | | ✓ | ✓ | ✓ |

**Table 6.1:** Ensemble-RCS configurations: for each ensemble configuration set up, the various perturbations applied and the coupling strategy used are indicated.

The aim of the first numerical experiment was twofold: first, to isolate the impact of applying the RP2 stochastic physics scheme to the 18-member ensemble created by using IC and LBC perturbations and second, to determine what fraction of the sensitivity to the stochastic perturbations is attributable to perturbation of the Charnock parameter. We do not investigate the sensitivity of Ciaras intense surface wind speeds to other parameters perturbed in the full RP2 scheme that could likely to influence air-sea interactions, such as the stability function and mixing length parameters, as we expect the sensitivity to Charnock parameter perturbations to dominate over them. Extreme midlatitude cyclones, such as Ciara, are associated with a strong wind forcing at the top of the boundary layer, which leads to a strong wind shear in the boundary layer, dominating in turn the production of turbulent kinetic energy. Because of the mechanical nature of turbulence production, momentum transfer from air to sea is more sensitive to changes in the sea state roughness $z_{0m}$(sea), via the Charnock parameter which in turn affects the sea-surface roughness and frictional dissipation at the surface (see Eq. 6.6 and more in detail Lewis *et al.* (2019); Gentile *et al.* (2021)), than to changes in the stability of the boundary layer.

Thus, in this experiment, three uncoupled Ensemble-RCS configurations were set up as follows.

1. The Control_ENS configuration, with IC, LBC, and RP2 stochastic perturbations. The latter is applied to the model parametrizations using $P_{min}$ and $P_{max}$ values listed in McCabe *et al.* (2016).
2. The Atm-crk_ENS configuration with IC and LBC perturbations and with RP2 stochastic physics perturbations applied only to the Charnock parameter. In particular, the RP2 scheme sets $P_{min} = 1 \times 10^{-2}$ and $P_{max} = 2.6 \times 10^{-2}$ for the Charnock parameter.
3. The Atm-only_ENS configuration using only IC and LBC perturbations.

The aim of the second numerical experiment was to isolate and quantify the impact of atmosphere-ocean coupling on the Control_ENS configuration of Ensemble-RCS, and in particular the impact of dynamical SST simulated by the ocean model. Therefore, the two-way atmosphere-ocean coupled configuration AO_ENS of Ensemble-RCS was set up by coupling each of the 18 Control_ENS members with the AMM15 deterministic ocean model.

Lastly, the aim of the third experiment was to isolate and quantify the impact of additionally coupling to the wave model on the Control_ENS configuration. The two-way atmosphere-ocean-wave coupled configuration AOW_ENS of Ensemble-RCS was set up by coupling each of the 18 Control_ENS members with the AMM15 deterministic ocean model and the AMM15-SMC deterministic wave model.

All the simulations were initialised at 0000 UTC 7 February 2020, after cyclone Ciara had formed in the MOGREPS-G and well before it came into the MOGREPS-UK domain. The simulations were run for five days until 0000 UTC 11 February 2020; however, the analysis of meteorological fields of interest does not extend beyond 0000 UTC 10 February 2020 as after this time cyclone Ciara exited the domain.

### 6.3.3 Characterization of ensemble dispersion

The spread between the ensemble members of a given Ensemble-RCS configuration provides an estimate of the uncertainty of that Ensemble-RCS forecast. To quantify the ensemble spread between the ensemble member forecasts of cyclone Ciara's 10-m wind speed of each of the five Ensemble-RCS configurations, two dispersion metrics were employed besides the commonly used box and whisker plots: the dispersion form of the Fractions Skill Score (dFSS), which provides a neighbourhood-based perspective on the ensemble spread, and the dispersion form of the Structure, Amplitude, Location score (dSAL), which provides an object-based perspective.

FSS (Roberts, 2008) and SAL (Wernli *et al.*, 2008) were initially developed, and have then been applied, to verify deterministic or ensemble convective-scale precipitation forecasts against radar observations (mainly for convective events). It is well known that, for such events, the precipitation field tends to be noisy, and so using well-established grid point forecast verification metrics likely leads to the double penalty problem where a small spatial displacement of localised precipitation in a forecast is penalised twice (for being absent where the precipitation was observed and present where no precipitation was observed). The FSS and SAL metrics can be used to overcome this problem. The FSS overcomes the problem because it considers the grid point fraction exceeding the chosen percentile threshold in a neighbourhood of grid cells, whose centre corresponds to the observing site. The SAL overcomes the problem by considering separately the structure (S), amplitude (A), and location (L) components of the ensemble forecast objects, identified by the contiguous sets of grid cells exceeding the chosen percentile threshold. Thus, a displaced precipitation object with the correct amplitude and structure would only have a poor location score.

Similarly to the precipitation field, the 10-m wind speed field in convective-scale simulations also tends to be noisy which implies that the FSS and SAL metrics could be more suitable than grid point forecast verification metrics for the assessment of the Ensemble-RCS configurations forecasts of cyclone Ciara's wind speeds. To date, this is the first study in which the FSS metric is applied to 10-m wind speeds while the SAL metric has previously been applied to

10-m wind speed gusts associated with wind storms by Zschenderlein *et al.* (2019). Since we want to compare ensemble member simulations against one another to determine the ensemble spread, rather than verifying a forecast against observations, the dispersion forms of FSS and SAL, termed dFSS and dSAL, are used here.

The dFSS, introduced by Dey *et al.* (2014) (termed dFSSmean there) and applied to ensemble precipitation forecasts, is used here to compare the similarity in wind fields between the 18 ensemble members of each Ensemble-RCS configuration. First, for each grid cell in each ensemble member forecast, it is determined the fraction of surrounding grid cells within a given size square neighbourhood whose field values exceed a specified wind speed percentile threshold. Then, for each of the $\binom{18}{2} = 153$ pairs of ensemble member forecasts, the FSS is computed as:

$$\text{FSS} = 1 - \frac{\text{FBS}}{\text{FBS}_{worst}}, \tag{6.9}$$

where FBS is the Fractions Brier Score, a variation of the Brier score (Brier, 1950) in which both forecasts probabilities (fractions) can take any value between 0 and 1, according to:

$$\text{FBS} = \frac{1}{N}\sum_{j=1}^{N}(M_{lj} - M_{nj})^2, \tag{6.10}$$

where $N$ is the number of grid cells in the domain, and $M_{lj}$ and $M_{nj}$ are the ensemble member forecast fractions of the $(l,n)$ pair at grid cell $j$. $\text{FBS}_{worst}$ is the worst possible FBS (largest) that is obtained when there is no collocation of non-zero fractions. It is calculated as:

$$\text{FBS}_{worst} = \frac{1}{N}\left[\sum_{j=1}^{N} {M_{lj}}^2 + \sum_{j=1}^{N} {M_{nj}}^2\right]. \tag{6.11}$$

Second and lastly, the dFSS is computed for neighbourhoods of increasing size, by evaluating the mean of the 153 FSS scores in Eq. 6.9. Larger values of dFSS indicate greater spread between ensemble members with possible values between zero and one.

The dSAL is the dispersion form of the object based verification method SAL, computed here by evaluating the spread of the SAL scores for each of the 153 pairs of ensemble members. The dSAL presented here compares ensemble member pairs to evaluate ensemble dispersion. It differs from that discussed in Zschenderlein *et al.* (2019) which is instead based on comparing each ensemble member and the ensemble mean with truth. Following the description of SAL in Wernli *et al.* (2008), a percentile wind speed threshold value is chosen for each ensemble pair $(l,n)$ to identify contiguous wind speed objects. The amplitude component for each pair $(l,n)$ is computed as:

$$A = \frac{D(M_l) - D(M_n)}{0.5[D(M_l + M_n)]}, \tag{6.12}$$

where the $D$ operator performs the average of a forecast field over the model domain. The location component $L$ is the sum of two parts $L = L_1 + L_2$. The first term, $L_1$, measures the normalized distance between the two centres of mass $\mathbf{x}(M_l)$ and $\mathbf{x}(M_n)$ of the $(l,n)$ ensemble member pair:

$$L_1 = \frac{|\mathbf{x}(M_l) - |\mathbf{x}(M_n)|}{d}, \tag{6.13}$$

where $d$ is the largest distance between two boundary points of the domain. The second term, $L_2$, measures the averaged distance between the centre of mass of the system of the forecast objects and the individual forecast objects. The structure component $S$ describes the shape and size of the forecast objects. It is computed as the difference between the weighted means of the scaled forecast field volume, $V$, of all objects in the ensemble member pair $(l,n)$, normalized as in component $A$:

$$S = \frac{V(M_l) - V(M_n)}{0.5[V(M_l + M_n)]}. \tag{6.14}$$

The amplitude, $A$, and structure, $S$, components are scaled so that their values extend from -2 to +2, and the possible values of location component, $L$, range from 0 to 1.

## 6.4 Results

In this section we present the results of the relative sensitivities of the wind speeds forecast by the ensembles to stochastic perturbations compared to ICs and LBCs perturbations (the first experiment described in Sec. 6.3.2) followed by results of the sensitivity to coupling to ocean and coupling additionally to waves (the other two described experiments). We conclude by comparing the spread characteristics of the coupled and uncoupled Ensemble-RCS forecasts.

### 6.4.1 Sensitivity to stochastic physics perturbations

This sensitivity experiment aims at determining the relative impacts of applying the RP2 stochastic physics scheme and the IC and LBC perturbations on the ensemble forecasts of cyclone Ciara's low-level wind jets. Figure 6.3a presents the 12-hourly time series of the distributions of the 95th percentile 10-m wind speed for the model domain obtained from each of the three atmosphere-only ensembles: the control ensemble with the full set of stochastic perturbations (Control_ENS), the ensemble with stochastic perturbations to the Charnock parameter only (Atm-crk_ENS), and the ensemble with no stochastic perturbations (Atm-only_ENS). For each simulation, the 95th percentile was computed over sea-only grid points to isolate the impact of stochastic perturbations of the Charnock parameter. The median (from the 18 ensemble members) of the Control_ENS 95th percentile 10-m wind speed increases from 15.7 m $s^{-1}$ at 0000 UTC 7 February 2020 (hour 0) to the peak value of 23.8 m $s^{-1}$ at 0900 UTC 9 February (hour 57). This rapid increase of wind speed highlights the rapid intensification of cyclone Ciara while crossing the North Atlantic, as discussed in Section 6.2. At peak wind time, the maps of the spread of the Control_ENS 10-m wind speed and MSLP, measured as the standard deviation of the ensemble members with respect to the mean, are depicted in Fig. 6.4a-b. An overlay of the spread of 10-m wind speed with the MSLP spread shows a close spatial agreement. The largest 10-m wind speed spread is localised around the area with sharp wind speed gradient, between the near-surface winds exceeding 18 m $s^{-1}$ associated with Ciara's densely packed isobars and the winds slower than 10 m $s^{-1}$ to the north. In this region of sharp gradient, the spreads in 10-m wind speed and MSLP arise from the slightly different tracks and frontal positions that each ensemble member simulates for Ciara. These differences between ensemble members in forecasts of Ciara's large-scale evolution are likely linked to the Control_ENS perturbations in ICs and LBCs. Shortly after cyclone Ciara makes landfall in the UK, the Control_ENS shows a rapid decrease of the median 95th percentile 10-m wind speed (between 1200 and 1800 UTC, corresponding to

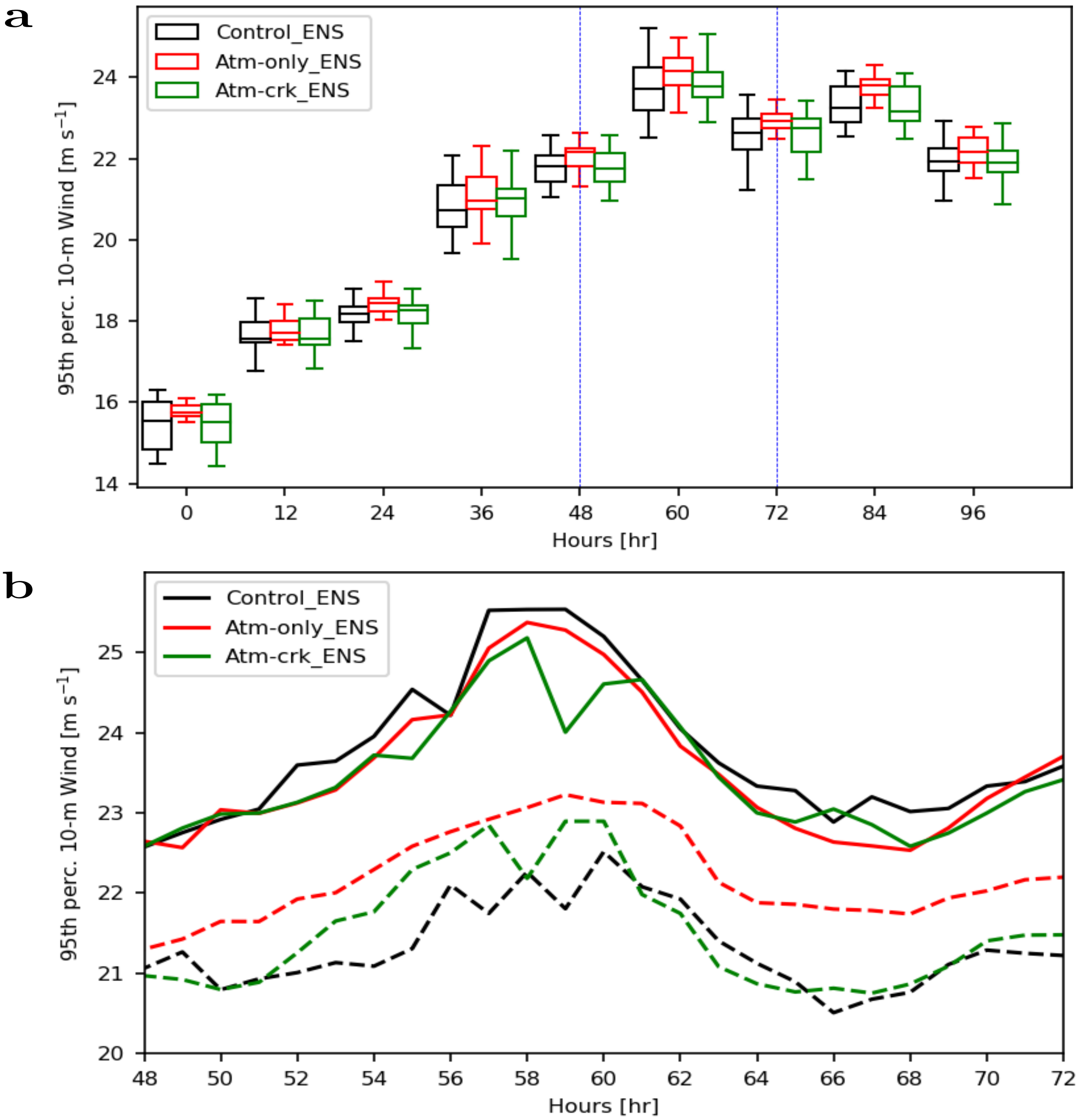

**Figure 6.3:** Time evolution of the spread of the 95th percentile 10-m wind speed forecast (computed on sea-only points) for the Control_ENS (black), Atm-only_ENS (red), and Atm-crk_ENS (green) ensembles. (a) 12-hourly box and whiskers plot for the three ensembles over the period 0000 UTC 7 February (hour 0)–0000 UTC 11 February 2020 (hour 96). The three plotted boxes of different colours relative to the same simulation hour are represented side by side, instead of overlapping, for greater clarity. (b) Hourly time series for the three ensembles over the period 0000 UTC 9–0000 UTC 10 February of the upper (solid) and lower (dashed) whiskers. In (a), each box indicates the first and the upper quartile of the 18 members of the associated ensemble and the median value; the upper and lower whisker limits indicate the maximum and minimum wind value, respectively, within $3\sigma$ from the mean. The blue vertical lines in (a) delimit the time period shown in (b).

hours 60 and 66 respectively, in Fig. 6.3a) associated with Ciara's decay. The Atm-only_ENS and Atm-crk_ENS of 10-m wind speed follow the same trend as the Control_ENS in

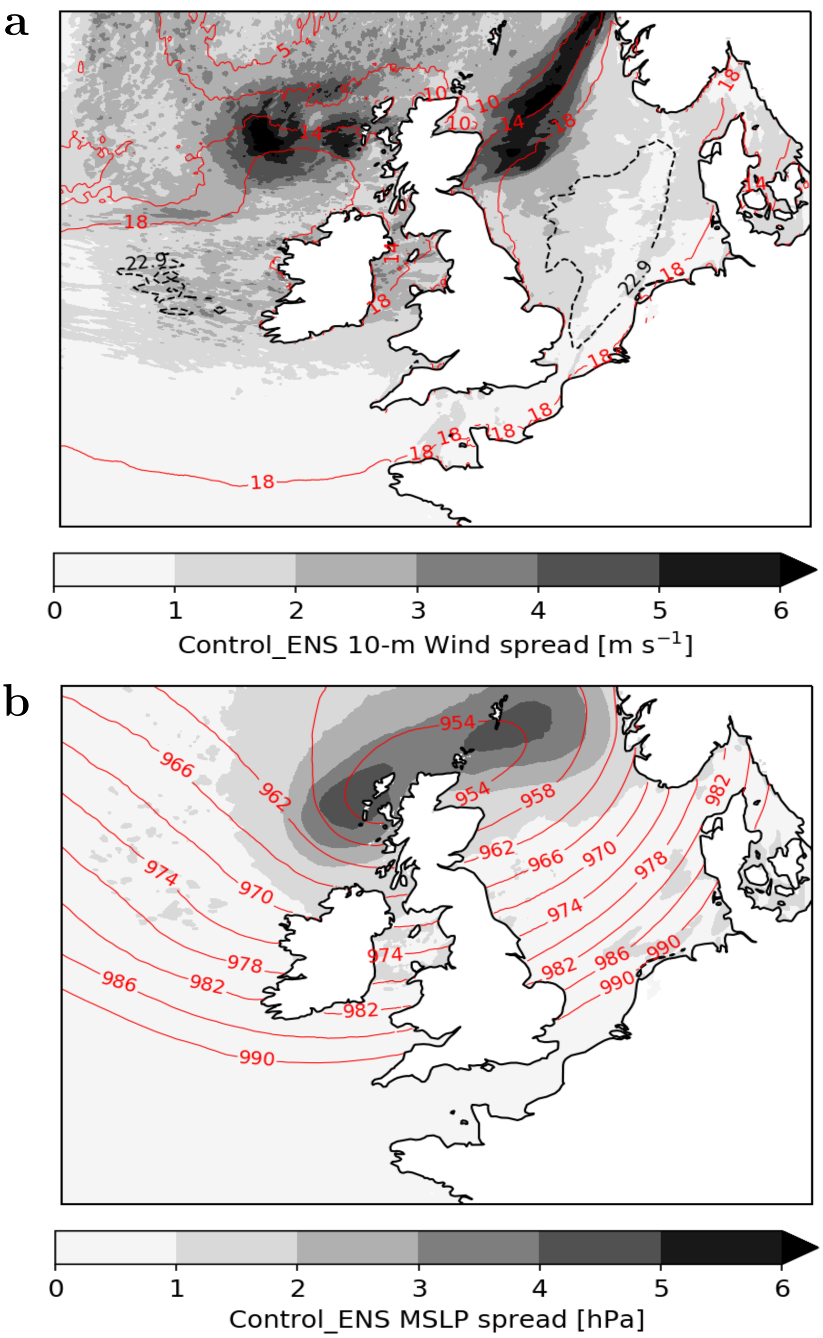

**Figure 6.4:** Contours plotted as solid red lines of the mean of the 18 Control_ENS ensemble member forecasts of (a) 10-m wind speed and (b) MSLP overlaid on the corresponding ensemble spread (grey scale) at 0900 UTC 9 February 2020. The spread is computed as the standard deviation of the 18 ensemble members with respect to the ensemble mean. The dashed black line in (a) indicates the contour of the 95th percentile of the 10-m wind speed field, computed over sea-only grid-points.

Fig. 6.3a over the entire simulation time. However, the median speed of the Atm-only_ENS ensemble forecast members is consistently slightly higher, by up to 0.5 m $s^{-1}$, than that of the Control_ENS and Atm-crk_ENS.

To examine more in detail the impact on the ensemble spread of applying the stochastic perturbations to the model physics parametrizations, the hourly time series of the upper and lower whiskers of the distribution of the 95th percentile 10-m wind speeds (indicating values $3\sigma$ from the mean) are shown in Fig. 6.3b focusing on the time period during which Ciara crossed the UK. The values of the upper whiskers for the Atm-only_ENS and Atm-crk_ENS follow those for Control_ENS values closely with only slight differences overall (values up to 0.3 m $s^{-1}$ smaller). In contrast, the lower-whisker values of the Atm-only_ENS and Atm-crk_ENS are more different to those of the Control_ENS. The lower-whisker values of the Atm-only_ENS are consistently above those of the other two ensembles (by up to roughly 1.5 m $s^{-1}$). The lower-whiskers values of the Atm-crk_ENS generally lie between those of the Control_ENS and Atm-only_ENS until 1200 UTC 9 February 2020 (hour 60); after this time, the Atm-crk_ENS values collapse to the Control_ENS values, and closely follow them for the rest of the period shown. Note that the dip at 59h in the upper whisker of the Atm-crk_ENS is an artificial feature that arises because, unlike at the other times, the second highest value of the 95th percentile 10-m wind speed distribution is plotted rather than the first.

The results of this first sensitivity experiment demonstrate that the larger ensemble spread between the upper and lower whisker values (which is dominated by the reduced lower whisker values) of the Control_ENS compared to that of the Atm-only_ENS stems from the application of the stochastic perturbations to the model parametrizations, consistent with the modest increase in the spread of MOGREPS-UK 10-m wind speeds found by McCabe *et al.* (2016) on applying the RP2 scheme to model physics parametrizations. In addition, the reduced median of the Atm-crk_ENS compared to the Atm-only_ENS can be explained by the increased surface stress simulated by the stochastic perturbations applied to the Charnock parameters. The perturbed Charnock parameters vary for the different ensemble members, but for a given ensemble member the Charnock parameter is spatially uniform over the grid cells. As a consequence of the $P_{min}$ and $P_{max}$ values used by the RP2 stochastic physics scheme for the Charnock parameter (given in Sect. 6.3.2), 16 of the 17 perturbed Charnock parameters created via Eq. 6.8 are larger than the constant value of $\alpha = 1.1 \times 10^{-2}$

used by the Atm-only_ENS (without stochastic perturbations) and Atm-crk_ENS reference (unperturbed) member, with a maximum of $\alpha = 2.6 \times 10^{-2}$. According to Eq. 6.6, a larger Charnock parameter leads to a larger aerodynamic sea-surface momentum roughness length, a larger air-sea momentum flux, and therefore reduced 10-m wind speeds in Ciara's low-level jets. It is also important to note the close similarity between the ensemble member spread of the 10-m wind fields for the Control_ENS and the Atm-crk_ENS between 60 and 72 hours (Fig. 6.3b), which suggests that the stochastic perturbations in the Charnock parameter are the main cause of the additional ensemble spread due to the stochastic perturbations during this time. However, the relative spread of the Control_ENS and Atm-crk_ENS may also be affected by the gradual divergence of ensemble member forecasts with time.

#### 6.4.1.1 Sensitivity to coupling to the ocean and waves

An indication of the sensitivity of cyclone Ciara's 95th percentile 10-m wind speed to ocean and wave coupling is given in Fig. 6.5 which shows time series of the absolute difference from the Control_ENS reference (unperturbed) member for the same members from the AO_ENS and AOW_ENS. To place the differences between the AO_ENS and AOW_ENS reference members and the Control_ENS reference member in context, the ensemble spread of the Control_ENS (spread of absolute differences of the members from the ensemble mean), arising from the perturbations to the ICs, LBCs and stochastic physics, is shown by the grey shading.

The absolute difference between the reference members of the AOW_ENS and Control_ENS is much bigger than that between the AO_ENS and Control_ENS (reaching maxima of $1.2\ \mathrm{m\,s^{-1}}$ and $0.2\ \mathrm{m\,s^{-1}}$, respectively). This implies that the impact of coupling to both ocean and wave models is much greater than that of coupling to the ocean model alone. Moreover, the difference between the AO_ENS and Control_ENS reference member is found to be comparable to about the lower quartile value of the control ensemble, while the difference between the AOW_ENS and Control_ENS reference member is found to be comparable to about the upper quartile value of the control ensemble. This result suggests that the impact of coupling the atmospheric model to both ocean and wave models is at least comparable in

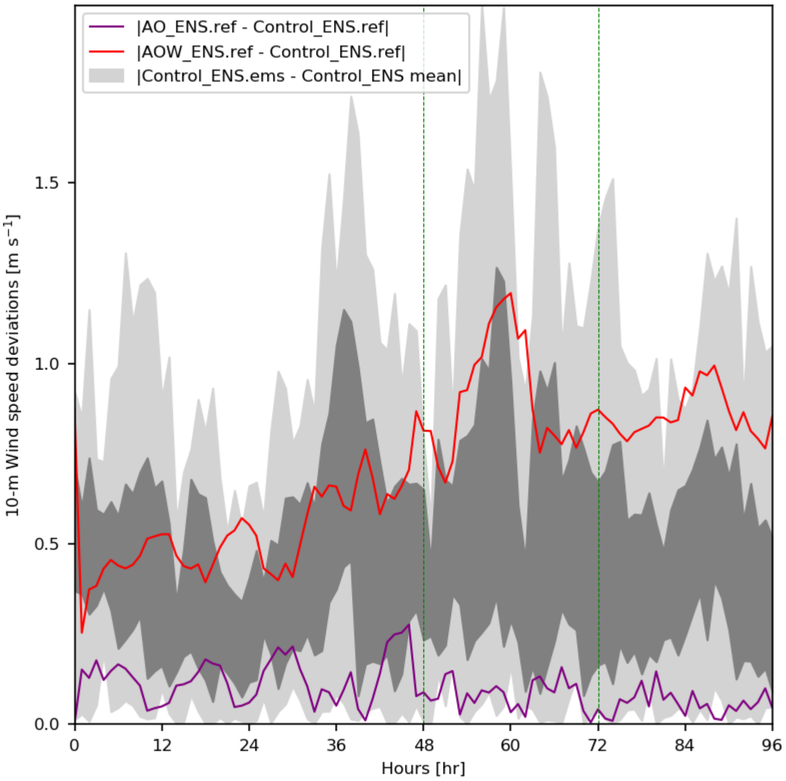

**Figure 6.5:** Time series of the quartile spread (light and dark grey bands) of the absolute difference in 95th percentile 10-m wind speed between the 18 Control_ENS members and the Control_ENS mean. The light grey indicates the control ensemble (Control_ENS) spread values below the lower quartile and above the upper quartile, while the dark grey represents the lower–upper quartile range. Overlaid is the absolute difference of the same quantity between the AO_ENS and Control_ENS reference members (purple) and between the AOW_ENS and Control_ENS reference members (red). Vertical green dashed lines indicate the range of hours of 9 February 2020.

size to that of adding IC, LBC and stochastic physics perturbations to the ensemble system when the near-surface wind speeds are intense (above 20 m s$^{-1}$, exceeding gale force).

The changes in behaviour of the simulated ensemble wind speeds on coupling to the ocean model, and to the ocean and wave models, are now described and further quantified in the following two subsections.

#### 6.4.1.2 Sensitivity to coupling to the ocean

The impact of coupling was further quantified by comparing the time series of the median, quartiles and extremes of the AO_ENS and the AOW_ENS against the Control_ENS (Fig. 6.6). The small sensitivity of cyclone Ciara's wind speeds to coupling to the ocean, for the reference simulations, relative to the Control_ENS spread arising from stochastic physics, IC and LBC perturbations indicated in Fig. 6.5 is confirmed by examination of Fig. 6.6a-b: the box plots of AO_ENS (red) and Control_ENS (black) wind speeds present negligible differences and the corresponding upper and lower whisker line plots nearly overlap. As a consequence, the spread of Ciara's wind speed forecasts in the AO_ENS can be attributed to the IC, LBC and stochastic physics perturbations with no marked effect from the coupling to ocean.

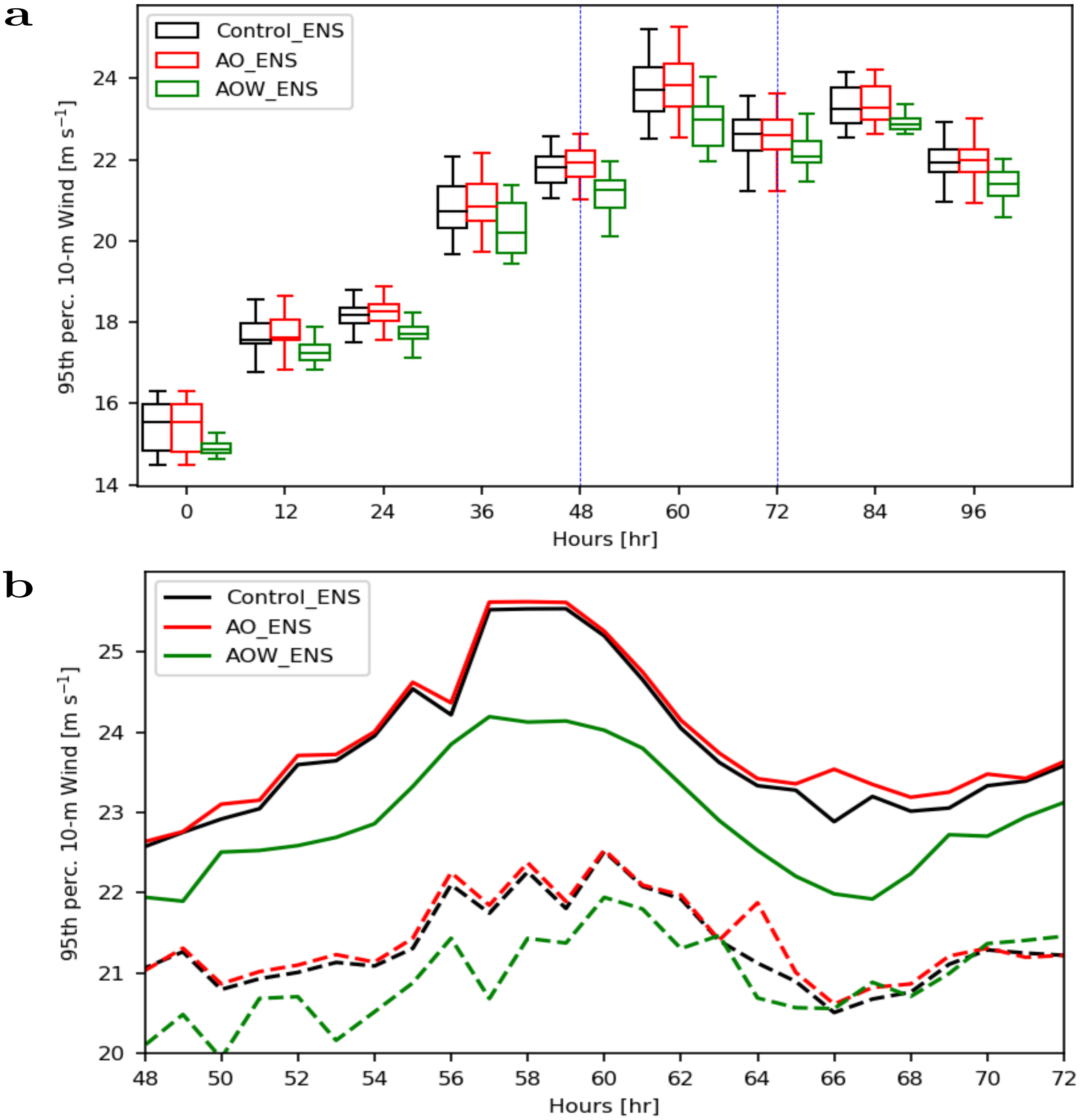

**Figure 6.6:** As for Fig. 6.3 but for Control_ENS (black), AO_ENS (red), AOW_ENS (green).

A closer inspection of instantaneous differences between the AO_ENS and the Control_ENS means of 10-m wind speed field at the peak wind speed time 0900 UTC 9 February 2020, reveals that the sensitivity of Ciara's winds to coupling to ocean is localised to three small regions in the domain (see Fig. 6.7a). The AO_ENS 10-m wind speeds exhibit reductions by up to 0.7 $\mathrm{m\,s^{-1}}$ compared to the Control_ENS off the west coast of Ireland, off the northern coast of France, and between the English Channel and the North Sea. In contrast, in the English Channel and in the Irish Sea increases of up to 1.5 $\mathrm{m\,s^{-1}}$ are found. Increases in the AO_ENS mean 10-m wind speed occur in those regions where this ensemble predicts warmer SSTs than the Control_ENS (Fig. 6.7b), and decreases occur where the SSTs are cooler; recall that the SST values for the Control_ENS are persisted from ICs. More specifically, SST reductions (and associated wind speed reductions) occur off the coast of Brittany and in the southern North Sea (up to 0.4 K in both regions), and off the west coast of Ireland (up to 0.7 K ). Ciara's strong low-level jets, identified by the 95th percentile 10-m wind speed contour, occur in the latter two regions at this time. A plausible physical argument for the response of the AO_ENS 10-m wind speed to SST follows. Cooler SSTs likely increase the near-surface potential temperature gradient, enhancing the stability of the surface layer in the AO_ENS forecasts. Since, typically, in the intense wind speed regions of a cyclone the boundary layer is quasi-neutral, a small increase in stability does not consistently alter the overall turbulent kinetic energy budget dominated by wind shear. This lack of consistency leads to very localised and patchy reductions in 10-m wind speeds over the domain. In the regions characterised by weaker wind speeds, such as off the coast of Brittany, the contribution of wind shear to the turbulent kinetic energy budget is likely to be less dominant. Consequently, near-surface wind speeds can be more susceptible to stability increases, as described by Monin–Obukhov similarity theory, leading to a uniform reduction in 10-m wind speeds across the region. In contrast, in regions such as the Irish Sea, where coupling to ocean increases the SSTs, the 10-m winds also increase because warmer SSTs reduce boundary layer static stability, increasing the entrainment of fast-flowing air from aloft. The impact of this mechanism is most evident far from the most intense Ciara winds.

The spread of the AO_ENS forecasts of SST at peak wind time increases poleward, as the distance from the greater reductions in SSTs increases, reaching a maximum of 1.2 K (roughly 6 times larger than that in the regions where the impact of coupling to ocean is more important (Fig. 6.7c)). Consequently, although the ensemble mean wind speed reduction on coupling to the ocean occurs in regions where there is a reduction in SST, and the wind speed increase occurs where there is increased SST, these regions are characterised by relatively small ensemble spread in SST. Moreover, the spread of SSTs in the AO_ENS at the initialisation and peak wind speed times (0000 UTC 7 and 0900 UTC 9 February, respectively) is very similar (compare Figs. 6.7d and c). Hence, the structure and size of the SST ensemble spread is predominantly attributable to the size and distribution of IC perturbations of SSTs, with these dominating over the dynamically evolved changes in the SST field. This result is expected because the MOGREPS-G SST perturbations (Tennant and Beare, 2014) downscaled to 2.2-km are added back to the AO_ENS SST ensemble forecasts

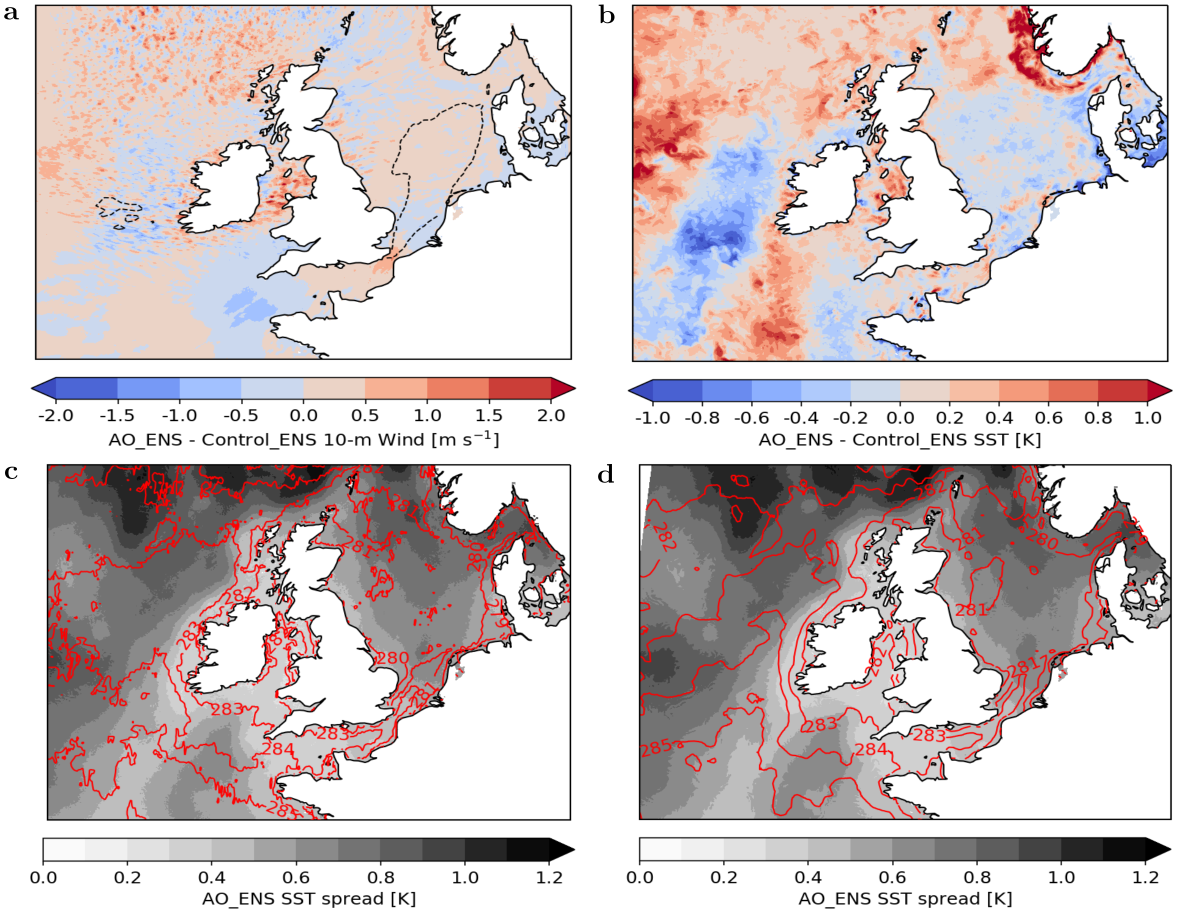

**Figure 6.7:** Maps of differences between the ensemble mean of AO_ENS and Control_ENS for (a) 10-m wind speeds and 95$^{\text{th}}$ percentile contour (dashed black line) of Control_ENS 10-m wind field ( (b) SSTs at 0900 UTC 9 February 2020. Maps of AO_ENS SST ensemble spread (grey colours) and SST AO_ENS ensemble mean contours (solid red lines) (c) 0900 UTC 9 February 2020 d) 0000 UTC 7 February 2020.

at each coupling time step (as described in Sect. 6.3.1.2).

#### 6.4.1.3 Sensitivity to coupling to waves

The time series illustrated in Fig 6.6a-b shows that the ensemble simulations of cyclone Ciara's wind speeds are characterised only by a small sensitivity to coupling to the ocean, but by a strong sensitivity to additionally coupling to waves. The AOW_ENS median of the 95th percentile 10-m wind speeds is consistently reduced by $\approx 1$ m $\mathrm{s}^{-1}$ compared to both the Control_ENS and AO_ENS ensemble median. Also the values of the upper and lower whiskers are reduced on additionally coupling to waves, particularly for the upper whisker, with a maximum reduction of $\approx 1.5$m $\mathrm{s}^{-1}$ around 0900–1200 UTC 9 September (especially evident after the peak wind speed time). As the Control_ENS and AO_ENS distributions are nearly identical, the downward shift of the AOW_ENS distribution of Ciara's 10-m wind speeds can be attributed to coupling to the wave model rather than to coupling to the ocean model.

The spatial structure of the sensitivity of Ciara's peak wind speeds to coupling to waves is illustrated by the instantaneous differences between the means of the AOW_ENS and the Control_ENS 10-m wind speed forecasts at the peak wind time (Fig. 6.8a). The mean values of the 10-m wind speeds are decreased over most of the domain in the AOW_ENS relative to the Control_ENS. More specifically, the wind speed is reduced by up to 1.5 m $\mathrm{s}^{-1}$ in the strong wind-speed regions extending from the central to the southern North Sea and off the west coast of Ireland (where the strong wind region is indicated by dashed contour outlining the 95th percentile wind speed) and by up to $\approx 1$ m $\mathrm{s}^{-1}$ off the north coast of Brittany. From comparison of Figs. 6.7a and 6.8a, it is evident that the reductions off Brittany and Ireland on coupling to ocean and wave are about 50% larger in size and geographical extent than those on coupling to ocean only. These results indicate that for this cyclone case the impact on the ensemble forecasts of additionally coupling to wave is stronger and more coherent than coupling to ocean only, as might be anticipated from the deterministic coupled simulations of cyclone case studies in Lewis *et al.* (2018), Wahle *et al.* (2017) , Lewis *et al.* (2019), and Gentile *et al.* (2021).

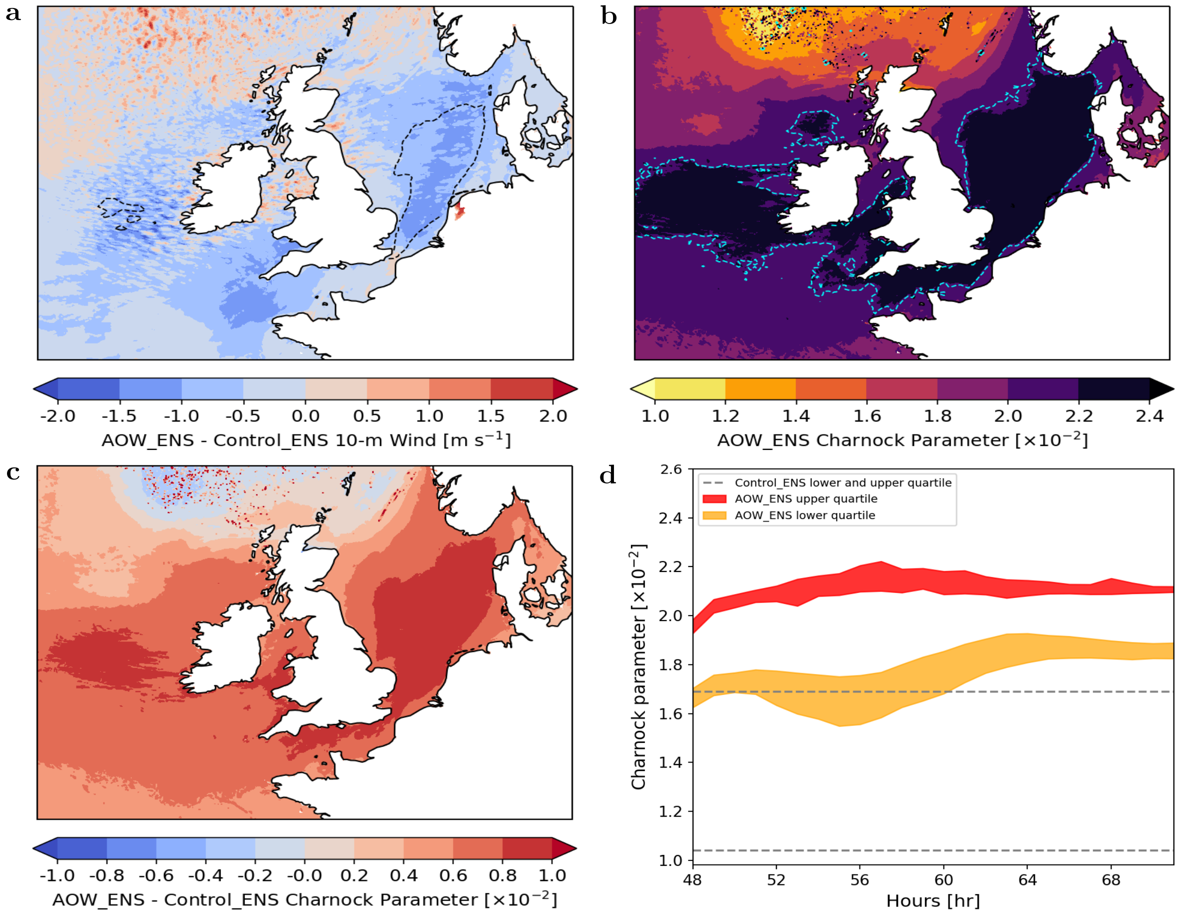

**Figure 6.8:** (a) Difference between the means of AOW_ENS and Control_ENS forecasts of 10-m wind speed and 95th percentile contour of Control_ENS 10-m wind field (dashed black). (b) AOW_ENS ensemble mean of Charnock parameters and contour (dashed cyan) of the corresponding upper quartile overlaid (c) Difference between means of AOW_ENS and Control_ENS Charnock parameters. (a-c) all at 0900 UTC 9 February 2020. (d) Time series computed over 9 February 2020 of the spread of the upper (red filling) and lower (orange filling) quartile of the of AOW_ENS forecasts of Charnock parameters, and upper quartile and lower quartile (dashed grey lines) of the Control_ENS stochastic Charnock parameters.

Regarding the dynamical evolution of the wave state at peak wind time, the snapshot of the AOW_ENS mean of the Charnock parameters (Fig. 6.8b) shows that the momentum transfer into the sea (as inferred from the Charnock parameter) is more pronounced where the 10-m wind speed reductions on additionally coupling to waves are larger (Fig. 6.8a). Comparison of Fig. 6.8b-c reveals that the mean of the AOW_ENS Charnock parameter field increases by up to $1 \times 10^{-2}$ from the Control_ENS mean value of $1.4 \times 10^{-2}$, reaching local maxima of $2.4 \times 10^{-2}$ where 10-m wind speed reductions are largest (nearing $-1.5$ m s$^{-1}$). Recall that, unlike in the Control_ENS, the AOW_ENS Charnock parameter field varies temporally as well as spatially. According to the momentum roughness length parametrization (Eq. 6.6), the increases in the Charnock parameters on coupling to ocean and waves lead to an enhanced simulated sea-surface aerodynamic roughness. Therefore, according to Eq. 6.4, the sea-surface stress is increased and consequently also the air-sea momentum transfer, explaining the 10-m wind speed reductions in the AOW_ENS compared to the Control_ENS.

Time series of the spread (over the ensemble members) of the Charnock parameter values are shown in Fig. 6.8d by the lower and upper quartile values; note that the range in these values shown for the AOW_ENS arises from the range across the domain (values are constant across the domain for the Control_ENS). The Charnock parameter values in the AOW_ENS are already markedly above those in the Control_ENS even at the start of the period during which Ciara crosses the model domain. As Ciara intensifies, the upper quartile of the AOW_ENS distribution of the Charnock parameter field diverges from that of the Control_ENS, growing in size and spread, with the maximum value of $\approx 2.1--2.2\times10^{-2}$ reached at peak wind time. The AOW_ENS upper quartile of Charnock parameter increases with time to a peak value at about 50 hours, similar to that of the 95$^{\text{th}}$ percentile distribution of wind speed shown in Fig. 6.6. In contrast, the lower AOW_ENS quartile only increases consistently after the peak wind speed time to lie about $0.7\times10^{-2}$ above the corresponding Control_ENS lower quartile. Hence, the increases in the Charnock parameter on coupling to waves seen in the instantaneous data shown in Fig. 6.8c are consistent across the simulation hours. Moreover, the upper quartile of the AOW_ENS Charnock parameters increases until a peak at 0900 UTC on 9 February 2020 when the 95$^{\text{th}}$ percentile 10-m wind speeds are maximum, which suggests that the most intense near-surface wind speeds are associated with regions of strongest wave growth.

The physical relationship between wind speeds and Charnock parameter explains the similarity between the temporal trends of the upper quartile of the AOW_ENS Charnock parameters and the 95$^{\text{th}}$ percentile 10-m wind speeds as follows. As the value of the upper quartile of the AOW_ENS distribution of Charnock parameters increases, the ocean becomes rougher and young growing waves extract an increasingly larger amount of momentum from the overlying airflow, driving the reductions in the AOW_ENS 10-m wind speeds observed in Fig. 6.6a-b. Space and time-varying Charnock parameters simulated by the AOW_ENS moderate the dynamic response of Ciara's near-surface wind speeds to the evolving wave state. This dynamic response cannot be captured by the Control_ENS and AO_ENS because they use stochastically perturbed Charnock parameter values that are constant at each ocean grid cell throughout the simulation time.

Finally, the impact of coupling to waves was also assessed in terms of wind strike probability for the control and the two coupled ensemble simulations during 9 February 2020, when cyclone Ciara crosses the model domain (Fig. 6.9). For each member, each grid point in the domain was labelled with a binary value to identify whether the 10-m wind speed exceeded, or not, a storm wind threshold chosen as $U_{10} = 24$ m s$^{-1}$, in a 300 km radius circle having that grid point as its centre. The wind storm threshold corresponds to a Beaufort scale of 9 (strong gale), which has associated effects over the sea of high waves with their crests beginning to topple, tumble and roll over. At the end of the labelling process, the probability of the ensemble members exceeding the storm wind threshold (strike probability) was computed for each grid point. As expected, the largest Control_ENS wind strike probability features (> 50%) are located in regions corresponding to the areas swathed by the cold and warm conveyor belts of cyclone Ciara (Fig. 6.9a). The strike probabilities for the AO_ENS are generally slightly higher (by between about 10–30%) over a wide region. Consistent with the peak wind speed instantaneous difference maps and the time series of the distributions of ensemble winds, the strike probability shows a stronger sensitivity to coupling to waves and ocean than coupling to ocean alone. Although the strike probabilities reach up to 100% for all three ensembles, the AOW_ENS wind strike probabilities are consistently reduced compared to the Control_ENS, by at least 10%, across most of the domain, resulting in an approximate halving of the size of regions where the strike probabilities exceed 50%. In the central North Sea, the Control_ENS wind strike probability is reduced by as much as 70%, with reductions between 50–70% in the southern North Sea and the English Channel. The marked reductions in strike probabilities on coupling to waves occur for all the times that Ciara is in the domain, consistent with the dynamical interpretation of the wind-wave feedback provided earlier.

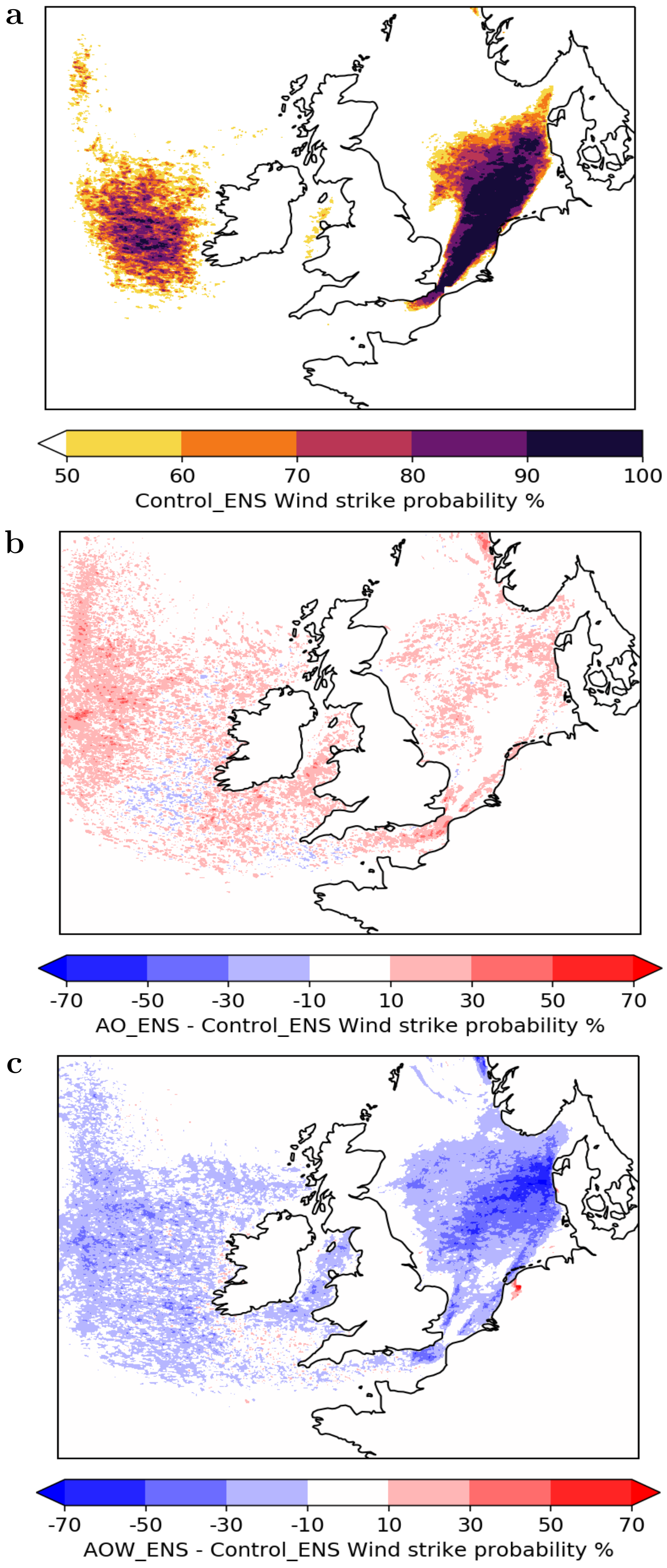

**Figure 6.9:** (a) Map of wind strike probability of exceeding the "storm wind" threshold, $U_{10} = 24$ m s$^{-}$1, computed over 9 February 2020 for Control_ENS. Map of wind strike probability differences (with sign) between (b) AO_ENS and Control_ENS (c) AOW_ENS and Control_ENS.

### 6.4.2 Ensemble dispersion

Two convective-scale metrics were used to characterize the spread of the five ensemble forecasts of Ciara's 10-m wind speed at peak wind speed time (0900 UTC on 9 February 2020): the dFSS and dSAL metrics described in Sect. 6.3.3 applied using the 95th percentile wind speed threshold.

The dFSS as a function of neighbourhood size for all the Ensemble-RCS configurations is shown in Fig. 6.10. Larger values of dFSS imply that the ensemble members are more similar to one another and the neighbourhood size is the width of the domain over which the similarity is calculated at each grid point. The Atm-only_ENS has the highest dFSS (i.e. most similar members) starting at $\sim 0.55$ at 2.2-km horizontal scale and reaching $\sim 0.75$ at 68.2 km horizontal scale. The Atm-crk_ENS dFSS is less than that of the Atm-only_ENS only by $\sim 0.05$ at the 2.2-km scale but, as the neighbourhood size increases, diverges slightly from that of Atm-only_ENS reaching $\sim 0.65$ at 68.2 km horizontal scale (0.1 lower than the Atm-only_ENS value). The dFSS values for the remaining three ensembles are similar to one another and lower than for the Atm-only_ENS by up to 0.2. The difference between the dFSS for the Atm-only_ENS and Atm-crk_ENS indicates that Charnock perturbations increase the

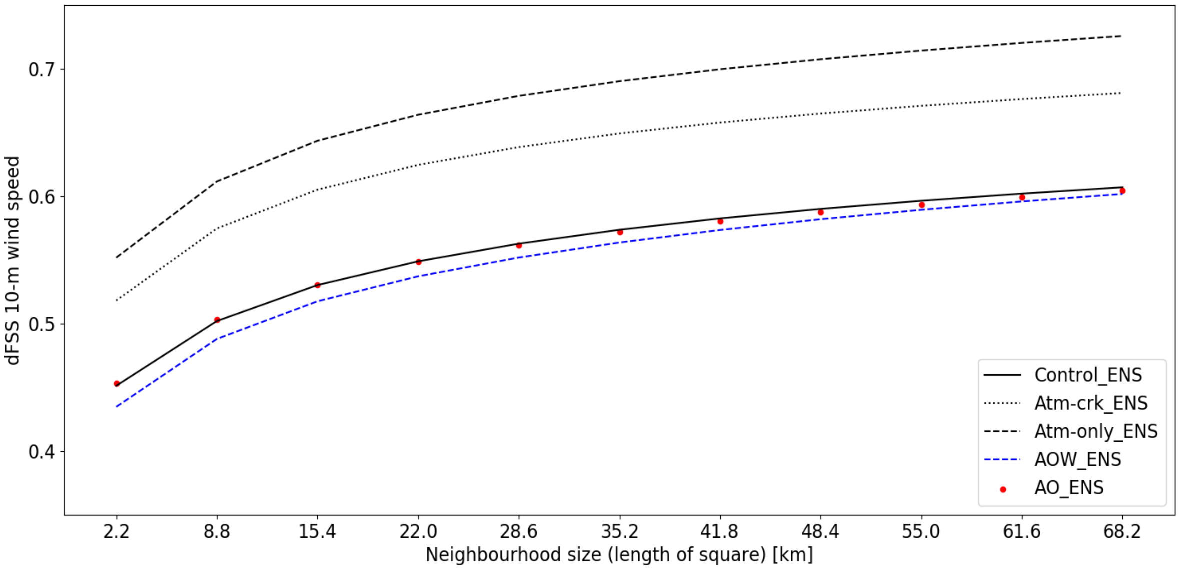

**Figure 6.10:** Dispersion metric dFSS evaluated at 0900 UTC on 9 February 2020 for the 95th percentile 10-m wind speed ensemble forecast of Control_ENS (solid black), Atm-crk_ENS (dotted black), Atm-only_ENS (dashed black), AO_ENS (red dots), AOW_ENS (dashed blue) as a function of neighbourhood of increasing size

ensemble spread by ≈ 20% relative to IC and LBC perturbations alone. Adding the complete set of stochastic perturbations (yielding the Control_ENS) enhances the ensemble spread by an additional ≈ 20%. In contrast, coupling to ocean and wave models does not change the dFSS of the ensembles relative to the Control_ENS. Overall, these results imply that coupling preserves, at all spatial scales considered, the dFSS in 95$^{\text{th}}$ percentile 10-wind speeds, unlike the addition of stochastic physics perturbations which instead increases the dFSS values.

The dispersion of the 95$^{\text{th}}$ percentile 10-m wind speed objects was investigated with the dSAL metric. Scatterplots showing the three dSAL components for each pair of ensemble members are shown in Fig. 6.11, with each panel showing results for a different ensemble. For each ensemble, larger amplitude component values are generally associated with larger structure component values so if the wind speed objects for an ensemble member have larger wind speed values, compared to the other member in the pair being considered, then they are usually also wider or flatter. Note that, because we are comparing pairs of equally likely ensemble members, the two members are arbitrarily assigned as member $l$ or $n$ in Eqs. 6.12–6.14 and hence also the sign of the structure and amplitude component is arbitrary as they could both have equivalently the opposite signs, but the same magnitudes, to those plotted. Higher location component values are generally associated with larger magnitudes of the amplitude and structure components implying that larger differences in amplitude or structure between the ensemble pairs are typically also associated with larger relative shifts in the 95th percentile wind speed area in the ensemble forecast pairs, as most of intense wind speed features occur in single objects.

The spread of the values of each component across the ensemble member pairs can be considered as a further metric for the ensemble spread. Comparison of the dSAL Control_ENS results in Fig. 6.11a against those for the Atm-only_ENS and Atm-crk_ENS in Fig. 6.11b-d, respectively, indicate that applying stochastic physics perturbations in addition to the IC and LBC perturbations enhances the ensemble spread, particularly in the amplitude component. The ensemble spread can also be inferred from the median values of the absolute dSAL components, as given in Table 6.2. The median values are largest for the structure component, followed by the location and amplitude components. However, comparison of the medians for the different ensembles (Table 6.2) shows, consistently with the visual impression from Fig. 6.11, that the proportional differences in the spread between the different ensembles is largest for the amplitude component. The spread in the amplitude component is smallest for the Atm-only_ENS and increases on adding the stochastic perturbations to the Charnock parameter (Atm-crk_ENS) and then further on adding the full set of stochatic perturbations (Control_ENS). As can be seen from Fig. 6.11a, c and e, the distribution of the Control_ENS dSAL scatter values is nearly identical to that of the AO_ENS, but exhibits a nearly 20% larger dispersion in the amplitude component, and slightly less than 10% larger dispersion in the structure and location components compared to the AOW_ENS. These results imply that coupling to ocean does not substantially affect the spread of the dSAL components. However, a small reduction in the medians of the absolute structure, location, and, particularly, amplitude component can be observed when coupling also to waves, likely attributable to the reduced wind speeds in the AOW_ENS simulations.

| RECS-UK configuration | S | A | L |
|---|---|---|---|
| Atm-only_ENS | 0.26 | 0.022 | 0.09 |
| Atm-crk_ENS | 0.27 | 0.030 | 0.10 |
| Control_ENS | 0.29 | 0.041 | 0.11 |
| AO_ENS | 0.27 | 0.039 | 0.11 |
| AOW_ENS | 0.27 | 0.033 | 0.10 |

**Table 6.2:** Median of absolute dSAL structure, amplitude, location components for the five Ensemble-RCS configurations.

Overall, the neighbourhood-based dFSS and object-based dSAL results agree with the grid-point-based box and whisker plots in indicating an enhancement of atmospheric ensemble spread on applying the stochastic perturbations to the Charnock parameter, and a further enhancement of spread on applying the full set of stochastic perturbations. Grid-point-, neighbourhood-, and object-based metrics also agree on the roughly equal size of the ensemble spread of the Control_ENS and AO_ENS. In contrast, when considering the AOW_ENS ensemble spread relative to those of the AO_ENS and Control_ENS, the dFSS disagrees with grid-point-based and object-based dSAL metrics. In particular, the box and whiskers plots and the amplitude component of the dSAL (but less so for the structure and location components)

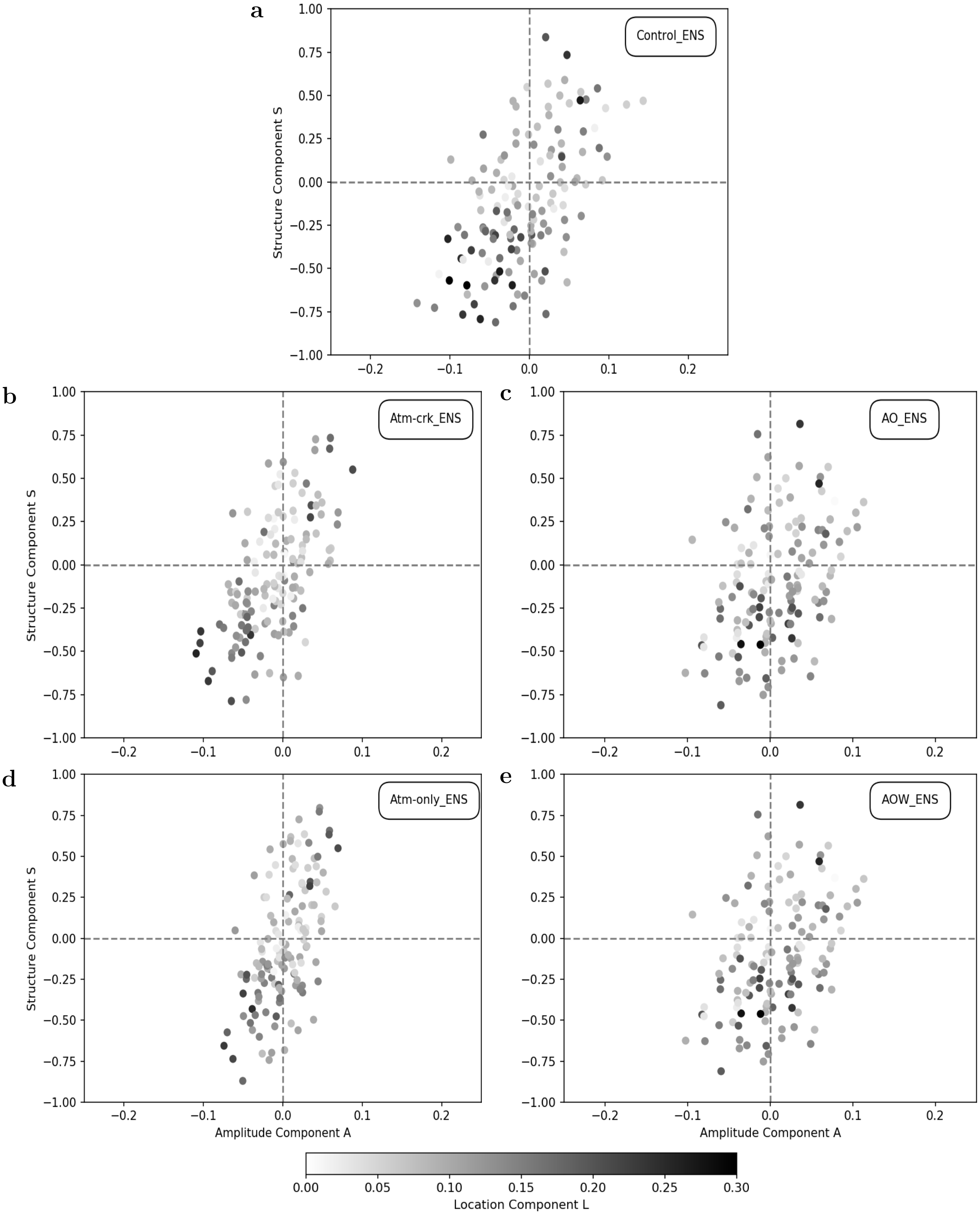

**Figure 6.11:** Diagram representing the dispersion SAL metric (dSAL score) computed at 0900 UTC on 9 February 2020 for each ensemble pair of the (a) Control_ENS, (b) Atm-crk_-ENS, (c) AO_ENS, (d) Atm-only_ENS, (e) AOW _ENS configurations.

show the AOW_ENS is slightly under-spread compared to the AO_ENS and Control_ENS, while the dFSS results indicate that AOW_ENS is slightly overspread compared to AO_ENS and Control_ENS. This difference is likely due to the box and whisker plots and the amplitude component of the dSAL being more sensitive to the magnitude of the wind speeds whereas the dFSS more sensitive to a shift in location of the wind structure object. However, note that coupling does not change the spread of the dSAL components as much as removal of the stochastic physics perturbations. Similarly, for a neighbourhood size of 68.2 km the dFSS value of AOW_ENS approaches those of AO_ENS and Control_ENS.

## 6.5 Conclusions

Integrating regional atmosphere, ocean, and wave model components into a coupled system is being increasingly trialled by research groups and operational centres (Lewis *et al.*, 2018; Wahle *et al.*, 2017; Ricchi *et al.*, 2017; Varlas *et al.*, 2017). Direct simulation of the effect of the dynamical ocean and wave state on air-sea surface exchange coefficients is expected to better represent surface fluxes and so improve forecasts of weather systems with strong near-surface wind speeds, such as extratropical cyclones. Undoubted benefits have been shown by coupling in convection-permitting, $\mathcal{O}1$ km, grid-spacing deterministic models and coarser medium-range, $\mathcal{O}10$ km, grid-spacing EPS (Varlas *et al.*, 2017; Ricchi *et al.*, 2017; Lewis *et al.*, 2019; Holt *et al.*, 2011). However, with the exception of Bousquet *et al.* (2020) which investigated the performance of a 1D ocean-mixed-layer model ensemble, there are, to date, no published studies considering whether dynamical coupling could also bring benefits to convective-scale short-range EPS.

The present study investigated, for an intense cyclone case study, the respective impacts of atmosphere-ocean-wave coupling, IC and LBC perturbations and stochastic physics perturbations within a convective-scale ensemble coupled system. For that purpose, we developed the first (to our knowledge) ensemble regional coupled system, the 18-member 2.2-km grid-spacing Ensemble-RCS focused on the British Isles and surrounding seas, by implementing the ensemble capability of the Met Office's operational ensemble system (MOGREPS) in their regional coupled system (RCS). The resulting Ensemble-RCS was run in coupled and uncoupled modes for the severe weather period of 7–10 February 2020, which saw the most intense cyclone, named Ciara, crossing the UK since storm Tini (12 February 2014). The impacts of coupling to ocean only and to both ocean and waves were assessed. Three different versions of the uncoupled system were also run to determine the impact of the stochastic physics perturbations, with these perturbations applied at initialisation time and persisted throughout the forecast. The spread between the ensemble members of a given configuration was quantified using, besides the commonly used box and whisker plots, the dispersion forms of the neighbourhood-based metric Fractions Skill Score (dFSS) and the object-based metric Structure, Amplitude, Location score (dSAL).

Applying the stochastic physics scheme to the ensemble created by using IC and LBC perturbations (Control_ENS and Atm-only_ENS, respectively) enhanced the ensemble spread of Ciara's 95th percentile wind speeds, as assessed by both box and whisker plots of wind speed values and the dFSS and dSAL metrics. Moreover, the reduction by up to 0.5 m $s^{-1}$ in the median of the ensemble wind speed indicated that the ensemble distribution of Ciara's intense wind speeds was shifted slightly downward by the stochastic physics perturbations. Comparison of Control_ENS and Atm-crk_ENS configurations showed that a substantial proportion of the impact obtained from applying the full set of stochastic physics perturbations was attributable to stochastic perturbations of the Charnock parameter alone, revealing the relative importance of this specific perturbation.

The ensemble spread was nearly unchanged on coupling to ocean (AO_ENS), indicating the localised nature of the ocean's impact on the ensemble. Small increases in the 10-m wind speeds occurred, likely due to decreased static stability in the surface layer by SST warming; similarly, small decreases in winds occurred, likely due to increased static stability by SST cooling. However, only the increases in wind speeds affected the AO_ENS strike probabilities, corresponding to enhancements of roughly 10–30%.

Additionally coupling to waves (AOW_ENS) led to a marked downward shift by 1 m $s^{-1}$ in the median of the ensemble distribution of Ciara's intense wind speeds, along with a consistent reduction of the ensemble mean by up to 1.5 m $s^{-1}$ at peak wind time. Although a comparable impact on coupling to waves has been observed by a number of studies running deterministic coupled forecasts of cyclones striking both the Mediterranean basin and the North Atlantic (Ricchi *et al.*, 2017; Varlas *et al.*, 2017; Wahle *et al.*, 2017; Ricchi *et al.*, 2019; Gentile *et al.*, 2021), here we report the consistency of this impact across all the perturbed (and the unperturbed) members of the ensemble forecast of Ciara for intense 10-m wind speeds. Moreover, this impact proved to be consistent for all Ciara's simulation hours, as indicated by the observed reduction by up to 70% in value and 50% in the extent of high (exceeding 50%) wind strike probability relative to the Control_ENS. The relationship between the ensemble distribution of the AOW_ENS Charnock parameters and the 95th percentile ensemble Ciara wind speeds confirmed that the coupling to wave impact could be attributed to the response of wind speeds to the young ocean waves dynamically simulated by the wave model. In contrast, the other ensemble configurations were unable to capture this feedback because, for a given simulation member, the Charnock parameter was constant in time and for all grid cells, though it is worth noting that a higher minimum bound for the stochastic Charnock parameters in Control_ENS would have probably lessened the impact of dynamical coupling to waves. Remarkably, the impact of coupling to both ocean and wave models on cyclone Ciara's intense wind speeds is found at least comparable in size to that of adding IC, LBC and stochastic physics perturbations to the ensemble system. Although a strong sensitivity to coupling to waves has been already observed in deterministic simulations of cyclone wind speeds (Lewis *et al.*, 2018; Wahle *et al.*, 2017; Varlas *et al.*, 2017; Lewis *et al.*, 2019; Gentile *et al.*, 2021), the Ensemble-RCS results establish, for the first time, the size of this sensitivity relative to the ensemble spread from IC, LBC and stochastic physics perturbations.

The spread characteristics of the Ensemble-RCS on coupling were further examined with dFSS and dSAL metrics. The reduced ensemble wind speeds on coupling to waves (in the AOW_ENS) led only to a slight impact on the dFSS metric and the structure and location component of the dSAL metric, compared to the Control_ENS, but to a 20% reduction in the median of the absolute value of the amplitude component of the dSAL metric. However, this reduction was only $\approx 1/2$ of that from removing the full stochastic perturbations applied to the model physics parametrizations. Together with the fact that AO_ENS showed similar dSAL and dFSS values to Control_ENS, these findings corroborate that coupling preserves the ensemble spread driven by IC, LBC and stochastic physics perturbations.

This study demonstrates that coupling to waves, thereby addressing model physics errors in convective-scale EPS arising from the failure in atmosphere-only model configurations to account for a dynamic sea state in the parametrization of air-sea momentum flux, can have a consistent impact across ensemble members while preserving the ensemble spread driven by IC, LBC and stochastic physics perturbations. Moreover, we demonstrate that object-based dSAL and neighbourhood-based dFSS dispersion metrics are useful for assessing the spread of convective-scale ensemble forecasts of cyclone wind speeds.

As future work, a broader range of weather conditions should be tested, such as a convective summer case study, assessing a wider range of meteorological variables. Moreover, the ensemble simulations should be compared against in-situ and satellite observations over a season-long case study to determine the impact on forecast skill. This aspect is outside the scope of this initial study, focused on characterising the sensitivity of cyclone near-surface wind speeds to ocean and wave feedbacks. Further investigation should also focus on the link between the uncertainty in the atmosphere and ocean boundary layers, implementing IC perturbations in the ocean and wave models and then integrating with an atmosphere-ocean-wave coupled data assimilation system (Lea *et al.* (2021)).

# Chapter 7

# Conclusions and future work

The research presented in this thesis was devoted to determine the impact of atmosphere-ocean-wave coupling on deterministic and ensemble convective-scale extreme surface wind speed forecasts in ETCs near the British Isles. Three main research objectives have been pursued, which, together, form a coherent body of knowledge:

- Characterise the systematic link of the observed extreme marine wind speeds to ETC conveyor belt jets near the British Isles
- Determine the sensitivity of ETC wind speed forecasts to air-sea fluxes, focusing on the air-sea momentum exchange and the role of time-varying SST
- Compare the sensitivity of ETC wind speed forecasts to air-sea fluxes relative to perturbations in initial conditions, lateral boundary conditions and stochastic physics.

These objectives provide a coherent context for addressing the three corresponding open questions below:

- How are ETC synoptic features (e.g. track) and mesoscale features (e.g. warm and cold sectors) associated with the extreme wind speed events observed in the British Isles surrounding seas?
- What is the sensitivity of extreme wind speeds associated with ETC low-level jets to air-sea surface exchanges?
- How does the sensitivity of ETC wind speed ensemble simulations to air-sea surface exchanges compare with sensitivity to initial conditions (ICs) and lateral boundary conditions (LBCs)?

These questions have been addressed in in three paper, two published and a third one submitted for publication, which form the research chapters Ch. 4-6.

The major conclusions are summarised in Sect. 4.4, Sect. 5.4, and Sect. 6.5 of the corresponding thesis chapters, while the contribution of this thesis to the field are discussed in Sect. 7.1. The implications of the research work carried out as part of this thesis are presented in Sect. 7.2, whilst the potential future work stemming from the results of this thesis is presented in Sect. 7.3. A final concluding remark is made in Section 7.4.

## 7.1 Contribution

This thesis has made many contributions to further the understanding of the importance of air-sea fluxes in controlling the near-surface wind speeds associated with ETCs, and to characterise the extreme wind speeds climatology over the seas surrounding the British Isles. In particular, this thesis has made more contributions than any published work for assessing the benefits of atmosphere-ocean-wave coupling in deterministic and probabilistic NWP forecasts of ETC extreme wind speeds. The key contributions of this work are summarised below:

**What is the main driver of the variability of the extreme wind speeds observed over the British Isles surrounding seas?**

The first climatology of observed offshore extreme wind speeds over the seas surrounding the British Isles is produced, based on a network of 26 stations, and extreme events have been objectively attributed by an algorithm to midlatitude cyclone conveyor belt jets. The climatology shows that ETCs drive the extreme wind speeds variability, with cyclone-dense winter months (December-February) contributing alone for 70% and 80% of all the extreme events exceeding the 20 and 25 $\mathrm{m\,s^{-1}}$ thresholds, respectively.

**What is the ETC jet which most frequently contribute to extreme 10-m wind speeds and what are the associated flow characteristics?**

The returning cold conveyor belt is shown to be the cyclone feature most frequently associated with offshore extreme 10-m wind speeds near the British Isles, followed by the warm conveyor belt, and the early cold cold conveyor belt. The 10-m winds and gusts are largest when associated with the returning cold conveyor belt, and the deeper boundary-layer heights, indicating that vertical momentum transport plays an important role in controlling the strength of the returning cold conveyor belt winds and gusts at the surface.

**What is the compound wind-wave hazard associated with each ETC jet?**

The returning cold conveyor belt is found to be the cyclone jet that leads to the largest number of compound wind-wave hazard events near the British Isles, 36, across the offshore network stations for the 9-year period considered, followed by the early cold conveyor belt, 24, and the warm conveyor belt, 10. In the North Sea, the S/SE early conveyor belt jet can generate nearly as many compound wind and wave hazards as the returning cold conveyor belt (only 2 less), despite their limited fetch.

**How is the ERA5 bias in extreme 10-m winds and wind-waves partitioned by ETC jets?**

The partitioning of ERA5 10-m wind speeds, gusts, and wind-wave heights bias in conveyor belt jets demonstrates the limitations of ERA5 in representing each ETC conveyor belt jet near the British Isles. The 10-m wind speeds and maximum gusts are most underestimated by ERA5 when associated with the returning cold conveyor belt, but wind-wave heights are most underestimated when associated with the early cold conveyor belt.

**Have atmosphere-ocean-wave coupled NWPs proved useful for simulation of ETCs?**

The extensive research work contained in this PhD thesis shows that atmosphere-ocean-wave coupled NWPs proved to be powerful tools to investigate, at convective-scale, the relative importance of the atmosphere surface layer parametrizations and ocean and wave feedbacks for the forecasts of ETC extreme wind speeds.

**What is the sensitivity of ETCs winds to coupling to ocean and coupling to waves?**

ETC near-surface wind speeds are not sensitive to atmosphere-ocean coupling, even when the SST decreases by 2K as a consequence of simulating a dynamical ocean state. Instead, ETC winds can be sensitive to additionally coupling to waves, which is demonstrated to be responsible for reduction of the ETC winds by up to 2 $\mathrm{m\,s^{-1}}$ (for a case study) as young, growing wind waves increase the sea-surface aerodynamic roughness, enhancing the air-sea momentum flux. It is shown that the following physical mechanism explains the sensitivity to coupling to waves: under the action of ETC winds, young waves (simulated by the wave component) grow and extract momentum and energy from the overlying atmospheric flow, increasing the frictional drag at the sea surface and thus reducing near-surface wind speeds.

**What is the impact on ETC winds of changing the drag parametrization compared to that of the coupling to ocean and waves?**

The use in the atmosphere-only model of a drag parametrization based on COARE4.0, with a cap on the neutral drag coefficient and reduction for wind speeds exceeding 27 $\mathrm{m\,s^{-1}}$, can mimick the physics of the momentum air-sea surface exchange incorporated in the fully coupled atmosphere-ocean-wave configuration. This new drag parametrization reduces the bias of ETC near-surface winds by up to 20% in the case study analysed, showing bias improvements equivalent to those of fully coupling.

**Have atmosphere-ocean-wave coupled convective-scale EPS proved useful for simulation of ETCs?**

The design of the novel regional ensemble coupled system (Ensemble-RCS) was developed as part of this thesis. The Ensemble-RCS runs 18 members at 2.2 km grid spacing, with domain covering the British Isles and surrounding seas. The extensive research work contained in this PhD thesis shows that the Ensemble-RCS proved to be an effective numerical tool to evaluate the respective impacts of coupling to waves and ICs, LBCs, and stochastic physics perturbations.

**How does the sensitivity of ETC wind speed ensemble simulations to air-sea surface exchanges compare with sensitivity to initial conditions (ICs) and lateral boundary conditions (LBCs)?**

Coupling to ocean may not impact the ensemble simulations of ETC wind speeds. Instead, additional coupling to waves is demonstrated to be capable of having a considerable impact on ensemble simulations of ETC wind speeds. Coupling to waves can reduce the median ensemble wind speed of up to 1 $\mathrm{m\,s^{-1}}$ in the case study analysed, and can lead to reductions as large as 70% in ETC wind strike probability. Remarkably, by placing the impact of coupling to ocean and waves into the context of the atmosphere-only ensemble spread, the impact of coupling to waves is found to be comparable in size to that of adding IC, LBC and stochastic physics perturbations to the uncoupled atmosphere-only ensemble simulation.

**What is the value in the research carried out in this thesis of using dFSS and dSAL convective-scale metrics to assess the coupled ensemble spread characteristics?**

The application of convective-scale neighbourhood-based dFSS and object-based dSAL metrics demonstrates that coupling to waves can have a consistent impact across all the ensemble members while preserving their spread, thereby showing that coupling to waves is a fundamental aspect of model uncertainty in convective-scale forecasts.

The implications of these contributions are discussed next.

## 7.2 Implications

There are three topics that the implications are related to: extreme marine winds near the British Isles (Sect. 7.2.1), atmosphere-ocean-wave coupling (Sect. 7.2.2), and convective-scale ensemble coupled systems (Sect. 7.2.3).

### 7.2.1 Extreme marine winds near the British Isles

- Marine surface observations are critical, when available, to capture the extreme wind speed and wave height variability, and they should be used to complement information extracted from reanalyses, when assessing wind and wave extreme trends.
- The attribution of compound wind and wave hazards to cyclone conveyor belt jets could assess the cyclone specific conditions leading to the largest number of compound wind and

wave hazards and associated ERA5 biases. This accurate and objective assessment could represent a good starting point for the evaluation of forecast models biases linked to the jets, and feature-based post processing of extreme wind speed and gusts.

- Extreme winds and gusts are highest when associated with the returning cold conveyor belt, and this demonstrates the importance of boundary-layer processes, such as vertical momentum transport, in controlling the magnitude of extreme wind speeds and gusts at the surface. Because these processes occur well below the ERA5 $\approx 31$ km resolution, this implies that other modelling tools are needed to study the boundary-layer processes controlling the strong surface wind speeds associated with ETCs jets.

### 7.2.2 Atmosphere-ocean-wave coupling

- The results of coupling to waves, which allows for the dynamic representation of the wind-wave interaction, imply that ETC wind speeds are sensitive to the physics-driven representation of the Charnock parameter field.

- Coupling to ocean, compared to coupling to waves, leads to only small and localised impacts on ETC intense wind speeds (in the case studies analysed), but it substantially improves the forecast skill of some ocean variables, such as SST (and its diurnal cycle). In atmospheric conditions where wind shear does not dominate the turbulent kinetic energy budget (heatwave), the substantial impact on SST simulated by coupling to ocean could lead to considerable changes in the boundary layer stability, and, in turn, to considerable changes in other surface variables other than SST, such as 10-m wind speeds and air temperature, as recently shown by Mahmood *et al.* (2021).

- The skill improvements found using the new drag parametrization, that better represents the impacts of waves on extreme winds, imply that it would be worthwhile to test the new drag parametrization over longer time periods for operational implementation in the regional convective-scale Met Office operational model (UKV).

### 7.2.3 Convective-scale ensemble coupled systems

- The demonstration, for the first time, that coupling to waves is a fundamental aspect of model uncertainty in convective-scale forecasts of ETCs, implies that operational convective-scale EPS should integrate the feedbacks between components of the earth system to better represent model uncertainty in extreme weather events forecasts.
- The successful application of the neighbourhood-based dFSS and object-based dSAL metrics for assessing the spread characteristics of the probabilistic coupled and uncoupled forecasts implies that neighbourhood- and object-based metrics are critical to disentangle the relative importance of complex feedbacks represented by convective-scale atmosphere-ocean-wave coupled EPS.
- The successful design and development of a prototype convective-scale coupled ensemble system, Ensemble-RCS, implies further research should be carried out to explore sensitivities and performances of convective-scale coupled EPS also to other extreme events, such as summer heat waves, Mediterranean cyclones, and tropical cyclones, as noted by Castillo *et al.* (2022). But it will probably take several years for coupled convective-scale ensemble systems to become operational due to their computational cost.

## 7.3 Future work

Two main interlinked future research works stem from the research presented in this thesis. In order to isolate the boundary-layer atmospheric processes misrepresented in current modelling capabilities (e.g. ERA5), the climatology of the offshore extreme wind speed regime observed near the British Isles should be extended to include a more detailed analysis of the boundary-layer structure associated with the wind and gust biases. Then, the importance of accurate modelling of air-sea interactions for the pre-conditioning environment of ETC cyclogenesis and downstream ETC development (track, intensity, and associated extreme wind speeds) should be investigated using current global operational state-of-art coupled NWPs whose domain cover both cyclogenesis region and area of landfall. Overall, these future research works, which directly builds on the findings of this thesis, is expected to improve the understanding of how the errors in the representation of air-sea momentum, heat, and moisture fluxes and the errors associated with the unresolved boundary-layer atmospheric processes such as the downward mixing of momentum can affect the wind and gust biases. These two works as a whole could contribute to pave the way for the next generation of convective-scale global operational atmosphere-ocean-wave coupled EPS.

### 7.3.1 Climatology of extreme wind speeds and understanding of model biases

As part of the work presented in this thesis, a climatology was created for the extreme marine wind speeds and wave heights observed near the British Isles over the 2012-2020 time period. Besides incorporating further analysis of SJ events as detailed in Sect. 4.4, the climatology should be extended to investigate the relationship between ERA5 wind and gusts bias and the diagnosed BL depth, improving the understanding of the associated misrepresented boundary-layer processes in ERA5. If ERA5 biases are found to be larger when the diagnosed boundary-layer depth is low, it could suggest that ERA5 underestimates the entrainment of high momentum air associated with the upper-level ETC jets into the boundary-layer. Instead, if the ERA5 biases are found to be larger when the diagnosed boundary-layer depth is high, the mixing of high momentum air from the top of the boundary-layer down to the surface layer might not be accurately represented in ERA5. The sensitivity of ERA5 gust biases to the diagnosed boundary-layer depth could be further explored by analysing the correlation between the bias in the gust magnitude and the bias in the mean wind. Moreover, the impact of errors in the model approximations of sub-grid boundary-layer processes on the ERA5 wind and gusts biases could be further assessed by extending the climatology to include surface observations of winds and gusts recorded over the British Isles landmass, and then comparing the boundary-layer structure (as inferred from model or reanalysis) associated with ERA5 biases in wind and gusts over land with that associated with biases over the sea. The sub-synoptic feature association carried out by Earl *et al.* (2017) for the British Isles land mass could be used as a benchmark for validation of the partitioning of the climatology into

ETC jets over land, though it is based on years which only partially overlap.

To address the research outlined above, in addition to using surface observations and ERA5 data, the observation dataset could be expanded with the wind profiles observed at three offshore research platforms in the North Sea and Baltic Sea (FINO), which measure wind speeds up to a 100 m height (FINO, 2022), and also with the Advanced Scatterometer (ASCAT) ocean vector wind observations (KNMI, 2018). Furthermore, it would be worthwhile to carry out a comparison between this extended climatology, and ERA5 and MetUM runs (though the latter would cover only a portion of the marine observations available), in order to assess the accuracy with which ERA5 and the MetUM represent the offshore extreme wind speed regimes.

### 7.3.2 Accurate modelling of air-sea interactions and the next generation of coupled models

Although the results of the deterministic and ensemble coupled and uncoupled numerical simulations of ETCs carried out in this thesis have highlighted the critical role of an accurate representation of the air-sea momentum flux in controlling the strength of ETC near-surface wind speeds, the domain used in the simulations performed did not allow to determine to what degree atmosphere-ocean-wave coupling could influence the pre-conditioning environment of ETCs cyclogenesis regions. Indeed, as discussed in detail in Sect. 2.6, numerical simulations of explosive ETCs, such as those of the well studied ETC Xynthia (2014), have shown that ETC intensity and associated surface wind speeds are greatly affected by changes in the SST and also in the boundary-layer moisture in the cyclogenesis regions (Ludwig *et al.*, 2014; Doyle *et al.*, 2014). Moreover, the representation of sea-surface drag to account for wave growth under intensifying ETC winds is also likely to play a role in cyclogenesis, since any change in wind speed magnitude alters the heat and moisture fluxes (Donelan, 2018).

The recent availability of global operational atmosphere-ocean coupled systems, such as the atmosphere-ocean coupled system which is currently operational at the Met Office, has made feasible to explore how a more accurate representation of air-sea heat and moisture turbulent fluxes (through atmosphere-ocean coupling) can modify the pre-conditioning environment of ETCs, and in turn their downstream development. Providing the atmosphere model with a time-varying SST simulated by the ocean model component is likely to modify the ocean evaporation rate, in turn changing the amount of moisture transported by the WCB. If it turns out that the ocean evaporation rate is enhanced by coupling to ocean, that would mean the WCB would transport a higher amount of moisture, plausibly leading to a larger amount of latent heat released through condensation, and thus a more intense simulated ETC. Conversely, a weaker evaporation rate, might reduce the intensity of the simulated ETC. Using an online PV tool such as the one implemented in the MetUM, the relative impacts of coupling on diabatic and baroclinic processes in ETCs could be quantified (Gray, 2006; Sánchez *et al.*, 2020).

Finally, the link between the uncertainty in the atmosphere and ocean boundary layer should be further investigated. Towards this aim, IC perturbations should be implemented in the ocean and wave models, and then integrated with the novel Ensemble-RCS atmosphere-ocean-wave ensemble prototype developed in this thesis. Currently, in most of the meteorological centres, an atmosphere-ocean-wave ensemble running atmosphere, ocean, and wave perturbations is not even at the prototype stage; but, as it is developed, this numerical tool could turn out determinant to understand how the sensitivity of ETCs wind speeds to air-sea fluxes compare to IC perturbations in the ocean and wave models. The dispersion FSS and dispersion SAL tools, successfully used in this thesis for characterising the dispersion of convective-scale ensemble simulated extreme wind speeds, can be used to assess the spread characteristics of the configurations of this new generation EPS.

## 7.4 Concluding remark

The turbulent momentum, heat, and moisture fluxes in the boundary layer play a critical role for both weather and climate, controlling the extreme surface wind speeds associated with ETCs, but also (moving away from the midlatitudes to the tropics) the extreme winds associated with tropical cyclones. Correct representation of boundary-layer turbulent fluxes remains one of the biggest challenges for the representation of the local details of extreme weather events (such as ETCs and tropical cyclones) in NWPs and climate simulations. As climate models are increasingly used at finer grid spacings, the improvement of the parametrizations of boundary-layer processes is critical for enhancing the understanding and the predictability of the climate system. A promising area of research is currently focusing on including a prognostic treatment of subgrid fluxes and, in particular, of momentum flux, in the next generation of km-scale climate models. Further research is focusing on developing suitable climate simulation verification strategies using a comprehensive hierarchy of observations and models. Overall, achieving an accurate km-scale climate prediction of hazards, such as extreme wind speeds, will help policy makers to shape legislation and governments to act to more effectively respond to the threat of a warming climate.

# Bibliography

Albrecht BA, Jensen MP, Syrett WJ. 1995. Marine boundary layer structure and fractional cloudiness. *J Geophys Res* **100**: 14 209–14 222.

Arya PS. 2001. *Introduction to Micrometereology*. Academic Press.

Bader MJ, Forbes GS, Grant JR, Lilley RBE, Waters AJ. 1995. *Images in weather forecasting*. Cambridge University Press.

Baker L. 2009. Sting jets in severe northern European wind storms. *Weather* **64**: 143–148.

Baker LH, Rudd AC, Migliorini S, Bannister RN. 2014. Representation of model error in a convective-scale ensemble prediction system. *Nonlinear Processes in Geophysics* **21**(1): 19–39, doi:10.5194/npg-21-19-2014.

Bauer P, Sandu I, Magnusson L, Mladek R, Fuentes M. 2020. ECMWF global coupled atmosphere, ocean and sea-ice dataset for the year of polar prediction 20172020. *Sci Data* **7**.

BBC. 2020. Storm Ciara: Flooding after 93mph winds battered wales. URL https://www.bbc.co.uk/news/uk-wales-51428651.

Belcher SE, Hunt JCR. 1993. Turbulent shear flow over slowly moving waves. *J Fluid Mech* **251**: 109–148.

Beljaars A. 1987. The influence of sampling and filtering on measured wind gusts. *J Atmos Ocean Techn* **4**: 613626.

Beljaars ACM, Holtslag AAM. 1991. Flux parameterization over land surfaces for atmospheric models. *J Appl Meteorol Climatol* **30**: 327–341.

Bell R, Gray S, Jones O. 2017. North Atlantic storm driving of extreme wave heights in the North Sea. *Geophys Res Lett* **122**: 3253–3268.

Beran J, Calveri L, Lange B, von Bremen L. 2005. FORWIND: Offshore wind modelling and forecast. WRF/MM5 Users Workshop, June.

Berner J, Ha SY, Hacker JP, Fournier A, Snyder C. 2011. Model uncertainty in a mesoscale ensemble prediction system: stochastic versus multiphysics representations. *Mon Weather Rev* **139**: 1972–1995.

Best MJ, Pryor M, Clark DB, Rooney GG, Essery RLH, Menard CB, Edwards J, Hendry MA, Porson A, Gedney N, Mercado LM, Sitch S, Blyth E, Boucher O, Cox PM, Grimmond CSB, Harding RJ. 2011. The joint UK Land Environment Simulator (JULES), model description  Part 1: Energy and water fluxes. *Geosci Model Dev* **4**: 677–699.

Bishop CH, Etherton BJ, Majumdar SJ. 2001. Adaptive sampling with the ensemble transform Kalman filter. Part I: Theoretical aspects. *Mon Weather Rev* **129**: 420–436.

Bishop CH, Thorpe AJ. 1994. Potential vorticity and the electrostatics analogy: Quasi–geostrophic theory. *Q J R Meteorol Soc* **120**: 713–731.

Bjerknes J. 1919. On the structure of moving cyclones. *Mon Weather Rev* **47**: 95–99.

Bjerknes J, Solberg H. 1922. *Life cycle of cyclones and the polar front theory of atmospheric circulation*, vol. 3. Geofysiske Publikationer.

Black PG, D'Asaro EA, Drennan WM, French JR, Niiler PP, Sanford TB, Terrill EJ, Walsh EJ, Zhang JA. 2007. Airsea exchange in hurricanes: Synthesis of observations from the coupled boundary layer airsea transfer experiment. *Bull Am Meteorol Soc* **88**: 357 – 374.

Bloom SC, Takacs LL, Brin E. 1991. A scheme to incorporate analysis increments gradually in the GLA assimilation system. preprints. In: *Ninth Conf. on Numerical Weather Prediction*. Amer. Meteorol. Soc., pp. 110–112.

Bolton D. 1980. The computation of equivalent potential temperature. *Mon Weather Rev* **108**: 1046 – 1053.

Bourassa MA, Meissner T, Cerovecki I, Chang PS, Dong X, De Chiara G, Donlon C, Dukhovskoy DS, Elya J, Fore A, Fewings MR, Foster RC, Gille ST, Haus BK, Hristova-Veleva S, Holbach HM, Jelenak Z, Knaff JA, Kranz SA, Manaster A, Mazloff M, Mears C, Mouche A, Portabella M, Reul N, Ricciardulli L, Rodriguez E, Sampson C, Solis D, Stoffelen A, Stukel MR, Stiles B, Weissman D, Wentz F. 2019. Remotely sensed winds and wind stresses for marine forecasting and ocean modeling. *Frontiers in Marine Science* **6**.

Bousquet O, Barbary D, Bielli S, Kebir S, Raynaud L, Malardel S, Faure G. 2020. An evaluation of tropical cyclone forecast in the South-west Indian Ocean basin with AROME-Indian ocean convection-permitting numerical weather predicting system. *Atmos Sci Lett* **21**(3).

Boutle I, Beare R, Belcher S, Brown A, Plant R. 2010. The moist boundary layer under a mid-latitude weather system. *Boundary Layer Meteorol* **134**: 367–386.

Bowler N, Arribas A, Beare S, Mylne K, Shutts G. 2009. The local ETKF and SKEB: Upgrade to the MOGREPS short-range ensemble prediction system. *Q J R Meteorol Soc* **135**(640): 767–776.

Bowler N, Arribas A, Mylne K, Robertson K, Beare S. 2008. The MOGREPS short-range ensemble prediction system. *Q J R Meteorol Soc* **134**: 703–722.

Brier GW. 1950. Verification of forecasts expressed in terms of probability. *Mon Weather Rev* **78**: 1–3.

Browning K. 2004. The sting at the end of the tail: damaging winds associated with extratropical cyclones. *Q J R Meteorol Soc* **130**: 375–399.

Browning KA. 1986. Conceptual models of precipitation systems. *Wea Forecasting* **1**: 23–41.

Browning KA, Roberts NM. 1994. Structure of a frontal cyclone. *Q J R Meteorol Soc* **120**: 1535–1557.

Brönnimann S, Martius O, von Waldow H, Welker C, Luterbacher J, Compo GP, Sardeshmukh PD, , Usbeck T. 2012. Extreme winds at northern mid-latitudes since 1871. *Meteorol Z* **21**:

1327.

Buizza R, Houtekamer P, Pellerin G, Toth Z, Zhu Y, Wei M. 2005. A comparison of the ECMWF, MSC, and NCEP global ensemble prediction systems. *Mon Weather Rev* **133**: 1076–1097.

Buizza R, Miller M, Palmer TN. 1999. Stochastic representation of model uncertainties in the ECMWF ensemble prediction system. *Q J R Meteorol Soc* **125**: 2887–2908.

Buizza R, Palmer TN. 1995. The singular-vector structure of the atmospheric global circulation. *J Atmos Sci* **52**: 1434–1456.

Bush M, Allen T, Bain C, Boutle I, Edwards J, Finnenkoetter A, Franklin C, Hanley K, Lean H, Lock A, Manners J, Mittermaier M, Morcrette C, North R, Petch J, Short C, Vosper S, Walters D, Webster S, Weeks M, Wilkinson J, Wood N, Zerroukat M. 2020. The first Met Office Unified Model–JULES Regional Atmosphere and Land configuration, RAL1. *Geosci Model Dev* **13**: 1999–2029.

Cardone V, Callahan BT, Chen H, Cox AT, Morrone MA, Swail VR. 2014. Global distribution and risk to shipping of very extreme sea states (VESS). *Int J Climatol* **35**: 69–84.

Castillo JM, Lewis HW, Mishra A, Mitra A, Polton J, Brereton A, Saulter A, Arnold A, Berthou S, Clark D, Crook J, Das A, Edwards J, Feng X, Gupta A, Joseph S, Klingaman N, Momin I, Pequignet C, Sanchez C, Saxby J, Valdivieso da Costa M. 2022. The regional coupled suite (RCS-IND1): application of a flexible regional coupled modelling framework to the indian region at kilometre scale. *Geosci Model Dev* **15**: 4193–4223.

Catto J, Raveh-Rubin S. 2019. Climatology and dynamics of the link between dry intrusions and cold fronts during winter. Part I: global climatology. *Clim Dyn* **53**: 1873–1892.

Charney JG, Phillips NA. 1953. Numerical integration of the quasi-geostrophic equations for barotropic and simple baroclinic flows. *J Atmos Sci* **10**: 71 – 99.

Charnock H. 1955. Wind stress on a water surface. *Q J R Meteorol Soc* **81**: 639–640.

Clark A, Gallus WA, Xue M, Kong F. 2010. Growth of spread in convection-allowing and convection-parameterizing ensembles. *Weather Forecast* **25**(2): 594–612.

Clark M. 2013. A provisional climatology of cool-season convective lines in the UK. *Atmos Res* **123**: 180–196.

Clark PA, Gray SL. 2018. Sting jets in extratropical cyclones: a review. *Q J R Meteorol Soc* **144**: 943–969.

Clark PA, Halliwell C, Flack D. 2021. A physically based stochastic boundary layer perturbation scheme. Part I: Formulation and evaluation in a convection-permitting model. *J Atmos Sci* **78**: 727–746.

Coelingh J, van Wijk A, Holtslag A. 1998. Analysis of wind speed observations over the North Sea coast. *J Wind Eng Ind Aerodyn* **73**: 125–144.

Cohen JE, Belcher SE. 1999. Turbulent shear over fast moving waves. *J Fluid Mech* **386**: 345–371.

Cook P, Renfrew IA. 2014. Aircraft–based observations of air–sea turbulent fluxes around the British Isles. *Q J R Meteorol Soc* **141**: 139–152.

Coronel B, Ricard D, Rivière G, Arbogast P. 2016. Coldconveyorbelt jet, sting jet and slantwise circulations in idealized simulations of extratropical cyclones. *Q J R Meteorol Soc* **142**: 1781–1796.

Craig M. 2003. A once in 50 year wind speed map for Europe derived from mean sea level pressure measurements. *J Wind Eng Ind Aerodyn* **91**: 1813–1826.

Csanady G. 2001. *Air-sea interaction: Laws and mechanisms*. Cambridge University Press.

Dacre H, Gray S. 2009. The spatial distribution and evolution characteristics of North Atlantic cyclones. *Mon. Weather Rev.* **137**: 99–115.

Dacre HF, Hawcroft MK, Stringer MA, Hodges KI. 2012. An extratropical cyclone atlas: A tool for illustrating cyclone structure and evolution characteristics. *Bulletin of the American*

*Meteorological Society* **93**: 1497 – 1502, doi:10.1175/BAMS-D-11-00164.1.

Davies T, Cullen MJP, Malcolm AJ, Mawson MH, Staniforth A, White AA, Wood N. 2005. A new dynamical core for the met offices global and regional modelling of the atmosphere. *Q J R Meteorol Soc* **131**: 1759–1782.

Dee D, Uppala S, Simmons AJ, Berrisford P Poli P, Kobayashi S, Andrae U, Balmaseda MA, Balsamo G, Bauer P, Bechtold P, Beljaars ACM, van de Berg L, Bidlot J, Bormann N, Delsol C, Dragani R, Fuentes M, Geer AJ, Haimberger L, Healy SB, Hersbach H, Hólm EV, Isaksen L, Kållberg P, Köhler M, Matricardi M, McNally A, Monge-Sanz BM, Morcrette JJ, Park BK, Peubey C, de Rosnay P, Tavolato C, Thépaut JN, Vitart F. 2011. The ERA-Interim reanalysis: configuration and performance of the data assimilation system. *Q J R Meteorol Soc* **137**.

Dey SRA, Leoncini G, Roberts NM, Plant RS, Migliorini S. 2014. A spatial view of ensemble spread in convection permitting ensembles. *Mon Weather Rev* **142**: 4091–4107.

Dobson FW. 1971. Measurements of atmospheric pressure on wind-generated sea waves. *J Fluid Mech* **48**: 91–127.

Donelan MA. 1982. The dependence of the aerodynamic drag coefficient on wave parameters. In: *Proceedings of the First Intern. Conf. on Meteorology and the Air/Sea Interaction of the Coastal Zone, The Hague, The Netherlands*. American Meteorological Society, Boston, Mass., pp. 381–387.

Donelan MA. 2018. On the decrease of the oceanic drag coefficient in high winds. *J Geophys Res* **123**: 1485–1501.

Donelan MA, Dobson FW, Smith SD, Anderson RJ. 1993. On the dependence of sea surface roughness on wave development. *J Phys Oceanogr* **23**: 2143–2149.

Donelan MA, Haus B, Reul N, Plant WJ, Stiassnie M, Graber HC, Brown OB, Saltzman ES. 2004. On the limiting aerodynamic roughness of the ocean in very strong winds. *Geophys Res Lett* **31**: 1–5.

Donlon CJ, Martin M, Stark JD, Roberts-Jones J, Fiedler E, Wimmer W. 2012. The Operational Sea Surface Temperature and Sea Ice Analysis. *Remote Sens Environ* **116**: 140–158.

Doyle JD. 1995. Coupled ocean wave/atmosphere mesoscale model simulations of cyclogenesis. *Tellus* **47**: 766–778.

Doyle JD. 2002. Coupled atmosphereocean wave simulations under high wind conditions. *Mon Weather Rev* **130**: 3087–3099.

Doyle JD, Amerault C, Reynolds CA, Reinecke PA. 2014. Initial condition sensitivity and predictability of a severe extratropical cyclone using a moist adjoint. *Mon Weather Rev* **142**: 320 – 342.

Dupont E, Koppelaar R, Jeanmart H. 2018. Global available wind energy with physical and energy return on investment constraints. *Appl Energy* **209**: 322–338.

Eady ET. 1949. Long waves and cyclone waves. *Tellus* **3**: 33–52.

Earl N, Dorling S. 2013. 1980-2010 Variability in U.K. surface wind climate. *J Clim* **26**: 1172–1191.

Earl N, Dorling S, Starks M, Finch R. 2017. Subsynoptic scale features associated with extreme surface gusts in UK extratropical cyclone events. *Geophys Res Lett* **44**: 3932–3940.

Edwards J, Slingo A. 1996. Studies with a flexible new radiation code. part I: Choosing a configuration for a large-scale model. *Q J R Meteorol Soc* **122**: 689–719.

Edwards JM. 2007. Oceanic latent heat fluxes: Consistency with the atmospheric hydrological and energy cycles and general circulation modelling. *J. Geophys. Res.* **112**.

Eisenstein L, Schulz B, Qadir GA, Pinto JG, Knippertz P. 2022. Objective identification of high-wind features within extratropical cyclones using a probabilistic random forest (RAMEFI). Part I: Method and illustrative case studies. *Weather and Climate Dynamics Discussions* **2022**: 1–39.

Ertel H. 1942. Ein neuer hydrodynamischer wirbelsatz. *Meteor. Z.* **59**: 277–281.

Field PR, Wood R. 2007. Precipitation and cloud structure in midlatitude cyclones. *J Clim* **20**: 233–254.

FINO. 2022. Forschungsplattformen in Nord- und Ostsee nr. 1,2,3. https://www.fino-offshore.de/en/index.html.

Flack DLA, Clark PA, Halliwell CE, Roberts NM, Gray SL, Plant RS, Lean HW. 2021. A physically based stochastic boundary layer perturbation scheme. Part II: Perturbation growth within a superensemble framework. *J Atmos Sci* **78**: 747 – 761.

Frame THA, Methven J, Roberts NM, Titley HA. 2015. Predictability of frontal waves and cyclones. *Weather Forecast* **30**: 1291–1302.

Garratt J. 1992. *The atmospheric boundary layer*. Cambridge University Press.

Gentile E, Gray S, Barlow J, Lewis H, Edwards J. 2021. The impact of atmosphereoceanwave coupling on the near-surface wind speed in forecasts of extratropical cyclones. *Boundary-Layer Meteorol* **180**: 105–129.

Gentile E, Gray S, Lewis H. 2022. The sensitivity of probabilistic convective-scale forecasts of an extratropical cyclone to atmosphereoceanwave coupling. *Q J R Meteorol Soc* **148**: 685–710.

Geyer B aWR, Bisling P, Winterfeldt J. 2015. Climatology of North Sea wind energy derived from a model hindcast for 19582012. *J Wind Eng Ind Aerodyn* **147**: 18–29.

Gibson R, Christou M, Feld G. 2014. The statistics of wave height and crest elevation during the december 2012 storm in the North Sea. *Ocean Dyn.* **64**: 1305–1317.

Gill. 1982. *Atmosphere–ocean dynamics*. Academic Press.

Goyette S. 2008. Development of a model–based high–resolution extreme surface wind climatology for Switzerland. *Natural Hazards* **44**: 329–339.

Graham JA, O'Dea E, Holt J, Polton J, Hewitt HT, Furner R, Guihou K, Brereton A, Arnold A, Wakelin S, Castillo Sanchez JM, Mayorga Adame CG. 2018. AMM15: a new high-resolution NEMO configuration for operational simulation of the European north-west shelf. *Geosci Model Dev* **11**: 681–696.

Grant ALM. 2001. Cloud-base fluxes in the cumulus-capped boundary layer. **127**: 407421.

Gray S. 2006. Mechanisms of midlatitude cross-tropopause transport using a potential vorticity budget approach. *J Geophys Res* : 1–14.

Gregory D, Rowntree PR. 1990. A mass flux convection scheme with representation of cloud ensemble characteristics and stability-dependent closure. *Mon Weather Rev* **118**: 1483 – 1506.

Grønås S. 1995. The seclusion intensification of the New Year's day storm 1992. *Tellus A* **47**: 733–746.

Hagedron R, Doblas-Reyes FJ, Palmer T. 2005. The rationale behind the success of multi-model ensembles in seasonal forecasting - I. basic concept. *Tellus A* **57**: 219–233.

Hagelin S, Son J, Swinbank R McCabe A, Roberts N, Tennant W. 2017. The Met Office convective-scale ensemble, MOGREPS-UK. *Q J R Meteorol Soc* **143**: 2846–2861.

Hart NCG, Gray SL, Clark PA. 2017. Sting-Jet Windstorms over the North Atlantic: Climatology and Contribution to Extreme Wind Risk. *Journal of Climate* **30**: 5455–5471.

Hasselmann D, Bĺosenberg J. 1981. Field measurements of wave-induced pressure over wind sea and swell. *J Fluid Mech* **230**: 391–428.

Haualand KF, Spengler T. 2020. Direct and indirect effects of surface fluxes on moist baroclinic development in an idealized framework. *Journal of the Atmospheric Sciences* **77**: 3211–3225.

Hawcroft M, Shaffrey LC, Hodges KI, Dacre HF. 2012. How much northern hemisphere precipitation is associated with extratropical cyclones? *Geophys Res Lett* **39**.

Hawker M. 2007. Climate change and the global insurance industry. *Geneva Pap Risk Insur: Issues Pract* **32**: 22–28.

Hersbach H, Bell B, Berrisford P, Hirahara S, Horányi A, Muñoz-Sabater J, Nicolas J, Peubey C, Radu R, Schepers D, Simmons A, Soci C, Abdalla S, Abellan X, Balsamo G, Bechtold P, Biavati G, Bidlot J, Bonavita M, De Chiara G, Dahlgren P, Dee D, Diamantakis M, Dragani R, Flemming J, Forbes R, Fuentes M, Geer A, Haimberger L, Healy S, Hogan R, Hólm E, Janisková M, Keeley S, Laloyaux P, Lopez P, Lupu C, Radnoti G, de Rosnay P, Rozum I, Vamborg F, Villaume S, Thépaut JN. 2020. The ERA5 global reanalysis. *Q J R Meteorol Soc* **146**: 1999–2049.

Hewson TD, Neu U. 2015. Cyclones, windstorms and the IMILAST project. *Tellus A* **67**: 27–128.

Hewston R, Dorling S. 2011. An analysis of observed daily maximum wind gusts in the UK. *J Wind Eng Ind Aerodyn* **99**: 845–856, doi:doi.org/10.1016/j.jweia.2011.06.004.

Hodges KI. 1995. Feature tracking on the unit sphere. *Mon Weather Rev* **123**: 3458 – 3465.

Hodges KI, Lee RW, Bengtsson L. 2011. A Comparison of Extratropical Cyclones in Recent Reanalyses ERA-Interim, NASA, MERRA, NCEP, CFSR, and JRA-25. *Journal of Climate* **24**: 4888 – 4906.

Holt T, Cummings J, Bishop C, Doyle J, Hong X, Chen S, Jin Y. 2011. Development and testing of a coupled ocean-atmosphere mesoscale ensemble prediction system. *Ocean Dyn* **61**: 19371954.

Holton JR. 1992. An introduction to dynamical meteorology. academic press. *Academic Press* .

Hoskins BJ, Hodges KI. 2002. New perspectives on the northern hemisphere winter storm tracks. *J Atmos Sci* **59**: 1041 – 1061.

Hoskins BJ, Hodges KI. 2019a. The Annual Cycle of Northern Hemisphere Storm Tracks. Part i: Seasons. *J Clim* **32**.

Hoskins BJ, Hodges KI. 2019b. The Annual Cycle of Northern Hemisphere Storm Tracks. Part ii: Regional Detail. *J Clim* **32**: 1761 – 1775.

Hoskins BJ, James IN. 2014. *Fluid dynamics of the midlatitude atmosphere*. Wiley.

Hoskins BJ, McIntyre ME, Robertson AW. 1985. On the use and significance of isentropic potential vorticity maps. *Q J R Meteorol Soc* **111**: 877–946.

Houtekamer P, Lefaivre L, Derome J, Ritchie H, Mitchell H. 1996. A system simulation approach to ensemble prediction. *Mon Weather Rev* **124**(6): 1225–1242.

Hristov T, Miller S, Friehe C. 2003. Dynamical coupling of wind and ocean waves through wave-induced air flow. *Nature* **422**.

Hsu J, Lien RC, DAsaro EA, Sanford T. 2017. Estimates of surface Wind Stress and Drag Coefficients in Typhoon Megi. *J. Phys. Oceanogr.* **47**: 545–565.

IMAREST. 2018. Metocean procedures guide for offshore renewables. https://www.imarest.org/reports/650-metocean-procedures-guide/file.

Janssen P. 1989. Wave–induced stress and the drag of air flow over sea waves. *J Phys Oceanogr* **19**: 745–772.

Janssen P. 1991. Quasi–linear theory of wind–wave generation applied to wave forecasting. *J Phys Oceanogr* **21**: 1631–1642.

Janssen P. 2004. *The interaction of ocean waves and wind*. Cambridge University Press.

Jeffreys H. 1925. On the formation of waves by wind, II. In: Proceedings of the royal society. A110.

Jenkins A, Paskyabi B, Fer M, Gupta A, Adakudlu M. 2012. Modelling the effect of ocean waves on the atmospheric and ocean boundary layers. *Energy Procedia* **24**: 166–175.

Kalverla PC, Steeneveld GJ, Ronda RJ, Holtslag AA. 2017. An observational climatology of anomalous wind events at offshore meteomast ijmuiden (north sea). *J Wind Eng Ind*

*Aerodyn* **165**: 86–99.

Katsafados P, Mavromatidis E, Papadopoulos A, Pytharoulis I. 2011. Numerical simulation of a deep mediterranean storm and its sensitivity on sea surface temperature. *Nat Hazards Earth Syst Sci* **11**: 1233–1246.

Katsafados P, Papadopoulos A, Korres G, Varlas G. 2016. A fully coupled atmosphere–ocean–wave modeling system for the Mediterranean Sea: interactions and sensitivity to the resolved scales and mechanisms. *Geosci Model Dev* **9**: 161–173.

Kendon M. 2020. Met Office report of storm Ciara URL https://www.metoffice.gov.uk/binaries/content/assets/metofficegovuk/pdf/weather/learn-about/uk-past-events/interesting/2020/2020_02_storm_ciara.pdf.

Kita Y, Waseda T, Webb A. 2018. Development of waves under explosive cyclones in the northwestern pacific. *Ocean Dyn* **68**: 1403–1418.

Klawa M, Ulbrich U. 2003. A model for the estimation of storm losses and the identification of severe winter storms in Germany. *Nat Hazards Earth Syst Sci* **3**: 725–732.

KNMI. 2018. Global ocean daily gridded reprocessed L3 sea surface winds from scatterometer, EU copernicus marine service information. Available at: http://marine.copernicus.eu/services-portfolio/access-to-products/.

Komen GJ, Cavaleri L, Donelan M, Hasselmann K, Hasselmann S, Janssen PAE. 1994. *Dynamics and modelling of ocean waves*. Cambridge University Press.

Lamb H, Frydendhal K. 1991. *Grading of storms. in: Historic storms of the north sea, british isles and northwest europe*. Cambridge University Press (UK).

Laurila TK, Sinclair VA, Gregow H. 2021. Climatology, variability, and trends in near-surface wind speeds over the North Atlantic and Europe during 19792018 based on ERA5. *Int. J. Climatol.* **41**: 2253–2278.

Lavergne T, Sørensen AM, Kern S, Tonboe R, Notz D, Aaboe S, Bell L, Dybkjær G, Eastwood S, Gabarro C, Heygster G, Killie MA, Brandt Kreiner M, Lavelle J, Saldo R, Sandven S, Pedersen LT. 2019. Version 2 of the EUMETSAT OSI SAF and ESA CCI sea-ice concentration climate data records. *The Cryosphere* **13**: 49–78.

Lea D, While J, Martin J, Weaver A, Storto A, Chrust M. 2021. A new global ocean ensemble system at the Met Office: Assessing the impact of hybrid data assimilation and inflation settings. In prep. for. *Q J R Meteorol Soc* .

Lean H, Clark P. 2003. The effects of changing resolution on mesocale modelling of line convection and slantwise circulations in FASTEX IOP16. *Q J R Meteorol Soc* **129**: 2255–2278.

Leckebush G, Renggli D, Ulbrich U. 2008. Development and application of an objective storm severity measure for the Northeast Atlantic region. *Meteorol Z* **17**: 575–587.

Lewis HW, Castillo Sanchez JM, Graham J, Saulter A, Bornemann J, Arnold A, Fallmann J, Harris C, Pearson D, Ramsdale S, Martnez-de la Torre A, Bricheno L, Blyth E, Bell VA, Davies H, Marthews TR, O'Neill C, Rumbold H, O'Dea E, Brereton A, Guihou K, Hines A, Butenschon M, Dadson SJ, Palmer T, Holt J, Reynard N, Best M, Edwards J, Siddorn J. 2018. The UKC2 regional coupled environmental prediction system. *Geosci Model Dev* **11**: 1–42.

Lewis HW, Sanchez JMC, Arnold A, Fallmann J, Saulter A, Graham J, Bush M, Siddorn J, Palmer T, Lock A, Edwards J, Bricheno L, de la Torre AM, Clark J. 2019. The UKC3 regional coupled environmental prediction system. *Geosci Model Dev* **12**: 6.

Li JG. 2011. Global transport on a spherical multiple-cell grid. *Mon Weather Rev* **139**: 1536 – 1555.

Lionello JD, Malguzzi P, Buzzi A. 1998. Coupling between the Atmospheric Circulation and the Ocean Wave Field: An Idealized Case. *J Phys Oceanogr* **28**: 161–177.

Lock A, Edwards J, Smith R. 2013. Unified Model Documentation Paper 24: The Parametrization of Boundary Layer processes, technical report, UM version 8.6, Met Office.

Lock AP. 2001. The numerical representation of entrainment in parametrizations of boundary layer turbulent mixing. *Mon Weather Rev* **129**: 11481163.

Lock AP. 2007. The parametrization of boundary layer processes. unified model documentation paper, **24**.

Lorenz EN. 1963. Deterministic nonperiodic flow. *J Atmos Sci* **20**: 130–141.

Ludwig P, Pinto JG, Reyers M, Gray SL. 2014. The role of anomalous sst and surface fluxes over the southeastern North Atlantic in the explosive development of windstorm Xynthia. *Q J R Meteorol Soc* **140**: 1729–1741.

Madec G. 2016. Nemo reference manual 3_6_stable:nemo ocean engine.

Madonna E, Wernli H, Joos H, Martius O. 2014. Warm conveyor belts in the era-interim dataset (19792010). part i: Climatology and potential vorticity evolution. *J Clim* **27**: 3–26.

Mahmood S, Lewis H, Arnold A, Castillo J, Sanchez C, Harris C. 2021. The impact of time-varying sea surface temperature on uk regional atmosphere forecasts. *Meteorol Appl* **28**: 1–16.

Manning C, Kendon E, Fowler H, Robertst NM, Berthou S, Suri D Roberts M. 2021. Extreme windstorms and sting jets in convection-permitting climate simulations over Europe. *Clim Dyn* .

Martínez-Alvarado O, Baker L, Gray S, Methven J, Plant S. 2014. Distinguishing the cold conveyor belt and sting jet airstreams in an intense extratropical cyclone. *Mon Weather Rev* **142**: 2571 – 2595.

Martínez-Alvarado O, Gray S, Catto J, Clark P. 2012. Sting jets in intense winter north-atlantic windstorms. *Environ Res Lett* **7**: 1–8.

McCabe A, Swinbank R, Tennant W, Lock A. 2016. Representing model uncertainty in the Met Office convection-permitting ensemble prediction system and its impact on fog forecasting. *Q J R Meteorol Soc* **142**: 2897–2910.

Merchant CJ, Jonah O, Emma RJ, Fiedler E, Bulgin C, Corlett GK, Good S, McLaren A, Rayner N, Morak-Bozzo S, Donlon C. 2014. Sea surface temperature datasets for climate applications from Phase 1 of the European Space Agency Climate Change Initiative (SST CCI). *Q J R Meteorol Soc* **1**: 179–191.

Met Office. 2008. Met office (2008): Ship synop reports from ship, buoy and fixed platform stations collected by the met office metdb system. ncas british atmospheric data centre, date of citation. https://catalogue.ceda.ac.uk/uuid/65ca7898647cc3686492bcb8bb483a1cl. Accessed: 2021-12-10.

MetOffice. 2018. Storm ali. URL https://www.metoffice.gov.uk/weather/warnings-and-advice/uk-storm-centre/storm-ali.

Miles J. 1960. On the generation of surface waves by shear flows. *J Fluid Mech* **7**: 469–478.

Miles JW. 1957. On the generation of surface waves by shear flows. *J Fluid Mech* **3**: 185–204.

Mogensen KS, Magnusson L, Bidlot JR. 2017. Tropical cyclone sensitivity to ocean coupling in the ECMWF coupled model. *J Geophys Res Oceans* **122**: 4392–4412.

Molina MO, Gutiérrez C, Sánchez E. 2021. Comparison of ERA5 surface wind speed climatologies over Europe with observations from the HadISD dataset. *Q J R Meteorol Soc* **144**: 943–969.

Molteni F, R B, Palmer T, Petroliagis T. 1996. The ECMWF ensemble prediction system: Methodology and validation. *Q J R Meteorol Soc* **122**: 73–119.

Motzfeld H. 1937. Die turbulente strömung an welligen wänden. *Z angew Math mech* **17**: 193–212.

Munich Re. 2002. Winter storms in europe (II) - Analysis of 1999 losses and loss potentials. Munich Reinsurance Group. Munich.

Neu U, Akperov MG, Bellenbaum N, Benestad R, Blender R, Caballero R, Cocozza A, Dacre HF, Feng Y, Fraedrich K, Grieger J, Gulev S, Hanley J, Hewson T, Inatsu M, Keay K, Kew

SF, Kindem I, Leckebusch GC, Liberato MLR, Lionello P, Mokhov II, Pinto JG, Raible CC, Reale M, Rudeva I, Schuster M, Simmonds I, Sinclair M, Sprenger M, Tilinina ND, Trigo IF, Ulbrich S, Ulbrich U, Wang XL, Wernli H. 2013. IMILAST: A community effort to intercompare extratropical cyclone detection and tracking algorithms. *Bull Am Meteorol Soc* **94**: 529547.

NOAA. 2020. www.cpc.ncep.noaa.gov/products/precip/CWlink/pna/nao.shtml. Accessed: 2022-03-30.

Norris JR. 1998. Low cloud structure over the ocean from surface observations. Part I: Relationship to advection and the vertical distribution of temperature and moisture. *J Clim* **11**: 369–382.

Nuss W, Anthes R. 1987. A numerical investigation of low-level processes in rapid cyclogenesis. *Mon Weather Rev* **115**: 2728–2743.

PAFA Consulting Engineers. 2001. Weather-sensitive offshore operations and Metocean data. https://www.hse.gov.uk/research/otopdf/2001/oto01022.pdf.

Panofsky H, Tennekes H, Lenschow D, Wyngaard J. 1977. The characteristics of turbulent velocity components in the surface layer under convective conditions. *Boundary-Layer Meteorol* **11**: 355361.

Parton GA, Dore A, Vaughan G. 2010. A climatology of mid-tropospheric mesoscale strong wind events as observed by the MST radar, Aberystwyth. *Meteor Appl* **17**: 340–354.

Pfahl S, Wernli H. 2012. Quantifying the relevance of cyclones for precipitation extremes. *J Clim* **25**: 6770 – 6780.

Phillips OM. 1957. On the generation of waves by turbulent wind. *J Fluid Mech* **57**: 417–445.

Pinto J, Gómara I, Masato G, Dacre HF, Woollings T, Caballero R. 2014. Large-scale dynamics associated with clustering of extratropical cyclones affecting Western Europe. *J Geophys Res* **119**: 704–713.

Ponce de León S, Bettencourt J. 2021. Composite analysis of North Atlantic extra-tropical cyclone waves from satellite altimetry observations. *Adv Space Res* **68**: 762–772.

Ponce de León S, Guedes Soares C. 2014. Extreme wave parameters under North Atlantic extratropical cyclones. *Ocean Model* **81**: 78–88.

Porson A, Carr J, Hagelin S, Darvell R, North R, Walters D, Mylne K, Mittermaier M, Willington S, Macpherson B. 2020. Recent upgrades to the Met Office convective-scale ensemble: An hourly time-lagged 5-day ensemble. *Q J R Meteorol Soc* **146**: 3245–3265.

Powell M, Vickery P, Reinhold T. 2003. Reduced drag coefficient for high wind speeds in tropical cyclones. *Nature* **422**: 279–283.

Pryor S, Barthelmie R. 2021. A global assessment of extreme wind speeds for wind energy applications. *Nat Energy* **6**: 268–276.

Raynaud L, Bouttier F. 2017. The impact of horizontal resolution and ensemble size for convective-scale probabilistic forecasts. *Q J R Meteorol Soc* **143**: 3037–3047.

Ren X, Perrie W, Long Z, Gyakum J. 2004. Atmosphereocean coupled dynamics of cyclones in the midlatitudes. *Mon Weather Rev* **132**: 2432–2451.

Ricchi A, Miglietta MM, Barbariol F, Benetazzo A, Bergamasco A, Bonaldo D, Cassardo C, Falcieri F, Modugno C, Russo A, Sclavo M, Carniel S. 2017. Sensitivity of a Mediterranean Tropical-Like Cyclone to different model configurations and coupling strategies. *Atmosphere* **8**: 1–23.

Ricchi A, Miglietta MM, Bonaldo D, Cioni G, Rizza U, Carniel S. 2019. Multi-physics ensemble versus atmosphereocean coupled model simulations for a tropical-like cyclone in the Mediterranean Sea. *Atmosphere* **10**: 1–22.

Roberts N. 2008. Assessing the spatial and temporal variation in the skill of precipitation forecasts from an NWP model. *Meteorol. Appl.* **15**: 163–169.

Roberts NM, Lean HW. 2008. Scale-selective verification of rainfall accumulations from high-resolution forecasts of convective events. *Mon Weather Rev* **136**: 78 – 97.

Rockel B, Will A, Hense A. 2008. The Regional Climate model COSMO–CLM (CCLM). *Meteorol Z* **17**: 347–348.

Rulent J, Calafat FM, Banks CJ, Bricheno LM, Gommenginger C, Green JAM, Haigh ID, Lewis H, Martin ACH. 2020. Comparing Water Level Estimation in Coastal and Shelf Seas From Satellite Altimetry and Numerical Models. *Front Mar Sci* **7**.

Schellander-Gorgas T, Wang Y, Meier F, Weidle F, Wittmann C, Kann A. 2017. On the forecast skill of a convection-permitting ensemble. *Geosci Model Dev* **10**: 35–56.

Schultz DM, Bosart LF, Colle BA, Davies HC, Dearden C, Keyser D, Martius O, Roebber PJ, Steenburgh WJ, Volkert H, Winters AC. 2019. Extratropical Cyclones: A Century of Research on Meteorology's Centerpiece. *Meteorological Monographs* **59**: 16.1–16.56.

Schultz DM, Keyser D, Bosart LF. 1998. The effect of large–scale flow on low–level frontal structure and evolution in midlatitude cyclones. *Mon Weather Rev* **126**: 1767–1791.

Schultz DM, Zhang F. 2007. Baroclinic development within zonally–varying flows. *Q J R Meteorol Soc* **33**: 1101–1112.

Seity Y, Brousseau P, Malardel S, Hello G, Bénard P, Bouttier F, Lac C, Masson V. 2011. The AROME-France convective-scale operational model. *Mon Weather Rev* **139**: 976–991.

Shapiro MA, Keyser D. 1990. *Fronts, jet streams and the tropopause. extratropical cyclones: the erik palm'en memorial volume, c. newton and e. e o holopainen*. American Meteorological Society.

Shapiro MA, Wernli H, Bao JW, Metheven J, Zou X, Doyle J, Holt T, Donall-Grell E, Neiman P. 1999. *A planetary–scale to mesoscale perspective of the life cycles of extratropical cyclones: The bridge between theory and observations*. in The life cycles of extratropical cyclones, Shapiro MA, Grønas S (eds), 139–185pp., Amer. Meteorol. Soc.

Sharp E, Dodds P, Barrett M, Spataru C. 2015. Evaluating the accuracy of CFSR reanalysis hourly wind speed forecasts for the UK, using in situ measurements and geographical information. *Renew Energy* **77**: 527–538.

Sinclair V, Belcher S, Gray S. 2010. Synoptic controls on boundary–layer characteristics. *Boundary-Layer Meteorol* **134**: 387–409.

Skamarock WC, Klemp JB. 2008. A time–split non–hydrostatic atmospheric model for weather research and forecasting applications. *J Comput Phys* **227**: 3465–3485.

Smart D, Browning K. 2014. Attribution of strong winds to a cold conveyor belt and sting jet. *Q J R Meteorol Soc* **140**: 595–610.

Smith GC, Bélanger JM, Roy F, Pellerin P, Ritchie H, Onu K, Roch M, Zadra A, Colan DS, Winter B, Fontecilla JS, Deacu D. 2018. Impact of coupling with an ice-ocean model on global medium-range NWP forecast skill. *Mon Weather Rev* **146**: 1157 – 1180.

Smith RNB. 1990. A scheme for predicting layer clouds and their water content in a general circulation model. *Q J R Meteorol Soc* **116**: 435–460.

Smith S. 1988. Coefficients for sea surface wind stress, heat flux, and wind profiles as a function of wind speed and temperature. *J Geophys Res* **93**: 15 467–15 472.

Smith SD, Anderson RJ, Oost W. 1992. Sea surface wind stress and drag coefficients: the HEXOS results. *Boundary-Layer Meteorol,* **60**: 109–142.

Snyder R. 1974. A field study of wave-induced pressure fluctuation above surface gravity waves. *J Marine Res* **32**: 497–531.

Snyder R, Dobson F, Elliott J, Long R. 1981. Array measurements of atmospheric pressure fluctuations above surface gravity wave. *J Fluid Mech* **102**: 1–59.

Staniforth A, White A, Wood N, Thuburn J, Zerroukat M, Cordero E, Davies T, Tiamantakis M. 2006. Unified model documentation paper no. 15. joy of u.m. 6.3 - model formulation. URL http://cms.ncas.ac.uk/wiki/Docs/MetOfficeDocs.

Stull RB. 1988. *An introduction to Boundary Layer Meteorology*. Cambridge University

Press.

Sullivan PP, Edson J, Hristov T, McWilliams J. 2008. Large-eddy simulations and observations of atmospheric marine boundary layers above nonequilibrium surface waves. *J Atmos Sci* **65**: 12251245.

Sullivan PP, McWilliams JC, G PE. 2014. Large-eddy simulation of marine atmospheric boundary layers above a spectrum of moving waves. *J Atmos Sci* **71**: 4001–4027.

Sullivan PP, McWilliams JC, Moeng CH. 2000. Simulation of turbulent flow over idealized water waves. *J Fluid Mech* **404**: 47–85.

Swiss Re. 2011. Natural catastrophes and man-made disasters in 2010: a year of devastating and costly events. Sigma. No 1/2011. "https://www.swissre.com/dam/jcr:d58dea24-f966-4614-8b90-3acd9b0a361f/sigma1_2011_en.pdf".

Sánchez C, Methven J, Gray SL, Cullen M. 2020. Linking rapid forecast error growth to diabatic processes. *Q J R Meteorol Soc* **146**: 3548–3569.

Tang Y, Lean HW, Bornemann J. 2013. The benefits of the Met Office variable resolution NWP model for forecasting convection. *Meteorol Appl* **20**: 417–426.

Tennant W, Beare S. 2014. New schemes to perturb sea-surface temperature and soil moisture content in MOGREPS. *Q J R Meteorol Soc* **140**: 1150–1160.

Tennant W, Shutt G, Arribas A, Thompson S. 2011. Using a stochastic kinetic energy backscatter scheme to improve MOGREPS probabilistic forecast skill. *Mon Weather Rev* **139**: 1190–1206.

Theis SE, Hense A, Damrath U. 2005. Probabilistic precipitation forecasts from a deterministic model: a pragmatic approach. *Meteorol Appl* **12**: 257–268.

Thorncroft C D HBJ, McIntyre ME. 1993. Two paradigms of baroclinicwave life-cycle behaviour. *Q J R Meteorol Soc* **119**: 17–56.

Titchner HA, Rayner NA. 2014. The Met Office Hadley Centre sea ice and sea surface temperature data set, version 2: 1. sea ice concentrations. *J Geophys Res* **119**: 2864–2889.

Tolman H. 2016. User manual and system documentation of wavewatch iiiő, version 5.16, tech. note 329.

Tonani M, Sykes P, King RR, McConnel N, Péquignet AC, ODea E, Graham JA, Polton J, Siddorn J. 2019. The impact of a new high-resolution ocean model on the Met Office North-West European Shelf forecasting system. *Ocean Sci* **15**: 1133–1158.

Toth Z, Kalnay E. 1997. Ensemble forecasting at NCEP and the breeding method. *Mon Weather Rev* **125**(12): 3297–3319.

Troen I, Mahrt L. 1986. A simple model of the atmospheric boundary layer; sensitivity to surface evaporation. *Boundary-Layer Meteorol* **37**: 129–148.

Ulbrich U, Bürger G, Schriever Dea. 1993. The effect of a regional increase in ocean surface roughness on the tropospheric circulation: a GCM experiment. *Clim Dyn* **8**: 277–285.

Ursell F. 1956. *Wave generation by wind. in surveys in mechanics (ed. G.K. Batchelor).* Cambridge University Press.

Valcke S, Craig T, Coquart L. 2015. OASIS3–MCT user guide, oasis3–mct 3.0, technical report, tr/cmgc/15/38, cerfacs/cnrs.

Valiente NG, Saulter A, Edwards JM, Lewis HW, Castillo Sanchez JM, Bruciaferri D, Bunney C, Siddorn J. 2021. The impact of wave model source terms and coupling strategies to rapidly developing waves across the North-West European Shelf during extreme events. *J Mar Sci Eng* **9**(4).

Varlas G, Katsafados P, Papadopoulos A, Gerasimos K. 2017. Implementation of a two–way coupled atmosphere-ocean wave modeling system for assessing air-sea interaction over the Mediterranean Sea. *Atmos Res* **208**: 201–217, doi:10.1016/j.atmosres.2017.08.019.

Vautard R, Cattiaux J, Yiou P, Thepaut JN, Ciais P. 2010. Northern hemisphere atmospheric stilling partly attributed to an increase in surface roughness. *Nat Geosci* **3**: 756–761.

Vellinga M, Copsey D, Graham T, Milton S, Johns T. 2020. Evaluating benefits of two-way oceanatmosphere coupling for global NWP forecasts. *Weather Forecast* **35**: 2127–2144.

Vemuri A. 2019. A new coupled modelling framework for turbine inflow generation: mesoscale-synthetic turbulence. Master's thesis, Delft University of Technology.

Volonté A, Turner AG, Schiemann R, Vidale PL, Klingaman NP. 2022. Characterising the interaction of tropical and extratropical air masses controlling East Asian summer monsoon progression using a novel frontal detection approach. *Weather Clim Dynam* **3**: 575–599.

Vries H, Scher S, Haarsma R, Drijfhout S, van Delden A. 2019. How Gulf-Stream SST-fronts influence Atlantic winter storms. *Clim Dyn* **52**: 5899–5909.

Wahle K, Staneva J, Koch W, Fenoglio-Marc L, Ho-Hagemann H, Stanev E. 2017. An atmospherewave regional coupled model: improving predictions of wave heights and surface winds in the southern North Sea. *Ocean Sci* **13**: 289–301.

Walters D, Boutle I, Brooks M, Melvin T, Stratton R, Vosper S, Wells H, Williams K, Wood N, Allen T, Bushell A, Copsey D, Earnshaw P, Edwards J, Gross M, Hardiman S, Harris C, Heming J, Klingaman N, Levine R, Manners J, Martin G, Milton S, Mittermaier M, Morcrette C, Riddick T, Roberts M, Sanchez C, Selwood P, Stirling A, Smith C, Suri D, Tennant W, Vidale PL, Wilkinson J, Willett M, Woolnough S, Xavier P. 2017. The Met Office Unified Model Global Atmosphere 6.0/6.1 and JULES Global Land 6.0/6.1 configurations. *Geoscientific Model Development* **10**: 1487–1520.

Wang XL, Zwiers FW, Swail VR, Feng Y. 2009. Trends and variability of storminess in the northeast Atlantic region, 1874-2007. *Clim Dyn* **33**: 1179–1195.

Weber S. 1994. Statistics of the air-sea fluxes of momentum and mechanical energy in a coupled wave-atmosphere model. *J Phys Oceanogr* **24**: 1388–1398.

Wernli H, Paulat M, Hagen M, Frei C. 2008. SAL-A novel quality measure for the verification of quantitative precipitation forecasts. *Mon Weather Rev* **136**: 4470–4487.

Whittaker LM, Horn LH. 1984. Northern Hemisphere extratropical cyclone activity for four mid-season months. *Journal of Climatology* **4**: 297–310.

Wilson DR, Ballard SP. 1999. A microphysically based precipitation scheme for the UK Meteorological Office Unified Model. *Q J R Meteorol Soc* **125**: 1607–1636.

WMO. 1970. Commission for maritime meteorology. The Beaufort scale of wind force : (technical and operational aspects).

Wood R. 2012. Stratocumulus clouds. *Mon Weather Rev* **140**: 2373 – 2423.

Woods Hole Oceanographic Institute. 2022. Air-sea interaction graphics. URL `https://www2.whoi.edu/site/casimas/`.

Zhang DL, Radeva E, Gyakum J. 1999. A family of frontal cyclones over the western atlantic ocean. Part II: Parameter studies. *Mon Weather Rev* **127**: 1745–1760.

Zschenderlein P, Pardowitz T, Ulbrich U. 2019. Application of an object-based verification method to ensemble forecasts of 10-m wind gusts during winter storms. *Meteorol Z* **28**: 203–213.